THE UNIVERSITY *of* EDINBURGH

High Performance Drive Circuits for Integrated MicroLED/CMOS Arrays for Visible Light Communication (VLC)

Ahmad Wafi Mahmood Zuhdi

A thesis Submitted for the degree of Doctor of Philosophy

The University of Edinburgh

2014

Abstract

Wireless communication is a form of communication that has been around for over hundreds of years and is the fastest growing segment of the communication industry. Today, wireless communication has become an essential part of almost everyone's daily life, and the number of users has increased exponentially over the last decade with the introduction of the internet, mobile devices and smart phones. Radio Frequency (RF) transmission is arguably the most popular method of communication and is available worldwide. With the rapid progress in technology and the increase of number of users, the limited RF spectrum is becoming more congested which led to numerous research efforts to find an alternative that can help to alleviate the pending problem. One of the proposed solutions is Visible Light Communication (VLC), which uses visible Light Emitting Diode (LED) for data transmission. In this thesis, three integrated microLED/Complementary Metal Oxide Semiconductor (CMOS) Integrated Circuits (ICs) are presented with the main aim of increasing the data rate of transmission.

The first microLED/CMOS IC presented here is the Generation V microLED/CMOS driver which represents the continuation of the earlier work in the HYPIX project, which aimed to develop a microLED/CMOS driver to optically pump an organic polymer laser. A 40x10 pixel-array of Generation V microLED/CMOS driver was thus designed, primarily for optical pumping polymer lasing purposes, but has also demonstrated the ability to perform communication transmission using an On-Off Keying (OOK) modulation scheme. The driver consumes up to 330mA current and produces approximately 12mW of optical power from a single pixel, which is about 3 times higher than its predecessor.

The second microLED/CMOS IC is the microLED/CMOS Current Feedback (CCFBK) driver which was designed to facilitate Orthogonal Frequency Division Multiplexing (OFDM) modulation. OFDM is one of the modulation schemes, adopted from the RF domain, that was proposed to be implemented in VLC in order to increase the data transmission rate. To the best of the author's knowledge, the microLED/CCFBK driver is the first CMOS driver for microLED that was designed to perform analogue modulation for VLC purposes. The driver is characterised and shows the ability to produce up to 3.5mW of optical power with a data transmission rate of up to 486Mbit/s.

The microLED/CMOS Optical Feedback (COFBK) driver is the third microLED/CMOS IC presented in this thesis. The driver looks to improve on the performance of the microLED/CCFBK driver. OFDM transmission requires high linearity to ensure low Bit Error Rate (BER) transmission. However, the optical power output of an LED is not, in general, linear with the input voltage signal. The microLED/COFBK driver looks to increase the linearity of the optical power output by integrating a microLED and a photodiode in a single pixel to create a feedback loop. Once again, to the best of the author's knowledge, the microLED/COFBK driver is the first CMOS driver for microLED which integrates both optical source and sensor in a single pixel to help linearise the optical power output for communication purposes; in this case, VLC. For a similar range of optical power, the microLED/COFBK driver shows a reduction about 5.3% in the degree of non-linearity compared to the microLED/CCFBK driver and produces lower Total Harmonic Distortion (THD). The microLED/COFBK driver showed the potential to increase the data rate by a factor of four over that of microLED/CCFBK driver.

The analogue modulated microLED/CMOS ICs described here are the first-generation drivers that have demonstrated the possibilities to increase the data rate using OFDM. A number of possible design improvements have been identified which will enhance future performance and integration with the standard VLC system.

Declaration of Originality

I hereby declare that:

(a) The thesis has been composed entirely by myself;

(b) The work is my own and originated in the School of Engineering at the University of Edinburgh except where clearly indicated

(c) The work has not been submitted for any other degree or professional qualification

Ahmad Wafi Mahmood Zuhdi

Table of Contents

Abbreviation

ACO-OFDM	AC-Orthogonal Frequency Division Multiplexing
AGC	Automatic Gain Control
AlGaAs	Aluminium Gallium Arsenide
AlGaP	Aluminium Gallium Phosphide
AlIn-GaN	Aluminium Indium Gallium Nitride
AM	Amplitude Modulation
AMS	Austria Microsystem
BER	Bit Error Rate
BERT	Bit Error Rate Test
CCFBK	CMOS Current Feedback
CCVS	Current Controlled Voltage Source
CD	Coherent Detection
CMOS	Complementary Metal-Oxide Semiconductor
COFBK	CMOS Optical Feedback
CP	Cyclic Prefix
DAB	Digital Audio Broadcasting
DCO-OFDM	DC-Orthogonal Frequency Division Multiplexing
DD	Direct Detection
DMT	Discrete Multi-tone
DSL	Digital Subscriber Line
DVB	Digital Video Broadcasting
EM	Electromagnetic
EPSRC	Engineering and Physical Science Research Council
FEC	Forward Error Correction

FFT	Fast Fourier Transform
FM	Frequency Modulation
F-OFDM	Flip-Orthogonal Frequency Division Multiplexing
FPGA	Field Programmable-Gate Array
GaAs	Gallium Arsenide
GaAsP	Gallium Arsenide Phosphide
GaN	Gallium Nitride
GUI	Graphic User Interface
HIT-KIT	High Performance Interface Kit
I/O	Input/Output
IC	Integrated Circuit
ICP	Inductively Coupled Plasma
IEEE	Institute of Electrical and Electronics Engineers
IFFT	Inverse Fast Fourier Transform
IM-DD	Intensity Modulation-Direct Detection
IMNS	Institute of Micro and Nano Systems
InGaN	Indium Gallium Nitride
IoP	Institute of Photonics
I-Q	In-phase and Quadrature
IR	InfraRed Communication
IrDA	InfraRed Data Association
IRED	InfraRed Light Emitting Diode
ISI	Inter-Symbol Interference
I-V	Voltage-Current Characteristic
JEITA	Japan Electronics and Information Technologies Industries Associations
Laser	Light Amplification by Stimulated Emission of Radiation

LED	Light Emitting Diode
L-I	Current-Light Characteristic
L-V	Voltage-Light Characteristic
MCM	Multi-Carrier Modulation
microLED	Micro-pixelated Light Emitting Diode
MOSFET	Metal-Oxide-Semiconductor Field Effect Transistor
MOVCD	Metal Organic Vapour Chemical Deposition
MQW	Multiple Quantum Well
Ni-Au	Nickel-Gold
OC	Optical Communication
OFDM	Orthogonal Frequency Division Multiplexing
OOK	On-Off Keying
OSL	Organic Semiconductor Lasing
PA	Power amplifier
PAPR	Peak Average Power Ratio
PBO	Power Back-off
PCB	Printed Circuit Board
PCM	Pulse Code Modulation
Pd	Palladium
PLC	Power Line Communication
PLCC	Plastic Leaded Chip Carrier
PM	Phase Modulation
PSK	Phase Shift Keying
PWL	Piecewise Linear
QAM	Quadrature Amplitude Modulation
R&D	Research and Development
RF	Radio Frequency

RMS	Root Mean Square
SC-BPSK	Sub-Carrier Binary Phase Shift Keying
SCM	Single Carrier Modulation
SFDR	Spurious Free Dynamic Range
SiC	Silicon Carbide
SIM-OFDM	Sub-Index Modulation Orthogonal Frequency Multiplexing
SiO2	Silicon Dioxide
SNR	Signal to Noise Ratio
TED	Technology, Entertainment and Design
THD	Total Harmonic Distortion
TIA	Transimpedance Amplifier
Ti-Au	Titanium-Gold
TSV	Through-Silicon Via
U-OFDM	Unipolar Orthogonal Frequency Division Multiplexing
UP-VLC	Ultra Parallel Visible Light Communication
VCCS	Voltage Controlled Current Source
VCO	Voltage-Controlled Oscillator
VCVS	Voltage-Controlled Voltage Source
VLC	Visible Light Communication
VLCC	Visible Light Communication Consortium
WLAN	Wireless Local Area Network
XML	Extensible Markup Language
ZnSe	Zinc Selenide
α	Feedforward gain
β	Feedback gain

List of Figures

List of Tables

List of Symbols and Constant

Symbol		Value
e	Electron Charge Constant	1.602×10^{-19} C
k	Boltzmann Constant	1.380×10^{-23} JK^{-1}
h	Planck Constant	6.626×10^{-34} Js^{-1}
c	Speed of Light	2.998×10^{8} ms^{-1}
ε_0	Dielectric constant in air	8.85×10^{-12}F/m
ε_i	Relative Dielectric constant in Silicon	11.68

Chapter 1 : Introduction

1.1. Wireless Visible Light Communication

Wireless communication is a form of communication that has been around for hundreds of years. Smoke signals in the pre-industrial age can be described as one of the earliest methods of wireless communication. Since then, wireless communication has gone through many evolutions, and today, it is the fastest growing segment of the communication industry [1].

Radio is a transmission of signals through free space by means of electromagnetic (EM) waves with frequencies in the range of 3 kHz to 300 GHz. These transmission frequencies are called the radio wave frequency transmission, or RF. RF was invented in the late 1890s and by the early 1900s RF transmission across the Atlantic Ocean had been established [2]. Since then, there has been rapid progress of the technology and at the present time, RF is available worldwide and is possibly the most widely used method of communication. To avoid any interference between RF transmissions, different transmissions are allocated to their respective spectrums [3]. In addition to the introduction of the internet, mobile devices and smart phones, the fast growing number of users is somewhat pushing the system's capability to its limit as the bandwidth to allow reasonable spatial coverage is running out rapidly. The allocation of the spectrum in the United Kingdom as of February 2013 clearly indicates the need for "extra" spectrum [3].

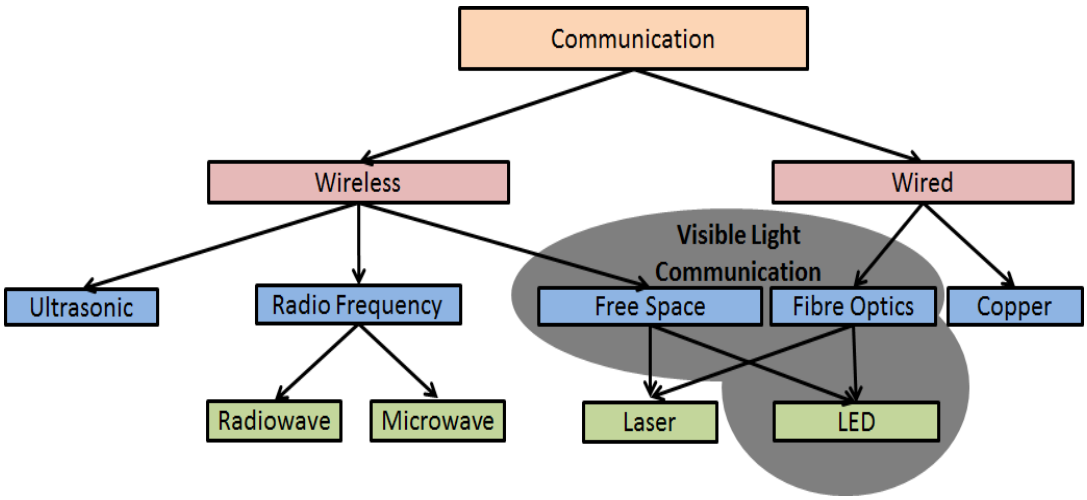

Figure 1-1 – Communication divisions. VLC is highlighted in the grey area

As the RF spectrum becomes more congested, there is increasing interest in communication in other frequency ranges in the EM spectrum to assist the problem. One of the options is Visible Light Communication, or VLC for short, that has gathered interest over the last couple of years. One of the main reasons for its growing popularity is that it addresses the spectrum problem in RF and does not interfere with existing systems. Visible light is at a higher frequency in the EM spectrum, ranging from 400 THz to 800 THz, which is about 1000 times larger than the radiowave spectrum. VLC is categorised under Optical Communication (OC), which until recently, dealt mostly with lasers and guided waves. The name "VLC" describes a communication system that uses electromagnetic radiation that is visible to the human eye (light), in either optical fibre or free-space. For free-space applications, visible Light Emitting Diode (LED) is the most widely used light source for illumination that has the capability for fast modulation. Nowadays, visible LED is already incorporated into many devices such as mobile phones, televisions, automotive lighting systems, traffic lights and some lighting units for domestic, commercial and industrial use. The LED illumination market is predicted to grow and with the growth comes the broader potential for a range of VLC systems. Figure 1-1 shows the communication division with VLC is highlighted in grey. In this thesis, however, the focus is on free-space VLC.

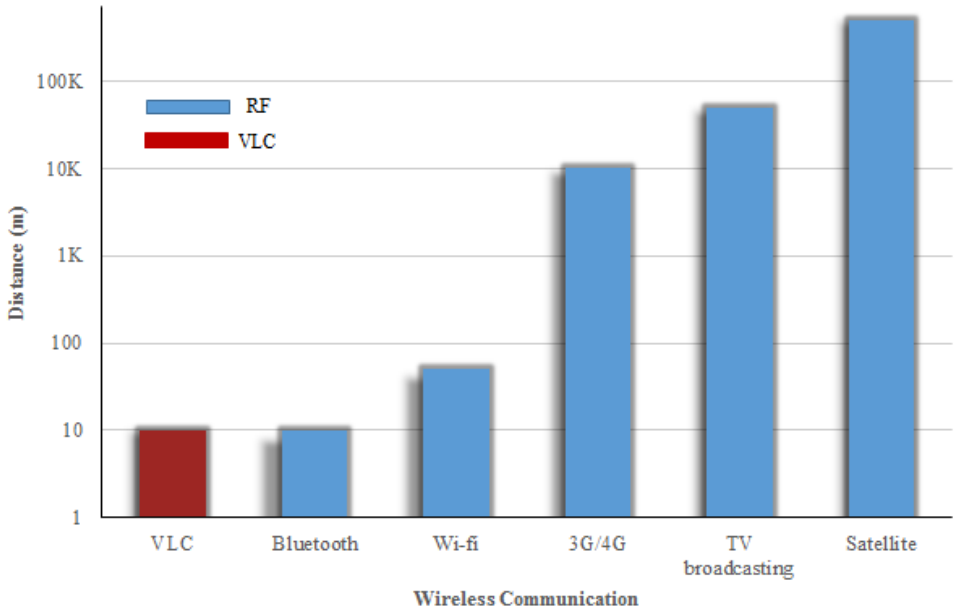

Figure 1-2 – comparison of the distance covered by RF and VLC

Figure 1-2 shows a comparison between RF and VLC against distance covered by both types of wireless communication. Fundamentally, VLC inherits greater bandwidth than RF. Even so, VLC would not be able to fully replace RF as the main method of communication. This is

mainly due to the short distance covered (as shown in Figure 1-2) and light, in general, cannot penetrate any obstacles in its path. Given the drawbacks, however, VLC is still an exciting prospect especially for short distance communications which could potentially give higher data rates than conventional Wi-Fi [4].

1.2. Contribution to Knowledge

LED is a rapidly developing area and its field of applications has expanded over the years. Apart from its low power consumption and relatively high efficiency, which has seen LED replacing incandescent lights in households for general illuminations; these solid-state sources can modulate at a rate many times higher than their predecessor, thus offering a possibility of broadcasting information at the same time as illuminating the room. Because of this, LED is seen as a very exciting prospect and the prime source of illumination for the VLC system.

As VLC is still fairly new compared to the mature RF system, there is much space that needs to be explored, i.e. the illumination source, the source driver and the modulation method. The main objective of this thesis is to explore and design high performance LED driver circuits to increase the data rate of a VLC transmission.

This project looks to integrate micro-pixelated LED (microLED) and Complementary Metal Oxide Semiconductor (CMOS) to produce a highly integrated system to serve as a VLC module on a single substrate. microLED was chosen in this project because of its ability to have higher bandwidth than commercial LEDs, thus giving potential for a higher transmission data rate. CMOS, on the other hand, was chosen due to its potential to be mass manufactured while having the ability to integrate many elements on a single substrate. Therefore, both optical source (microLED) and sensor can be integrated into a single pixel which opens up a new application to the system. The work in this thesis, to the best of the author's knowledge, is the first demonstration of CMOS drive integrated circuits (IC) for microLED arrays that modulate an analogue signal for VLC applications. Moreover, also to the best of the author's knowledge, the project is the first demonstration that integrates an optical source and a sensor within a single pixel to improve the performance of the optical source driver for communication purposes.

1.3. Aims

The aim of the project is to explore and develop drivers that integrate microLED on a CMOS substrate and to increase the transmission data rate in a VLC system. In this thesis, three CMOS drive ICs for microLED arrays are presented. One of the microLED/CMOS drive ICs integrates an optical source and a sensor in a single pixel to create a novel hybrid technology. The source-sensor integration is performed to linearize the optical power output signal of the microLED in order to transmit higher data rates. The performance of the three microLED/CMOS drive ICs and their ability to perform communication links were verified in practical laboratory environment. The specific aims of the projects are:

- Design and investigate the maximum possible optical power output from a microLED/CMOS drive IC for VLC application.
- Study and design a microLED/CMOS drive IC which facilitates analogue modulated signal which can increase the data rate of a VLC transmission.
- Characterise and demonstrate the microLED/CMOS drive IC ability and its performance limitation.
- Demonstrate the microLED/CMOS driver IC's performance for the communication environment.
- Identify the microLED/CMOS driver IC's strengths and weaknesses in possible future development to improve the performance of these drivers.

1.4. Thesis Outline

Chapter 2 provides the background knowledge and an overview on VLC including its history, comparison with RF and the chosen modulation scheme that is implemented in this project. The chapter continues to investigate and identifies the weakness of the modulation scheme and proposes a solution in order to increase the VLC data rates. The chapter also discusses the basic operation of the LED and CMOS photodiode.

Chapter 3 introduces the microLED and the model that was developed and used in the project. The chapter later presents the first of the three microLED/CMOS drive ICs that were developed during the duration of the project. The microLED/CMOS driver that is presented in this chapter is a continuation from the previous work under the HYPIX project, which is not

only designed for VLC applications, but also for optical pumping polymer lasing purposes. The characteristic of the driver was verified and presented in the chapter.

Chapter 4 describes the second microLED/CMOS drive IC, which is based on negative feedback that was designed to facilitate an analogue modulation signal. The theory of negative feedback is discussed in the chapter together with the driver's macromodel and the transistor level design. The characteristic of the driver is presented and discussed at the end of the chapter.

The final microLED/CMOS drive IC is presented in Chapter 5. The driver was designed as an improvement and as a performance comparison to the microLED/CMOS driver presented in Chapter 4. The microLED/CMOS driver presented in this chapter integrates both microLED and CMOS photodiode in a single pixel, creating an optical negative feedback loop, in order to linearize the optical power output signal. The feedback light from the microLED to the CMOS photodiode mechanism is discussed in the chapter followed by the driver's macromodel, transistor level design and measured characteristics.

Having presented the microLED/CMOS drive ICs and their characteristics in the previous chapters, Chapter 6 compares the drivers' characteristics and their performances in transmitting communication signals.

Chapter 7 concludes the thesis with a summary of the work and proposes a number of different areas of research that could be investigated in the future to advance this work further.

Chapter 2 : Visible Light Communications System

2.1. Overview

2.1.1. Wireless – Radio Frequency vs. Visible Light Communication

Visible light and RF radiation inhabit different frequency bands within the EM spectrum therefore, they exhibit some similarities and some differences. While their similarities allow the VLC system to adopt some of the techniques used in RF, their differences need to be recognised. The differences are summarised in Table 2-1. The spectrum bandwidth available in VLC is about 1000 times greater than RF. However, the carrier frequency of a VLC system is determined by the optical source and its material. In RF, the carrier frequency can be determined by the electrical current that oscillates (local oscillator) in the required radio frequency. A basic property of a light generator, except for lasers, is that it produces incoherent emission. The signal is encoded in optical intensity and therefore no "negative" value can be transmitted, thus making the signal unipolar. RF transmission, on the other hand, exploits the wave by varying the signal's amplitude, frequency and phase or a combination of the three. Therefore, RF signal is a coherent, bipolar and complex signal.

RF has a relatively long wavelength (1 mm to 100 km compared to visible light wavelength of 380nm to 750nm) and can penetrate through most electrically-non-conducting materials such as building walls. Therefore, RF has been used mainly for long distance communication since its early days [2]. The reliable range of operation of VLC is somewhat limited by line of sight. This is because visible light has a much shorter wavelength than radiowaves and is therefore unable to penetrate most obstacles. This reduces the operation of VLC to a relatively short-distance in building communication. However, this would also mean that VLC performs with better security than RF, as the information does not "escape" the intended area. Additionally, because the bandwidth of the spectrum appears 'locally' to the area of illumination, the whole visible spectrum is available and not regulated by any authority. RF in contrast, requires regulatory permission and sharing is limited. This has led to some places such as airplanes and hospitals to ban the use of devices that employ RF so as to avoid any interference with their system. Both RF and visible light present no hazard to the user under a regular level of exposure, although there have been studies on how it could affect if overexposed [5, 6].

The first demonstration of modern VLC was performed by the Visible Light Communication Consortium (VLCC), a Japanese research group consisting of many companies in 2001 [7]. Today's VLC, however, is very much still in its research and development (R&D) phase. RF on the other hand, as mentioned in the previous chapter, has been developed and used widely since the early 1900's.

Property	VLC	RF
Bandwidth (Wavelength / Frequency range)	Very wide (400nm – 700nm / 400 THz – 800 THz)	Wide (1mm – 100km / 3 kHz – 300 GHz)
Carrier frequency	Determined by optical source material	Determined through the oscillating electrical field
Wave	Incoherent	Coherent
Transmission	Optical Intensity (LED)	Electrical field
Signal Polarity	Unipolar	Bipolar
Signal Type	Real value only (scalar)	Complex value (Vector)
Distance	Short	Medium to Long
Line of Sight limitation	Yes	No
Security	Higher security. Signals are secured within the illumination range	Lower Security as RF signal can penetrate wall
Spectrum availability and sharing restrictions	Unlicensed and widely available	Under regulatory and limited for sharing
Noise sources	Ambient light and interference from other users	Interference from other users
Health Hazard	No health hazards to human body at regular level of illumination	No health hazard at regular level of exposure
Standard	Beginning (new, in R&D stage)	Matured

Table 2-1 – Table of comparison between Visible Light Communication and Radio Frequency [8]

2.1.2. Legislation and Standards

The prospect of incorporating VLC components into an everyday lighting system has led to many research projects and developments by a numbers of universities, companies and organisation throughout the world. VLC standards were first published in Japan in 2007 when Japan Electronics and Information Technologies Industries Associations (JEITA) released its VLC standard (JEITA CP-1221 and JEITA CP-1222) which was used in its "Visible Light ID" system [9, 10]. In 2008, one of the first VLC based consortium called Visible Light

Communication Consortium (VLCC) released its own specification standard as a result of its joint cooperation with the InfraRed Data Association (IrDA). This standard adopts and expands the IrDA Physical Layer to the new VLCC specification [11]. The Institute of Electrical and Electronics Engineers (IEEE) Wireless Personal Area Network committee is also working on developing a standard for VLC technologies (Group 802.15 Task Group 7) since May 2008 [12, 13].

2.2. History

The term "Visible Light Communication" was only adopted recently to describe the technique and device used by the system. Generally known as "Optical Communications", the principle of using light to communicate is not new. Smoke and fire beacons were one example of the early forms of visible communication. Another ancient method was performed during the Greek and Roman era where soldiers used shiny shields as mirrors to reflect the sun for signalling. This method was later refined and renamed as the "Heliograph" [14].

The Heliograph was first presented by a German Professor, Carl Friedrich Gauss in 1821 [15]. Like the ancient Greeks, Heliograph uses the reflection of mirrors to transmit messages over a long distance. The flashes are produced by momentarily interrupting the beam using a shutter. In 1836, Samuel B. Morse introduced a method for transmitting text information for electrical telegraph system called the 'Morse Code'. This method sent pulses of electrical current which could be understood by a skilled translator at the receiving end [16]. The introduction of Morse code helped the development of light communication and was later adopted as series of lights on-lights off; which was widely used as a communication between ships or ship-to-light house. Alexander Graham Bell presented the Photophone in 1880, a few years after his other invention, the Telephone, was patented. While the telephone modulates electricity over conductive wire circuits, the photophone uses modulated light as a mean of projecting information. The photophone is the closest historical concept to the modern VLC [17].

The idea of communication using light was neither more widely adopted nor did it gain much attention due to the success of the telephone and RF communication in the early twentieth century. However, studies were still conducted and in 1957, Gordon Gould proposed the use of a high intensity light source called "Light Amplification by Stimulated Emission of Radiation" (Laser) to transmit light along a fibre [18]. Optical communication started to gain

more attention when semiconductor lasers were first realised in 1962 [19]. Fibre optic communication further developed as an important network of communication. Still, lasers were never intended to be used in free-space as its high powered light is a hazard to the human eye [20]. An alternative light source is needed if a low-cost, user friendly, free-space light communication is to be achieved.

Infrared communication (IR), on which the concept of VLC is based, was introduced by Gfellar and Bapst in 1978, which uses Infrared LED (IRED) for indoor wireless communication. Like VLC, IR was recognised as offering a major advantage particularly through the large and unregulated bandwidth [21]. However, a strong infrared radiation may result in eye or skin strain [22]. Therefore the use of IR has been limited to the public with low optical power applications such as TV or radio remote controls and handheld gadgets. With the development of higher bandwidth IRED recently, IR has been incorporated in gaming devices such as the Wii and X-box Kinect.

The first LED was introduced in 1907 when Henry Joseph Round discovered it unintentionally during his research on Silicon Carbide (SiC) crystals for possible use as a rectifier solid-state detector [23]. SiC, however, was never seen as a practical technology due to its very low brightness and very low electrical-to-optical power conversion [24]. Since SiC LED did not make the grade, various efforts have been made to find a more suitable compound. One of the range of compounds considered were the class III-IV compounds; mainly Gallium Arsenide (GaAs) and Aluminium Gallium Arsenide (AlGaAs) [25]. In 1962, the first III-IV LED was demonstrated with both GaAs and AlGaAs produced light in the red and infrared region. The success of GaAs and AlGaAs LED has led to further research in the III-IV compound such as Gallium Arsenide Phosphide (GaAsP). With GaAsP LED, emissions in the red, orange, yellow and green wavelength were achieved. GaAsP was first used as indicator lights on devices such as printed circuit boards (PCB) and computers to indicate the status and function of the systems. By 1987, AlGaAs LEDs were bright enough to begin to replace light bulbs in vehicles brake lights and traffic lights. This was the first time LED had displaced incandescent light bulbs in lighting applications. The same trend also followed GaAsP LED. In 1993, Aluminium Gallium Phosphide (AlGaP) was revealed that offers almost four times the improvement in brightness and has become widely used in traffic light signals ever since [26]. The GaAs/AlGaAs IREDs on the other hand, was and still is widely used to this day in video and audio remote control and also as sources for local-area communication networks.

Although the LED has made significant progress in brightness in the red and green regions, there was no clear improvement in the blue region. SiC, Zinc Selenide (ZnSe) and Gallium Nitride (GaN) were all potential semiconductor materials for blue LED in the 1970's. As stated above, SiC was considered an unsuitable candidate due to low efficiency while ZnSe could not be developed for commercial use due to its short lifespan. GaN thin film, on the other hand, was considered almost impossible to fabricate with good quality and uniform thickness because there were no substrates possessing a lattice constant near GaN [27]. This changed in the late 1980's when GaN had a key breakthrough in epitaxial growth and p-type doping [27]. Since then, teams of researchers from Nichia Chemical Industries Corporation, which included Shuji Nakamura and Takahashi Mukai, made numerous contributions towards the development of GaN based LEDs. Nakamura presented the first commercially feasible blue LED; a double-heterostructure blue-violet device on sapphire substrate in 1993 [28]. Naruhito Iwasa, another Nichia employee, found a way to get Indium (In) into GaN to pull the wavelength to a "blue-ish green". By then end of 1995, a pure green Indium Gallium Nitride (InGaN) device was presented, which was brighter and had replaced AlGaP LED in traffic lights.

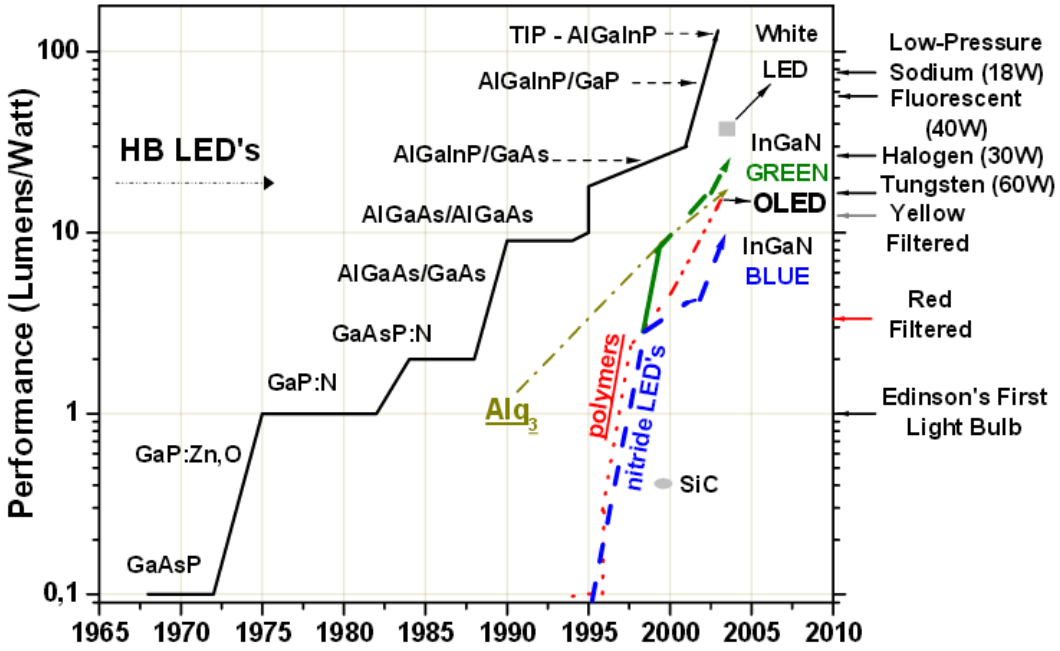

Figure 2-1 – Evolution of LED performance [29]

The availability of blue GaN LED opens the opportunity for white LEDs. "White" however, is not a colour but a human perception of a mixture of colours and, to the best of the author's knowledge, cannot be created directly from a single semiconductor device. There are some techniques that are used to create "white" light indirectly. These include mixing red, green and

blue LED in the correct ratio, using a semiconductor wavelength converter, or mixing blue LED with phosphor wavelength converter [26]. White LEDs is expected to progress further, with expected potential to deliver a significantly higher luminous efficacy than that of conventional incandescent and fluorescent light sources. Conventional light sources have typical luminous efficacies of 15 to 100 lm/W, while white LEDs have the potential for luminous efficacies more than 300 lm/W [26]. The evolution of the efficacy of LED from 1965 to 2005 in comparison to other light sources is shown in Figure 2-1. In a report published by Strategies Unlimited in April 2013, the average efficacy of commercially available LEDs for lighting applications has increased to greater than 100 lm/W [30]. With such high luminous efficacy, LEDs are predicted to replace incandescent light as the main lighting sources in the near future. In a technical briefing by the European Commission, LED is expected to become the main light source for households in Europe by 2016 [31].

The technical progress made on white and coloured LEDs builds a foundation for VLC. Early discussions of VLC include Akanegawa [32] in which he discussed the use of LED for traffic lights. This is followed by Pang [33] who proposed to broadcast information using optical wireless systems based on the controlled traffic lights and Komine [34] suggested the integration of white LED into Power Line Communication (PLC). These were the early ideas behind VLC, proposing the utilisation of white and coloured LEDs to transmit data. The first demonstration of indoor VLC was conducted by VLCC in 2003 by modulating the intensity of the LED, known as Intensity Modulation with Direct Detection (IM-DD). On-Off Keying (OOK) was proposed as a modulation scheme to send information.

Since then, VLC have gathered more interest from around the world, and many research projects from companies and universities have taken place. Apart from VLCC in Japan, some of the notable research groups include the OMEGA project, which was funded by the European Commission, the Smart Lighting Engineering Centre in the United States (USA), The O'Brien group at the University of Oxford and D-Light at the University of Edinburgh. The OMEGA project consists of 20 partners from industries and academia focuses on developing user friendly home area network to deliver high bandwidth Gigabit per second (Gb/s) transfer combining RF, IR, VLC and PLC [35]. The Smart Lighting Engineering Centre was established by three core university members (Rensselaer Polytechnic Institute, Boston University and the University of New Mexico) under the National Science Foundation (NSF) [36]. The centre focuses on the development of the LED device and system technologies for VLC communication. Meanwhile, in the UK, the D-Light group from the University of

Edinburgh focuses on developing Orthogonal Frequency Division Multiplexing (OFDM) as the system modulation scheme. The Ultra-Parallel VLC (UP-VLC) project started in October 2012, funded by the Engineering and Physical Science Research Council (EPSRC), focuses on exploring the possibility of potentially ultra-high data density array of microLEDs in a compact and versatile form that delivers data in Terabit per second per millimetre square (Tb/s/mm2) [37]. In 2011, VLC's idea and operation was demonstrated to the public at a Technology, Entertainment and Design (TED) conference. The demonstration was presented by Professor Harald Hass, introducing and signalling the intention, significance and importance of VLC for the future [38].

2.3. Modulation Scheme: OFDM in VLC

2.3.1. Basic Properties of the Optical Channel

VLC uses a technique which was used in IR communication where the links are based on intensity modulation and direct detection (IM-DD). On the transmitter side, intensity modulation is performed by varying the drive current of LED, which correlates to the input electric current, encoded from the incoming signal. On the receiver side, direct detection is performed by a photo-detector (normally photodiode) which in turn produces electric current proportional to the incident optical power. Figure 2-2 shows a simple representation using block diagram of IM-DD.

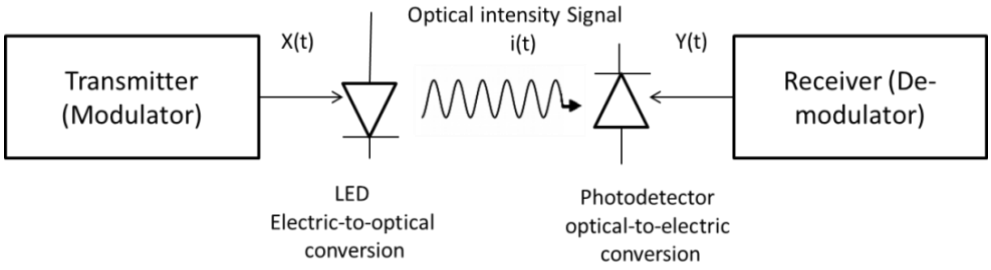

Figure 2-2 – Block diagram of Intensity Modulation-Direct Detection method

IM-DD as mentioned has been the popular choice of implementation for VLC in the past. The term "Direct Detection" (DD) is used in optical communication which implies that the detector (photodiode or other photodetectors) directly detects the optical power level of the signal. Another common method of detection implemented in optical communication is the Coherent Detection (CD). With CD, the received signal is optically combined with a reference signal to

produce an electronic receiver output signal. Therefore, the electrical signal produced is not directly proportional to the incident optical power and temporally requires coherent radiation. CD is normally used with laser based optical communication and a laser acting as a local oscillator is needed at the receiver. Because LED is an incoherent light source, IM-DD method is preferred.

2.3.2. Basic Optical Modulation Scheme

A Modulation scheme can be described as a process of changing or varying one or more properties of a periodic waveform, called a carrier signal, by mixing it with a modulated signal which contains the information to be transmitted. Three key parameters of a periodic waveform are its amplitude, frequency and phase. These are the basis for the most basic type of modulation, namely the Amplitude Modulation (AM), Frequency modulation (FM) and Phase Modulation (PM). AM is a form of modulation that varies the strength (amplitude) of the transmitter signal in relation to the information being sent, while FM and PM work by varying the frequency and phase respectively in relation to the data. AM is the popular type of modulation in VLC and is directly related to intensity modulation.

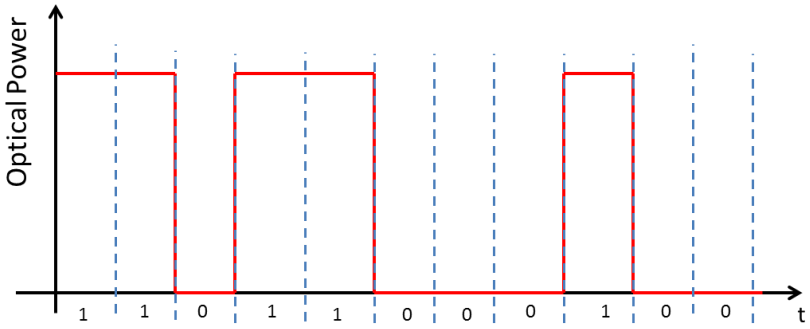

Figure 2-3 – Example of OOK operation

One of the AM techniques used in IM-DD is the on-off keying (OOK) method [39]. The implementation of OOK comes as no surprise because VLC was still very new and the simplest form of modulation scheme was needed as a proof of the concept. OOK can be best described as representing an analogue waveform in the form of digital data of ‘zeros’ and ‘ones’. This is done by varying the LED optical intensity or amplitude between two levels, where each level represents a digital bit ‘one’ or bit ‘zero’ respectively. For example, a digital bit ‘one’ can be represented when light is present and bit ‘zero’ is when the light is absent as shown in Figure 2-3. The time duration of each digital pulse can be defined as

$$T = \frac{1}{R}$$ **Equation 2-1**

where R is the bit rate of the transmission. If a high data rate transmission is performed, the time duration T has to be very short which means the bandwidth of both the driver and LED have to be very high. Generally speaking, for an OOK transmission, the bandwidth of the system needs to be at least half of the data transmission rate. For example, if a 100 Mb/s data rate is intended in a VLC system, then both the driver and the LED are required to have at least 50 MHz bandwidth. This clearly shows the limitation of the OOK modulation scheme as rate of data is limited by the driver and the LED. Moreover, as the transmission rate increases, Inter-Symbol Interference (ISI), which is normally caused by multipath propagation and a dispersive channel, becomes an issue because of the very short data duration. Therefore, a more robust modulation technique is required.

A more robust modulation scheme, which is also implemented in this thesis, is OFDM. One of the first works of using OFDM in VLC was made by Tanaka in 2001 [40]. Other modulation schemes including (but not exhaustively) Pulse Code Modulation (PCM), Sub-Carrier Binary Phase Shift Keying (SC-BPSK) [39], and Discrete Multi-tone (DMT) [41, 42] have been explored for VLC application. These modulation schemes, however, are not implemented in this project.

2.3.3. OFDM: History and Its General Operation

It is important to note that the research of this thesis work is not on the development of advance OFDM, but rather on designing a VLC-LED-based driver that facilitates the implementation of the former. A good basic knowledge of OFDM operation is, therefore, required to understand the problem investigated and to provide a good solution.

The first proposal to use orthogonal frequencies for transmission appeared in a 1966 patent by Chang of Bell Labs [43]. Many papers have been published since then reporting the development of OFDM to what it is today [44, 45, 46]. OFDM was first considered to be used for a practical wireless system in the middle of the 1980's with Cimini of Bell labs published a paper on OFDM for mobile communications [47]. Later, Lassale and Allard also published a paper that noted the importance of OFDM in radio broadcasting and communication [48]. Since then, many research projects have been carried out and OFDM is now implemented in

many practical RF telecommunication standards. This includes the wireless local area network (WLAN) [49], Digital Subscriber Line (DSL), and television and radio broadcasting [50]. OFDM in optical communication was only developed recently. The differences between RF and VLC as listed earlier in Table 2-1, affect the design and implantation of OFDM for a VLC system.

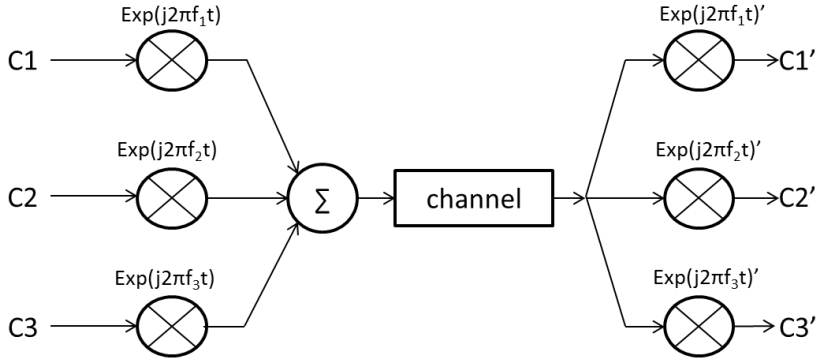

Figure 2-4 – Multi-carrier Modulation (MCM) concept

There exist many versions of OFDM to suite specific implementations and applications. The basic concept of these versions, however is the same. OFDM in general is a special class of Multi-Carrier Modulation (MCM), where its generic implementation is shown in Figure 2-4. MCM on the whole is an alternative approach to the classical Single-Carrier Modulation (SCM). OOK is one of the examples of SCM and the limitation of OOK was discussed in Section 2.3.2. The general idea of OFDM is to split the total available bandwidth into many narrowband subcarriers (or subchannels) at equal separation which means that the data are transmitted on a number of parallel channels of different frequencies. As a result, the period of a symbol for an MCM approach is much longer than SCM. Because of the longer symbol period, the ISI effect is reduced. Typically in an MCM (or OFDM) implementation, any residual ISI is removed by using a guard interval called Cyclic-Prefix (CP). Furthermore, channel equalization is simplified because OFDM signals may be viewed as many slowly modulated narrowband signals rather than one rapid modulated wideband signal.

Classical MCM uses non-overlapped band-limited signals. This technique, however, is at a disadvantage because it requires excessive bandwidth where the channel spacing has to be a multiple of the symbol rate therefore, greatly reduces the spectral efficiency. OFDM was introduced to solve this problem by employing an overlap and orthogonal signal set [43]. This is the key distinction between OFDM and non-overlapping MCMs. Figure 2-5 depicts the difference between the two MCM classes. Notice how OFDM sub-channel frequency

spectrum overlaps each other, thus increasing the spectral efficiency compared to general MCMs.

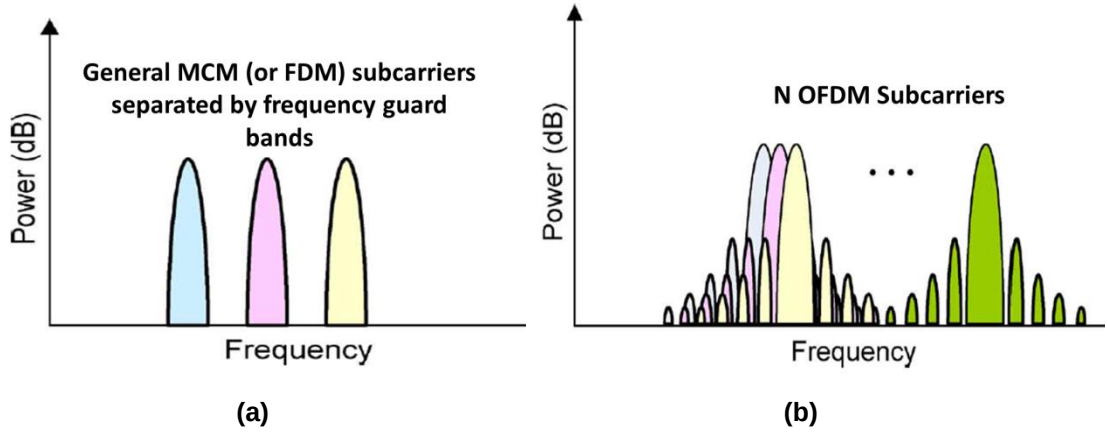

Figure 2-5 – A typical representation of spectrum of (a) general MCM subcarriers and (b) OFDM signal [51]

Figure 2-6 shows the basic operational block for OFDM on the transmitter side. In general, the first blocks in an OFDM transmitter are the interleaving and coding. Most OFDM systems such as Digital Audio Broadcasting (DAB) and Digital Video Broadcasting (DVB) use some form of error correction. This is crucial in achieving low overall Bit-Error-Rate (BER) especially in a very noisy channel [51]. After coding, the serial high data rate stream is converted into parallel data. The parallel data is then mapped onto the complex plane. Quadrature Amplitude Modulation (QAM) and Phase Shift Keying (PSK) are the two most common modulations used in OFDM transmission. Constellations of 4 (QAM-4 or PSK-4) to 64 (QAM-64 or PSK-64) are typically used.

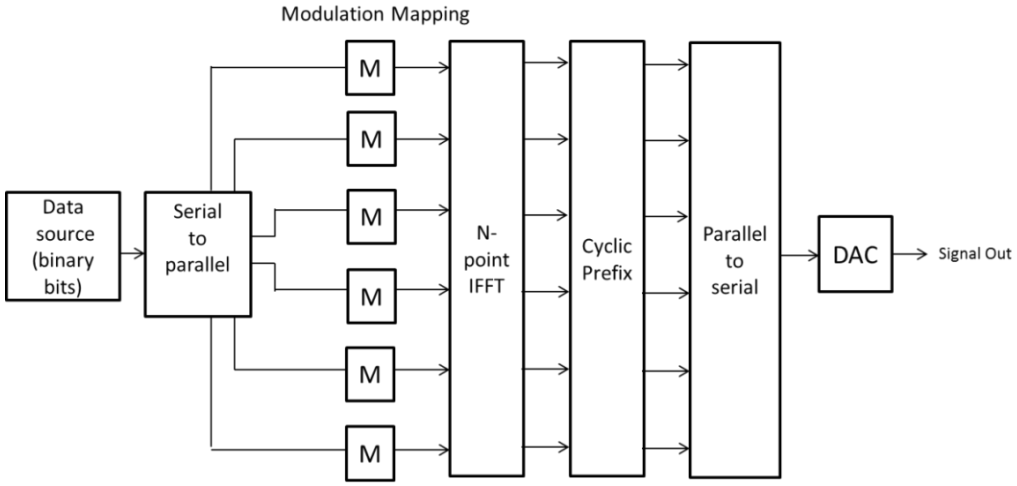

Figure 2-6 – The basic operation OFDM block diagram [51]

The next stage is the application of Fast Fourier Transform (FFT) to the modulation process which distinguishes OFDM from SCM and is the major contribution to its complexity. On the transmitter's side, an inverse FFT (IFFT) is performed and FFT is at the receiver's side. The input to the IFFT is the complex vector of N length where N is also the size of the IFFT. The IFFT operation modulates and multiplexes the subcarriers by assembling input information into blocks of N complex numbers; one for each sub-carrier. For example, consider a complex vector $\boldsymbol{X}$ of N length ($\boldsymbol{X}_N$); each element of $\boldsymbol{X}$ represents the data on the corresponding subcarrier. If the complex vector input is a QAM modulation mapping output, each element of $\boldsymbol{X}$ is a complex number representing a particular QAM modulation constellation point [51].

The modulated subcarriers are transmitted simultaneously in a superimposed and parallel form. Therefore, an OFDM signal consists of N number of orthogonal subcarriers within the symbol duration of length T_S, spaced by separation Δf on the frequency axis. Thus, the orthogonality requires that the subcarrier spacing is

$$T_S = \frac{k}{\Delta f} \text{ (s)} \qquad \textbf{Equation 2-2}$$

where k is a positive integer, which normally equals 1. Hence, for a transmission with N subcarriers, the total bandwidth, BW, of an OFDM transmission is given by

$$BW \approx N \times \Delta f \; Hz \qquad \textbf{Equation 2-3}$$

In addition to modulation of many orthogonal subcarriers, multipath propagation effects need to be taken into account. Multipath propagation occurs where a signal from a transmitter reaches the receiver by several independent paths and leads to interference or distortion on the receiver. This is known as ISI. As explained earlier, the longer symbol period of OFDM reduces the effect of ISI. This effect can be further reduced by employing CP between successive symbols. Since the system BW is subdivided into N narrowband subcarriers, the OFDM symbol duration (T_S) is N times longer than in the case of the SCM transmission system covering the same bandwidth. Therefore the use of a guard interval is allowed because of the low symbol rate of each sub-carrier, thus making the OFDM transmission even less susceptible to ISI, hence improving the overall BER [52]. Typically, for a given BW, the number of subcarriers is chosen in such a way that the T_S is sufficiently larger compared to the maximum multi-path delay. In most OFDM systems, CP is added to the start of each time domain OFDM

symbol before transmission. This is done by taking a small number of samples from the end of the symbol and appending them to the start of the symbol. For ease of explanation, let $\boldsymbol{X}(i)$ be the OFDM signal. Instead of transmitting only OFDM signal as shown in Equation 2-4

$$\boldsymbol{X}(i) = [x_0(i)x_1(i)x_2(i)x_3(i) \dots \dots \dots x_{N-1}(i)] \quad \textbf{Equation 2-4}$$

The sequence is added with a CP at the start. The adjusted sequence as shown in Equation 2-5

$$\boldsymbol{X}(i) = [x_{N-G}(i) \dots x_{N-1}(i)x_0(i)x_1(i)x_2(i)x_3(i) \dots \dots \dots x_{N-1}(i)] \quad \textbf{Equation 2-5}$$

is transmitted, where G is the length of the CP. Although CP reduces the ISI effect in the transmission, it comes at the price of reducing the overall data rate and redundancy. The result of IFFT and CP addition is then converted from parallel to serial and transmitted serially. Again, it is important to note that what was discussed here is the basic operation of OFDM. There are many versions of OFDM, which have each been designed to suit a specific application.

2.3.4. Optical OFDM

	Conventional OFDM system (RF)	**Optical OFDM system (LED based)**
Signal type	Bipolar and Complex	Positive and Real
Transmission	Conducted through electrical field	Conducted through optical intensity
Detection type	Coherent detection	Direct Detection
Synchronisation	Requires local oscillator at the receiver	Does not require local oscillator

Table 2-2 – Summary of comparison between RF-OFDM and Optical-OFDM (LED based)

OFDM has gained popularity and achieved widespread use in RF based wireless communication such as WLAN and Digital Television/Radio Transmission. However, the difference in transmission characteristics between conventional OFDM and optical OFDM need to be addressed. Table 2-2 summarised these differences.

The signal in OFDM, in general is mathematically 'complex' and generated by IFFT. Equation 2-6 shows a simple example of a sampled waveform generated by IFFT, where $\boldsymbol{X}_i$ is the complex number representing the constellation point on the i-th subcarrier symbol and $\boldsymbol{x}(k)$

are the baseband time domain samples for that symbol. This means that the signal transmitted is bipolar in nature.

$$\boldsymbol{x}(k) = \frac{1}{\sqrt{N}} \sum_{i=0}^{N-1} \boldsymbol{X}_i \exp\left(\frac{-j2\pi ki}{N}\right) \qquad \textbf{Equation 2-6}$$

For LED based optical wireless communication, where the IM-DD technique is implemented, the value of the OFDM signal is represented by its intensity. This means that the modulating signal must be both real and positive as opposed to complex (real and imaginary) and bipolar (positive and negative). In order to produce only a "real" signal, the input to the transmitter's IFFT is constrained to have Hermitian Symmetry. This causes cancellation of the imaginary components of the IFFT resulting only in real components.

The next step is to make the signal unipolar. Two of the earliest unipolar conversion techniques are called the DC-biased optical OFDM (DCO-OFDM) [53, 54] and the asymmetrically clipped OFDM (ACO-OFDM) [55]. The two sub-OFDM techniques are discussed here for comparison sake. However, only DCO-OFDM is used in this thesis project. It is essential to note that there are more transformations to produce unipolar signals that were developed after DCO-OFDM and ACO-OFDM with higher complexity, but lower BER. These techniques, however, are not discussed in this thesis. Some of the notables are the Sub-Index Modulation OFDM (SIM-OFDM) [56], Unipolar OFDM (U-OFDM) [57] and flip OFDM (F-OFDM) [58].

DCO-OFDM is the most basic and the easiest to implement. It consists of adding a bias level to the signal. The problem with this technique is that it causes clipping noise due to the large peak-to-average power ratio (PAPR) requirement, especially in the negative peaks of the signal. The clipping noise results in distortion which limits and degrades the performance of the system. Using a higher bias power reduces the noise, but at the same time, it needs higher normalised bit energy to noise power spectral density (SNR) to achieve an acceptable BER [59]. Therefore, a trade-off exists between choosing higher power efficiency and noise in the selection of the bias. [60] discusses the performance of DCO-OFDM in more detail.

ACO-OFDM, on the other hand addresses the clipping problem faced in DCO-OFDM. In ACO-OFDM, all "negative" signals in the bipolar OFDM signal are clipped at the zero-level, therefore, only transmitting the "positive" going signal. This is done by only modulating the odd subcarriers at the IFFT input and set zero to the even subcarriers. In this way, all clipping

noise falls on the even subcarriers, and because the signal has an odd symmetry, the negative going data can be clipped without any information being lost [55]. Using this method, the optical power is substantially reduced, but only carries useful information on half of the available bandwidth. Although DCO-OFDM are able to transmit more information with the same bandwidth (higher spectral efficiency), ACO-OFDM signals have lower noise and lower BER performance [59].

2.3.5. The OFDM Problem

Optical OFDM bears both differences and similarities to its RF counterpart. On the one hand, optical OFDM is different from RF in terms of its physical transmission characteristics which lead to some modifications to the conventional OFDM. On the other hand, despite being different, it inherits the same problems as conventional OFDM in RF. These are the peak-to-average power ratio (PAPR) and the sensitivity to phase noise and frequency offset [51]

$$PAPR = \left[\frac{P_{peak}}{P_{rms}}\right] \qquad \textbf{Equation 2-7}$$

PAPR is defined as the ratio between the instantaneous peak amplitude and the root mean square (RMS) of the output power, as shown in Equation 2-7. A high PAPR indicates a high peak in the signal compared to its average value. Any OFDM symbol is generated by superimposing several carriers by IFFT at the transmitter side. These carriers may add up constructively resulting in a high PAPR. Basically, a high PAPR implies that the probability for clipping of the signal is higher than a low PAPR signal. In the optical system, PAPR is the ratio of the peak optical power (intensity) compared to the average optical power. Because of the high PAPR requirements, non-linearity and signal clipping are critical sources of distortion. In the RF case, the power amplifier is usually the main source of non-linearity [61]. One of the ways to overcome this issue in RF is a technique called “power back-off” (PBO), where the input signal power is “backed-off” to ensure that the transmitter operates only in the quasi-linear region, although this comes with a trade-off, such as higher power consumption and lower power efficiency [62, 63]. In VLC, the main source of non-linearity is the LED itself [64]. Therefore, the optical OFDM signals suffer from significant in-band and out-band distortions due to the non-linearity introduced by the LED [65]. The in-band component determines the system BER [66] degradation and the out-of-band component affects adjacent frequency bands [67]. The PBO technique can also be applied in optical communication.

However, this technique would have the same trade-off as its RF counterparts. Therefore, in an optical OFDM system, a driver capable of producing a highly linear optical power output is essential to satisfy the high PAPR requirements. Hence, a different method to PBO is to be explored to solve this problem.

2.3.6. Effect of Non-linearity on OFDM

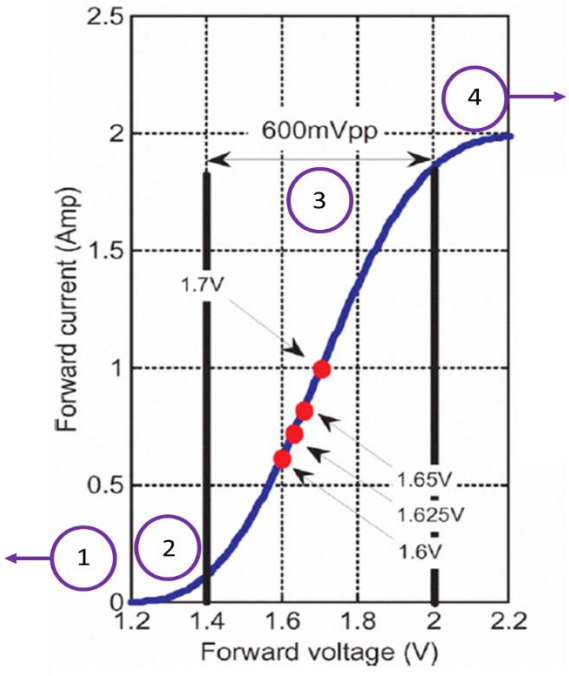

Figure 2-7 – The LED I-V characteristics of the OSRAM, SFH 4239 [65]

Figure 2-7 shows a typical Current-Voltage (I-V) characteristic of an LED. A more detailed discussion on LED operation is discussed in Section 2.6.1. In general, for ease of explanation, the operation of the LED can be divided into four regions of operations: **(1)** turn-off, **(2)** exponential, **(3)** quasi-linear and **(4)** saturated region. The LED has a minimum threshold voltage which is the "on" state of the current flow and light emission. Referring to Figure 2-7, if the voltage applied across the LED is below 1.2V, no light will be produced and the LED is considered to be in a "turn-off state". As the voltage increases, the current increases exponentially over a limited range before behaving in a "quasi-linear" manner around 1.4 V for about 600 mV range. As the voltage is further increased, the current starts to saturate. For analogue operation, the LED is normally biased at somewhere midpoint in the "quasi-linear" region. Then the OFDM signal modulates around this DC bias point.

Irina Stefan et al. reported the results of an experiment using a high-powered IRED from Hewlett Packard (HSDL-4220) to see the effect of LED non-linearity on OFDM [68]. The chosen LED had a threshold voltage of 1.3V and allows 100mA of forward current at 1.5V. The maximum allowed forward current is 500mA at 2.5V. A BER test was conducted in two separate experiments using a 4-QAM OFDM with the mentioned LED.

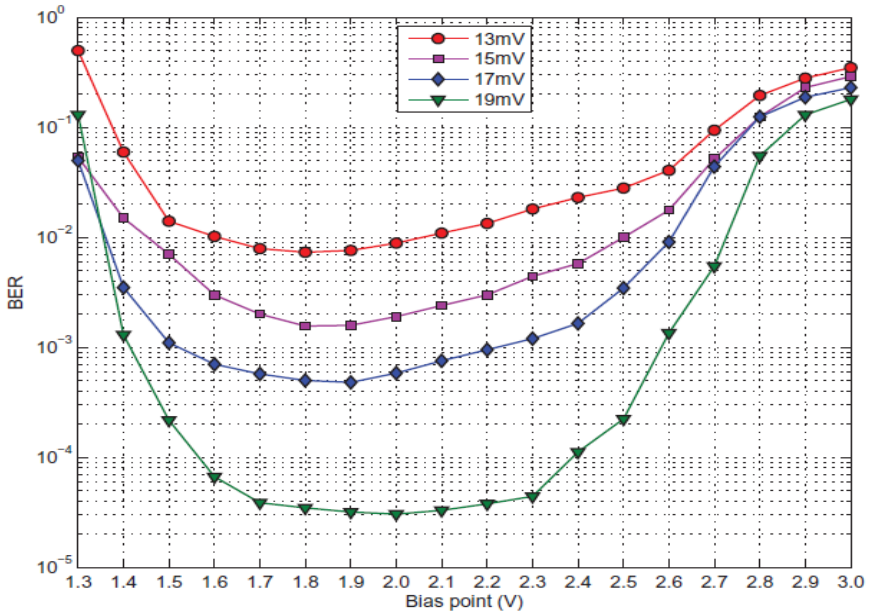

Figure 2-8 – BER vs. bias point. Different RMS OFDM signal voltages are considered as measured by Stefan et al. [68]

The first experiment looked at the relationship between the BER and LED bias points for 4 different signal amplitudes. The bias voltage was varied from 1.3V to 3V. As shown in Figure 2-8, there are two points where the BER is highest which is when bias voltage is 1.3 and 3V. At 1.3V, signal clipping and low SNR contributes to the high BER reading. As the bias point increases, the LED enters the "quasi-linear" region, where the clipping of the lower signal is reduced thus, lowering the BER value. Furthermore, lower BER value is also contributed to by higher optical power detected at the receiver end, producing higher SNR. As the bias point is further increased, the BER starts to increase due to clipping of the upper OFDM signal.

The effect of the OFDM signal amplitude on the BER function was further investigated. The OFDM signal voltage applied across the LED is varied from 10mV to 35mV with different bias points. The highest BER was recorded when 10mV was applied, as shown in Figure 2-9. As the signal amplitude increases, this in turn improves the SNR and hence reduces the BER. The same trend was apparent for all bias points. As the signal amplitude further increased, the

BER started to increase for bias points of 1.4V, 1.5V and 2.5V. This shows that the bias points are either too low or too high which causes the signal to clip. The two experiments showed the importance of choosing a nominal LED bias point and its signal amplitude. More importantly, it shows the significance of having a high PAPR in an OFDM transmission in order to achieve low BER performance.

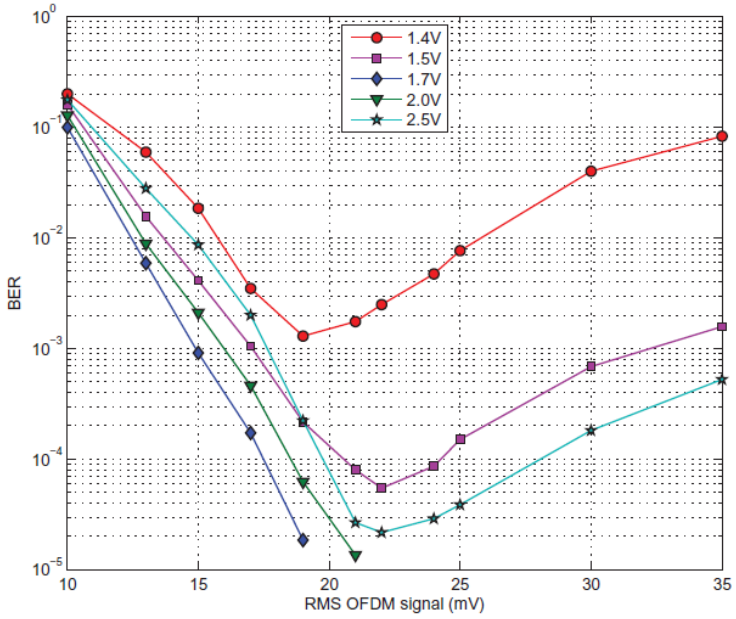

Figure 2-9 – BER vs. the RMS OFDM signal voltage where different bias points are considered. Measurement was conducted by Stefan et al. [68]

In addition, an LED is normally described as having a linear relationship between its input (drive current) and its output (the emitted light intensity or optical power). The two experiments discussed earlier in this section were conducted under the assumption that the LED drive current and its optical power response (L-I characteristic) exhibits a linear relationship. Unfortunately, a real LED does not demonstrate a linear relationship between its input and output as discussed in [64]. Figure 2-10 shows the normalised L-I characteristic taken from three different LEDs, which clearly shows the non-linearity of the transfer function. The non-linearity of the transfer function is the main source of distortion of the emitted signal, even if the LED is biased in its 'quasi-linear' region. Therefore, an LED driver that can produce a linearly proportional optical power output with respect to the input current is very desirable in order to achieve a low BER transmission.

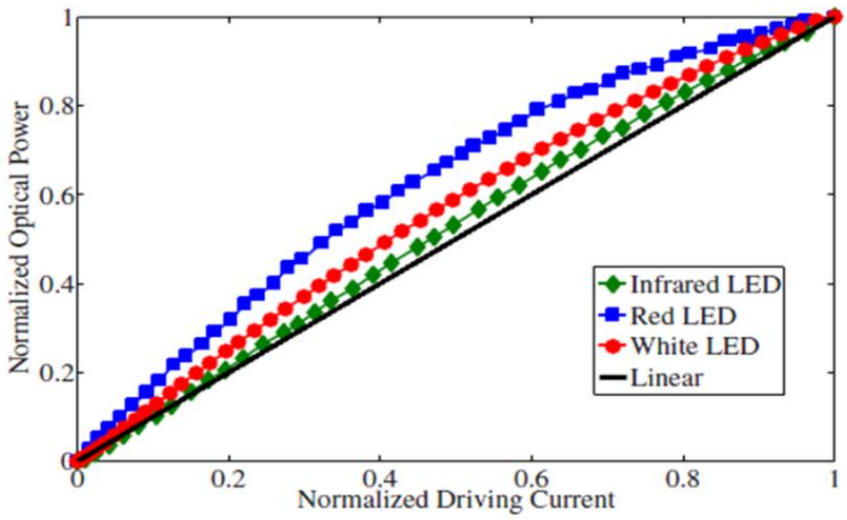

Figure 2-10 – Normalised comparison of real and linear LED from [64]

2.4. Linearization Techniques in RF

In general, a system with a highly linear response, be it the amplifier, antenna response or light source, is very desirable. Therefore, linearization techniques are not something new. There have been many research efforts on linearization techniques with different focuses depending on the target application. In RF communication, linearity was emphasised due to the requirement of the modulation scheme, such as OFDM. Generally, the main aim of linearization is to cancel distortions introduced by both internal and external components by modifying the signal. Taking techniques used in RF as examples, linearization techniques can be divided into three classes:

1. Feedback linearization
2. Pre-distortion linearization
3. Feedforward linearization

2.4.1. Feedback Linearization

2.4.1.1. Simple Feedback

This technique is based on the standard feedback scheme used in moderate frequency amplification and control systems, as shown in Figure 2-11. The system gain, H, is defined in terms of the feedforward amplification gain (α) and feedback gain (β). Therefore, H is written as

$$H = \frac{V_o}{V_i} = \frac{\alpha}{1 + \alpha\beta}$$ **Equation 2-8**

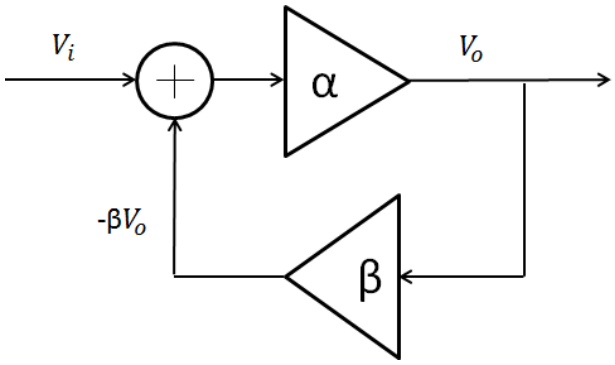

Figure 2-11 – Negative feedback basic architecture

In the simple negative feedback loop, distortion reduces with the increasing gain, but at the cost of reducing bandwidth. Therefore, a trade-off must be made between α and β. Furthermore, as with all feedback circuits, the simple feedback technique has a potential stability issue. Therefore, a good design is important to ensure that the circuit functions properly.

2.4.1.2. Envelope Feedback

The main principle of the envelope feedback linearization technique is comparing the amplified output signal with the input signal and correcting any distortion caused by the system by quickly adjusting the gain variation of the amplifier to compensate. As shown in Figure 2-12, input and output signals are compared using a differential amplifier that simultaneously produces an output which acts as an adjustable gain control (AGC) to the amplifier. As with the simple negative feedback, this technique also inherits stability issues. The peak detectors play a major role in order to maintain stability and reduce distortion [69]. Both peak detectors are required to have a high dynamic range and at least twice the bandwidth of the signal path. This technique gives slightly better performance than simple feedback, but at the cost of an increase in phase error.

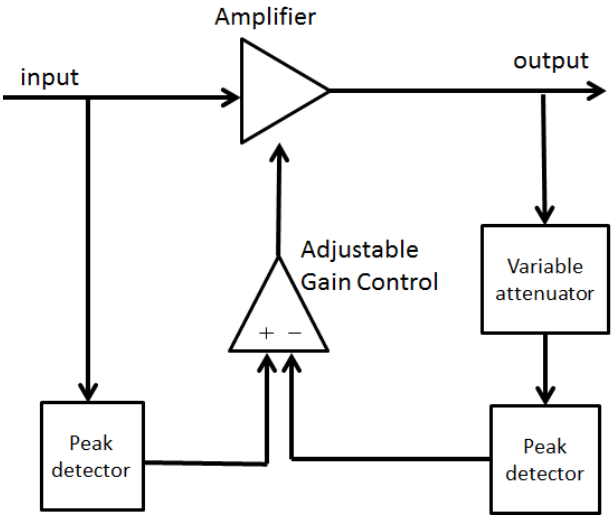

Figure 2-12 - Envelope feedback basic architecture

2.4.1.3. Polar Loop

Polar loop is a modified envelope feedback technique. The main difference between polar loop and envelope feedback is the incorporation of phase comparison in the polar loop. Therefore, in polar loop, both amplitude and phase are compared, as shown in Figure 2-13. The amplitude comparison is used to adjust the gain of the main amplifier while the phase comparison is used to control the voltage-controlled oscillator (VCO) which is fed into the amplifier as frequency control. While this improves the linearity of the amplitude and phase, the additional components add to the complexity of the design and have a huge influence in determining the linearity of the system [70].

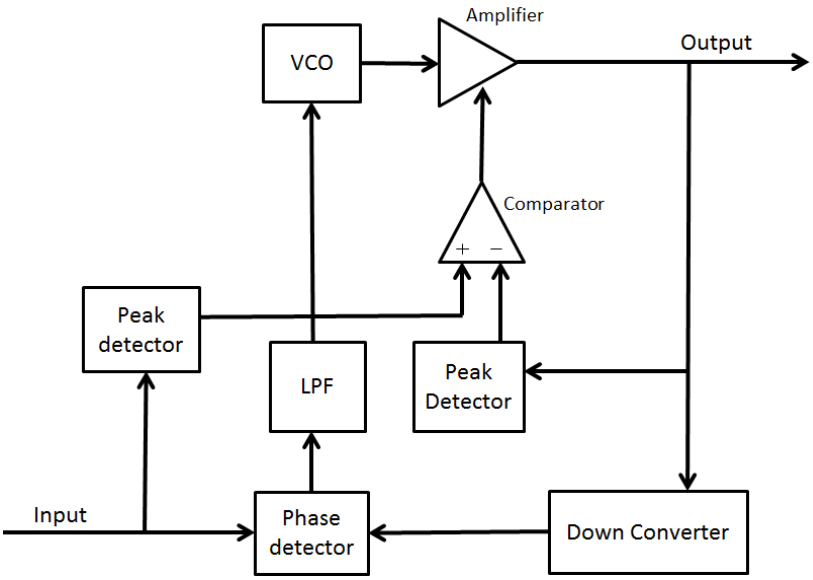

Figure 2-13 – Polar loop basic architecture

2.4.1.4. Cartesian Loop

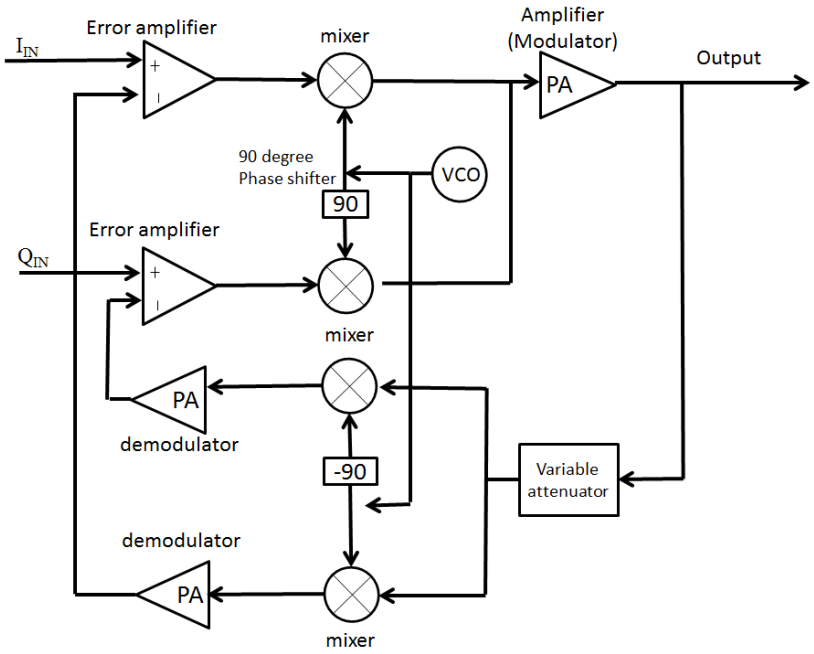

Figure 2-14 – Cartesian loop basic architecture

The basic scheme of the Cartesian Loop architecture is shown in Figure 2-14. The Cartesian loop divides the RF signal into In-phase and Quadrature (I-Q) components. Each signal component is applied to an error amplifier. The output of the error amplifier is then fed to a power amplifier (PA) which generates the RF signal. A sample of the RF output is attenuated and fed back into a PA where it is compared to the input signal at the error amplifiers. The system attempts to correct the signal at the output to match the I-Q input signals applied to the error amplifier. The Cartesian loop, therefore acts as two orthogonal control loops in I and Q. Because of the complexity of the design, key factors such as loop stability and DC offsets must be addressed carefully in the design. The linearization improvement very much depends on the gain and bandwidth characteristics of the differential amplifiers and the linearity of the demodulator device.

2.4.2. Pre-Distortion Linearization

The name “Pre-distortion linearization” is self-explanatory. Pre-distortion techniques attempt to modify the incoming signal to complement and, therefore, cancel the non-linear characteristic of the transfer function of the system. The basic architecture is shown in Figure

2-15. Pre-distortion has been used with great success where correction up to third order distortion can be applied [71].

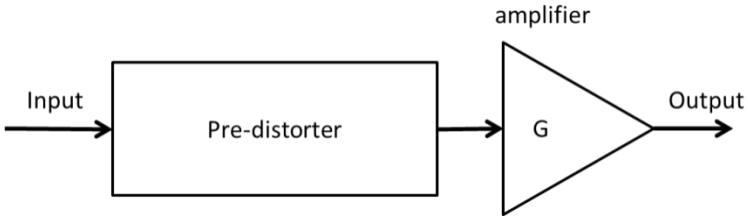

Figure 2-15 – Pre-distortion basic architecture

This technique is an unconditionally stable system due to the open loop architecture. However, the open loop nature of the pre-distortion means that external effects, for example, ageing or temperature change, are not compensated. This can be solved by adding a dynamic feedback loop, which again, complicates the design.

2.4.3. Feedforward Linearization

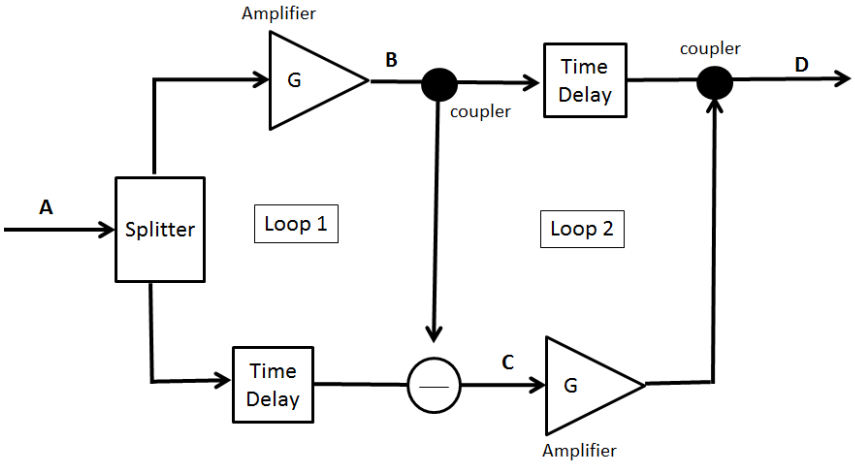

Figure 2-16 – Basic Feedforward Architecture

In a feedforward system, a sample of the distortion generated by the main amplifier is fed forward and is combined with the amplifier output in a way that the amplifier distortion is cancelled. The basic feedforward architecture is shown in Figure 2-16, where it requires two cancellation loops [72]. The input signal is split to follow two paths. In the first loop, the undistorted reference signal (A) is subtracted from the distorted amplifier output (B), leaving a signal consisting purely of distortion products (C). This signal is amplified by the error amplifier in the second loop and, using a directional coupler, is inserted in anti-phase back into the main output path. The sampled distortion products will therefore cancel with amplifier

distortion, leaving the amplifier wanted signal (D) [72]. One of the main advantages of feedforward is its inherent stability compared to feedback due to its open-loop nature. On the other hand, the feedforward technique requires precise phase and gain adjustment, making the implementation more challenging.

2.4.4. Linearization Technique Summary

A summary of these linearization techniques is given in Table 2-3. One of the characteristics of the LED is that it is an incoherent light source. Therefore, any feedback architecture that requires phase information can be ruled out. These include the Polar loop, the Cartesian Loop and, to some extent, the Feedforward technique. Furthermore, these techniques require complex system design. Given that there are many uncertainties of the integration between the LED and CMOS photodiode, such as coupling efficiencies (detail discussion in Chapter 5), this would further complicate the design.

Technique	Comparative Bandwidth	Linearity Improvement	Relative Complexity
Simple Feedback	Narrow to Moderate	Moderate	Low
Envelope Feedback	Narrow to Moderate	Moderate	Moderate
Polar Loop	Narrow to moderate	High	High
Cartesian Loop	Narrow to Moderate	High	High
Pre-distortion	Moderate to Wide	Low	Low to Moderate
Feedforward	Wide	Moderate	High

Table 2-3 – Summary of linearization technique comparison

This project serves as the first version of its kind. Therefore, it is sensible to keep the design complexity to a minimum as it would serve as a learning tool for future design. Furthermore, the techniques mentioned were applied in RF. Although the same technique can be applied to optical communication, there is a possibility of unforeseen problems due to the differences of the physical transmission. Therefore, a simple feedback design was chosen because it has less complexity in the design, and the performance is comparable to the envelope feedback.

2.5. Mission Statement

An OFDM system requires a driver with a highly linear response to transmit a high PAPR signal in order to achieve a low BER. However, Section 2.3.6 has shown that this is not the case for optical (LED-based) communication where the L-I characteristic of the LED is the main source of distortion. Because of the non-linear response, the signal amplitude is somewhat limited to clipping and, therefore, high PAPR is harder to achieve. This overall has affected the BER performance. Therefore, the main aim of this research is to explore ways to improve the linearity performance of an LED-based optical OFDM system for VLC application. Although there have been number of research projects in the same field, they have been more focused on the modulation scheme rather than the actual driver itself [57, 73, 74, 75, 76]. The main focus of this research will look at the hardware level, i.e. driving circuit of the LED. Three microLED/CMOS drive ICs were designed during the duration of this. project:

1. This research is closely associated with the HYPIX project which started in October 2008. During the early stages of this research, HYPIX was in its final phase and had already designed four microLED/CMOS drivers primarily for optically pumped polymer lasing. However, it also showed potential for a VLC application using OOK as its modulation scheme. As a continuation, a fifth driver, named "Generation V CMOS driver", was designed to seek a maximised optical power output whilst keeping the same pixel pitch as its predecessors. Due to its digital output behaviour, the driver is sometimes called the "digital driver" in this thesis. Further detail on the Generation V CMOS driver is presented in Chapter 3.
2. Two analogue drivers are presented in this thesis, which were designed to facilitate the implementation of OFDM. The first analogue driver is called the "CMOS Current Feedback driver" which linearized the current driving the microLED. Further detail of the CMOS Current Feedback driver is presented in Chapter 4,
3. The second analogue driver is called the "CMOS Optical Feedback driver". The term "optical feedback" refers to the technique implemented by the driver which uses a photodetector to detect a small portion of light from microLED for feedback purposes. This driver seeks to improve the linearity of the transmitter optical power output and is discussed in detail in Chapter 5.

One of the key features of the project is the linearization of the optical power by integrating the LED with a photodetector. In this thesis, photodiode is chosen as the light detection

mechanism. The fundamental operation of the LED and photodiode is discussed in the next section.

2.6. LED and Photodiode

2.6.1. Principles of Operation and Properties of LED

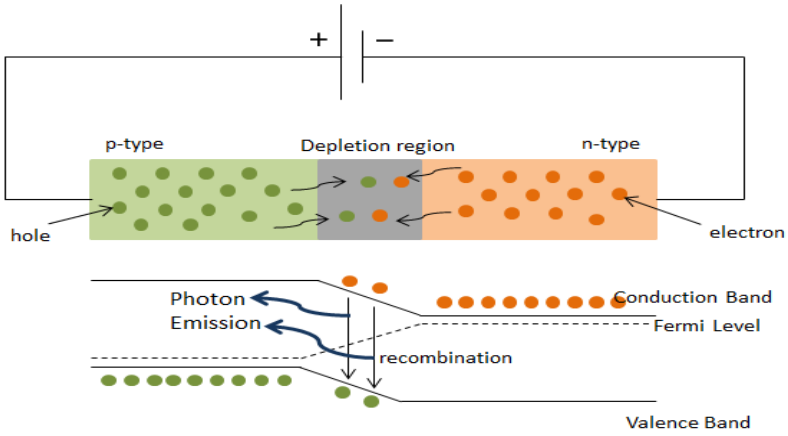

Figure 2-17 – LED operation under forward bias condition and recombination process

In principle, the basic operation of a generic LED occurs when it is placed in a forward-bias condition by applying a positive voltage across the device, as shown in Figure 2-17, which cause sufficient current to flow. Under this condition, electrons in the n-type and holes in the p-type drift into the depletion region (p-n junction) and recombine with carriers of opposite polarity. When these carriers recombine, photons are emitted from the device. As the voltage across the device is increased, the current flowing in the device is also increased. As a result, more carriers recombine, hence usually producing higher photons emission.

During the recombination process, electrons and holes can recombine either radiatively or non-radiatively. Radiative recombination results in the emission of photons. Non-radiative recombination, on the other hand, causes the electrons and holes to convert into vibrational energy of the lattice with no photons emitted. One of the main reasons for non-radiative recombination is the impurities and defects of the crystal structure.

The Current-Voltage (I-V) characteristic is given by the Shockley diode equation [26]. The Shockley equation for the current, I_D in a diode as a function of the applied voltage is given, as shown in Equation 2-9, where q, k and T are the electron charge constant, the Boltzmann constant and the device temperature respectively.

$$I_D = I_S \left(e^{\frac{q(V-V_{TH})}{kT}} - 1 \right)$$ **Equation 2-9**

where I_S is the reverse bias saturation current and V_{TH} is the diffusion voltage of the diode, or also known as the diode threshold voltage. Under the reverse bias condition, I_D saturates and I_S depends on the cross-sectional area, electron and hole concentrations, diffusion constant and minority carrier lifetime. Under the forward bias condition, the current increases rapidly as the diode voltage approaches V_{TH}. This is presented in the exponential part of the equation.

The wavelength of the emitted photons can be determined by the band-gap energy of the semiconductor material, which also affects its V_{TH}. V_{TH} can be approximated by dividing the band-gap energy by the electron charge constant, q. The relationship between the band-energy gap (E_g) and the wavelength (λ) is described by Equation 2-10 while the relationship between V_{TH} and E_g is given in Equation 2-11.

$$E_g = hf = h\left(\frac{c}{\lambda}\right)$$ **Equation 2-10**

$$V_{TH} = E_g/q$$ **Equation 2-11**

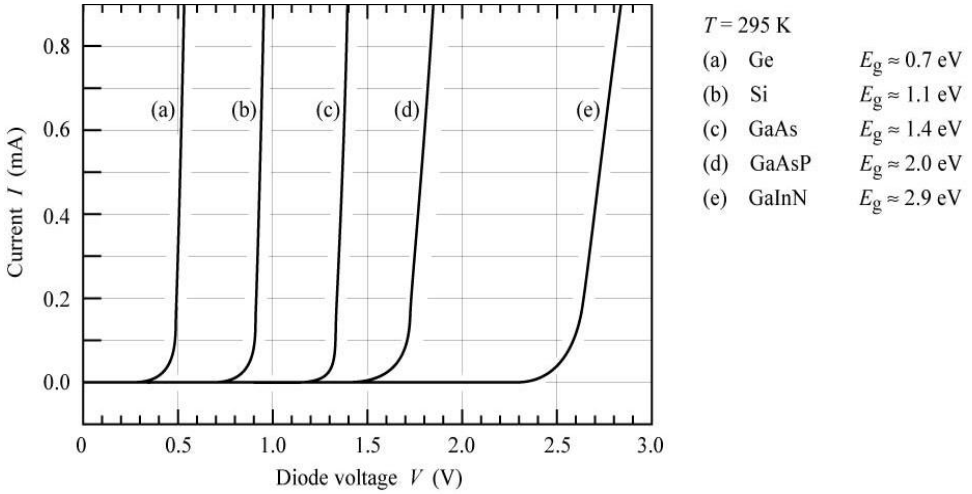

Figure 2-18 – Diode I-V characteristics with different materials [26]

where f is the frequency of the photon, c is the speed of light and h is the Planck constant. Figure 2-18 shows several diode I-V characteristics of the semiconductor made from different materials tabulated alongside with the band-gap energy of these materials [26].

2.6.1.1. LED Bandwidth

The –3dB bandwidth of an LED is defined from 0Hz to the frequency at which the optical power transmitted by the LED that is detected by a photodetector of higher bandwidth is reduced to half of its low frequency value. For LEDs which are used for lighting applications only, the diode p-n junction area (current injected active region area) is large. Such LEDs have large capacitance and consequently large RC time constant which determines the bandwidth. On the other hand, a dedicated communication LED has a smaller active region, thus a smaller RC time constant. As a result, a communication LED is designed for higher bandwidth and, therefore, can be modulated much faster.

Consider an LED with a very small active region, where the RC time constant is assumed to be negligible for explanation purposes. As voltage is applied, electrons are injected into the active region, increasing the minority carrier concentration. Then, the optical power produced by the LED increases as the injected minority carrier concentration increases. The relationship between the optical power and the injected minority carrier concentration can be explained using the monomolecular model [26] . Its rate equation is given as

$$n_a = \frac{I\tau}{qAd}\left(1 - e^{-\frac{t}{\tau}}\right) \qquad \textbf{Equation 2-12 [26]}$$

where n_a is the carrier concentration in the active region while A and d is the area of the p-n junction and its thickness respectively, and τ is the spontaneous recombination lifetime. From the equation, it can be said that it takes τ to fill the active region with the steady-state carrier concentration. Thus, the rise time is given by the spontaneous recombination time. A similar consideration applies to the fall time of the photodiode. Thus, the fall time of an LED is also given by the spontaneous recombination lifetime. Therefore, for a small active area LED where the RC time constant may be negligible, the bandwidth of an LED is limited by its spontaneous recombination lifetime.

2.6.2. Basic Operation and Properties of Photodiode

A photodiode converts light into electrical current called “photocurrent”. Electron-hole pairs are generated when incident photons with a greater energy than the semiconductor bandgap are absorbed. Photons with energy smaller than the bandgap energy of the semiconductor

(Silicon), however, cannot be absorbed and the semiconductor appears transparent [77]. The optical absorption coefficient (α) is the most important optical constant for a photodetector. α determines the penetration depth of the light in the semiconductor material. This is used to determine the photodiode structure which contributes to its responsivity. The responsivity of a photodiode is a measure of its light-to-current conversion efficiency. A highly responsive photodiode means a higher photocurrent generated from a given incident optical power. Responsivity of an "ideal" photodiode is defined mathematically in Equation 2-13.

$$\Re_{PD} = \frac{I_{ph}}{P_{inc}} = \frac{q\lambda_0}{hc}\,\eta_{ext} \qquad \textbf{Equation 2-13}$$

where I_{ph} is the photocurrent, P_{inc} is the incident optical power and λ_0 is the wavelength of the photons in μm.

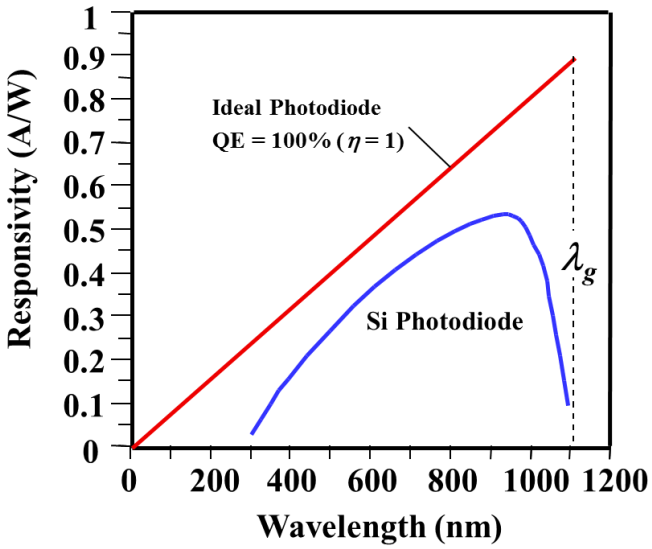

Figure 2-19 – Example of ideal vs. real responsivity curve for a typical Si-photodiode [77]

The responsivity of a "real" photodiode, however is always lower due to partial reflection of the light at the semiconductor surface and due to partial recombination of photogenerated carriers in the semiconductor or at its surface [77]. Figure 2-19 illustrates the difference of responsivity of a "real" and "ideal" photodiode. The difference can generally be described due to η_{ext} in Equation 2-13. η_{ext} is sometimes defined as the external quantum efficiency, representing the fraction of incident photons leading to I_{ph}. η_{ext} can be approximated by

$$\eta_{ext} = \eta_i (1 - \mathcal{R}_{ref}) \left(1 - \frac{e^{-\alpha X_d}}{1 + \alpha L_n}\right) \quad \textbf{Equation 2-14}$$

where $\mathcal{R}_{ref}$ is the optical reflectivity between air and the semiconductor, X_d is the thickness of the depletion region and η_i is the internal quantum efficiency defined as the ratio of number of electron-hole pairs created to the number of absorbed photons. In pure material, η_i is almost unity. $L_n$is the minority carrier diffusion length.

2.6.2.1. Photodiode Bandwidth

The bandwidth of a photodiode is defined as the frequency at which the responsivity of the photodiode has fallen by –3 dB from its low frequency values. The bandwidth of a photodiode can be written as

$$f_{RC} = \frac{1}{2\pi R_L C_{pd}} \quad \textbf{Equation 2-15}$$

where R_L is the load resistance and C_{pd} is the photodiode junction capacitance. C_{pd} is proportional to the area of the diode and inversely proportional to the depletion width of the p-n junction, X_d as depict in Equation 2-16

$$C_{pd} \propto \frac{A}{X_d} \quad \textbf{Equation 2-16}$$

X_d can be found using Equation 2-17 where ε_o is the dielectric constant in a vacuum and ε_i is the relative dielectric constant of the semiconductor, while N_p and N_n are impurity concentrations of the p and n region. ΔV is the reverse biased voltage applied to the photodiode and ϕ_i is the junction potential across the p-n junction. The value of ϕ_i can be found using Equation 2-18 where N_i is the intrinsic carrier density of silicon.

$$X_d = \sqrt{\frac{2\varepsilon_o \varepsilon_i}{q}\left(\frac{1}{N_n} + \frac{1}{N_p}\right)(\Delta V + \phi_i)} \quad \textbf{Equation 2-17}$$

$$\phi_i = \frac{kT}{q} log\left(\frac{N_n N_p}{N_i^2}\right) \quad \textbf{Equation 2-18}$$

From Equation 2-17 and Equation 2-18, it can be seen that the bandwidth of a photodiode is determined by

1. The area of the diode – Biggest contribution to C_{pd}. Thus, smaller photodiode has higher bandwidth.
2. Reverse bias voltage – increasing the reverse bias voltage will reduce C_{pd} but will be limited by the breakdown voltage of the diode.
3. Doping level – this, however, is fixed and depends on the foundry's technology process parameters.

Therefore, from Equation 2-15 to Equation 2-18, the bandwidth of the photodiode is mainly dominated by its area. However, it is important to note that while smaller photodiode area can give higher bandwidth, it also means that there is a smaller area for the incident photons. This in turn reduces the responsivity. Therefore, there is a trade-off between bandwidth and responsivity.

2.7. Summary

As the RF spectrum becomes more congested, there has been many research projects to find other forms of communication to reduce the dependency on RF and to realize the demand for higher data transmission. VLC using LED is seen as one of the options that have gathered much interest over the recent years due to its higher efficiency compared to normal incandescent light bulbs and can perform fast modulation. Two modulation schemes, OOK and OFDM, were discussed in this chapter. The OOK scheme was implemented in the previous microLED/CMOS drivers which were designed under the HYPIX project. In this thesis, an improved CMOS driver implementing OOK, called the Generation V CMOS driver or the digital driver, was designed. The aim, design and performance of the Generation V CMOS driver are discussed in detail in Chapter 3.

The OFDM scheme, on the other hand is recognised as a potential modulation to achieve higher transmission rate. The fundamental operation of OFDM and its problem was discussed in this chapter. Linearizing the optical power output was identified as one of the ways to improve the OFDM performance. Two CMOS drive ICs, called the CMOS Current Feedback driver and the CMOS Optical Feedback driver, were designed for this purpose and are discussed in detail in Chapter 4 and Chapter 5 respectively. Table 2-4 summarises the drivers that were designed and presented in this thesis.

Driver	Pixel pitch	Modulation Scheme	Correction method
Generation V microLED /CMOS driver	100um x 100um	OOK	N/A
microLED/CMOS Current Feedback driver	100um x 100um	OFDM	Simple electrical current feedback
microLED/CMOS Optical Feedback driver	100um x 100um	OFDM	Simple optical-feedback

Table 2-4 – CMOS drivers that were designed and discuss in the thesis

Chapter 3 : Generation V MicroLED/CMOS Driver

3.1. Introduction

This thesis project was closely associated with the HYPIX project, which is a collaboration between four universities; the University of Edinburgh, the University of Strathclyde, the University of St. Andrews and Imperial College London. The main goal of the HYPIX project was to demonstrate optically pumped polymer lasing with microLED as its optical source. A number of microLED/CMOS drivers were previously designed for this purpose before this project began. Although the microLED/CMOS drivers were designed primarily for optically pumped polymer lasing, it had previously been demonstrated that it could be used as a communication device [78, 79].

Design of CMOS driver array	University of Edinburgh
Fabrication of CMOS driver array	Austria Microsystem (AMS)
Design and fabrication of MicroLED array	Institute of Photonics (IoP), University of Strathclyde
Flip-chip bonding of CMOS and MicroLED	Optocap Ltd
Electrical Characterisation of microLED/CMOS Driver array	University of Edinburgh
DC Optical Characterisation of microLED/CMOS Driver array	University of Edinburgh
AC Optical Characterisation and communication test using microLED/CMOS Driver array	Institute of Photonics, University of Strathclyde
Optical Pumping Polymer Lasing Experiment using microLED/CMOS Driver array	Institute of Photonics, University of Strathclyde

Table 3-1 – Summary of work under the HYPIX project

This chapter introduces the microLED technology and the model used in the design of the Generation V microLED/CMOS driver array. Note that the works around the Generation V microLED/CMOS driver array involves several parties as summarised in Table 3-1. Therefore, only the design, layout and the DC characterisation of the Generation V microLED/CMOS driver array are presented in detail in this chapter. Results on communication test and polymer lasing experiment, on the other hand were supplied by IoP and are discussed briefly in this chapter.

3.2. The HYPIX Project

The HYPIX project was funded by the UK EPSRC. It started in October 2008 and ended in September 2012. The main objective of HYPIX was to demonstrate a new family of optoelectronics communication interfaces by fully hybridise organic semiconductor optoelectronics with inorganic CMOS based electronic control circuitry by using intermediate GaN optoelectronics, as illustrated schematically in Figure 3-1 [80]. One of the goals of the project was to design and develop a microsystem which is capable of doing "optically pumped organic semiconductor lasing (OSL)". Polymer was chosen as the organic semiconductor material while GaN microLED was chosen as the optical source. Early experiments have shown that polymer materials have high current density threshold [81], therefore a high intensity optical power from the microLED is very much required. The high optical power requirement for the polymer lasing, in a way, helps in achieving the work of this chapter, which is to explore and demonstrate the feasibility of an "Optical-Serial-Link (OSL)/microLED/CMOS" transceiver system that is capable of producing 100 Mb/s to 1 Gb/s data rates for free-space optical communication.

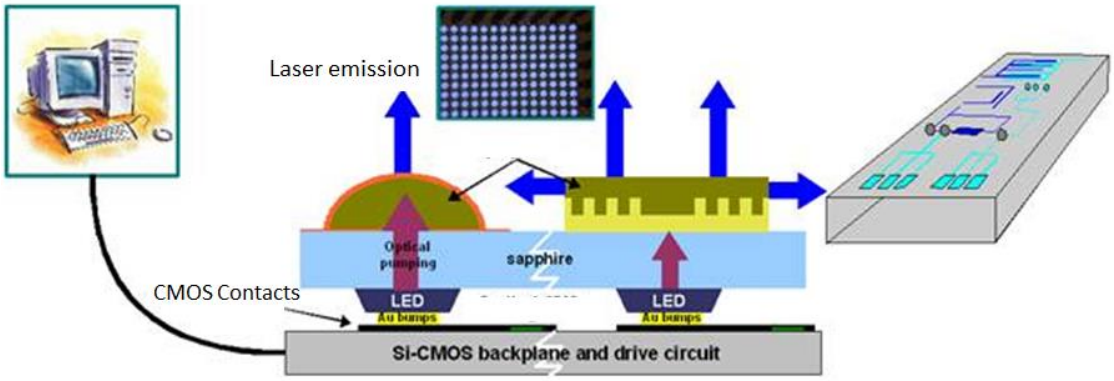

Figure 3-1 – Schematic image of hybrid optoelectronic interface concept [80]

When the work described in this chapter started in February 2011, HYPIX was already heading into its final year. Four chips, namely Generation I to Generation IV had previously been designed pre-2011, with each generation as an improvement from its predecessor to achieve the goal of demonstrating optically pumped polymer lasing. The microLED/CMOS drivers of previous generations were designed by Dr. Bruce Rae of the University of Edinburgh as part of his Ph.D. research [82].

3.3. AlIn-GaN MicroLED Array

MicroLED arrays based on Aluminium Indium Gallium Nitride (AlIn-GaN) alloy were developed by the IoP. The term “micro” refers to the size of the individual LED which is in the order of 10s to 100s of micrometer scale. While most VLC literatures describe the use of white LEDs, the microLEDs that were developed by the IoP and used in this project were blue microLEDs with a peak emission wavelength of 450nm [83]. A “white” emission LED can be derived from a blue emission LED (as discussed in Chapter 2), but such LEDs were not used in this research. Therefore, all experiments and results in this thesis were measured under blue emission.

AlIn-GaN microLEDs were developed using an n- and p- type GaN layers grown on a c-plane sapphire substrate by means of Metal Organic Chemical Vapour Deposition (MOVCD) [84]. The emission wavelength of the microLED is defined by the InGaN-GaN multiple quantum well (MQW) thickness and composition and therefore can be controlled [84]. Contacts to the p-type area of the dice are made using either Nickel-Gold (Ni-Au) or Palladium (Pd). These p-contact pads are placed in each pixel. Global ground plane contacts (n-contact) are made using Titanium-Gold (Ti-Au) deposition and placed at the edge of the array. The AlIn-GaN microLED fabrication steps are explained below and shown in Figure 3-2 [85, 86, 82]:

(a) The device structure consists of a layer of buffer GaN layer over the substrate, followed by an undoped GaN and n-doped GaN, an MQW of InGaN wells and AlGaN barriers, and p-doped AlGaN cladding and GaN contact layer.
(b) Pillar-mesa structures for isolation are formed by photolithographic patterning and inductively coupled plasma (ICP) etching. Subsequently, trenches are created on the edge of the active area by ICP giving access to the n-type GaN layer below the active region (this is not shown in the figure).
(c) The metal layers, including the spreading and pad layers, are deposited using electron beam evaporation patterned by a standard lift-off procedure.
(d) Silicon Dioxide (SiO2) layer is deposited on the etched structured using plasma-enhanced chemical vapour deposition. The SiO2 on the top of the pillars is partially removed using photolithographic patterning.
(e) The interconnection of each pillar is done by metal lines using a sputtering process, defining the p-contact pads, n-contact pads and tracks.

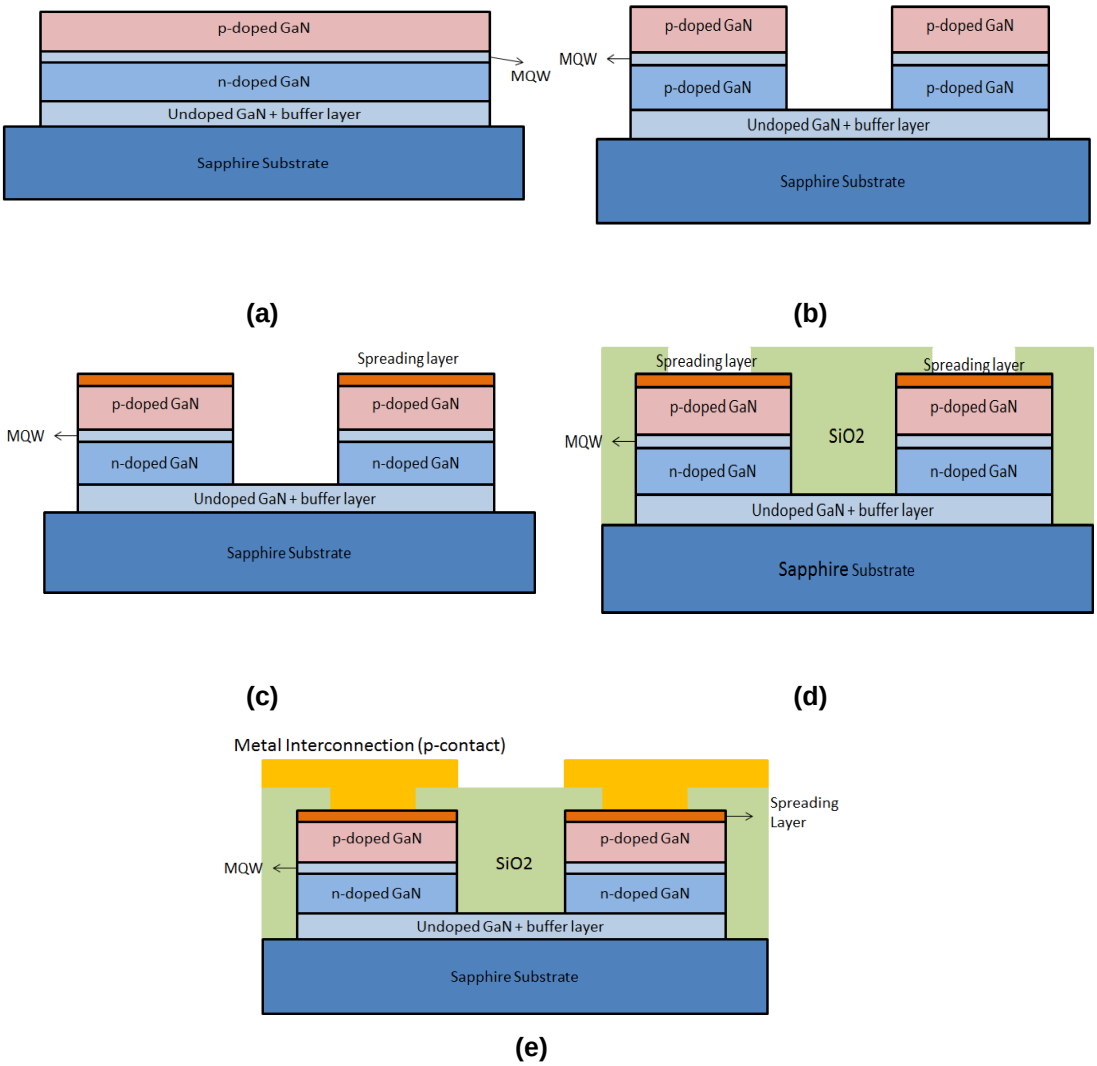

Figure 3-2 – MicroLED device schematic cross-section fabrication steps: (a) Device structure (b) Formation of mesa structure (c) Deposition of metal layer (d) Deposition of SiO2 (e) Defining interconnection

A MicroLED is a quantum well based device that exhibits increased radiative efficiency and reduced recombination lifetime by confining the free carriers to the narrow well region [85]. This has resulted in increased optical output power and shorter rise and fall times compared to p-n homo junction LEDs. Furthermore, due to the microLED's smaller dimensions, the switching time is potentially shorter due to lower capacitance compared to conventional LEDs as explained in Section 2.6.1. This is an advantage for communication applications, such as VLC, where a large bandwidth optical source is very much desired.

3.4. Generation V CMOS Driver

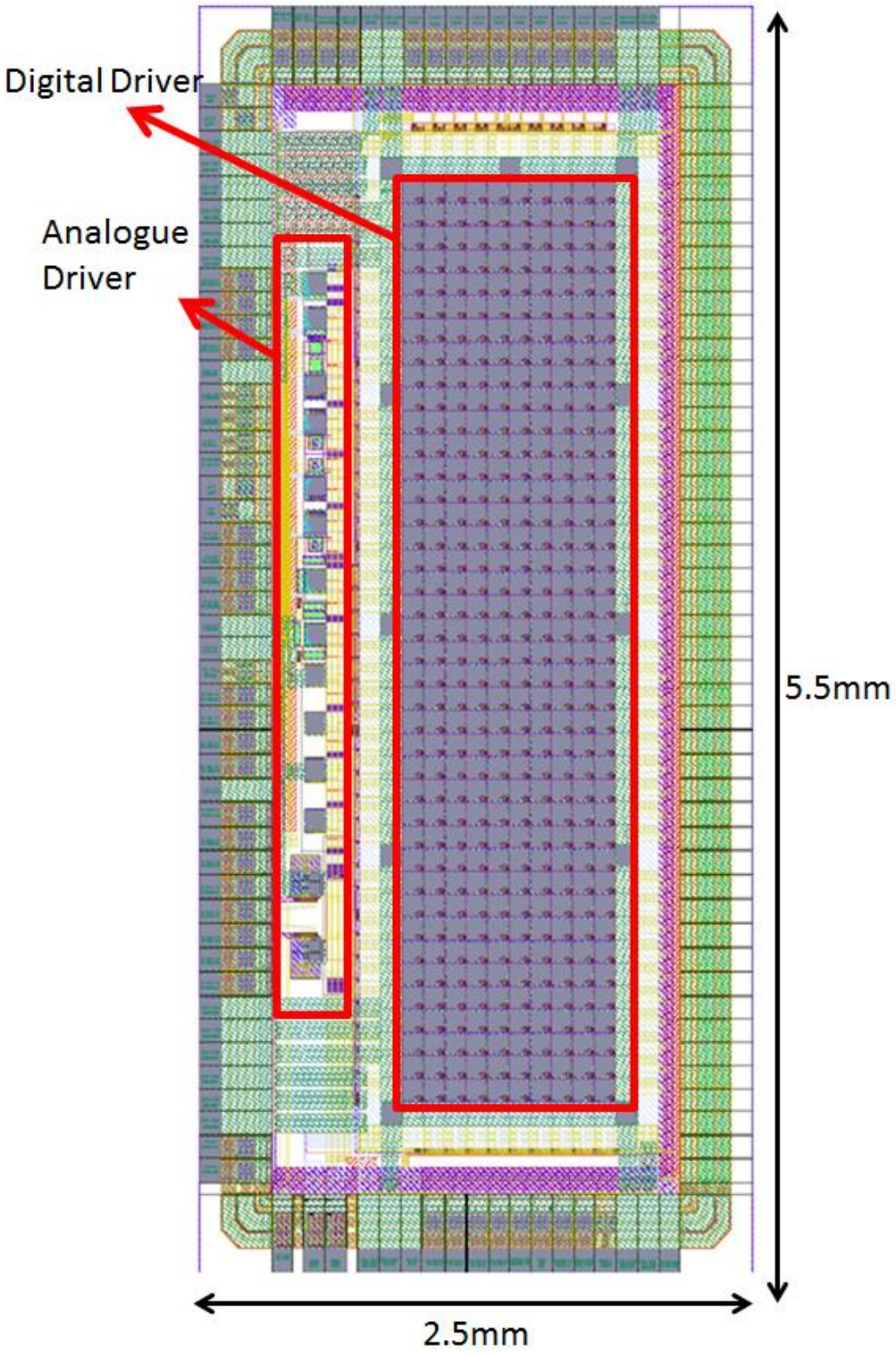

Figure 3-3 – Schematic layout floor plan of the CMOS driver chip

The CMOS driver chip for MicroLED reported in this thesis was the final CMOS driver chip that was taped out under the HYPIX project. As mentioned before, four CMOS driver chips were previously designed under the HYPIX project. For ease of explanation, these CMOS drivers are named as Generation I, Generation II, Generation III and Generation IV CMOS driver respectively. A summary description of these drivers is included in Table 3-2 and details are presented in Appendix A. Some of the results on VLC from these drivers can be found in [79, 87].

	Generation I	**Generation II**	**Generation III**	**Generation IV**
Technology Process	AMS 0.35µm High Voltage process	AMS 0.35µm Standard process	AMS 0.35µm Standard process	AMS 0.35µm Standard process
Pixel Pitch	100µm x 100µm	100µm x 100µm	200µm x 200µm	100µm x 100µm
Number of Pixel in Array	16x4	16x16	8x8	16x16
Driving Current per Pixel	5mA	-	90mA	180mA
Optical Power per Pixel	10uW	-	550uW	1.5mW
LED Drive Method	Current drive	Voltage drive	Voltage drive	Voltage drive
Note	- Very low optical power	-Bonding Problem	- Bond stack introduced - Crosstalk problem	- Optical power still low for polymer lasing

Table 3-2 – Summary of Generation I to Generation IV microLED/CMOS drivers array

Demonstrations of VLC application presented in [78, 79] using Generation III and Generation IV CMOS drivers prompted a dedicated CMOS driver for communication. Based on this, two general CMOS drivers were designed on the new CMOS driver chip:

1. **Generation V CMOS Driver or the Digital Driver -** A direct development based on the previous generations, designed for optical pumping polymer lasing and VLC application using the OOK modulation scheme. Sometimes called "digital driver" in this thesis because of the nature of OOK mimicking digital output
2. **Analogue Driver -** two CMOS drivers that are specifically designed for VLC purposes which uses OFDM as its modulation scheme (as mentioned in Section 2.5). The drivers are called the "analogue drivers" because the microLED light output can be modulated depending on the input level to the driver rather than only "on" or "off".

Figure 3-3 shows the high-level floorplan of the new CMOS driver chip. Both the digital driver and analogue driver are highlighted in the diagram. This chapter only focuses on the design of the digital driver while the design of the two analogue drivers is presented separately later in Chapter 4 and Chapter 5. The specification for the digital driver, however, was primarily set by the requirement of the polymer lasing experiment that higher optical power is still needed to lase the polymer.

3.4.1. Generation V MicroLED/CMOS Driver Target Specification

The main specification for this chip was determined by the requirement to perform the optically pumped polymer lasing experiment. The target specification is described below and is summarised in Table 3-3.

Parameter	Value
Pixel Pitch	100µm x 100µm
Active Area Dimension	3mm x 5mm
Current Drive	360mA
Optical Power	8mW
Voltage Droop	Minimize
Bandwidth	147MHz

Table 3-3 – Table of target specification

1. **Pixel Pitch –** The pixel area was specified to be 100µm x 100µm (Square pixel), which is the same as its predecessor (Generation IV microLED/CMOS driver).
2. **Active Area for Polymer Lasing Experiment –** To help and provide more efficiency with the polymer lasing experiment, the active area (Illumination area) of the microLED array was required to be long and narrow. The dimension of the active area was specified to be at least 3mm x 0.5mm.
3. **Improve Optical Power Output –** The Generation IV microLED/CMOS driver was capable of producing about 180mA of current which in turn produced approximately 3.5mW of optical power. However, this is still not enough to overcome the polymer current density threshold. Although no specific number was given, the Generation V is expected to drive at least two times greater than its Generation IV predecessor.
4. **Voltage Droop Minimisation –** Due to the dimension of the active area specified, voltage droop due to the resistive track would be an issue. Voltage droop across the array would have to be minimised in order to keep the optical power uniform across the array.

5. **Bandwidth –** In the Generation IV microLED/CMOS driver, two types of driving methods were included known as **Common_Input** and **Parallel_Input. Common_Input** drives the pixels with a single common input signal while **Parallel_Input** allows multiple pixels to be driven with multiple input signals. However, it was found on Generation IV that the **Common_Input** signal gives a higher bandwidth than when using **Parallel_Input.** The Generation V microLED/CMOS driver will be looking to investigate and solve the problem.

3.4.2. MicroLED Equivalent Circuit Model for Generation V CMOS Driver

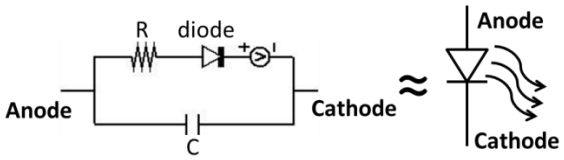

Figure 3-4 – Schematic of MicroLED model

In electrical terms, an LED is conventionally modelled as a series combination of a resistor (R), an ideal diode and a voltage source in parallel with a capacitor (C), as shown in Figure 3-4. The resistor and capacitor in parallel represent the RC time constant due to the device parasitic component which is usually dominated by the metal contacts. The I-V characteristic, based on the Shockley equation (Equation 2-9), is represented by the diode. Because an ideal diode would have a threshold voltage of about 0.7V, a voltage source is connected in series to give the desired representation of an LED threshold voltage.

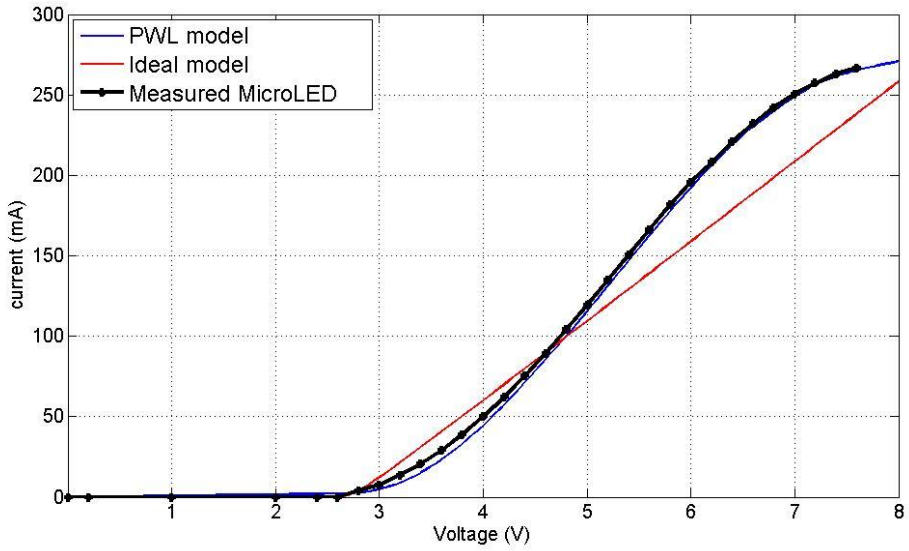

Figure 3-5 – I-V characteristics comparison

The ideal diode model, however, is not accurate enough to represent a real LED. A more accurate method known as a "Piecewise Linear" (PWL) approximation model was employed to replace the ideal diode and voltage source. PWL is a mathematical method of taking a function and separating it into many linear segments. Using this approach, PWL models the microLED I-V characteristic curve as a series of linear segments. The model measures the voltage across the device and forces a fixed current through the device. Therefore, the current is a more accurate interpolation between two defined I-V characteristic points. The points defined in the PWL model are based on the measurement from a bare microLED die that was used for the Generation IV CMOS driver. The simulated result is shown in Figure 3-5 where the PWL closely matched the microLED I-V characteristic curve compared to the ideal diode model. The values of R and C are 15Ω and 10pF respectively, based on measurements conducted by researchers at the IoP on the bare microLED die. The PWL model is written in Verilog-A and simulated in Cadence.

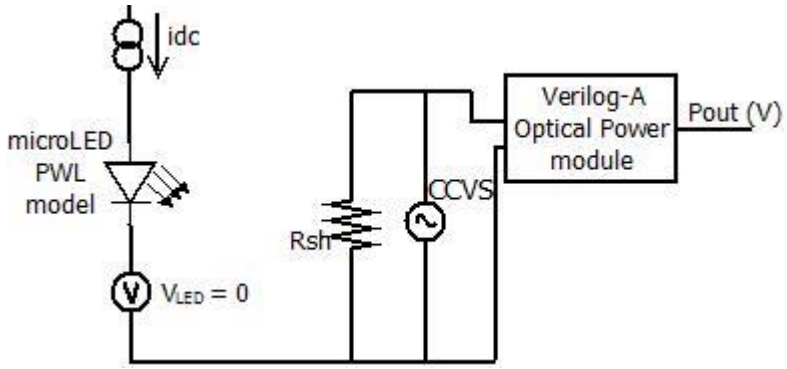

Figure 3-6 – Optical Response simulation configuration

The microLED optical power response was also modelled with Verilog-A using the configuration shown in Figure 3-6. A Current-Controlled Voltage Source (CCVS) converts the microLED current to a voltage which is then passed into the Verilog-A module. The Verilog-A module is a transfer function based on a third-order polynomial curve fitting of the optical power response of the same bare-die microLED that was used to measure the I-V characteristic. The optical power (P_{OUT}) is presented as a voltage in the simulation.

The choice of an optimum degree for a polynomial curve representing the LED optical power response is discussed in [88]. Although higher polynomial orders will give a more accurate optical power response model, a third-order polynomial has already shown close approximation of the non-linearity of the L-I characteristic of the microLED as presented in Figure 3-7. The polynomial equation is

$$P_{out}\,(V) = p_4(I_{LED})^3 + p_3(I_{LED})^2 + p_2(I_{LED}) + p_1 \qquad \textbf{Equation 3-1}$$

where p_4, p_3, p_2, and p_1 are the 3rd order non-linearity coefficient, 2nd order non-linearity coefficient, the linear gain and the DC term respectively.

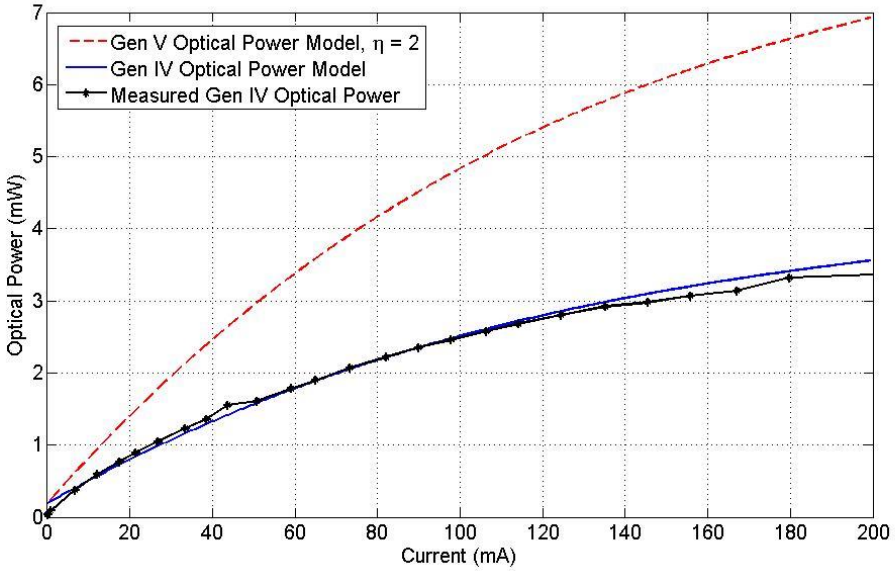

Figure 3-7 – L-I characteristic comparison

The transfer function is important to predict the non-linearity of the optical power response of the microLED, especially for the design of the optical feedback driver (which is discussed in detail in Chapter 5). A batch of microLEDs was under construction during the design of the Generation V CMOS driver. This batch was expected to give higher quantum efficiency than its predecessor. Assuming the transfer function remains approximately the same; the optical power response for the new batch of microLEDs can be predicted by multiplying the coefficients by η, where η is the optical power ratio of the new batch of microLEDs to its predecessor. The optical response of the new batch of microLEDs is shown in Figure 3-7 with η = 2.

3.4.3. Design of Generation V MicroLED/CMOS Driver

The Generation V microLED/CMOS driver was fabricated on the AMS 0.35µm BiCMOS process. The BiCMOS process was chosen because of the availability of the thick top metal layer which:

1. Adds additional mechanical strength to protect the CMOS circuitry during the bonding process between the microLED and CMOS die. The purpose of this is to avoid the

problem that occurred in the Generation II CMOS driver, in which the top metal layer can break during the bonding process, thus short-circuiting the circuitry underneath (Appendix A.2) [82].

2. Replaces the bond stack that was employed in Generation III and Generation IV CMOS driver (Appendix A.3 and A.4) which was a solution to the bonding problem faced in Generation II. The employment of the bond stack solves the bonding problem, but it comes at a cost of reducing the area available for driver circuitry within each pixel.

An array of 40x10 pixels was implemented and the pixel pitch was set to 100µmx100µm, thus keeping the pixel pitch to be the same as its predecessors. This was based on the specification given which will assist the polymer lasing experiment. Therefore, the microLED active area will be 4mm x 1mm, approximately 66% more than the minimum specified.

The aim for the Generation V microLED/CMOS driver was to produce optical power at least two times greater than that of Generation IV. This can be realised, from a CMOS driver point of view, by delivering at least two times more current to the microLED, which could be achieved by using wide transistors. However, this would also mean that the CMOS circuitry would demand the maximum use of the limited space specified by the 100µm square pitch. In order to accomplish this, the use of a bond-stack in Generation IV was replaced by a thick top-metal layer, as explained earlier, and the microLED is bump-bonded directly onto the pixel. Removing the bond-stack provides about 3600µm^2 (i.e. 36%) "additional" area for the CMOS circuitry. The thickness of the top metal layer in the BiCMOS process is 2800nm, three times more than the standard process. With the increase in thickness of the top metal layer, it was expected to be able to withstand the high pressure process during the bump-bonding procedure.

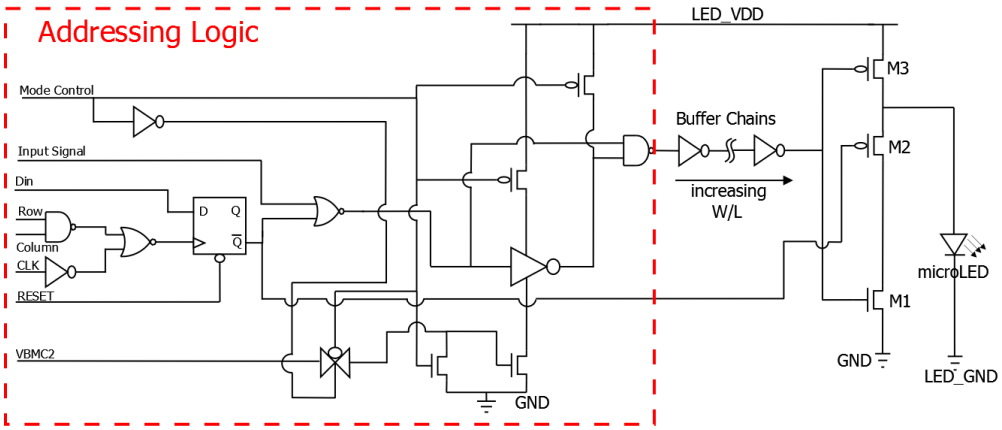

Figure 3-8 – Circuit Schematic of Generation V CMOS MicroLED Driver

The circuit of the Generation V CMOS driver followed that of Generation IV (A.4) as shown in Figure 3-8, and used only 3.3V transistors. The block labelled as ”addressing logic” was provided from the AMS 0.35µm library using minimum size transistors, which is only used for addressing purposes. The driver can perform two modes of operation: continuous wave (CW) and pulse mode to help with polymer lasing experiments. The mode can be selected using a **Mode_Control** pin and the pulse width is determined by changing the input voltage on **VBMC2**. The driver also has the ability to switch input signal between **Common_Input** and **Parallel_Input,** as with Generation IV. The changes that were implemented in the Generation V driver include re-designing of the clock tree (not shown in Figure 3-8) for **Common_Input** and **Parallel_Input** to solve the bandwidth discrepancy, the number of parallel inputs, and the width of the driving transistor (M1, M2 and M3 in Figure 3-8) and buffer chain transistors. Parallel inputs were reduced to 10 from 16 inputs in Generation IV due to the shape of the array and the number of columns available. M1, M2 and M3 are the transistors that drive the microLED; thus the width of these transistors needs to be as large as possible (within the constraint of the pixel pitch) to maximise the current supplied to the microLED. To compensate the voltage reduction across the microLED, LED_GND was made tuneable in a reverse bias condition. Therefore, the current flow through the microLED is dictated by the reverse bias condition set to LED_GND, which is fully determined by its I-V characteristic.

Using a minimum length of 0.35 µm, the width of the each transistor is 660 µm, 800 µm and 2000 µm for M1, M2 and M3 respectively. These are twice the width of its predecessor, and together fill more than 50% of the pixel area. The current produced at the output of the driver can be estimated using a first order calculation. The current is supplied by the large p-channel Metal-Oxide-Semiconductor Field Effect Transistor (MOSFET) device (M3). K_p' is the device transconductance-gain and is defined by the process and foundry [89]. The process K_p' value and its threshold voltage (V_T) is given as 58 µA/V^2 and 0.65 V respectively. M3 parameters are summarised in Table 3-4.

Device Width	2000 µm
Device Length	0.35 µm
K_p'	58 µA/V^2 (typical)
V_T	– 0.65 (typical)

Table 3-4 – p-channel MOSFET (M3) parameters [89]

When the driver first begins to supply current to the microLED, no voltage is dropped across the diode. Therefore, the ideal instantaneous drain-source voltage (V_{DS}) across M3 is equal to –LED_VDD. Assuming that the gate-source voltage (V_{GS}) is –3.3V (which is equal to V_{DS}) when supplying current, M3 is operating in the saturation region. In the saturation region, M3 is capable to deliver about 1.16A of current per pixel. This calculation is shown in Equation 3-2.

$$I_D = -\frac{K_p' W}{2L}(V_{GS} - V_T)^2 = -1.16 \text{ A} \qquad \textbf{Equation 3-2}$$

where $I_D$is the current produced by M3. Once I_D flows through the microLED, there is a voltage drop across the device. This results in a reduction to V_{DS} of M3 and hence placing it to operate in the linear region. Under the linear region, Equation 3-3 can be used to predict the current supplied to the diode. This calculation is made by assuming there has been a 2.75V drop across the microLED. This value is chosen based on the microLED turn-on voltage. The same K_p', W and L parameters are used to calculate the value.

$$I_{DS} = -\frac{K_p' W}{L}\left(V_{GS} - V_T - \frac{V_{DS}}{2}\right)V_{DS} \approx -430mA \qquad \textbf{Equation 3-3}$$

The initial large current delivered by M3 in the saturation region could potentially improve the rise time when the driver is first switched on [82]. When M3 shifts into the linear region, the current is then reduced. Therefore, in DC mode or continuous wave operation mode, the maximum current produced by the Generation V CMOS driver can be approximated to be around 430 mA.

The width of individual transistors within each stage of the buffer chain was optimised to handle the high capacitance loading of the huge drive transistors (M1, M3). By sequentially increasing the width of each buffer stage, the drive strengths are increased and so the ability to drive higher capacitance. This is vital in order to maintain the bandwidth of the CMOS driver. The MOSFET width of successive buffer-chain inverters was increased by 2.5 to 2.85 times the original size. P-channel MOSFETs are approximately two times wider than n-channel MOSFETs due to the difference in mobility. This parameter would vary depending on the chosen technology and process node [89].

3.4.4. Simulation

Transient simulation was performed in Cadence, comparing the performance of Generation IV and Generation V CMOS drivers. The driving capability of the drivers was investigated by short circuiting the output of the drivers to ground. Figure 3-9 shows the driving capability comparison between the Generation IV and Generation V CMOS drivers where the simulated current was found to be about 221mA for the former and the latter produced approximately 445mA. This is as expected as the width of the output transistors (M1, M2 and M3 in Figure 3-8) in Generation V are two times that of Generation IV. The maximum transient current produced in the simulation is slightly higher than previously estimated because it is more accurate than the first order derivation used in Equation 3-3. Current overshoots at the edge of the pulse are caused by M3 operating very briefly in the saturation region before moving into the linear region, as explained in the previous section.

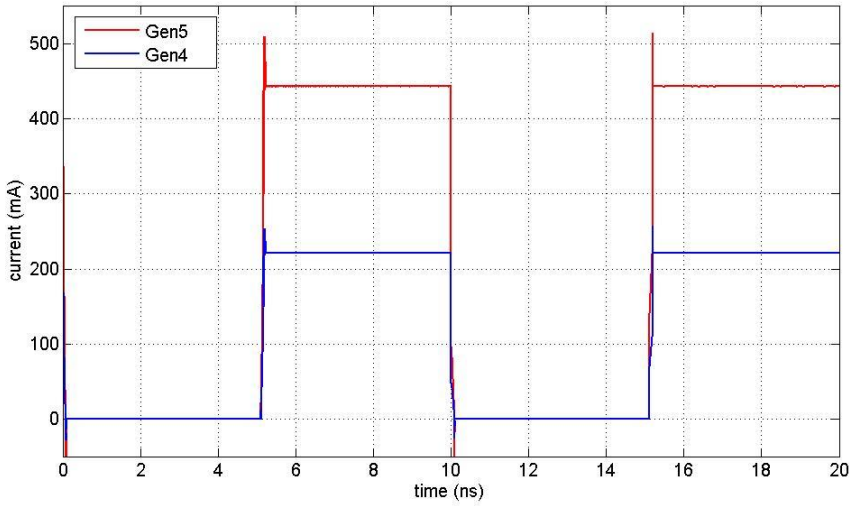

Figure 3-9 – Transient simulation comparison of current produced between Generation IV and Generation V

Figure 3-10 (a) shows the CMOS driver's operation when drawing load from the microLED model with LED_GND node biased at –5V. There is a significant drop in the current produced by both drivers of the short circuit simulations, with Generation V producing about 270mA and Generation IV produces about 185mA, reducing the Generation V to Generation IV current ratio $\left(\frac{I_{Gen5}}{I_{Gen4}}\right)$ from 2 to approximately 1.46. Biasing LED_GND more negative results in minimal change in the driving current. The reduction in current is mainly due to the internal (parasitic) resistance of the microLED. The simulated result for the Generation IV driver is

consistent with the measured result (as presented in Appendix A.4). Thus, the actual performance of the Generation V CMOS driver is expected to be close to the simulated result in Figure 3-10. The Generation V driver suffers bigger current drop than Generation IV because of the higher current produced, therefore causing a higher voltage drop across the microLED and hence pushing M3 further into the linear region.

Figure 3-10 also shows the speed of operation for both drivers. The ability to keep the rise and fall time in the Generation V driver was helped by the high current produced by the driver when it operates briefly in the saturation region. The rise time close-up is shown in Figure 3-10(b), where it shows that the rise time for Generation V driver is about 800ps, faster than Generation IV which is about 1ns. Therefore, Generation V is expected to have a higher bandwidth than generation IV.

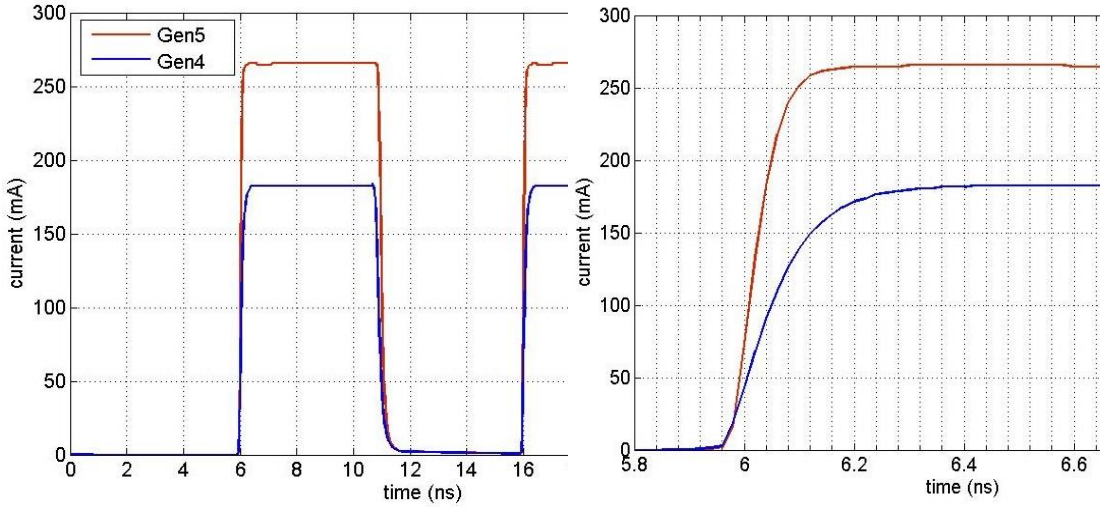

(a) **(b)**

Figure 3-10 – (a) Transient Simulation with MicroLED model and (b) Rise time close-up

Figure 3-11 shows the optical power transient simulation. In this simulation, two optical power models were used, named as "Gen IV Optical Power Model" and "Gen V Optical Power Model" (Figure 3-7). The configuration and simulated result are summarised in Table 3-5.

Simulation	CMOS Driver	MicroLED Optical Power Model	Simulated Optical Power
1	Generation V	Gen V	7.6mW
2	Generation V	Gen IV	3.8mW
3	Generation IV	Gen IV	3.3mW

Table 3-5 – Transient simulation summary

From Table 3-5, it can be said that, although $\left(\frac{I_{Gen5}}{I_{Gen4}}\right)$ has a ratio of 1.46, the optical power ratio of the Generation V to Generation IV CMOS driver $\left(\frac{P_{Gen5}}{P_{Gen4}}\right)$ is only 1.15 if no improvement is made on the microLED. The decrease in the ratio is because of the non-linear characteristic of the current-to-optical power conversion by the microLED. On the other hand, if the microLED current to light conversion efficiency is increased by a factor of 2, as predicted, then $\left(\frac{P_{Gen5}}{P_{Gen4}}\right)$ is increased to 2.3. Therefore, it can be summarised here that in order to improve the performance of the Generation V microLED/CMOS driver, both the microLED and CMOS driver need to be improved.

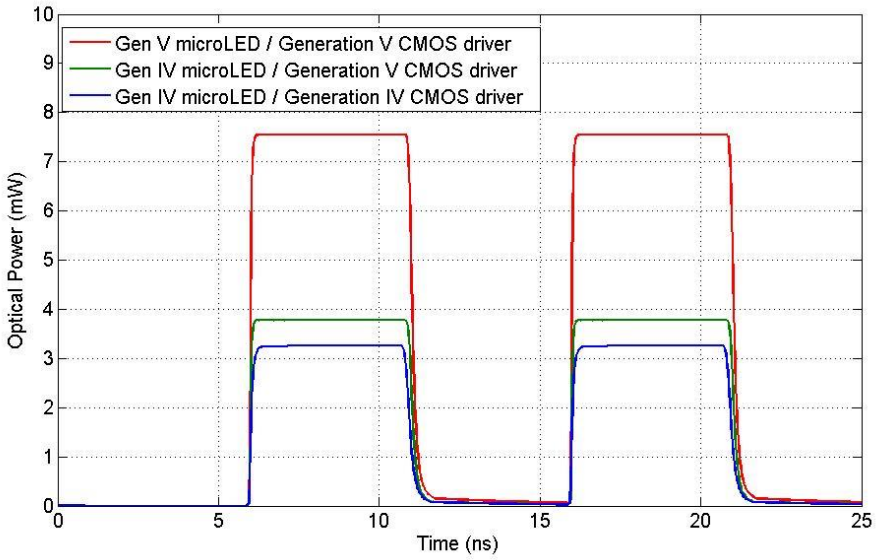

Figure 3-11 – Optical Power Transient Simulation

3.5. Layout of the Generation V MicroLED/CMOS Driver

As mentioned earlier, the main objective of the design was to produce optical power output as high as possible. This then led to the increment of the width of the drive transistors (Buffer-chain, M1, M2 and M3). The width of these transistors, however, was limited by the pixel pitch that was set to 100µm square. In theory, wider transistors would be able to produce higher current, but would require a greater area. Therefore, it is fair to say that the chosen size of these transistors is at the limit for a given pixel pitch area and process. The method of choosing the width of these transistors was based on a manual optimisation method. A set of drive transistor width was calculated and was quickly laid out. This gives a clearer image if

the pixel area has been optimally used. The chosen set of values is then optimised for the final value.

Under the BiCMOS process, four layers of metal were available. This is the same as Generation IV, which uses the standard process. For ease of explanation, the metal layers are named as Metal1, Metal2, Metal3 and Metal4, where Metal4 is the top metal layer. The schematic layout of the Generation IV and Generation V CMOS drivers is shown in Figure 3-12 (a) and (b) respectively. Metal2, Metal3 and Metal4 were omitted from the figure for a clearer presentation of the underlying devices. The figure shows a clear advantage of removing the large bond-stack, which leads to a much greater width of M1, M2 and M3 as well as the buffer chain.

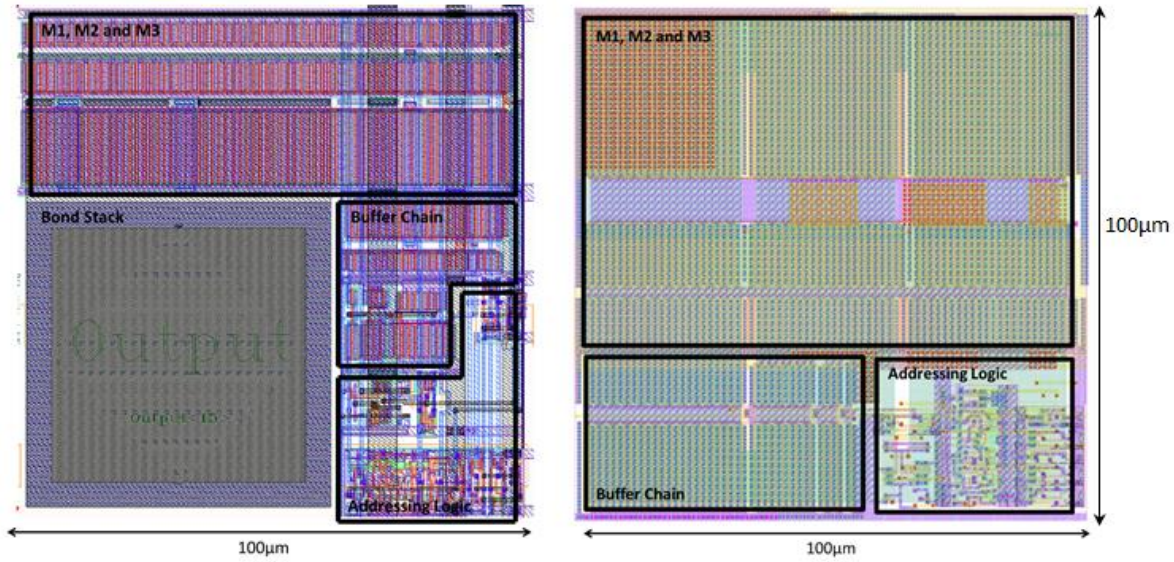

(a) **(b)**

Figure 3-12 – Comparison of Layout Plan between (a) Generation IV and (b) Generation V CMOS Driver Pixel

Two important aspects were prioritised when designing the layout for the Generation V driver:

1. The full use of the top metal layer (Metal4) as electrode and protection to the circuitry underneath. The BiCMOS process with thick top metal layer was chosen for this reason.
2. To reduce the voltage droop effect and improve uniformity across the array. Therefore the metal-rail resistance needed to be minimised.

In order to accommodate the first requirement, Metal4 is used exclusively for bonding and circuitry protection purposes. Therefore, Metal4 is no longer available for any circuitry

interconnections. The dimensions of Metal4 are 94 µm x 94µm, covering approximately 88% of the pixel. A passivation window was opened on top of the Metal4, which consists of an area of 80µm x 80µm, in accordance with the process design rule [89]. The horizontal diameter of the gold-bump after bonding was the reason why the Metal4 pad opening was made large. Based on past bonding experiences, typical gold-bump diameter after bonding is 70µm to 75µm. The opening was made wider to provide slight headroom and flexibility during the bump bonding process.

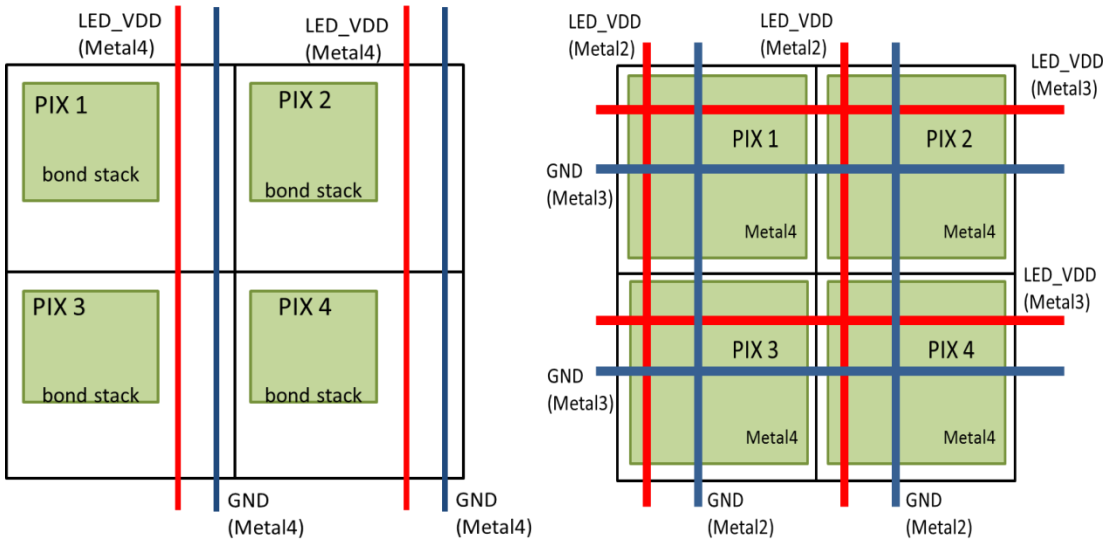

Figure 3-13 – Changes in power tracks Layout on (a) Generation IV (b) Generation V

Other available metal layers were used as circuitry interconnections (Metal1 and Metal2) and LED_VDD and GND power rails (Metal2 and Metal3). To fulfil the second requirement, power rails were made as wide as possible to minimise voltage droop due to the rail sheet resistance, hence providing more uniformity across the array. Figure 3-13 shows a schematic representation comparison of the power rails laid out in both Generation IV and Generation V CMOS driver.

Table 3-6 summarises the comparison of the sheet resistance of the metal layers in BiCMOS and standard process. In Generation IV, Metal4 was used to route the power rails. In Generation V, however, such luxury is no longer available as Metal4 is used as the bonding pad for the microLED. Therefore, Metal2 and Metal3 were used exclusively for routing power rails, leaving only Metal1 for circuitry interconnections. As noted in Table 3-6, the sheet resistance of Metal4 is 40mΩ/□ (on Standard process) and 70mΩ/□ for both Metal2 and Metal3 (on the BiCMOS process) [89]. Therefore, power rails on Generation V have to be at

least two times the width of its predecessor. Furthermore, an 'x-y grid' arrangement was implemented, which means that current will flow both vertically and horizontally. This is to avoid the pixels from suffering a huge voltage drop, especially for pixels at the centre of the array, due to long power rails.

Layer	Typical Sheet Resistance (mΩ/□)	
	Standard process	BiCMOS process
Metal2	70	70
Metal3	70	70
Metal4	40	10

Table 3-6 - Sheet resistance of Metal tracks on two different processes [89]

Table 3-7 summarised the width of the tracks used in both Generation IV and Generation V.

	Generation IV	Generation V	
	Metal4	Metal3	Metal2
LED VDD	5.6 µm	40 µm	33 µm
GND	4 µm	17 µm	25 µm

Table 3-7 – Track Width used in Generation IV and Generation V

Taking the length of the tracks as 100um, using first order sheet resistance equation and values from Table 3-7, the track resistance of a single pixel can be estimated.

$$R_{track} = R_{sheet} \times \frac{L}{W} \qquad \textbf{Equation 3-4}$$

where R_{sheet} is the sheet resistance, W and L are the width and the length of the track respectively in a single pixel. Using this equation, LED_VDD and GND R_{track} for Generation IV was calculated to be 0.71Ω and 1Ω respectively. In Generation V, LED_VDD R_{track} was calculated to be 0.175Ω on Metal3 and 0.21Ω on Metal2 meanwhile R_{track} on the GND rail is 0.40Ω on Metal3 and 0.28Ω on Metal2. For the sake of comparison, average resistance is taken from the two metal layers which give 0.1925Ω for LED_VDD and 0.34Ω for GND on Generation V. This shows a potential reduction in voltage drop across the array by a factor of 3.6 and 2.9 for LED_VDD and GND respectively.

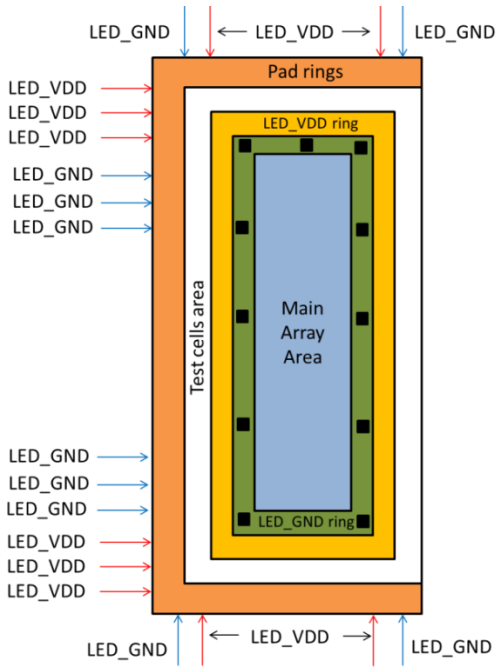

Figure 3-14 – Generation V microLED/CMOS driver outline schematic

Figure 3-14 shows the outline schematic of the Generation V CMOS microLED driver chip. The main array is surrounded by power rings (LED_VDD and LED_GND). On the LED_GND ring, there are 11 pad openings which are presented as black squares. The n-contacts of the microLED are bump-bonded on these openings while the p-contacts are bump-bonded to the windows on every pixel. Notice that pad rings are not available on the right hand side, which reduces the number of possible input/output (I/O) for this chip. The purpose of the single sided wire-bond is to avoid damage to the CMOS chip and provide more manoeuvrability during the integration of the microLED/CMOS driver with the polymer materials in the lasing experiment. To accommodate the higher current consumption of the microLED, LED_VDD and LED_GND are provided with 10 dedicated pads each. The placement of these input pads is shown in Figure 3-14. Moreover, this was planned to help achieve better uniformity across the array.

3.6. Bump Bonding

Bump bonding is a chip stacking technique, which in recent years, has become more prevalent in order to assist in maintaining Moore's Law. Other chip stacking techniques includes Through-Silicon Vias (TSV), conductive glues [90, 91] and solder re-flow [92]. Bump-bonding has been used in the HYPIX project since the start and has seen some success over

the duration of the project, as presented in Appendix A. The process of bump-bonding is discussed in detail here. The bump-bonding process for HYPIX was performed by OptoCap Ltd [93]. The process of bump-bonding involves two main steps:

1. Deposition of gold ball bonds on the CMOS chip
2. Bringing together and bonding of the microLED device onto the CMOS chip

3.6.1. Deposition of Gold Ball Bonds

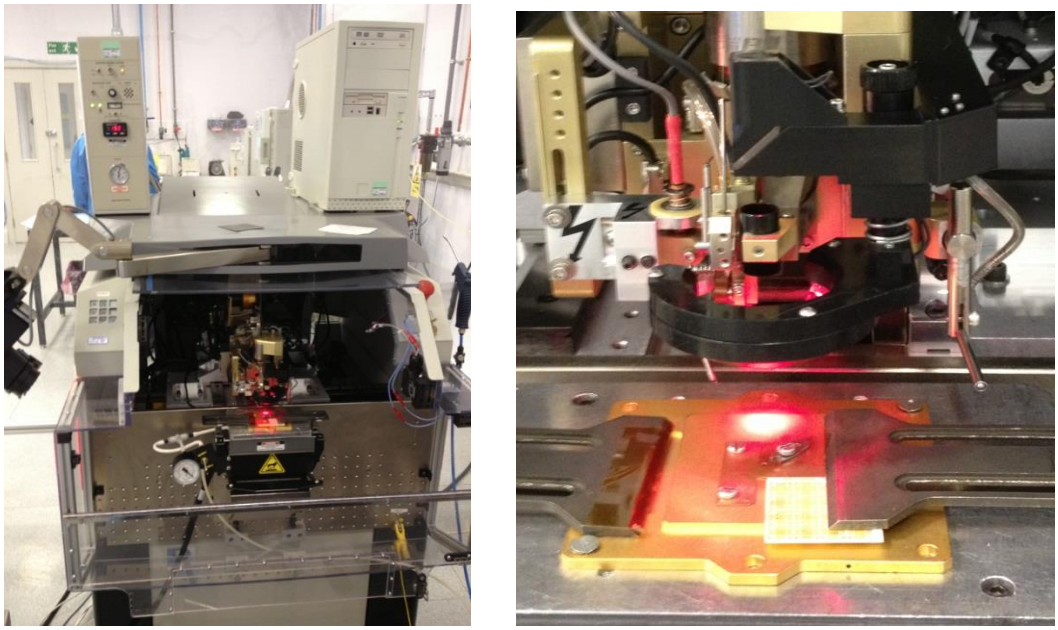

(a) **(b)**

Figure 3-15 – (a) Palomar 8000 Automatic Wire Bonder and (b) Close up of bonding capillary

The CMOS chip is mounted on a Palomar 8000 automatic wire bonder (Figure 3-15) [94] and the bonding tip is fed with a 25µm diameter gold wire via a capillary. A combination of thermal, electrical and ultrasonic energy is applied to form a gold wire ball bond to the die. The capillary is then raised and moved side-to-side to weaken the tail of the wire. Subsequently, a gentle pull is made by the capillary to break off the wire. The process forms a ball of 70µm to 75µm diameter with about 50µm height. The bonding procedure is initialised in a computer and the bonding machine automatically visits each bond pad in the CMOS chip based on the position set. This process is repeated until all elements on the chip are populated with gold ball bond.

3.6.2. Flip-chip Bond

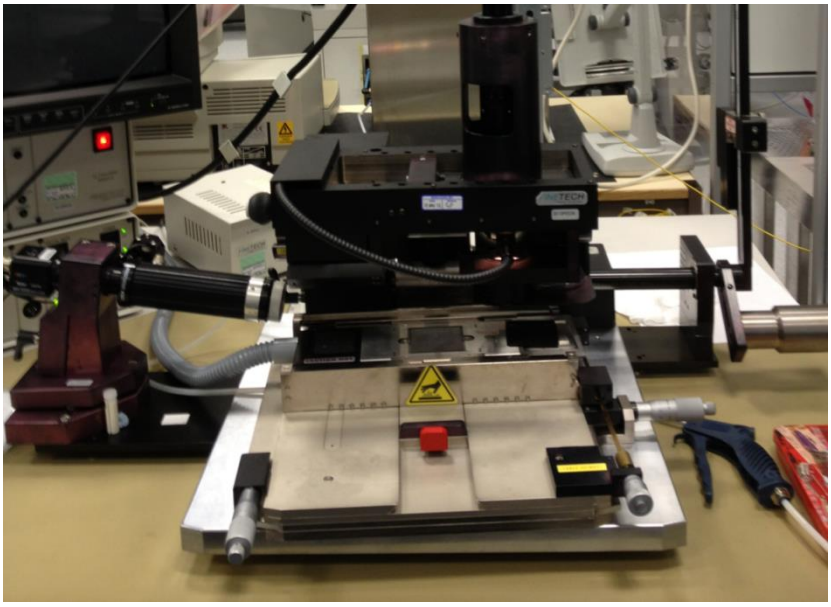

Figure 3-16 – Finetech FinePlacer flip chip bonder

The CMOS chip and the microLED device are bonded by means of flip chip. After the deposition of the gold ball, the chip is transferred to a Finetech FinePlacer flip chip bonder (Figure 3-16) [95]. The CMOS chip is held in a mechanical lock which uses a vacuum to keep the chip still. The microLED device, on the other hand, is placed on a heated vacuum plate. Then, the two devices are aligned and brought together carefully. The thermal energy (background heating) of the machine is 100°C, provided by a halogen lamp. During the flip-chip process, the thermal energy is heated to about 200°C for about 50seconds before ultrasonic energy of 1500mW for 800ms is applied. This softens the gold ball bonds which are situated between the two devices which creates the bond. After the flip-chip process, the chip is sent to an x-ray room to ensure that the gold bump bonds have fully attached. Due to the nature of sapphire, which is transparent, this step is sometimes replaced with optical inspection and is done under a microscope.

3.7. PCB Related

Three main boards are needed to drive and test the chip. These boards are the Institute for Integrated Micro and Nano Systems (IMNS) generic PCB motherboard, an Field-Programmable Gate Array (FPGA) board (Opal Kelly XEM3010) and a chip daughter card. All the tests in this thesis require all three boards. A Graphic User Interface (GUI) (as shown in Figure 3-17 by way of example) was developed using the Extensible Markup Language

(XML) programming language on Front Panel Software (version 3.1.0) provided by the Opal Kelly package. The software package handles the downloading of Verilog bit files to the FPGA board and acts as a communication link between the GUI and the FPGA that allows the user to write values into registers within the FPGA.

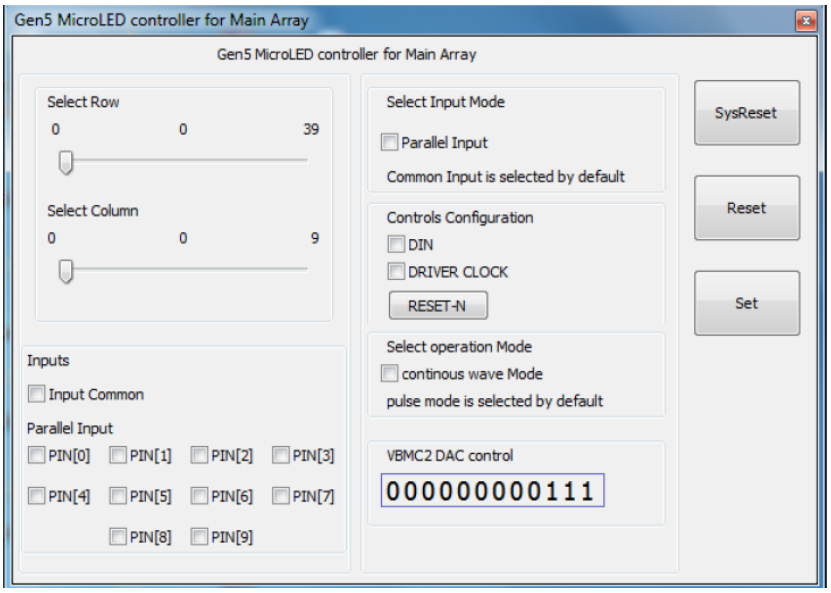

Figure 3-17 – Graphic User Interface (GUI) for microLED/CMOS drivers

3.7.1. IMNS Generic Motherboard

The IMNS Generic Motherboard was designed by Keith Muir and was used in other projects within the IMNS, the University of Edinburgh. The motherboard was incorporated with 12 analogue voltage sources, 4 current sources, 4 current sinks and regulated power supplies. The regulated power supplies, voltage and current sources can be powered using an external power supply or using the 5V USB supply. The board also includes a connector for the FPGA board.

3.7.2. FPGA Board

The FPGA chosen was a Xilinx Spartan-3 (XC3S1500-4FG320) in an Opal Kelly (XEM3010) Integration module [96]. Apart from the FPGA, the Opal Kelly has three on board phase locked-loops (PLLs), dedicated power supply regulators (1.2V and 3.3V) and a USB 2.0 Interface with access to 114 digital I/O channels from the FPGA. The availability of the USB 2.0 interface provides the PC-CMOS driver communication interface. The USB link can also be to supply power to the motherboard.

3.7.3. Daughter Card

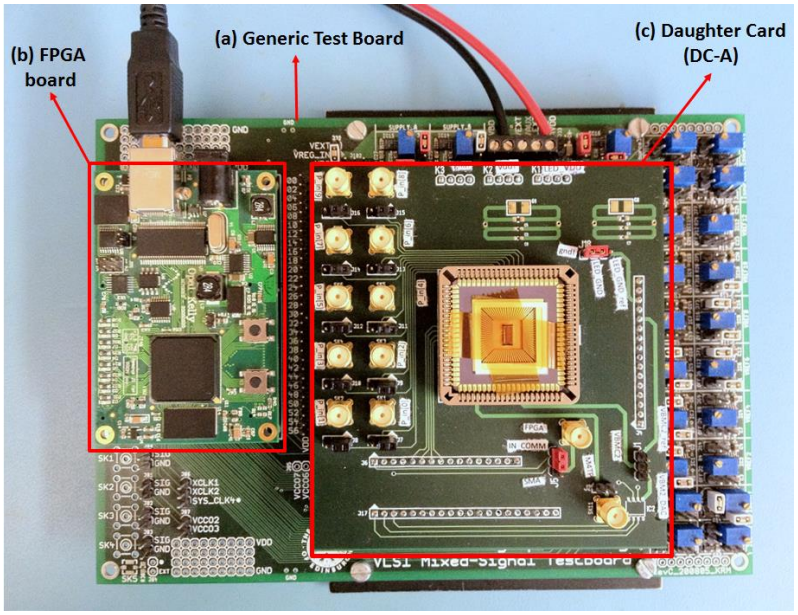

Figure 3-18 – microLED/CMOS driver Test Board

Two specific daughter cards were designed to test the digital driver (DC-A) and the analogue drivers (DC-B). These cards can be slotted into the IMNS Generic Motherboard and were used to re-map the signals of the generic board to ensure that the correct signals went to the correct locations of the device socket. Each card is equipped with an 84 pin Plastic Leaded Chip Carrier (PLCC-84) socket. Figure 3-18 shows an example of the full board setup to the microLED/CMOS drivers which includes the IMNS Generic motherboard, FPGA board and DC-A daughter card.

The DC-A contains 11 SMA inputs where 10 SMA inputs represent the 10 **Parallel_Inputs** to the chip and the other SMA input is for the **Common_Input**. The board also has a choice of connecting LED_GND to the board ground (GND) or to an external power supply. This allows negative biasing to the microLED.

The DC-B was designed to test the analogue drivers (Current Feedback drivers and Optical Feedback drivers). It has 3 SMA connectors which could be used as input for analogue signals and for measuring the output of the transimpedance amplifier (which is part of the optical feedback design). As with the DC-A, the DC-B also has the choice of connecting the LED_GND to either board ground or external power supply for negative biasing.

3.8. Measurements

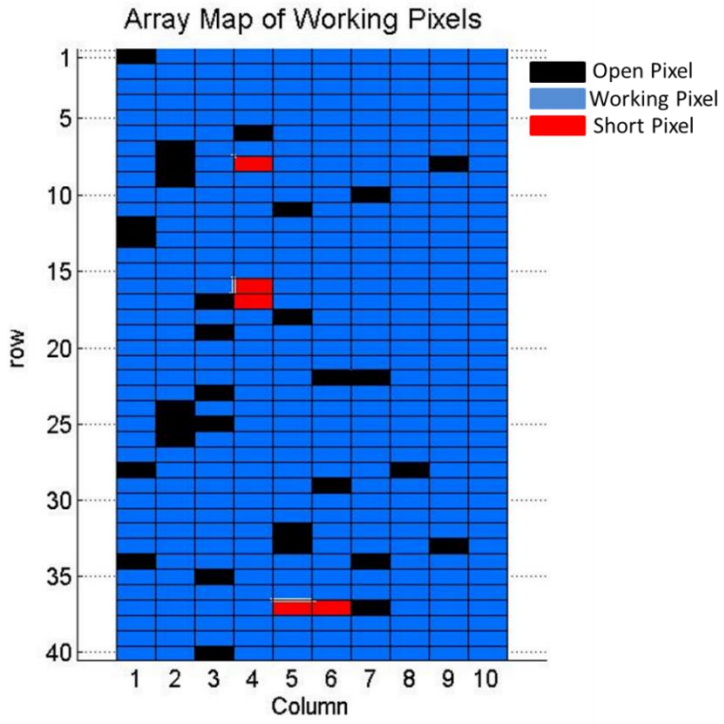

Figure 3-19 – MicroLED CMOS Driver pixels array map

Figure 3-19 shows the microLED/CMOS driver array map after bump-bonding, where each box represents one pixel. Out of the 400 pixels, 31 pixels are dead pixels which are highlighted in 'black' (open pixel) and 'red' (shorted pixel). There are two causes for dead pixels:

1) The pixel is an open circuit where there is no contact between the output of the CMOS driver (Metal4 opening) and the microLED. Therefore, no current can be drawn by these pixels. The failure is down to the yield in the bump-bonding process. During the deposition of the gold ball on the CMOS pads, there are a few pixels where the gold ball failed to stick to the bond pad due to the minimum pressure applied which was performed to avoid breaking the top metal layer. The gold ball deposition process on the defect pixel, however, was not repeated to avoid any damage to the CMOS chip
2) The pixel is a shorted LED. When the pixel is selected, it draws very high current and is not responding to any of the changes made to the LED_GND node. This is due to the variation and yield during the microLED fabrication.

3.8.1. DC Performance

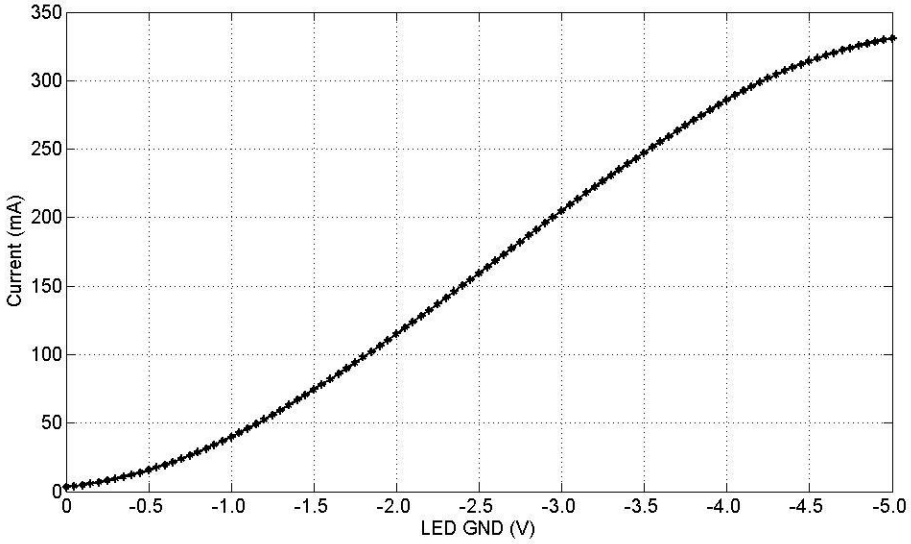

Figure 3-20 – Generation V microLED/CMOS Driver IV characteristic

Figure 3-20 shows the I-V characteristic of the Generation V microLED/CMOS driver. The measurement was conducted using a digital multimeter which was connected in series with the LED_GND node and the negative voltage output of the power supply. In this experiment, LED_VDD was supplied with 3.3V and LED_GND is swept from 0 to –5V. As the LED_GND bias voltage becomes more negative, the voltage across the microLED increases, hence increasing the current produce by the microLED/CMOS driver. The current begins to saturate as the LED_GND bias voltage approaches around –4.9V. Beyond this point, the current increment is small. The maximum measured current produced by the Generation V microLED/CMOS driver from a single pixel is when LED_GND is biased at –5V, producing about 330mA, about 60mA higher than predicted in the simulation and 140mA higher than Generation IV microLED/CMOS driver.

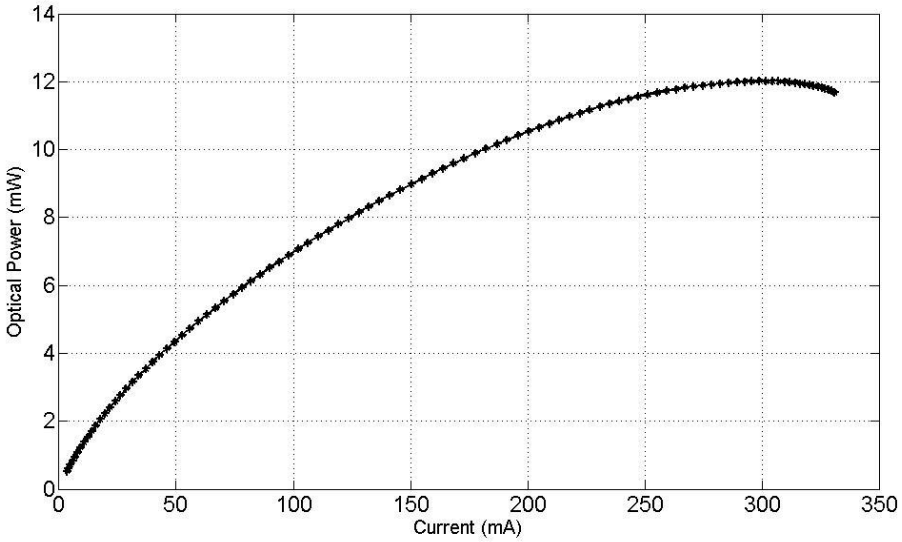

Figure 3-21 – Generation V microLED/CMOS Driver L-I characteristic

The L-I characteristic of the Generation V microLED/CMOS driver is shown in Figure 3-21, producing about 12mW of optical power. Notice that when the microLED current is above 250mA, the optical power response saturates and then starts to reduce. Apart from the parasitic resistance, as discussed before, another cause for the degradation is the saturation of the carriers in the quantum wells [26]. Any further increase of current will results in reduction of the optical power. Furthermore, the 'extra' carriers injected will lead to heating which can cause damage to the device [26].

3.8.2. Array Uniformity

The uniformity of current produced by each pixel across the array was investigated. This was performed by selecting one pixel at a time and current consumption of the selected pixel was recorded for all elements in the array. The experiment is then repeated with different LED_GND bias voltage. The recorded data is then saved in MATLAB and presented as surface plot. The results are presented in Figure 3-22, where dead pixels; both open and short circuit pixels are highlighted as 'black box'.

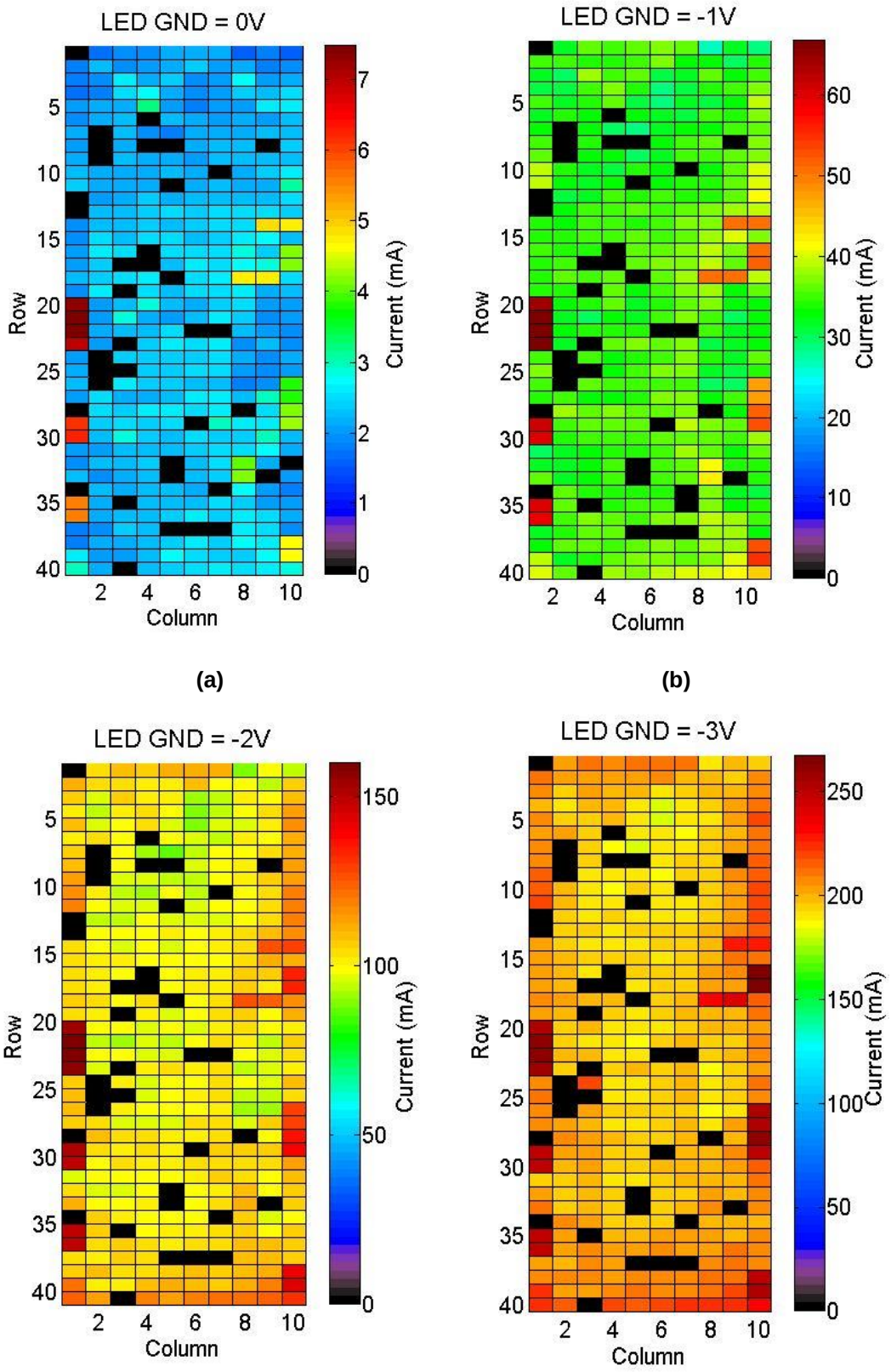

Figure 3-22 – Current per pixel across the pixel array as a function of LED_GND bias of (a) 0 V, (b) –1V, (c) –2V and (d) –3V

When LED_GND is biased at 0V, the mismatch of current produced in each pixel is dominated by the process variations of both the CMOS driver array and microLED array. As the LED_GND bias is made more negative, the pixels in the middle of the array sink lower current than the ones at the edge. The difference of the current produced between the pixel at the edge and the middle of the array becomes more apparent as the LED_GND bias continues to become more negative (Figure 3-22(d)). This effect occurs due to the voltage drop across the array caused by the power rail resistance, as explained in Section 3.5. The pixels in the middle of the array have longer rails from the power ring compared to a pixel that is closer to the edge of the array, thus causing a higher voltage drop. When LED_GND is biased close to 0V, the current is small and therefore the difference in voltage drop between pixels in the middle and the edge of the array is less significant. As the current increases, by making LED_GND more negative, the difference in voltage drop becomes more significant, thus resulting in the pixel in the middle of the array to sink lower current.

Figure 3-22 also highlights another problem occurred during the bonding process. For example, column1-Row 35 and 36 show that these 2 pixels are shorted together. This resulted in these two pixels turning on together when either of the pixel is selected, therefore drawing higher current than expected. The shorted pixels are due to the variation in the size and position of the gold ball during the gold ball deposition process. When the microLED array and CMOS driver came together and pressed during the flip chip process, the gold ball was squeezed and potentially touched the gold ball on the adjacent pixels.

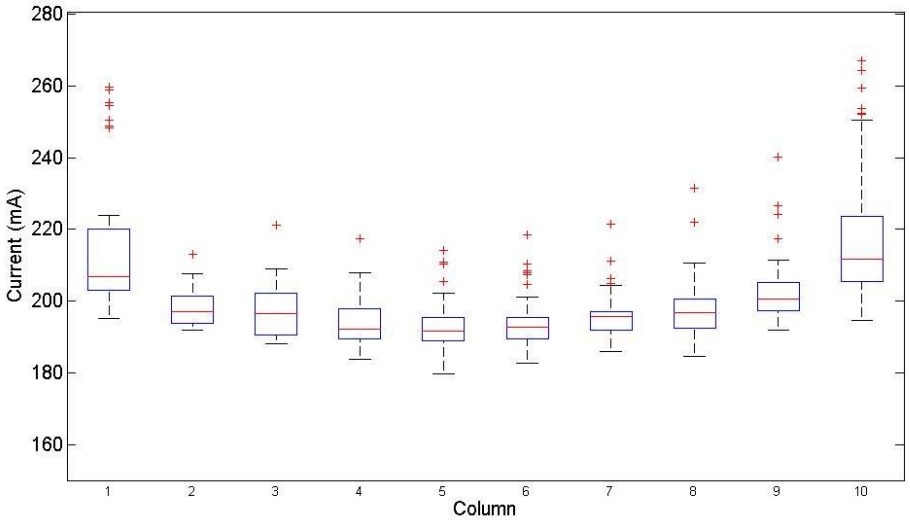

Figure 3-23 – Mean current produced by each column in the microLED/CMOS driver array

Figure 3-23 shows the box plot of the current variation across the array when LED_GND is biased at –3V, by taking the mean current produced by each column of the array. Dead pixels (black boxes in Figure 3-22) are excluded in this calculation. In the figure, Column 1 and Column 10 record the highest mean current of 217mA and 219mA respectively. The lowest mean current of 194mA is shown by both Column 5 and Column 6. This reaffirms the lower current sunk by the pixels in the middle of the array due to power supply voltage drop caused by the metal rail resistance. The high variation on Column 1 and Column 10 is due to some of the defect pixels which are found in these columns. This defect pixel was caused during the bonding process, as explained earlier, where the adjacent pixels are shorted together.

3.8.3. Voltage Droop

An investigation was made to see how voltage droop affected the performance of the microLED/CMOS driver array when two or more pixels are selected at the same time. Two experiments were conducted for this purpose. In the first experiment, two pixels were selected, named Pixel1 and Pixel2, at the edge of the array, minimizing the effect of resistance of the metal rail. Figure 3-24 shows the I-V characteristic of the individual pixel, the expected total current when both pixels were turned on at the same time and the measured value. The expected total current is the sum of the current produced by the two pixels. The measured value is about 74.7mA lower than expected, producing about 600mA when LED GND = –5V.

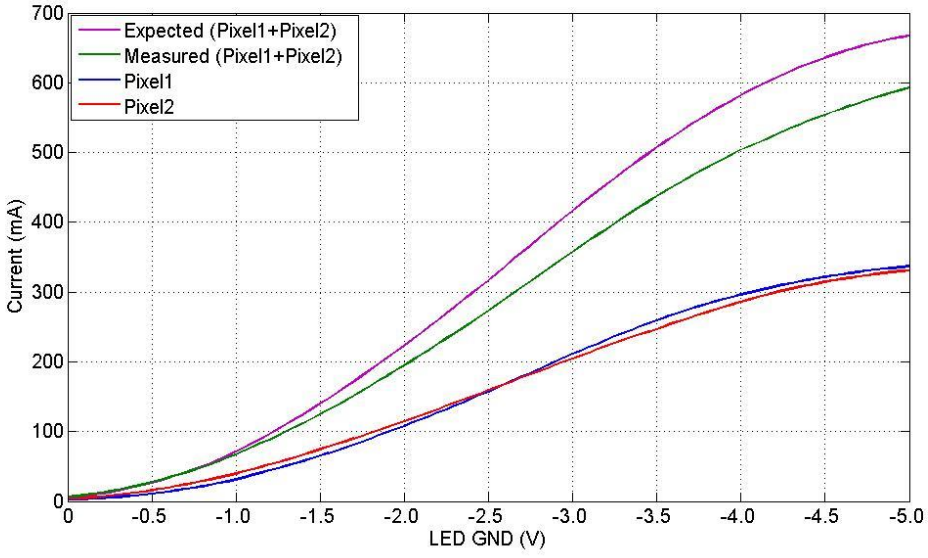

Figure 3-24 – Current reduction when 2 pixels at the edge of the array are selected at the same time

In the second experiment, another two pixels were selected. Pixel1, at the edge of the array and Pixel3, in the middle of the array were turned on at the same time. Figure 3-25 shows the I-V characteristic when these two pixels were turned on at the same time. The total measured current is 79.6mA less than the expected current. The amount of current drop is similar to the first experiment. This indicates that, while the resistance of the metal rails have some effect on the voltage drop, the major contribution of the current drop is from other parasitic resistances. Other parasitic resistances include, but are not exhaustive to, the power supplies resistance, connector wires and PCB's copper wire resistance. Because the CMOS driver array is operating at a very high current, the voltage droop across the system configuration plays a major contribution.

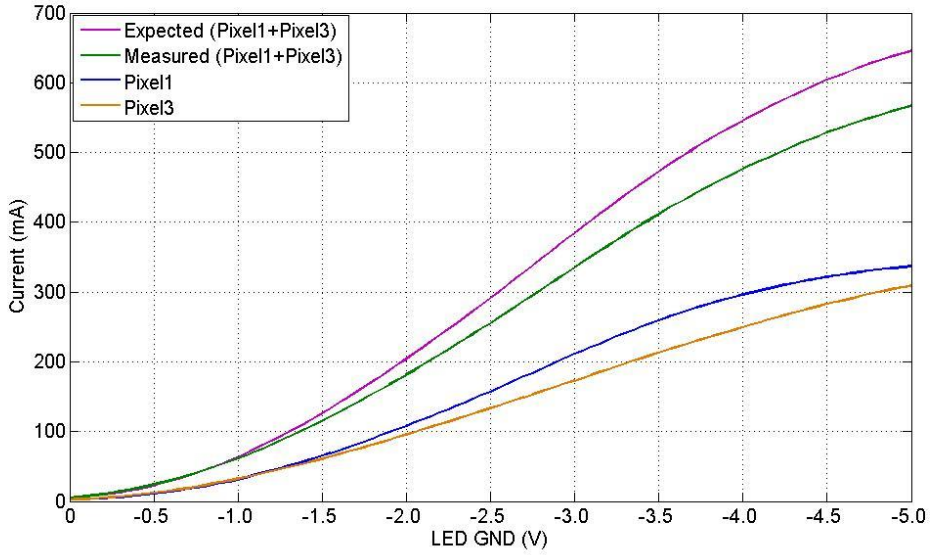

Figure 3-25 – Current reduction when a pixel at the edge and middle of the array are selected at the same time

Figure 3-26 shows the optical power when two pixels at the edge of the array were selected at the same time. The expected value in Figure 3-26 is the sum of the optical power of the individual pixel plotted against the total current consumed by the driver. The measured optical power follows closely with that of the expected optical power. However, the maximum optical power measured for two pixels was found to be 22.6mW before it started to degrade. The degradation of the measured optical power happens earlier than the expected value. The cause of earlier degradation is caused by the high current consumption by the microLED/CMOS driver array which causes the chip to heat up reasonably fast and degrading the performance of both the CMOS driver and the microLED.

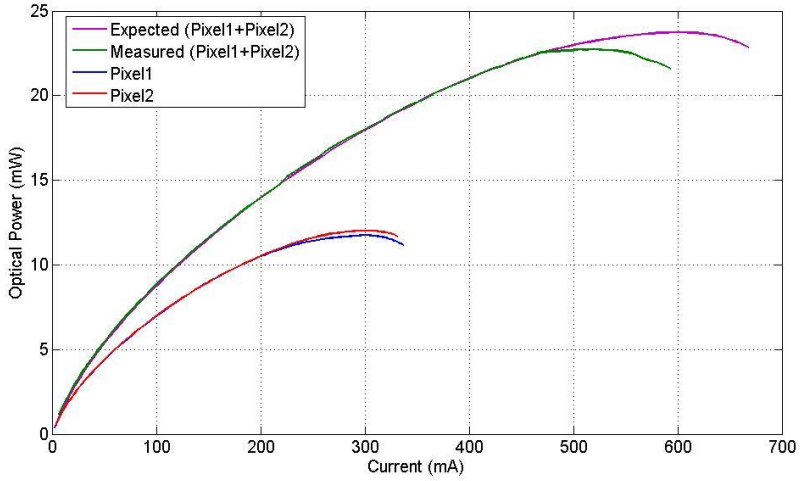

Figure 3-26 – Optical when 2 pixels at the edge of the array are selected at the same time

3.9. Results from IoP

Results presented in this section are the outcomes of the work done by researchers at the IoP as summarised in Table 3-1. In this section, the modulation characteristic of the Generation V microLED/CMOS driver and some of the early results for the pre-optical pumping polymer lasing are presented. The IoP has given permission for the results to be presented here. It is important to note that experiments were still being conducted during the writing of this thesis. Therefore the results published in this thesis is are the latest as of September 2013.

3.9.1. Modulation Characteristics

The bandwidth of the Generation V microLED/CMOS driver was investigated by ShuaiLong Zhang. The Generation V microLED/CMOS driver is a voltage "digital-logic" controlled type, therefore the microLED optical output can only switch between two optical power levels which change according to the state of the driver's input signal. Therefore, the Generation V microLED/CMOS driver performs an OOK modulation. The Frequency response of the Generation V was measured using a fast photodiode and a network analyser. The bandwidth was investigated by sending a modulation signal to the **Parallel_Input** (Figure 3-8). The frequency response of the driver with different applied bias (LED_VDD – LED_GND) is shown in Figure 3-27. The applied bias of the driver was varied by varying LED_GND from

0 to –3.3V. Figure 3-27 shows that the bandwidth of the driver increases as the applied bias increases.

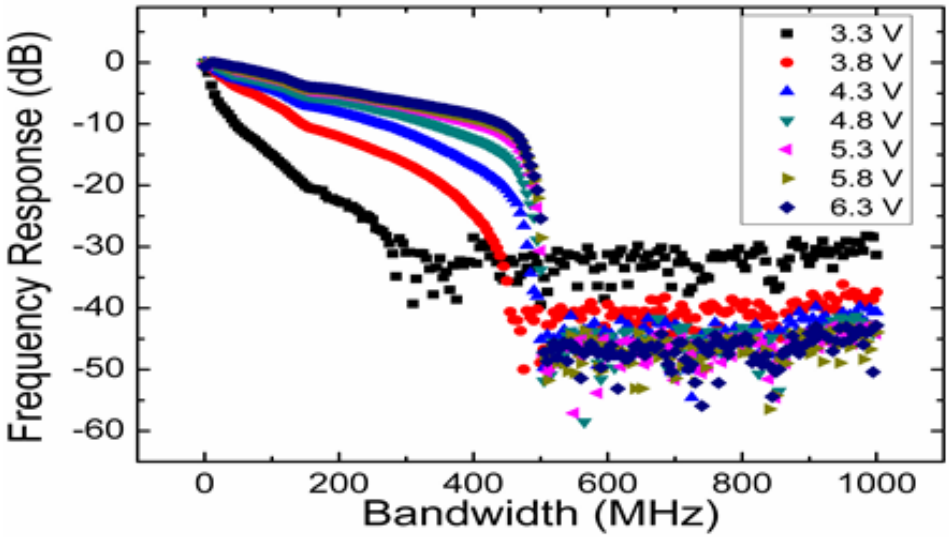

Figure 3-27 – Frequency response curves Generation V microLED/CMOS driver at various levels of applied bias (LED_VDD – LED_GND)

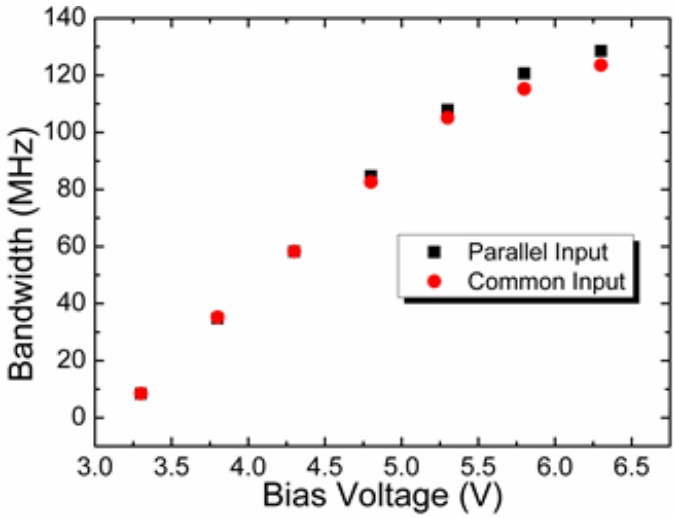

Figure 3-28 – Bandwidth of Generation V microLED/CMOS driver versus applied bias.

The bandwidth of the device was further investigated by sending the same modulation signal to both **Parallel_Input** and **Common_Input** (Figure 3-8)**.** The –3db modulation bandwidth data of **Parallel_Input** and **Common_Input** is shown in Figure 3-28, where it shows that the bandwidth of both inputs is similar**.** This fulfils the requirement of improving the performance of the Generation IV driver, where the **Parallel_Input** bandwidth was found to be much lower than the **Common_Input.** At an applied bias of 6.3V (LED_GND= –3V) the bandwidth of the

Generation V microLED/CMOS driver was found to be 123 MHz. In comparison with Generation IV, at applied bias of 6.5V (LED_GND= –3.2V), the bandwidth was found to be 147MHz, which is higher than Generation V. The shortfall of the bandwidth in Generation V is due to the parasitic components of the test PCB (DC-A) which was designed to accommodate both communication and optical pumping polymer lasing experiments. For Generation IV on the other hand, a specially designed board for communication was used to drive the device. Theoretically, the transmission data rate of the Generation V microLED/CMOS driver could be up to 246Mb/s (Equation 2-1).

3.9.2. Pulse Shape for Optical Pumping Polymer Lasing

To prepare for the optical pumping polymer lasing experiment, an initial test was conducted to find the optimum method to achieve the maximum peak intensity by varying the pulsing time and the optimum number of pixels used. The experiment was conducted by Dr. Johannes Herrnsdorf and Dr. Jonathan McKendry of the IoP using low-repetition-rate rectangular nanosecond pulses, generated using a Bit-Error-Rate Test (BERT) system, which was applied to the **Common_Input** (Figure 3-8) of the Generation V microLED/CMOS driver. Therefore, the optical power output from the microLED/CMOS driver will follow the signal applied to the **Common_Input** where a nanosecond pulse is emitted by the selected microLEDs. Pulse shapes from the microLED were recorded with a fast photodiode (PD). The microLED emission was focused on the PD by an imaging optics.

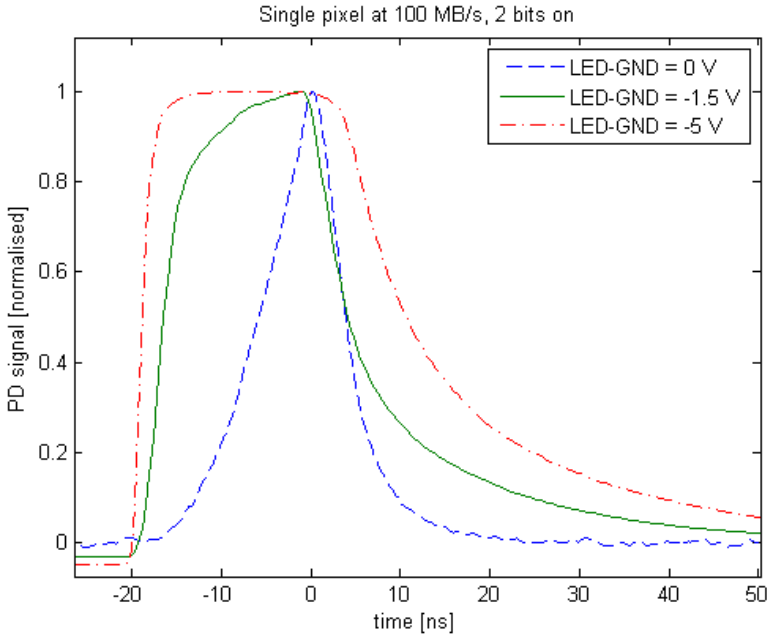

Figure 3-29 – Pulse shape of the Generation V microLED/CMOS driver

Figure 3-29 shows that the rise time is long when LED_GND is 0. The rise time reduces as the LED_GND is made more negative. This is consistent with the measurement of bandwidth of the microLED/CMOS driver shown in Figure 3-27. The fall time on the other hand, increases strongly as the LED_GND becomes more negative. This is due to the density of the carriers in the microLED. Pulse energies were recorded with a silicon energy meter and the collection efficiency was estimated using a Lambertian emission profile. In this experiment, a maximum peak intensity of 124W/cm2 from a row of six pixels was recorded, which is the highest peak intensity ever recorded under the HYPIX project [97]. With the obtained result, the high intensity of the microLED/CMOS driver is expected to be able to surpass the polymer current density threshold for lasing purposes [98, 99].

3.10. Summary

The Generation V microLED/CMOS driver was presented in this chapter. The driver, which represents a continuation of the work under the HYPIX project, was designed for two purposes:

a) To significantly increase the optical power output from a single pixel in comparison to its predecessor for optical pumping polymer lasing experiment and
b) To serve as a communication module for VLC purposes

This chapter briefly presents the HYPIX project background and the main motivation for the Generation V microLED/CMOS driver. The AlIn-GaN microLED, which is used on all the drivers presented in this thesis, is discussed in this chapter. The Generation V microLED/CMOS driver comprising of an array of 40x10, 100µmx100µm square pixels was designed in accordance to the specification to enable the optical pumping polymer lasing experiment. In order to achieve optimum performance, the pixel pitch is utilised by bump-bonding the microLED directly onto a thick metal layer which is placed directly above the driving circuitry. The removal of the bond-stack provides ‘additional’ space within the pixel which was used to layout larger transistors to increase the driving current. The maximum current drawn by the driver was measured to be approximately 330mA, which is about 140mA greater than that of the Generation IV microLED/CMOS driver. The microLED for the Generation V CMOS driver, on the other hand, was fabricated in the IoP and was expected to have at least two times higher efficiency than its predecessor. From the measurement, the optical power produced by the Generation V microLED/CMOS driver was recorded to be

around 12mW. This is more than three times greater than Generation IV. The uniformity of the array and the voltage droop effect caused by the high current consumed was also discussed in this chapter.

The Generation V microLED/CMOS driver was characterised at the University of Edinburgh. The measurement of the Generation V microLED/CMOS driver for VLC application and for polymer lasing experiments on the other hand, were conducted within the IoP. It is important to note that measurements continue to be conducted during and after the writing of this thesis. The modulation bandwidth of the driver was found to be 123MHz and a maximum peak intensity of 124W/cm^2 was measured. With the improved optical power performance, the Generation V microLED/CMOS driver is expected to be able to surpass the polymer threshold current density for lasing purposes.

Chapter 4 : MicroLED/CMOS Current Feedback Driver

4.1. Introduction

The drive to increase data transmission rates leads to the exploration of a more sophisticated modulation scheme. In Chapter 3, a digital microLED/CMOS driver, which uses OOK as a modulation scheme, was discussed. An OFDM scheme is proposed as an alternative which requires an analogue microLED/CMOS driver to implement the scheme. As mentioned in Chapter 2 (Table 2-4), two analogue CMOS drive ICs for microLED have been designed for the modulation scheme. In this chapter, the first of the two analogue drivers called the CMOS Current Feedback (CCFBK) driver is presented. This chapter reports on the feedback concept, the macromodel, transistor level design and simulation of the CCFBK driver. The measured results are compared with simulations and are discussed at the end of the chapter. The second analogue driver is presented in Chapter 5.

4.2. Analogue Modulated Driver for MicroLED

4.2.1. Overview

The advantages of OFDM over OOK have already been discussed in Chapter 2. Section 2.3.5 and 2.3.6 also discuss the challenges in implementing OFDM in the optical domain. High linearity is one of the key requirements for the OFDM signal in order to achieve a low BER. The detrimental effect of non-linearity was also discussed in Section 2.3.6.

One of the objectives of this project is to design a microLED/CMOS driver system that facilitates the implementation of OFDM. This is achieved by designing a microLED/CMOS drive IC that performs analogue modulation, meaning that the optical power output of the driver is a replica of the input signal. One of the proposed solutions is the CCFBK driver. The aim of the CCFBK driver is to supply the microLED with current that is linearly proportional to the driver's input voltage. The name "current feedback" refers to the operation of the driver where a small portion of the current driving the microLED is fed back to the input for linearization purposes. The BER is targeted to be lower than 10^{-3}, in accordance with the Forward Error Correction (FEC) limit. FEC is a technique used for controlling errors in data

transmission over noisy communication channels. A BER < 10^{-3} means there is at most only 1 error per 1000 bits at the receiver. Under this requirement, the data is recoverable and the channel is said to exhibit "error-free" transmission.

4.2.2. Target Specification

The CCFBK driver (together with Optical Feedback Driver) is the first analogue modulated driver taped-out within the HYPIX project. The microLED/CCFBK driver target specification is described below and summarised in Table 4-1:

Parameter	Value
Signal type	Analogue
Pixel Pitch	100µm x 100µm
Drive Current	100mA
Optical Power	4.5mW
Bandwidth	100MHz
BER	< 10^{-3}
MicroLED current Dynamic Range	0 – 100mA

Table 4-1 – Summary of CCFBK driver Target Specification

1. **Analogue Modulation –** The driver should perform analogue modulation to facilitate OFDM. The current driving the microLED is expected to be linearly proportional to the input voltage.
2. **Pixel pitch –** The pixel area was specified to be 100µm x 100µm, the same as the digital driver.
3. **Driving Current and Optical Power –** The driving current is limited by the pixel pitch and the design of the driver. Furthermore, this is the first time an 'analogue' driver has been taped-out, therefore the current produced is expected to be significantly lower than the digital driver for study purposes. Taking these into account, a moderate driving current up to 100mA was specified. The microLED/CCFBK driver optical output power is expected to be about 4.5mW (Figure 3-7) for the given driving current.
4. **Flexibility –** The driver should have a selectable quiescent DC operating point and dynamic range. This is essential in order to reduce the effect of non-linearity exhibited by current to optical power transfer function of the microLED
5. **Bandwidth –** The bandwidth of the CCFBK driver depends on the microLED injection current and its capacitive load. For the given current drive, the bandwidth

of the microLED die was specified to be approximately 100MHz. The bandwidth of the driver is expected to be higher to avoid being the limitation in the system.

6. **BER** – BER is specified to be $\leq 10^{-3}$. This is in accordance with the FEC limit for the standard correction mechanism.

4.3. Negative Feedback Technique

4.3.1. Theory and Operation

In general, feedback can be described as the process of sending some part of the signal at the output back to the input to oppose the former (in the case of negative feedback). Negative feedback is a method which finds wide applications in analogue circuit design. This method is popular due to its advantages, such as gain desensitization, terminal impedance modification, bandwidth modification and non-linearity improvement [100]. The last property is of most interest in this project. As mentioned in Section 2.4.1, the method can also cause the system to become unstable due to the existence of multiple poles in the loop. A typical feedback system usually contains four main elements:

1. A feedforward network
2. A way to detect the output
3. A feedback network
4. A means of generating the feedback error

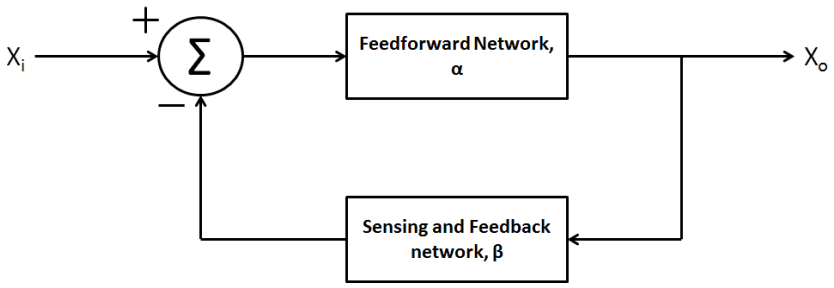

Figure 4-1 – Block diagram of a typical feedback system

Figure 4-1 shows a simple block diagram of a feedback system, where α is the open loop gain of the feedforward network and β is the feedback factor. The input to the feedforward network is called the feedback error which is given as $X_i - \beta X_0$, where the output of βX_0 is the output of the feedback network. Therefore the closed loop transfer function of a feedback system can be written down as

$$X_o = \alpha(X_i - \beta X_o) \quad \text{Equation 4-1}$$

$$\frac{X_o}{X_i} = \frac{\alpha}{1 + \alpha\beta} \approx \frac{1}{\beta} \quad \text{Equation 4-2}$$

Figure 4-1 with Equation 4-1 and Equation 4-2 show that a fraction of the output signal is sampled and compared with the input, thus generating an error term. The error term is minimised by making the loop gain αβ as large as possible. Assuming that $\alpha\beta \gg 1$, the closed loop gain can be approximated to $\frac{1}{\beta}$. Thus, the output of the system is linearly proportional to the input.

4.3.2. Feedback Topology

There are four common feedback topologies depending on the nature of the input and output (voltage or current) as summarised in Table 4-2. The first entry of each feedback topology denotes the quantity sensed at the output and the second quantity refers to the type of signal returned to the input. A simple sense mechanism for an output voltage is to place a voltage detector at the corresponding port (Shunt). To sense a current, a current detector is placed in series with the port.

Feedback topology	Output signal	Input signal	Sense Mechanism
Voltage Voltage Feedback	Voltage	Voltage	Shunt
Current Voltage Feedback	Current	Voltage	Series
Voltage Current Feedback	Voltage	Current	Shunt
Current Current Feedback	Current	Current	Series

Table 4-2 – Feedback topology

Current Voltage Feedback is chosen as the topology for the CCFBK driver. The reason for choosing this topology is:

1. The availability of a wide bandwidth voltage signal generator. Therefore the signal can be transferred directly from the signal generator to the CMOS driver without any conversion which may require extra circuitry that could affect the linearity of the input signal.
2. A voltage driven microLED exhibits two stages of transformation (voltage to current and current to light) as opposed to one in a current driven mode. Furthermore, as mentioned in Section 3.4.2, the microLED I-V characteristic is an exponential

function. Coupled with the non-linearity of the L-I characteristic; the linearization is more complicated than for a current driven microLED. Therefore, a current driven microLED driver was chosen.

4.4. Proposed CMOS Current Feedback Driver

4.4.1. Design Overview

Figure 4-2 illustrates the proposed microLED/CCFBK driver, which is based on a Current Voltage Feedback topology. The input voltage signal (V_{INPUT}) is applied at the inverting input of the operational amplifier (OP1). The output of OP1 sets the gate voltage of p-channel MOSFET M1, where it is designed to operate in the saturation region. The current sense and feedback network is performed by connecting a resistor (R_S) in series with M1. Using Ohm's Law, the current produced by M1 causes a voltage drop across R_S, thus linearly converts the current to voltage at the non-inverting input (V_F) of OP1. The high gain of OP1 regulates the gate voltage of M1, so that the current produced by M1 tends to drive the error voltage between V_{INPUT} and V_F to zero. Therefore, the current produced by M1 is linearly proportional to V_{INPUT}.

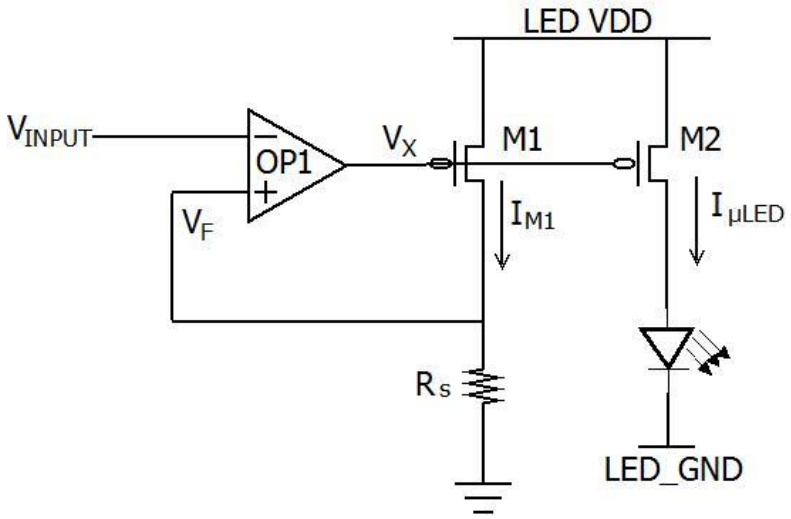

Figure 4-2 – Proposed microLED/CMOS Current Feedback (CCFBK) driver

The "feedback" current on M1 is mirrored in the p-channel MOSFET M2. The drain of M2 is connected to the anode of the microLED. Therefore, the current supplied to the microLED is also linearly proportional to V_{INPUT}. M2 is designed so that it is able to source up to 100mA. The microLED cathode is connected to a separate DC supply (LED_GND) to bias the

microLED above its threshold voltage. This is the same technique as described in Section 3.4.3. Looking at Figure 4-2 again, since that only M2 is supplying current to the microLED, the current in M1 can be much lower than the current in M2. Therefore, the channel width of M1 can be significantly smaller than M2.

Although the current supplied to the microLED is linearized, there still exists some residual non-linearity in the optical power output due to the microLED L-I characteristic (Figure 3-7). That non-linearity can be minimised by carefully choosing the CCFBK driver's optimum DC operating point and limiting the range of the amplitude of the signal. This is discussed in Section 4.7.2.

4.4.2. Macromodel

The DC operation can be examined by excluding M2 in Figure 4-2. Assuming that OP1 has a finite gain of A_{OP1}, then the transfer function can be written as

$$V_X = A_{OP1}(V_F - V_{INPUT}) \qquad \textbf{Equation 4-3}$$

where V_X is the output voltage of OP1. V_F is the output voltage from the feedback network, which converts the current through M1 (I_{M1}) to a voltage by sensing it using R_S. Therefore V_F can be written as shown in Equation 4-4 while I_{M1} can be approximated by Equation 4-5.

$$V_F = I_{M1} \times R_S \qquad \textbf{Equation 4-4}$$

$$I_{M1} = -V_X \cdot g_{m\_M1} \qquad \textbf{Equation 4-5}$$

where g_{m_M1} is the transconductance of M1. Combining Equation 4-3, Equation 4-4 and Equation 4-5, the transfer function of the feedback system is

$$\frac{I_{M1}}{V_{INPUT}} = \frac{A_{OP1}.g_{m\_M1}}{1 + (A.g_{m\_M1})R_S} \approx \frac{1}{R_S} \qquad \textbf{Equation 4-6}$$

Comparing Equation 4-6 with Equation 4-2, the loop gain ($\alpha\beta$) of the driver is found to be $(A_{OP1}.g_{m\_M1})R_S$ and the feedback gain, β, is R_S. Therefore, the closed loop gain can be approximated to be equal to $\frac{1}{R_S}$.

A first order Current Voltage Feedback macromodel, which includes OP1 and M1, was developed. The model was implemented in Cadence and simulated with the Spectre simulator using ideal resistors, voltage and current sources. The purpose of the model as a whole is to help understand the feedback system and the relationship between the open-loop gain of the amplifier (A_{OP1}) and its bandwidth, the transconductance of M1 (g_{m_M1}) and the feedback resistor (R_S) as shown in Equation 4-6.

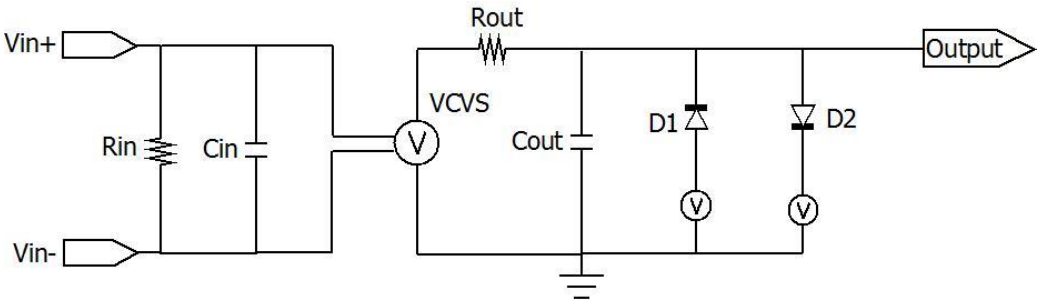

Figure 4-3 – Feedforward amplifier macromodel

Figure 4-3 shows the first order Macromodel of OP1. R_{IN} and C_{IN} represent the high input resistive and capacitive components of the amplifier. The Voltage Controlled Voltage Source (VCVS) represents the open loop gain (A_{OP1}), amplifying the voltage difference between the inputs (V_{IN+} and V_{IN-}). A high A_{OP1} is necessary to suppress non-linearity in a closed loop system. A_{OP1} for this macromodel was chosen to be 1000. The combination of R_{OUT} and C_{OUT} creates a low pass filter at the output representing the output impedance of the amplifier and therefore sets the cut-off frequency. The combination of the gain of the VCVS and the output impedance determines the gain-bandwidth of the amplifier. The output voltage range from 0 to 3.3V was implemented and is set by diode D1 and D2. The output voltage range is determined by the process node which only uses 3.3V transistors.

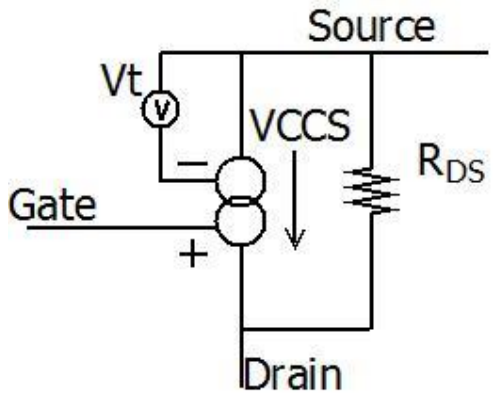

Figure 4-4 – First order p-channel MOSFET macromodel

Figure 4-4 shows the first-order macromodel of M1 which is modelled as a Voltage Controlled Current Source (VCCS). Voltage source Vt, sets the threshold voltage of M1 to –0.7V [89]. The current produced by the VCCS is set by a parameter named g_M which is proportional to the voltage of the gate node beyond Vt. R_{DS} is the output resistance of the transistor. The model of Figure 4-3 and Figure 4-4 are connected as in Figure 4-2 and simulated with cadence. It is important to note that the p-channel MOSFET model is a linear representation and 2nd order effect such as short channel and body effect is not included.

4.4.3. Macromodel Analysis

4.4.3.1. DC Simulation

As mentioned in Section 4.4.1, M2 is the current source for the microLED. The maximum current required to drive the microLED was specified to be 100mA. M1 on the other hand, is a mirror transistor to M2 with a ratio and does not supply any current to the microLED. Therefore, the width of M1 can be much smaller than M2. The width ratio of M2 to M1 $\left(\frac{W_{M2}}{W_{M1}}\right)$ is a trade-off between performance and the available area within the pixel. A small $\frac{W_{M2}}{W_{M1}}$ (i.e. M1 is large) improve the bandwidth of the driver due to higher driving capability. However, due to the large area occupied by both M1 and M2, it is limited by the pixel area specified. Increasing $\frac{W_{M2}}{W_{M1}}$ reduces the area occupied, but at a cost of reducing bandwidth. By taking the specification of bandwidth and pixel area into account, $\frac{W_{M2}}{W_{M1}}$ was chosen to be 30. With $\frac{W_{M2}}{W_{M1}}$ chosen, the value of Rs can be estimated using Equation 4-7

$$V_{RS} = I_{M1} \times R_S = \frac{I_{M2}}{30} \times R_S \qquad \textbf{Equation 4-7}$$

where I_{M1} is $\frac{1}{30}$ of the current produced in M2 (I_{M2}). V_{RS} is the voltage drop across R_S and is equal to V_F in Figure 4-2. Because M1 and M2 are mirror transistors, both must operate in the saturation region. A voltage drop of 0.8V across the source-drain of M1 (V_{DS_M1}) was assumed to keep M1 in saturation. Therefore, V_F and R_S can be estimated using Equation 4-8 and Equation 4-9 respectively.

$$V_F = V_{RS} = 3.3 - V_{DS\_M1} \quad \textbf{Equation 4-8}$$

$$R_S = V_F \div \left(\frac{I_{M2}}{30}\right) \approx 760\ \Omega \quad \textbf{Equation 4-9}$$

Using Equation 4-10, g_{m_M1} is estimated and was calculated to be 3.6mS. In this macromodel however, because M1 is modelled using a linear VCCS, g_{M_VCCS} is half of g_{m_M1}, as shown in Equation 4-11. g_{m_VCCS} of 1.8mS was used in the macromodel simulation.

$$g_{m\_M1} = \frac{2I_{M1}}{V_{GS\_M1} - V_t} \quad \textbf{Equation 4-10}$$

$$g_{m\_VCCS} = \frac{I_{M1}}{V_{GS\_M1} - V_t} = \frac{g_{m\_M1}}{2} \quad \textbf{Equation 4-11}$$

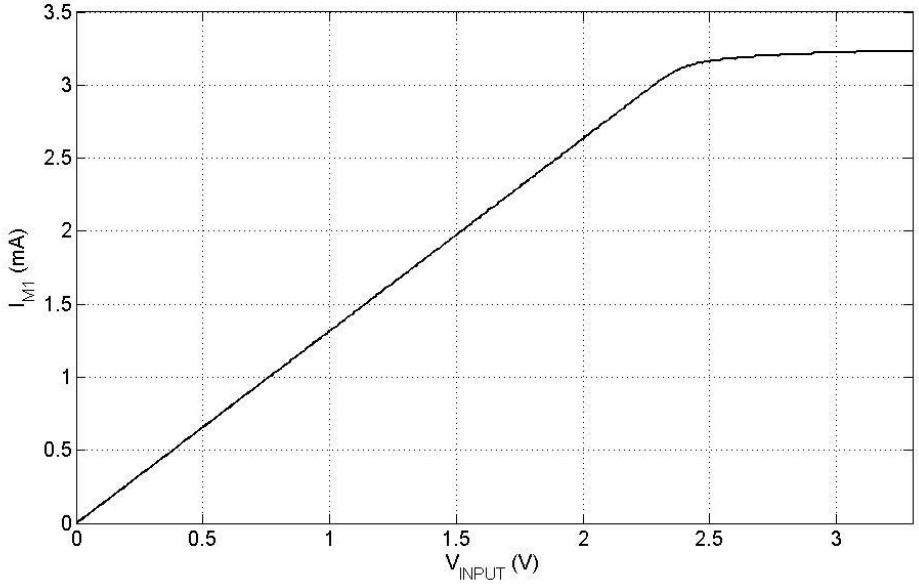

Figure 4-5 – I_{M1} response by sweeping V_{INPUT}

A DC simulation was performed based on the chosen parameters. Figure 4-5 shows the M1 current response when V_{IN} is swept from 0 to 3.3V. I_{M1} is linearly proportional to V_{INPUT}, producing up to about 3.2mA when V_{IN} is 2.4V before moving into saturation. The maximum current is determined by g_{m_VCCS}, as shown in Equation 4-11. The range of the saturation region is determined by the voltage drop across V_{DS_M1}. A Wider range can be achieved by reducing V_{DS_M1} at a cost of placing M1 in the linear region.

Figure 4-6 shows V_F (Figure 4-2) response with sweeping V_{INPUT}. As discussed earlier, the closed loop system forces the output of the feedback network to be as close as possible to the

input. This is determined by the gain of the system ($\alpha = A_{OP1}.g_{m\_VCCS}$) where higher α tends the error between V_{INPUT} and V_F closer to zero than a lower α.

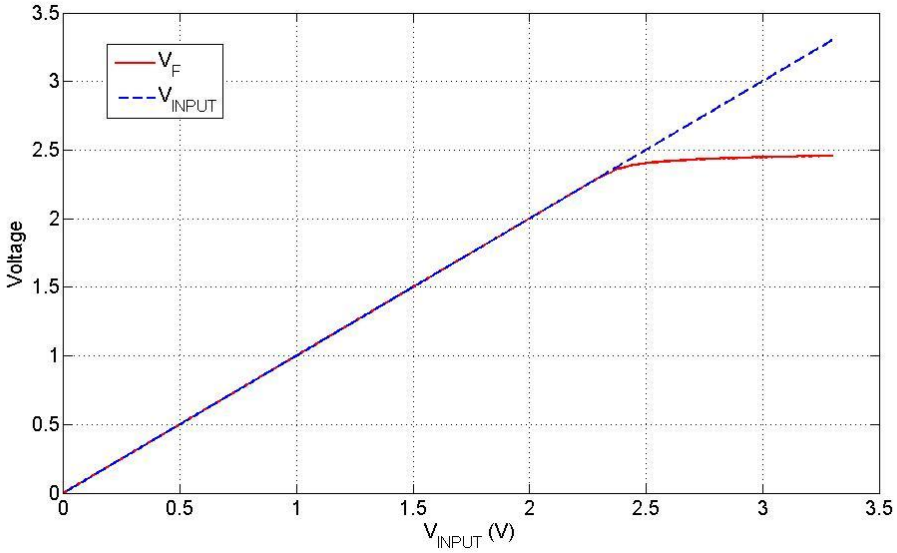

Figure 4-6 – Feedback network voltage (V_F) response with V_{INPUT}

4.4.3.2. AC Simulation

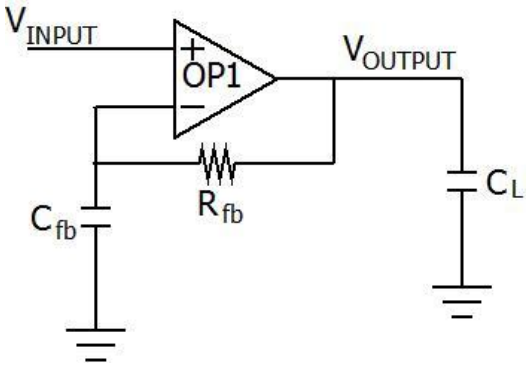

Figure 4-7 – AC simulation configuration for macromodel amplifier

Figure 4-7 shows the AC simulation configuration for the OP1 macromodel. R_{fb} and C_{fb} are a high value resistor and capacitor with values of 100MΩ and 100μF respectively. Under this condition, the DC value of V_{OUTPUT} is equal to V_{INPUT} until the frequency is approximately $\frac{A_{OP1}}{R_{fb}C_{fb}}$. Above this frequency, the ratio of $\frac{V_{OUTPUT}}{V_{INPUT}}$ is the open loop gain of OP1. C_L is the load capacitance to the amplifier which represents the gate capacitance of M1 and M2 (M2 dominates the load capacitance due to the chosen $\frac{W_{M2}}{W_{M1}}$). C_L was estimated to be 5pF in this case representing the gate capacitance of M1 and M2.

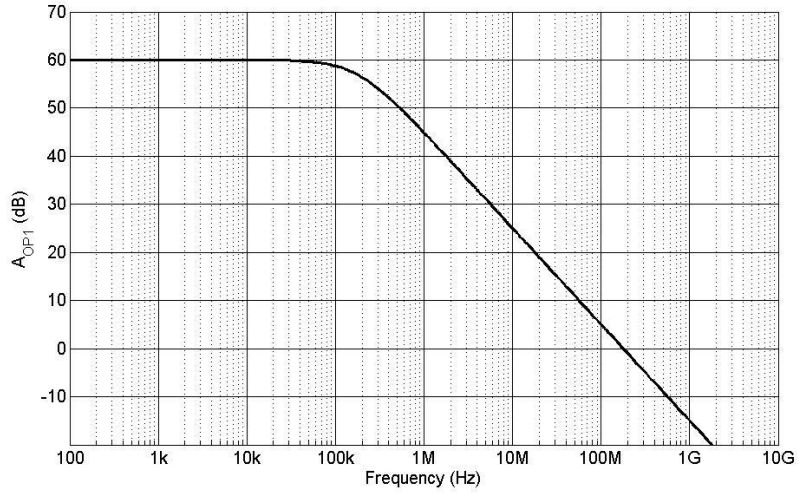

Figure 4-8 – Frequency response of the OP1 macromodel

The parameters of the OP1 macromodel were set such that A_{OP1} is 1000 and the value of the output impedance gives a gain bandwidth greater than 100 MHz. This is to allow the driver to operate up to 100MHz as specified. The frequency response of the amplifier is shown in Figure 4-8. The figure shows that the amplifier has a gain of 1000 ($20 \times \log(1000) = 60\ dB$) and a gain bandwidth product of 190MHz.

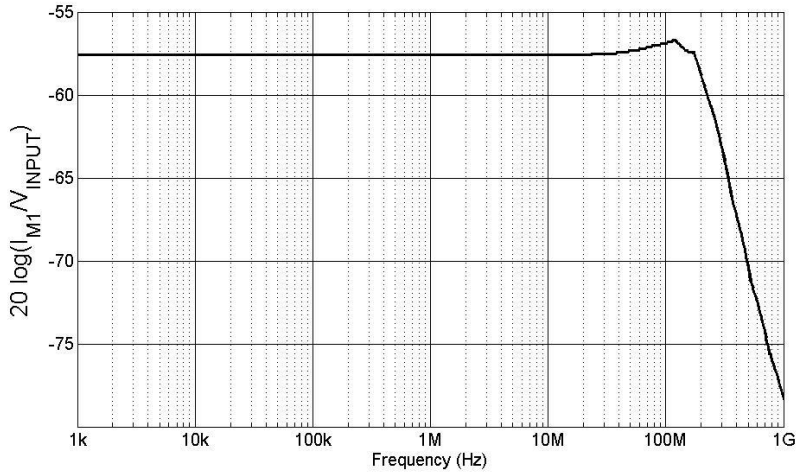

Figure 4-9 – Frequency response of the CCFBK driver

AC simulation of the CCFBK driver macromodel was conducted with the configuration shown in Figure 4-2. A load capacitance of 5pF was connected to the output of OP1. The gain of the feedback system is $\frac{1}{\beta} = \frac{1}{R_S} \approx -57\ dB$, as shown in Equation 4-6 and the bandwidth was found to be 243 MHz. The frequency response shows a flat band from very low frequency up to about 30 MHz where the response gradually increases until about 150MHz before

decreasing with a 20dB per decade roll-off. The cause of this peaking can be understood by looking at the loop gain phase response. This can be done by breaking the feedback loop as shown in Figure 4-10. AC current is injected in the feedback path and the response is observed by plotting I_{M1}.

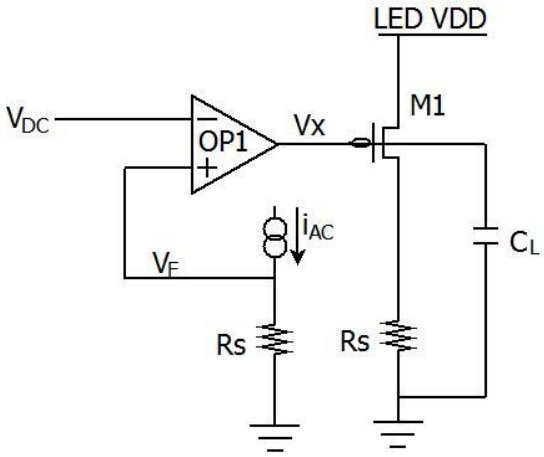

Figure 4-10 – Loop gain inspection

Figure 4-11 shows the loop gain and phase response of the feedback system. The loop gain of the system is $A_{OP1}g_{m\_M1}.R_S$ is given in Equation 4-6. Using the values of A_{OP1}, g_{m_VCCS} and R_S as 1000, 1.8mS and 760Ω respectively as discussed earlier, the loop gain was found to be 1368 or 62.7 dB, as shown in Figure 4-11. The important parameter shown in Figure 4-11 is the phase margin. To ensure stability, the loop gain must drop to unity before the phase response crosses –180°. In the figure, when $|A_{OP1}g_{m\_M1}.R_S| = 1$, the phase response is –130°. Therefore the phase margin was found to be around 50°, indicating that the closed loop system exhibits underdamped behaviour. This is the cause of the small peaking in the closed loop response, as shown in Figure 4-9. A phase margin of 60° is considered optimum to ensure the system exhibits little ringing and fast settling. Thus, the peaking effect can be minimised by adjusting the phase margin closer to 60°. This can be done by reducing 1) the gain-bandwidth product of OP1, either by reducing the gain or the bandwidth 2) the feedback gain R_S, and 3) the transconductance of M1 (g_{m_M1}).

It is important to note that, if R_S or $g_{m_M1}$is changed,the DC response of the system would also be affected, as discussed in Section 4.4.3.1. Therefore, reducing the gain or the bandwidth of OP1 is a better option.

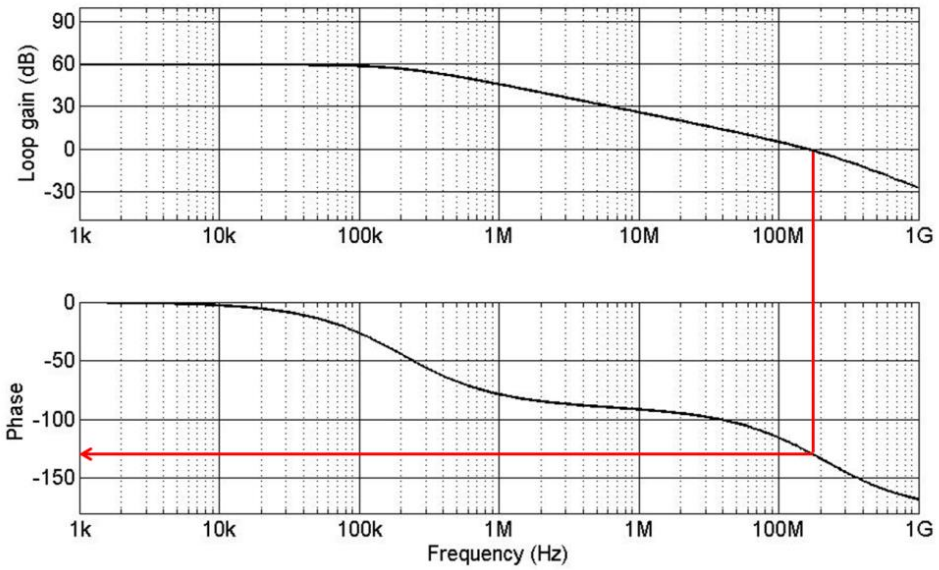

Figure 4-11 – The feedback system loop gain frequency response

Figure 4-12 shows the effect on the loop gain and phase response of the feedback system when the bandwidth of OP1 is reduced. By keeping the gain of the amplifier the same, the unity-gain bandwidth shifted to the left. This in turn improves the phase margin of the system. The gain-bandwidth was reduced from 190 MHz (indicated by the blue line. The same parameter used as simulated in Figure 4-8) to 160MHz (red line) and 130MHz (brown line). A phase margin of 50°, 56° and 62° was observed for the blue, red and brown lines respectively.

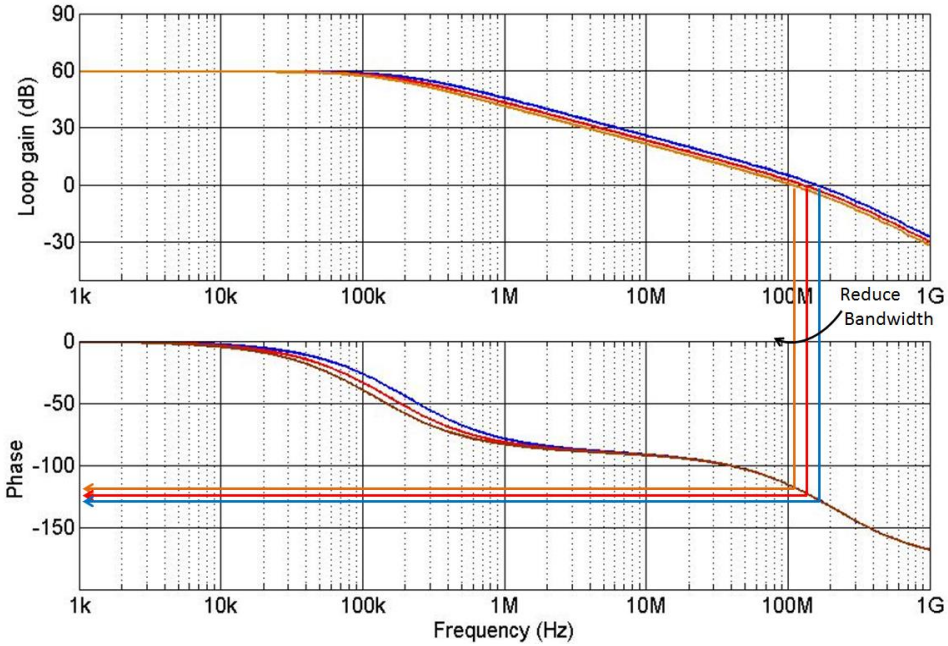

Figure 4-12 – Effect of reducing gain-bandwidth product of OP1

Using the gain-bandwidth of the amplifier as 130MHz, the feedback system was re-simulated. The result is shown in Figure 4-13 which shows the peak of the CCFBK driver frequency response has been significantly reduced. Based on the simulation, estimated values for the feedback system parameters were determined. These parameters are summarised in Table 4-3.

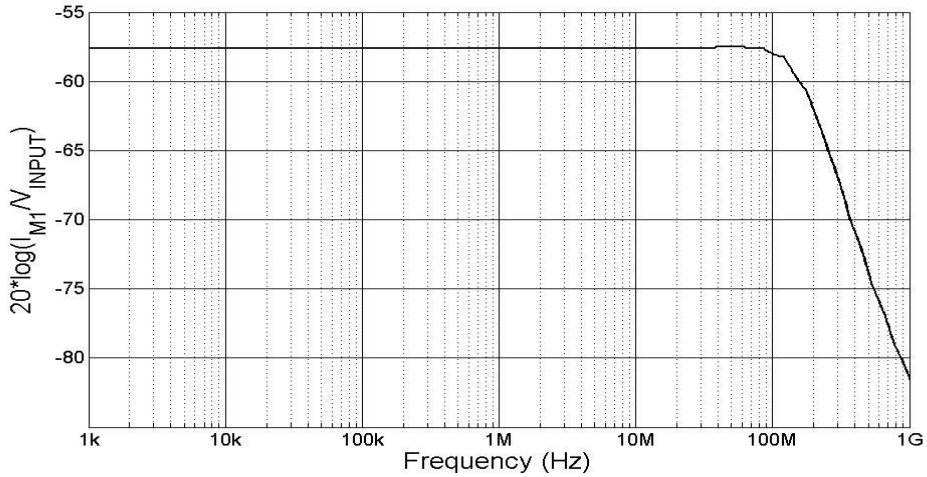

Figure 4-13 – Frequency response of the CCFBK driver showing no peaking

Parameters	Value
M1 current sink, I_{M1}	Up to 3.3 mA
Sense Resistor, R_S	760Ω
Transistor M1 transconductance, g_{m_M1}	3.6mS
Operational Amplifier gain, A_{OP1}	1000
Operational Amplifier gain-bandwidth product	130 MHz

Table 4-3 – Summary of the parameters for the design of the MicroLED/CCFBK driver

4.5. Transistor Level Design

The ideal model, as discussed in Section 4.4 is now replaced with MOSFET and resistor models provided in the AMS 0.35µm BiCMOS process High Performance Interface Kit (HIT-KIT). In this section, the design of the operational amplifier, M1, M2 and R_S is discussed.

4.5.1. Operational Amplifier (OP1)

A high gain amplifier is desired in a feedback application. Generally, there are three ways to increase the gain of an amplifier:

1. Multiple stage amplifier
2. Increase transconductance
3. Increase output impedance

Using a multi-stage amplifier is not favoured because of stability issues where the additional stages introduce extra poles, thus more attention is needed to ensure its stability. Increasing the output resistance is more attractive than increasing the transconductance because the output resistance increases in proportion with the decrease in bias current, whereas transconductance increases as the square root of the increase in bias current. The output impedance can be increased by cascoding [101]. A single stage telescopic amplifier was chosen for the driver, as shown in Figure 4-14.

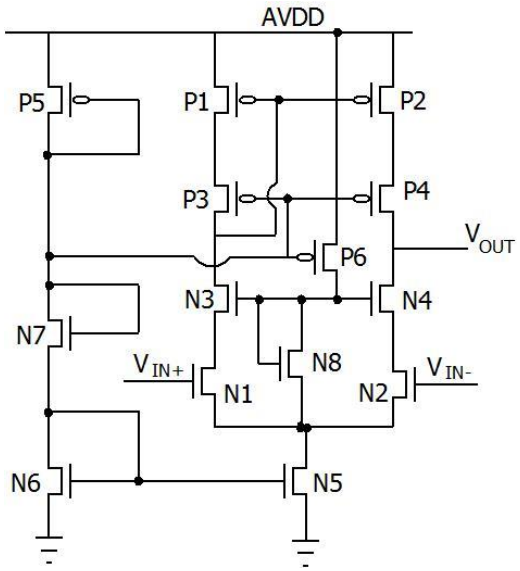

Figure 4-14 – Operational Amplifier (OP1) schematic diagram

where AVDD is the 3.3V supply and V_{IN+} and V_{IN-} are the non-inverting and inverting input of the amplifier respectively. Transistor N1 and N2 form a differential pair while P1 and P2 are its load. N3, N4, P3 and P4 are the cascode transistors while N5 is the current sink. N6, N7, N8, P5 and P6 comprise the biasing circuit. The gain of OP1 (A_{OP1}) can be estimated as

$$|A_{OP1}| = g_{mN1}[(g_{mN3}R_{ON1}R_{ON3})||(g_{mP4}R_{OP2}R_{OP4})] \qquad \textbf{Equation 4-12}$$

g_{mN1}, g_{mN3}, g_{mP4} are the transconductance of N1, N3 and P4 respectively and R_{ON1}, R_{ON3}, R_{OP2}, R_{OP4} are the output resistance of N1, N3, P2 and P4 respectively.

The DC performance of OP1 was simulated by connecting it in a voltage follower configuration, where voltage is applied at V_{IN+} and the output voltage (V_{OUT}) is fed directly back into V_{IN-}. Therefore V_{OUT} is expected to follow V_{IN+} very closely. The result of the DC simulation is shown in Figure 4-15. When V_{IN+} is below 0.5V, N4 is in triode region while other transistors are saturated. Under this condition, the open-loop gain of the amplifier is reduced, hence reducing the accuracy of the voltage follower. When V_{IN+} is between 0.5V and 2.5V, all transistors are the in saturation region and the open-loop gain increases and is at its maximum between 1V to 2V. As the input increases above 2.5V, P4 and P2 moves into the linear region and again the open loop gain is reduced. Around 2.7V, the amplifier reaches the voltage limit which is limited by the voltage drop across P2 and P4 $\left(V_{OUT\_MAX} = AVDD - \left(V_{DS_{P2}} + V_{DS_{P4}}\right)\right)$.

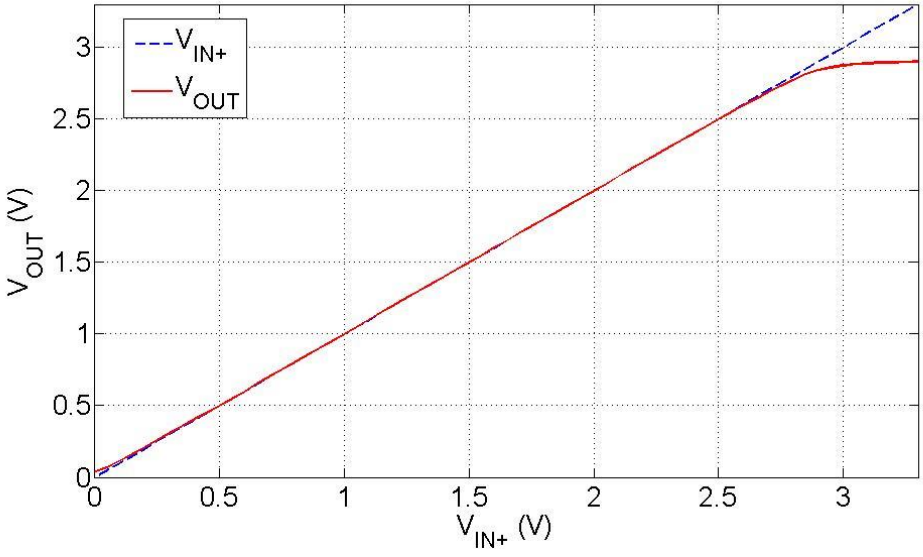

Figure 4-15 – DC simulation of the operational amplifier

Figure 4-16 shows the AC simulation of the operational amplifier. The simulation was conducted using the configuration shown in Figure 4-7 driving a 5pF load capacitance. From the simulation, the open loop gain of the amplifier was shown to be approximately 1100 (or 60.8 dB) with a cut off frequency of 160 kHz and a 20 dB per decade roll-off. This indicates that there is only one dominant pole exhibit by the amplifier with the second pole kicking in at about 700MHz. The gain bandwidth product of the amplifier is 177 MHz.

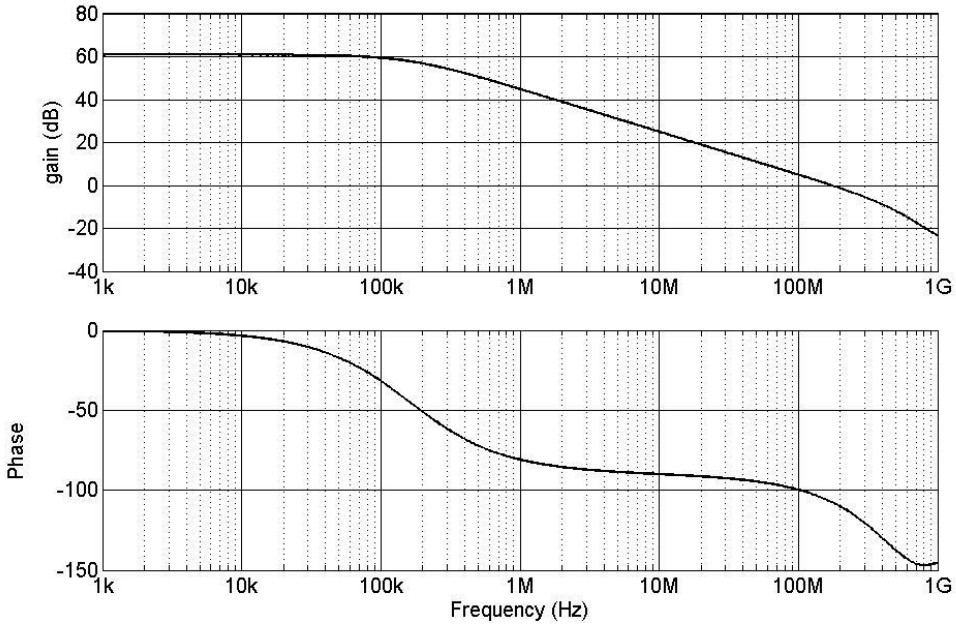

Figure 4-16 – AC simulation of the operational amplifier

4.5.2. Transistor M1, M2 and R_S and CCFBK DC Simulation

The amplifier was then connected to transistor M1, M2 and R_S to form a full feedback system as shown in Figure 4-2. Two conditions were considered for M1 and M2:

1. The CCFBK driver is specified to drive the microLED up to 100mA of current. Therefore M2 should be able produce about 100mA. As mentioned in Section 4.4.3, $\frac{W_{M2}}{W_{M1}}$ was set to be 30. Therefore M1 is expected to produce 3.3mA of current.
2. Because M1 and M2 are mirror transistors with a width ratio of 30, a non-minimum length was used on both transistors to improve matching.

The width of M1 (W_{M1}) can be estimated using Equation 4-13. K_p' and V_T of p-channel MOSFET is given in Table 3-4 (Chapter 3). For the chosen process, the minimum length of a transistor (p-channel MOSFET and n-channel MOSFET) is 350 nm. Therefore, the length of M1 (L_{M1}) was chosen to be 700nm, twice the minimum value, to improve current mirror matching. Assuming the effective voltage (V_{DS_M1}) is 0.8V to keep M1 operating in saturation, W_{M1} is calculated to be 125µm.

$$I_{M1} = -3.3mA = -\frac{K_p'}{2}\left(\frac{W_{M1}}{L_{M1}}\right)(V_{GS} - V_T)^2 \qquad \textbf{Equation 4-13}$$

Using the value of W_{M1} and the length of M2 (L_{M2}) kept the same as L_{M1}, the width of M2 (W_{M2}) is calculated to be 3.75mm. Unfortunately, such wide transistors are limited by the pixel area. To compromise this limitation, I_{M1} is reduced to 3mA and V_{DS_M1} is increased to 0.9V. Using the same equation and transistor length of 700nm, W_{M1} and W_{M2} are calculated to be 90µm and 2.7mm respectively. Due to the reduction of I_{M1}, the maximum current which can be supplied to the microLED is also reduced to about 90mA.

Using the value of I_{M1} and Equation 4-9, the value of R_S was calculated to be 800Ω. The value is higher than estimated in the macromodel simulation due to the reduction of I_{M1}. Figure 4-17 shows the DC simulation of the CCFBK driver, with the red dotted-line represents I_{M1}response with V_{INPUT} using the calculated values of W_{M1}, L_{M1}, W_{M2}, L_{M2} and R_S as discussed. The maximum simulated I_{M1} is 2.86mA, which is slightly lower than the 3mA calculated. The value of R_S was tweaked in order to increase I_{M1}. The final value of R_S used in this design is 773Ω, represented by the black line in Figure 4-17, with maximum simulated I_{M1} is 2.95mA.

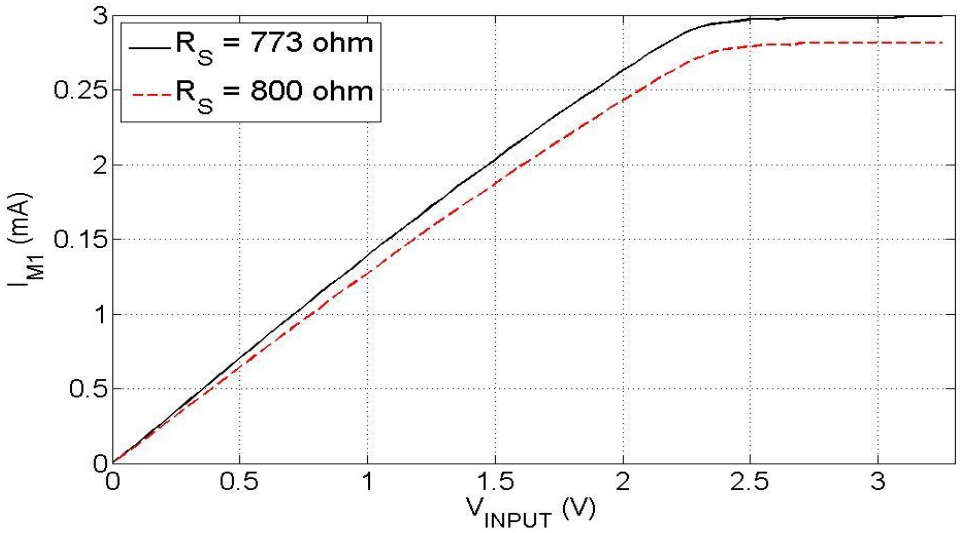

Figure 4-17 – I_{M1} as a function of V_{INPUT}

Figure 4-18 shows I_{M2} response as a function of V_{INPUT}. The output of the driver is connected to the microLED model (Section 3.4.2) and the LED_GND node is biased at –3V. From the figure, the maximum current produced by the CCFBK driver is approximately 91mA.

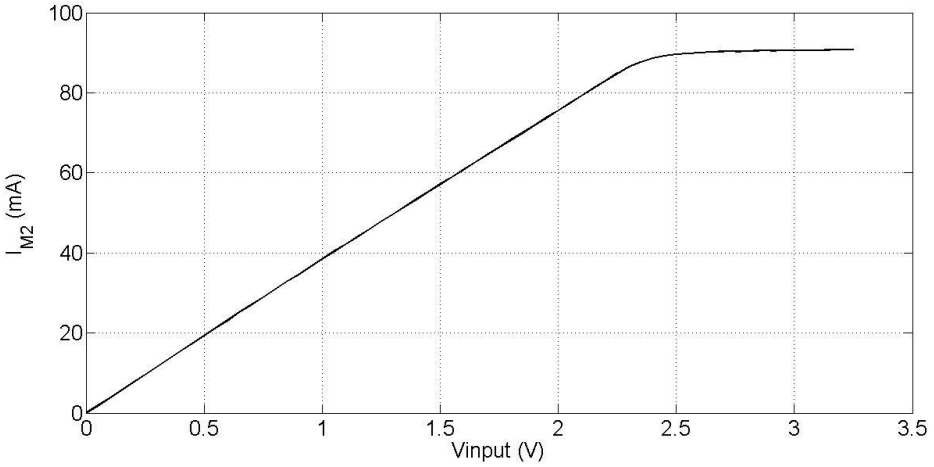

Figure 4-18 – I_{M2} (microLED/CCFBK driver output) as a function of V_{INPUT}

4.5.3. AC Simulation

Using the Cadence analysis tool for the DC simulation of the feedback system, g_{m_M1} was found to be around 3.8mS. With this information, as summarised in Table 4-4, the stability of the feedback system can be analysed by looking at a loop gain AC simulation by breaking the feedback loop and applying a signal input to the feedback network as shown in Figure 4-10 in Section 4.4.3.2. The frequency response of I_{M1} is observed in this analysis.

Parameters	Macromodel Estimated Value	Designed Value
M1 current sink, I_{M1}	Up to 3.3 mA	3mA
Sense Resistor, R_S	760Ω	773Ω
Transistor M1 transconductance, g_{m_M1}	3.6mS	3.8mS
Operational Amplifier open loop gain, A_{OP1}	1000 (60 dB)	1098 (60.8 dB)
Operational Amplifier gain-bandwidth product	130 MHz	177 MHz

Table 4-4 – Comparison between estimated value in macromodel and the actual designed value

Figure 4-19 shows the feedback system loop gain and phase response bode plot. Using the values of A_{OP1}, g_{m_M1} and R_S given in Table 4-4, the loop gain was calculated to be 3225 (70.2 dB) as shown in the figure. The phase margin when the gain is unity is 63° indicating that the loop gain of the system is stable.

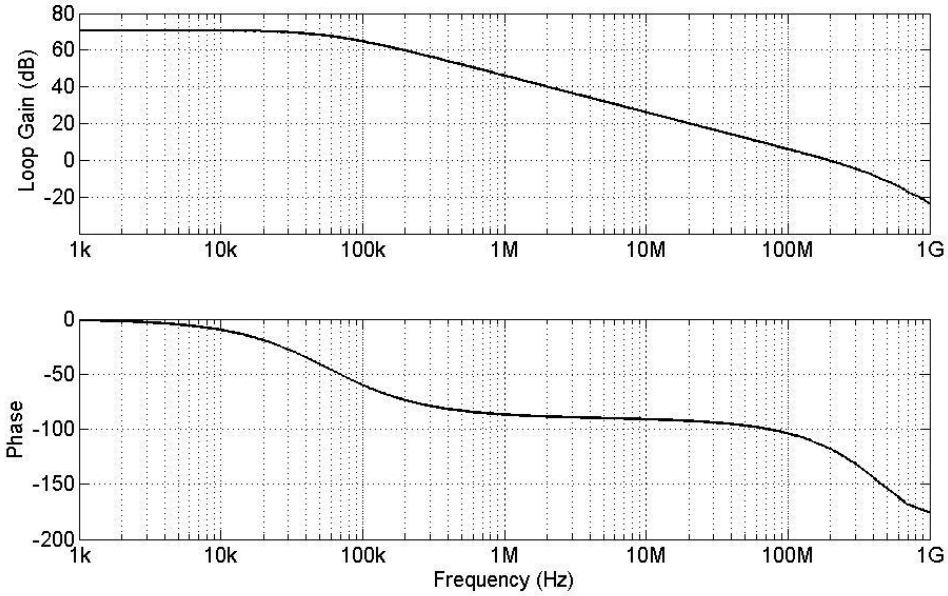

Figure 4-19 – Loop gain analysis bode plot

An AC simulation of the CCFBK driver was conducted by including the microLED model and the optical power response model (Section 3.4.2). The purpose of this simulation is to determine the small signal bandwidth of the CCFBK driver and to predict the performance of the microLED/CCFBK driver. The bandwidth of the CCFBK driver can be found by looking at the I_{M2} as a function of V_{INPUT} while the bandwidth of the microLED/CCFBK driver can be analysed by plotting the optical power output response from the microLED model.

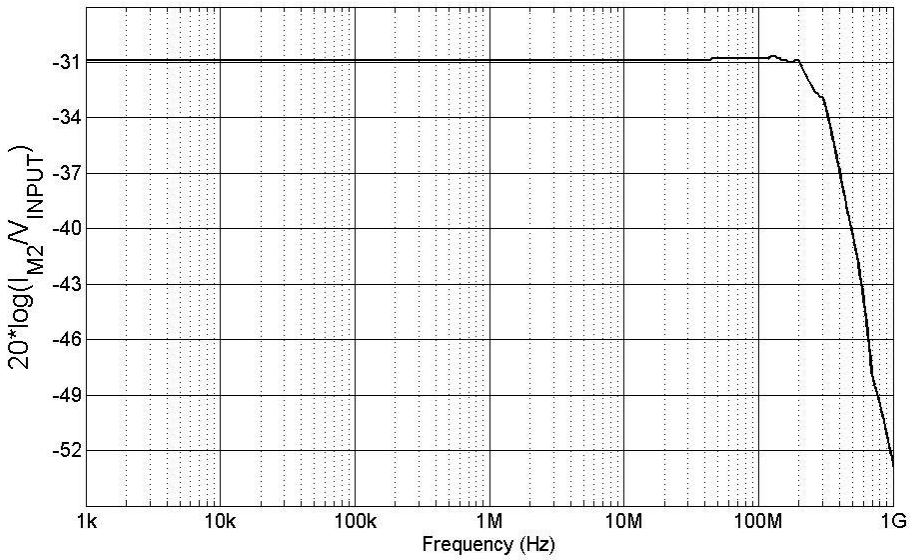

(a)

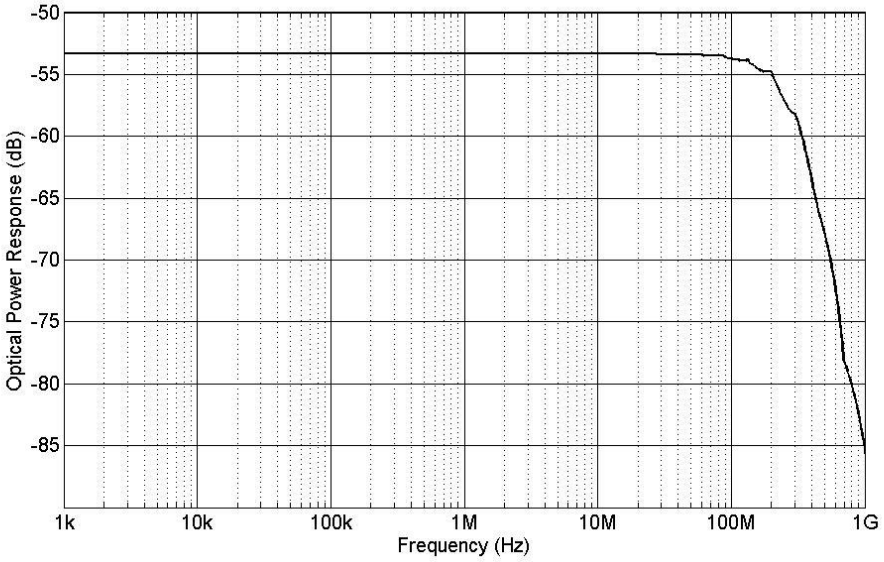

(b)

Figure 4-20 – Frequency response of (a) I_{M2} (CCFBK driver output) and (b) Optical power from CCFBK driver with MicroLED model

Figure 4-20 (a) shows the frequency response of I_{M2}. The bandwidth of the driver was found to be 332MHz. Figure 4-20 (b) on the other hand, shows the frequency response of the MicroLED/CCFBK driver's optical power. The bandwidth of the optical power response is lower than the CCFBK driver at 250MHz. This is limited by the RC constant of the microLED even though the driver could drive at higher frequencies.

4.5.4. Large Signal Bandwidth

Figure 4-20(b) in the previous section shows the optical power bandwidth of the microLED/CCFBK driver is approximately 250MHz. This, however, is the small-signal bandwidth where the circuit, in general, is operating in a single linear region and thus the frequency response is determined by the gain-bandwidth product. For the application of VLC, the large signal bandwidth may be more appropriate. This is because a large signal swing is preferable to achieve a high SNR. Furthermore, for OFDM application, a large PAPR is required which leads to low BER. In the large signal mode of operation, the input signal is large enough to no longer meet the linear approximation and the active devices may even change region of operation. Thus, the large signal frequency response is limited by the slew rate of the circuit

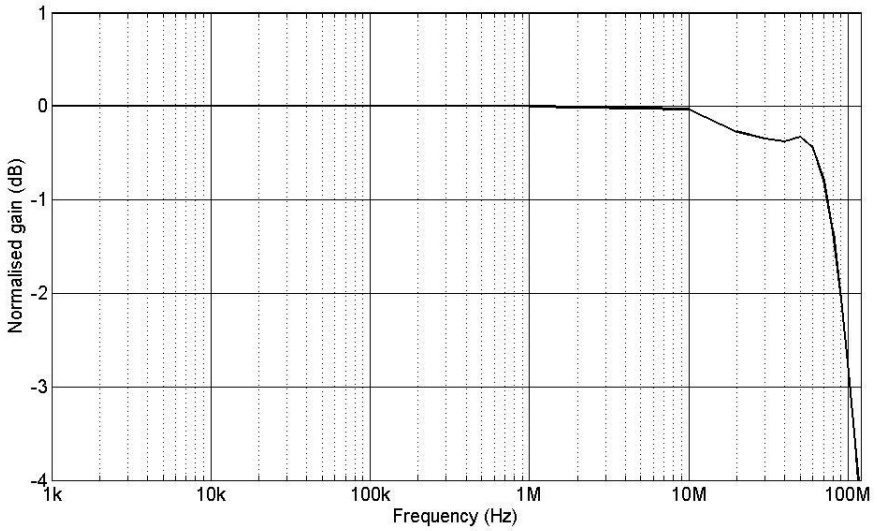

Figure 4-21 – I_{M2} large signal frequency response

The simulation of the large signal frequency response was conducted by means of transient simulation where a sine wave biased at 1.65V with 1V peak-to-peak of very low frequency is applied to the V_{INPUT} of the microLED/CCFBK driver and the peak to peak response from the output signal (I_{M2} or microLED optical power) is recorded. The frequency of the generated sine wave was then increased until the output response is –3 dB smaller than its original size. This is the large signal bandwidth of the microLED/CCFBK driver. Figure 4-21 shows the large signal bandwidth of the microLED/CCFBK driver by probing I_{M2} response. From the figure, the simulated bandwidth of the driver was found to be approximately 110MHz, which is approximately 1/3 of the small signal bandwidth (Figure 4-20(a)). Figure 4-22 on the other hand, shows the frequency response of the optical power from the microLED model driven by the CCFBK driver. The optical power large signal bandwidth was simulated to be about 95MHz, which is also about 1/3 of the small signal bandwidth shown in Figure 4-20(b).

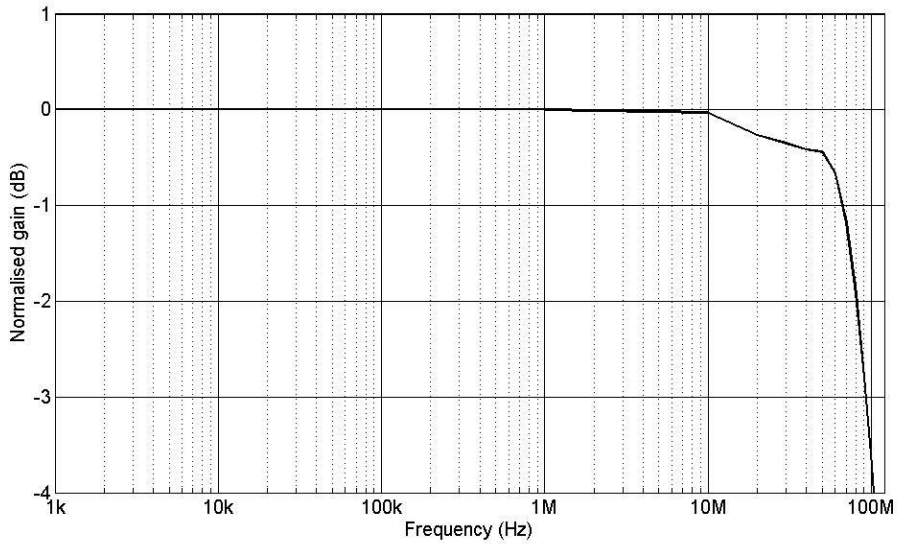

Figure 4-22 – MicroLED/CCFBK Driver optical power large signal frequency response

The large signal bandwidth, as mentioned, depends on V_{INPUT} signal peak-to-peak as denoted by Equation 4-14

$$BW_L = \frac{SR}{2\pi(I_{pk-pk})} \qquad \textbf{Equation 4-14}$$

where SR is the slew rate and BW_L is the –3 dB bandwidth of the driver while I_{pk-pk} is the current response produced by the driver with a given V_{INPUT}. Therefore, a higher bandwidth is achievable by reducing the peak-to-peak V_{INPUT}, but at a cost of reducing the SNR.

4.6. Circuit Layout

The pixel pitch of the CCFBK driver was specified to be 100µm x 100µm, the same as the digital driver. Like the digital driver, four layers of metal (Metal1, Metal2, Metal3, and Metal4) were available and the microLED is bump-bonded on top of the CMOS pixel. Therefore, the same technique of using the top metal layer (Metal4) as both electrode and shield to protect the CMOS circuitry during bonding was used. The area of Metal4 is 95µm x 95µm, covering about 90% of the pixel, with a passivation window of 80µm x 80µm. For this reason, Metal4 was excluded from use as power rails or interconnection. The area of the Metal4 was determined by the bump-bonding specification as discussed in Section 3.5. Metal1 and Metal2 were mainly used as circuit interconnections while Metal3 was used as power rails

(LED_VDD and GND in Figure 4-2). The power rails in the CCFBK driver were made as wide as possible to reduce the voltage drop due to resistive metal track. The layout of the CCFBK driver is shown in Figure 4-23 (excluding Metal4).

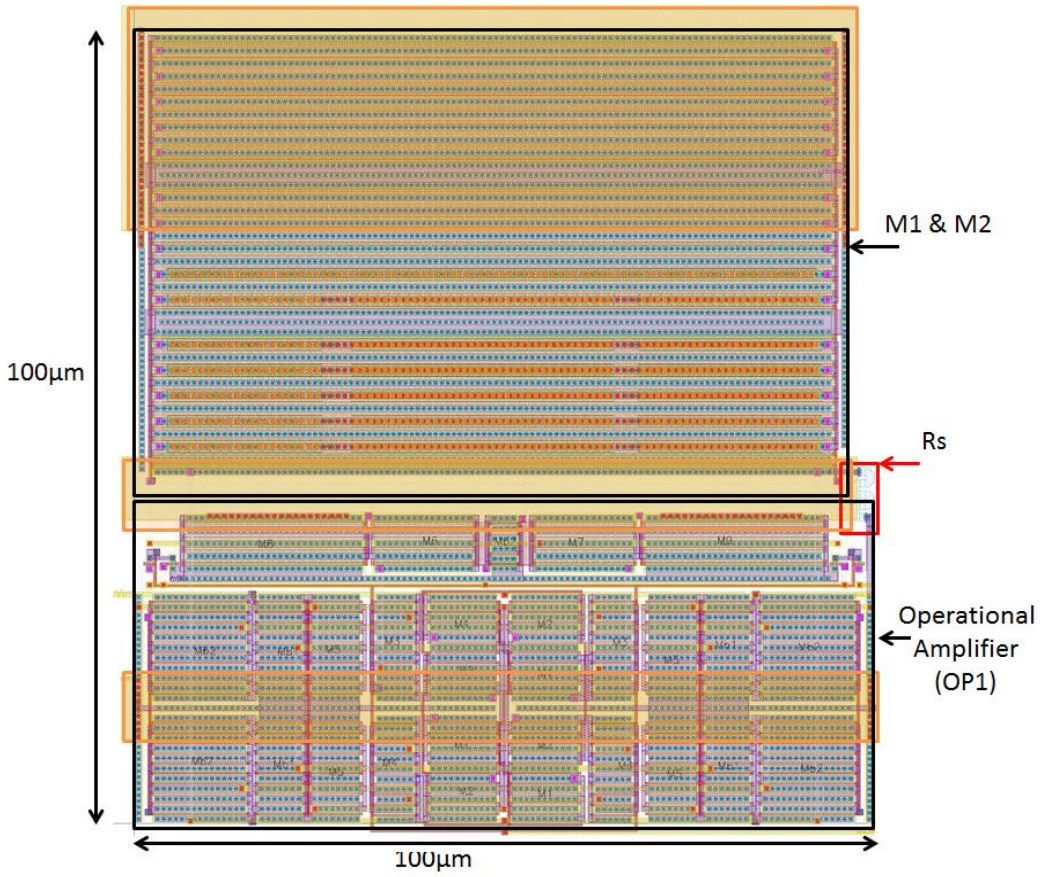

Figure 4-23 – Schematic layout of CMOS Current Feedback Driver (CCFBK)

As discussed in Section 4.5.2, $\left(\frac{W}{L}\right)$ of M1 and M2 were limited by the pixel area. As seen in Figure 4-23, the layout of OP1 has already taken approximately 50% of the total area. Therefore, only about 50% of the area is left for M1 and M2 which, as discussed in Section 4.5.2, were required to be very wide. To satisfy the limited space, the current produced by M1 and M2 was reduced from 3.3mA to 3mA and 100mA to 91mA respectively. The method of choosing the maximum width of M1 and M2 was using manual optimisation, as mentioned in Chapter 3. The set of transistors, including the amplifier, were quickly laid out and the width of M1 and M2 were optimised accordingly. Using initial parameters, the width of M2 was 3.75mm, producing about 99mA, and was reduced to 2.7mm to fit within the pixel specification.

The resistor R_S is a polysilicon type called POLY2. The nominal sheet resistance of POLY2 in this process is given as 50Ω/□ [89]. The dimension of R_S can be calculated using Equation 4-15.

$$R_S = R_{Sheet\_POLY2} \times \frac{\mathrm{L}_{eff}}{W_{eff}} \qquad \textbf{Equation 4-15}$$

where R_{Sheet_POLY2} is the sheet resistance of POLY2, L_{eff} and W_{eff} are the POLY2 track effective length and width. The width (W) of the resistor is defined by the AMS datasheet as

$$W_{eff} = W_{def} - W_D \qquad \textbf{Equation 4-16}$$

where W_{def} is the width defined and W_D is the width reduction during the fabrication which is given as 0.25µm. For a 773Ω POLY2 resistor, assuming that W_D is a constant and W_{def} of 1µm was chosen, L_{eff} was calculated to be 11.6µm. The layout of R_S is highlighted in red near the right of Figure 4-23.

4.7. Measurement

This section discusses the DC and AC performance of the microLED/CCFBK driver. The same bump-bonding technique was used for the CCFBK driver, as discussed in Section 3.6. An 80µm diameter round microLED was bump-bonded on the CCFBK driver. The DC-B daughter card and IMNS Generic Motherboard (Section 3.7) were used for all measurements.

4.7.1. DC Performance

Figure 4-24 shows I_{M1} response by sweeping V_{INPUT} from 0 to 3.3V. This measurement was conducted by leaving the LED_GND floating (Figure 4-2), making M2 and microLED an open circuit and hence no current would flow. I_{M1} was measured by connecting a digital multimeter in series between the power supply and the LED_VDD input port of the PCB. Because the path of M2 and microLED is an open circuit, $I_{M1}$is equal to the current into the LED_VDD node.

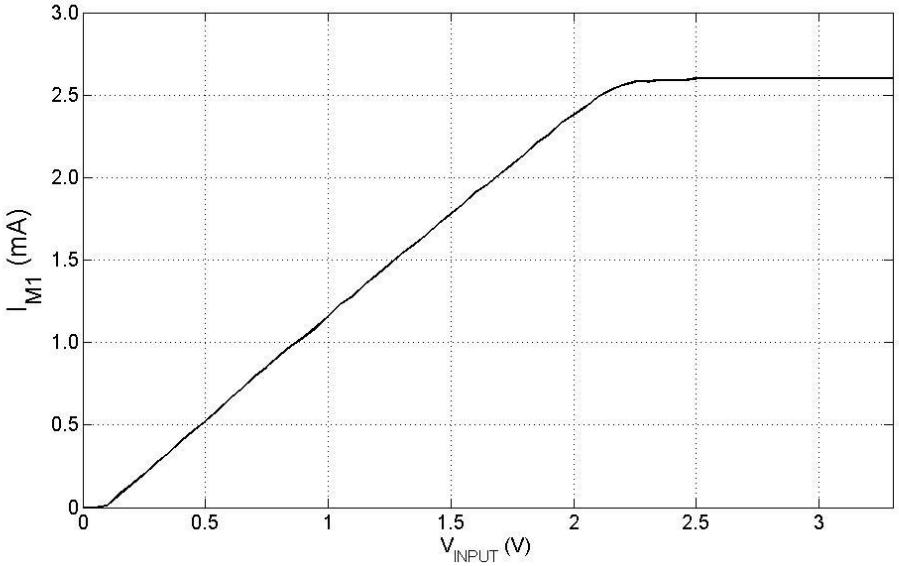

Figure 4-24 – I_{M1} response with V_{INPUT}

Figure 4-24 shows that I_{M1} has a linear response with V_{INPUT}. When V_{INPUT} is 0V, no current is consumed. When V_{INPUT} is between 0 and 0.07V, I_{M1} shows no response. Above 0.07V, I_{M1} increases linearly with V_{INPUT} until it is about 2.2V, after which it saturates. The maximum I_{M1} recorded is 2.67mA (about 0.33mA less than initially designed). The cause of this shortfall is discussed later in Section 4.8.1. Using this information, the maximum current consumed by the microLED can be predicted. Assuming that the ratio of M2 to M1 is 30 (neglecting any mismatching effect), the maximum current consumed by the microLED is expected to be about 80mA.

To measure the I-V and Voltage-to-Light (L-V) characteristics of the microLED/CCFBK driver, LED_GND was connected to an external power supply and biased at –3V. The current consumption of the microLED/CCFBK driver was measured by connecting a digital multimeter in series with the LED_GND node and the negative bias supply. The optical power on the other hand, was measured using Thorlab's photodiode power sensor (SC130C+PM100D) with a slim photodiode sensor (S130C) [102]. The photodiode sensor was placed on top of the chip and the position of the sensor was adjusted so as to be aligned directly with the selected pixel. The experiment setup is shown in Figure 4-25. The measurement of I-V and L-V characteristics were conducted simultaneously.

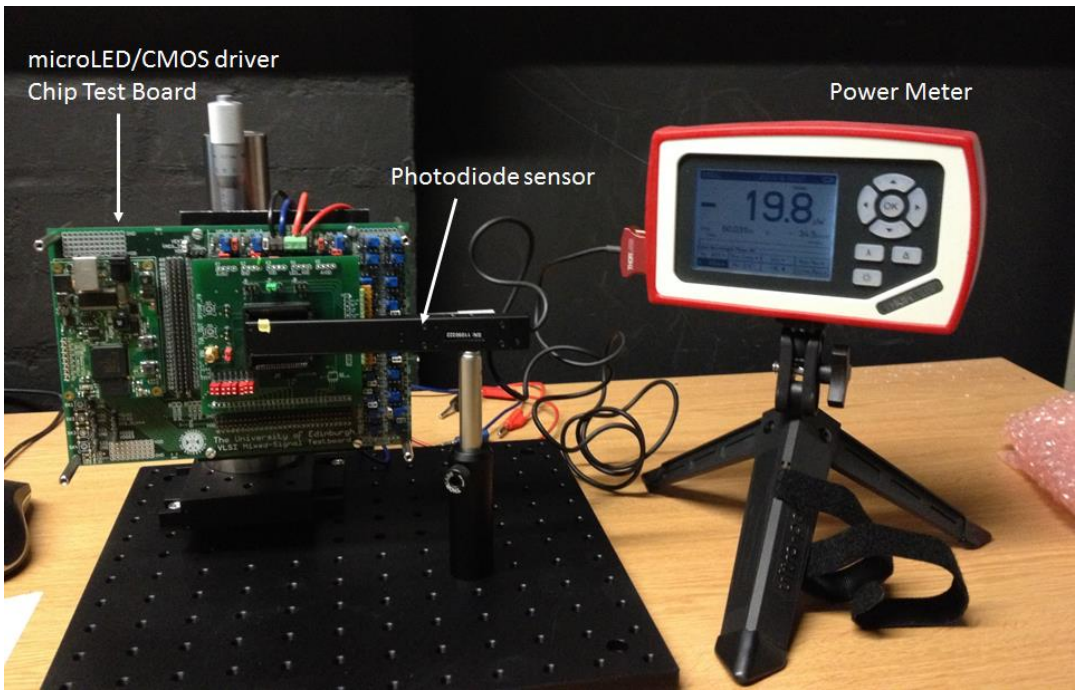

Figure 4-25 – I-V and L-V measurement setup

Figure 4-26 shows the I-V characteristic of I_{M2} of the microLED/CCFBK driver. The I-V characteristic of I_{M2} has a similar trend to that shown in Figure 4-24, where current increases linearly when V_{INPUT} is above 0.07V. However, the current saturates at around 1.85V, which is lower than the value of V_{INPUT} of I_{M1} response in Figure 4-24. Furthermore, as discussed, the maximum current produced by the microLED/CCFBK driver was expected to be around 80mA. However, the figure shows that maximum current is 66.7mA. The cause of these differences is explained in Section 4.8.1. The current matching between I_{M1} and I_{M2} then can be calculated using Equation 4-17.

$$Ratio = \frac{I_{M2}\,@\,V_{INPUT} = xV}{I_{M1}@V_{INPUT} = xV} \qquad \textbf{Equation 4-17}$$

where $I_{M1}@V_{INPUT} = xV$ and $I_{M2}\,@\,V_{INPUT} = xV$ is the current value taken from data presented in Figure 4-24 and Figure 4-26 respectively at the same V_{INPUT} value (xV). Table 4-5 summarises the M1 and M2 current value when V_{INPUT} is 0.5V, 1V and 1.5V. From the table, it can be seen that the ratio of current in M2 to current in M1 are 31 at lower currents dropping to about 30 at higher currents. The ratio at lower current is slightly higher than design expectation of 30 due to mismatching between M1 and M2. The ratio drops at higher current because of the differences in voltage drop in the path of current in M1 and M2 respectively. This is because M2 draws 30 times higher current than M1 and therefore the voltage drop

across the resistive metal track path in M2 is higher, causing it to produce a slightly lower current than otherwise expected.

V_{INPUT}	I_{M1}	I_{M2}	$Ratio$
0.5	0.52	16.1	30.9
1	1.16	35.8	30.8
1.5	1.78	53.2	30

Table 4-5 – Summary of Ratio of current in M2 to M1 at different input voltage

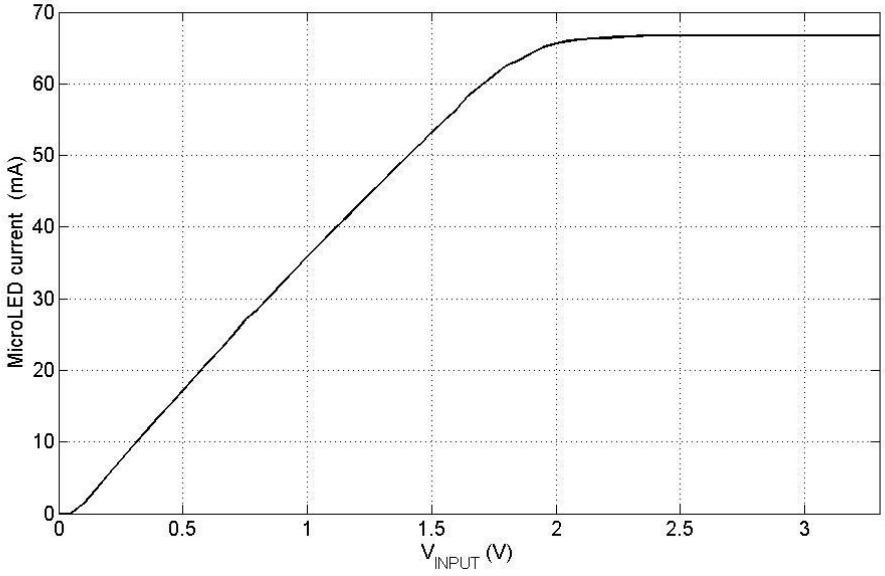

Figure 4-26 – MicroLED/CCFBK driver I-V characteristic

Figure 4-27 shows the L-V characteristic of the microLED/CCFBK driver which shows similar behaviour to the I-V characteristic (Figure 4-26). When V_{INPUT} is below 0.07V, the microLED/CCFBK driver does not respond to any changes in V_{INPUT}. The optical power of the microLED/CCFBK driver starts to increase when V_{INPUT} is biased above 0.07V. The optical power then saturates when V_{INPUT} is approximately 1.85V. It was shown in Figure 4-26 that the current consumed by the microLED/CCFBK driver is linear with respect to V_{INPUT}. However, due to the non-linear response of the L-I characteristic of the microLED, the L-V characteristic of the microLED/CCFBK driver does not increase linearly with V_{INPUT}. Therefore, it is fair to conclude that the microLED/CCFBK driver inherits the non-linearity of the L-I characteristic of the microLED.

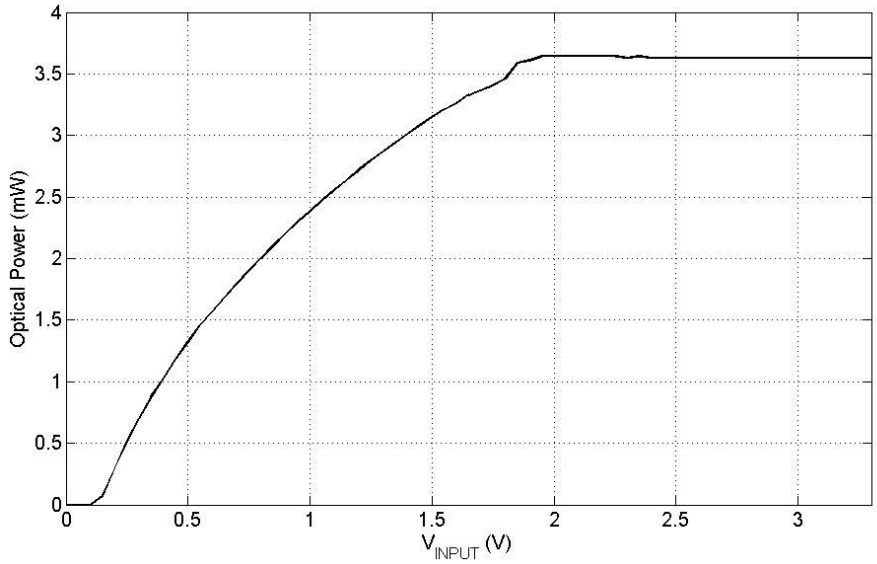

Figure 4-27 – L-V characteristic of microLED/CCFBK driver

4.7.2. Linearity

A linearity analysis was conducted on the measured result to investigate the linearity of the output of the microLED/CCFBK driver. There are two methods to quantify linearity in this thesis. The first method is done by looking at the coefficient of determination (R^2) which is used to describe how well a regression line fits the data set. In this case, a linear regression line is used. An R^2 close to 1 indicates that a linear regression line fits the data well.

The other method involves comparing two regression lines with the data set. This method is similar to finding the Integral Non-Linearity (INL) of a Digital to Analogue Converter (DAC). The two regression lines are:

1. Linear Regression Line
2. Polynomial Regression Line – High order polynomial is used for this regression line such that the R^2 coefficient is equal to 1 (to 4 decimal places). In the thesis analysis, a 6-degree Polynomial regression line was used.

Using the I-V characteristic measurement (Figure 4-26) as an example, the steps of comparing two regression lines are as follows:

1. The range of the linear response of the circuit is selected. As an example, in this case, V_{INPUT} was chosen to be in the range of 0.2V to 1.9V. This is the maximum range in the I-V characteristic plot that is considered linear.

2. The linear and the 6th degree polynomial regression line are obtained. The microLED current value for the two equations (linear and polynomial) are calculated and recorded as shown in Table 4-6. Note that Table 4-6 only shows the range of V_{INPUT} from 0.2V to 1V for example purposes
3. The "**Difference**" column is the difference between the linear point and the polynomial point. The "**Difference Percentage**" column shows the percentage of deviation of the polynomial regression line from the linear regression line. This is calculated as $\left|\frac{\textbf{Difference}}{\textbf{Linear Regression}}\right| \times 100$. The highest percentage obtained is the non-linearity percentage of the response

V_{INPUT}	(microLED current) Linear regression	(microLED current) Polynomial regression	Difference	Difference Percentage
0.2	6.81	6.55	0.26	3.78
0.25	8.58	8.28	0.30	3.44
0.3	10.34	9.95	0.39	3.80
0.35	12.11	11.65	0.46	3.80
0.4	13.88	13.34	0.54	3.87
0.45	15.65	15.27	0.37	2.39
0.5	17.41	17.19	0.22	1.26
0.55	19.18	19.11	0.07	0.36
0.6	20.95	21.02	– 0.07	0.35
0.65	22.72	22.93	– 0.21	0.92
0.7	24.48	24.82	– 0.33	1.36
0.75	26.25	26.70	– 0.45	1.70
0.8	28.02	28.56	– 0.54	1.93
0.85	29.79	30.41	– 0.62	2.08
0.9	31.56	32.24	– 0.68	2.16
0.95	33.32	34.04	– 0.72	2.17
1	35.09	35.83	– 0.74	2.12

Table 4-6 – Example of Two Regression Line comparison method

4. From the table above, the degree of non-linearity of the microLED/CCFBK driver can be quantified as 3.87%.

Figure 4-28 shows the linearity quantification using the method mentioned using the V_{INPUT} range from 0.2V to 1.9V. From the figure, R^2 value was found to be 0.9979, indicating that the microLED/CCFCBK driver exhibits good linearity. The non-linearity percentage is 3.98%, which indicates the highest deviation of the data from a linear regression line. The point at which this occurs is at V_{INPUT} of 1.9V, where the current response from the driver

starts to saturate. From the result, it can be concluded that the CCFBK driver produces a good linear current response to the microLED.

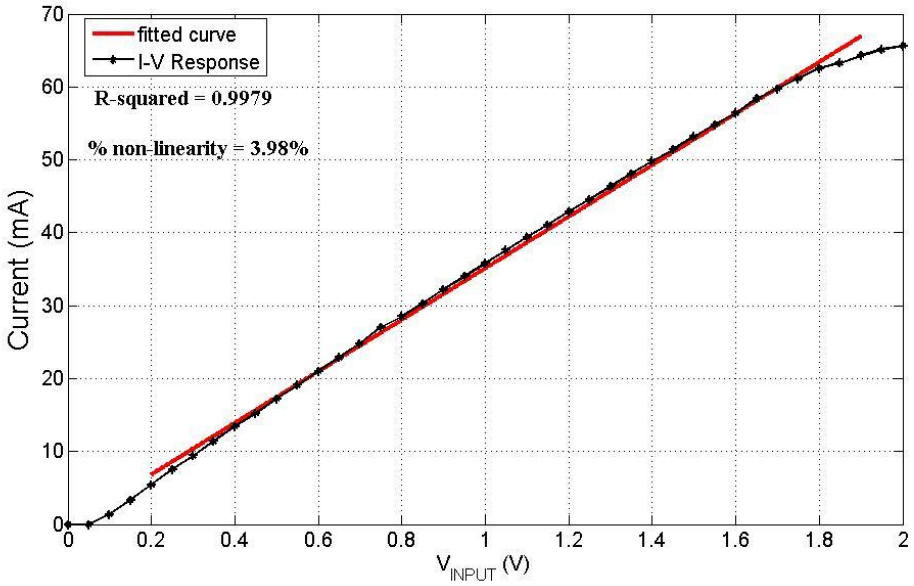

Figure 4-28 – Fitted I-V curve with R^2 and non-linearity percentage

For optical communication, however, the optical power response would be an important factor to determine the performance of the microLED/CCFBK driver. Although it was shown in Figure 4-28 that the microLED/CCFBK driver exhibits very good linear current response, the driver still inherits the microLED non-linearity as shown in Figure 4-29. The degree of non-linearity for optical power response was found to be 12.18% for the same V_{INPUT} range as the current response. The R^2 value was 0.9701.

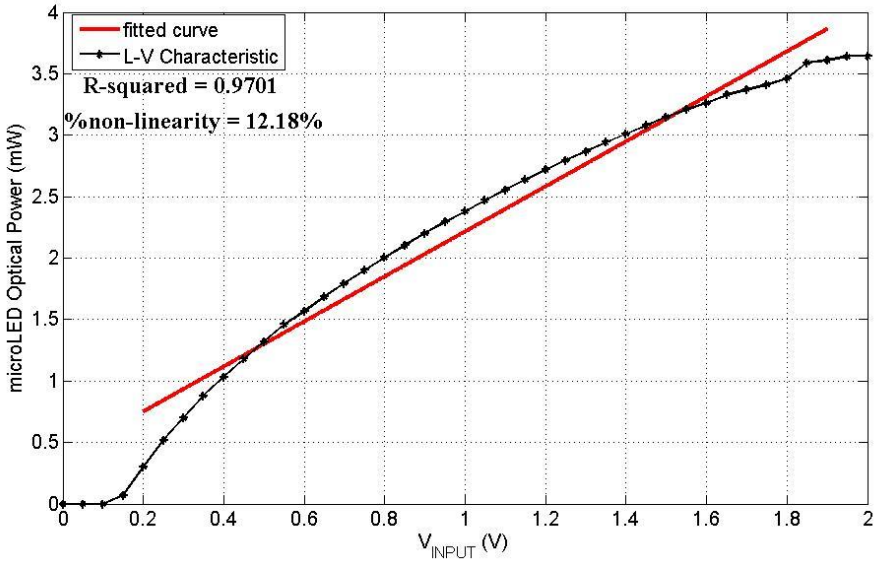

Figure 4-29 – Fitted L-V Characteristic with R^2 and non-linearity percentage

The linearity of the optical power response can be improved by reducing the range of V_{INPUT}. The range of V_{INPUT} was reduced from 1.7V in Figure 4-29 to 1.2V in Figure 4-30(a), 1V in Figure 4-30 (b) and (c) and 0.6V in Figure 4-30 (d). The R^2 value and the non-linearity percentage of each selected range are shown in the figure respectively.

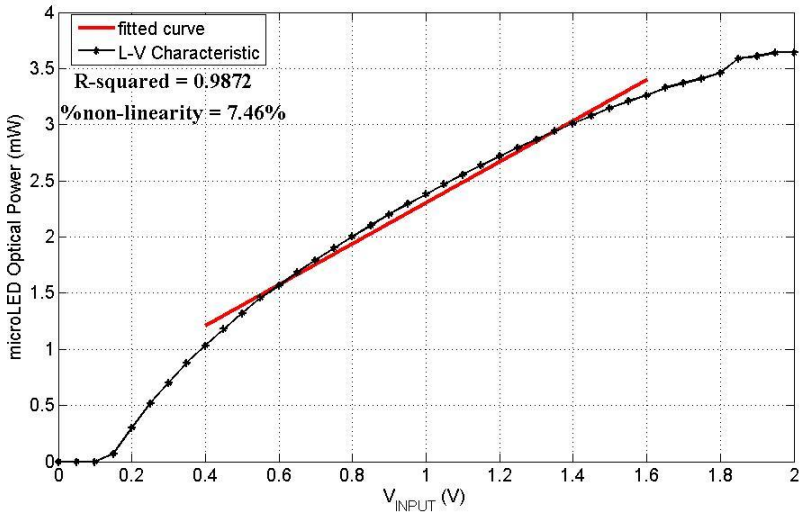

(a) V_{INPUT} range from 0.4V to 1.6V (input range of 1.2V)

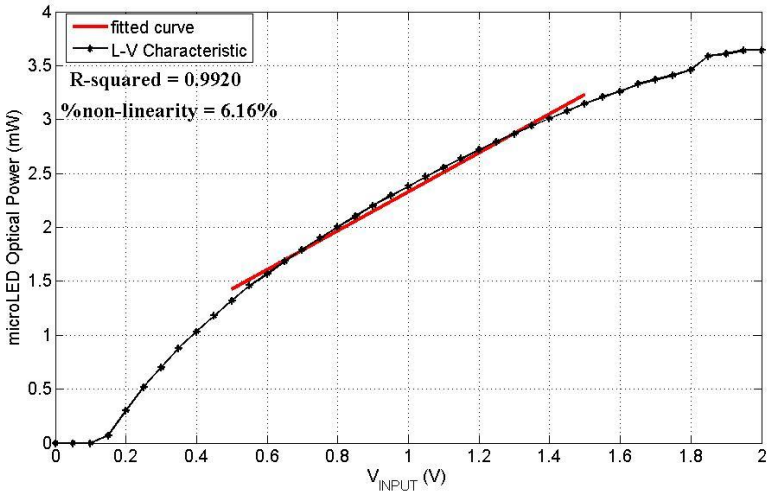

(b) V_{INPUT} range from 0.5V to 1.5V (input range of 1V)

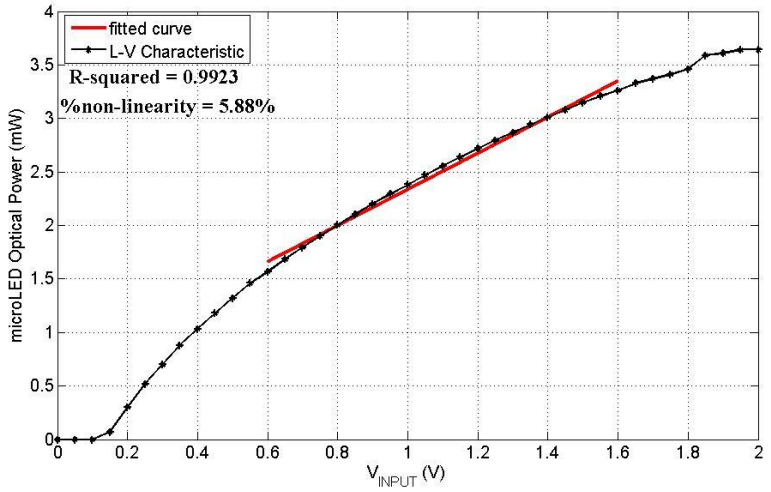

(c) V_{INPUT} range from 0.6V to 1.6V (input range of 1V)

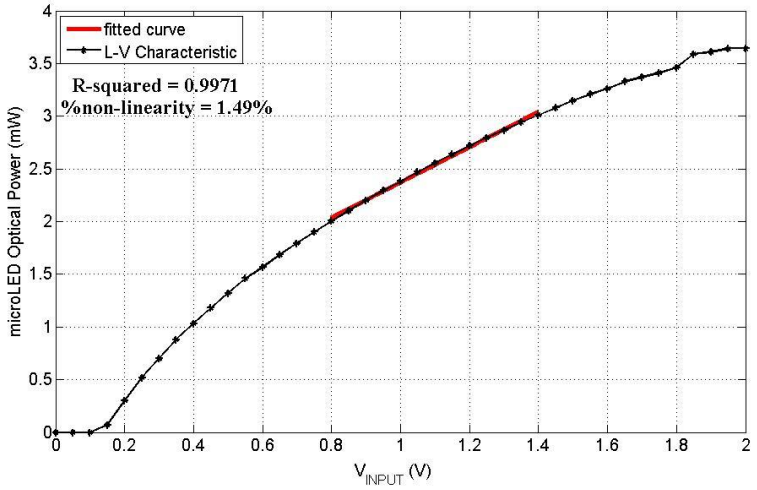

(d) V_{INPUT} range from 0.8V to 1.4V (input range of 0.6V)

Figure 4-30 – Linearity improvement by reducing the V_{INPUT} range

Figure 4-30 (a – d) clearly shows the improvement in optical power linearity by reducing the range of V_{INPUT}. The non-linearity percentage was reduced from 12.18%, when the V_{INPUT} range is 1.7V, to 1.49% when the V_{INPUT} range is 0.6V. This technique is similar to the 'power back-off' method as mentioned in Section 2.3.5, where the input signal power is backed off to ensure the microLED/CCFBK driver operates with a higher degree of linearity, which is an advantage for OFDM applications. The disadvantage of this technique, however, is that the PAPR of the optical power is also reduced. The effect of this reduction is discussed in Chapter 6 (Section 6.4.3). In Figure 4-30 (b) and (c), the same V_{INPUT} range was selected, but at different bias points where the range in (b) was biased at a lower point than (c). Even though the V_{INPUT} range selected was the same, the non-linearity in (b) is greater than in (c). This suggests that the microLED optical power response is more linear in the upper range of the curve than the lower range. The R^2 and non-linearity percentage is summarised in Table 4-7.

V_{INPUT} Range	Figure	R^2	% Non-linearity	Optical Power Range
0.2 - 1.9V (1.7V)	4-32	0.9701	12.18	0.3 - 3.61 mW (3.31mW)
0.4 - 1.6V (1.2V)	4-33(a)	0.9872	7.46	1.03 - 3.26mW (2.23mW)
0.5 - 1.5V (1V)	4.33(b)	0.9920	6.16	1.32 - 3.15mW (1.83mW)
0.6 - 1.6V (1V)	4.33(c)	0.9923	5.78	1.56 - 3.36mW (1.8mW)
0.8 - 1.4V (0.6V)	4.33(d)	0.9971	1.49	2 - 3mW (1mW)

Table 4-7 – Summary of the non-linearity improvement by V_{INPUT} range reduction

4.7.3. Bandwidth Measurement

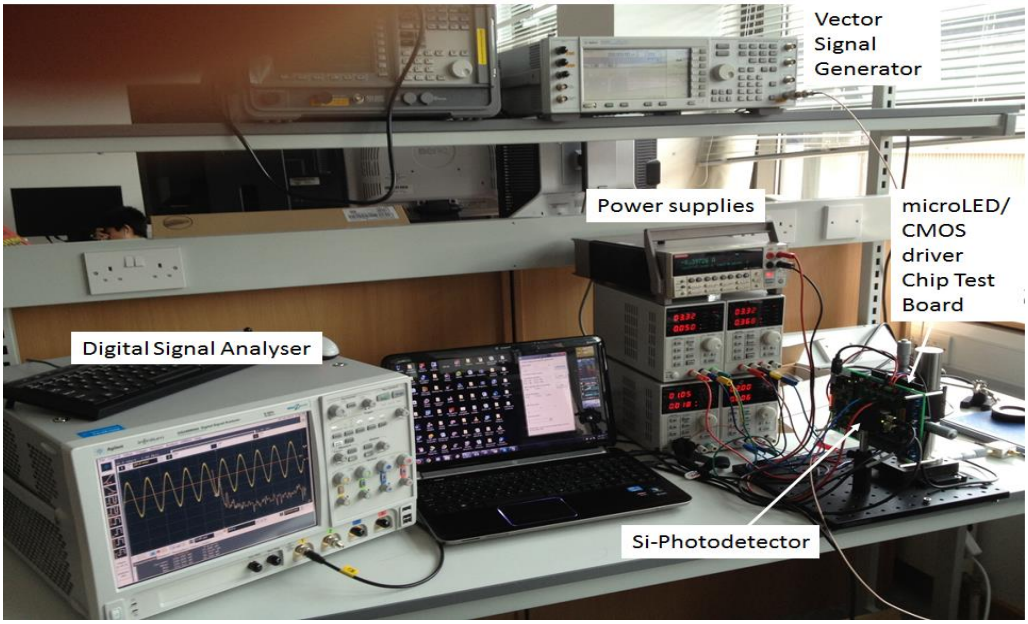

Figure 4-31 – Frequency response measurement setup

A frequency response measurement was conducted to find the bandwidth of the microLED/CCFBK driver. The frequency response was measured using the ThorLab's Silicon Transimpedance Amplifier PDA10A [103](Si-Photodetector), Agilent ESG Vector Signal Generator (EC4438C) [104] and Agilent Digital Signal Analyser (DSA90804A) [105]. The output of the signal generator was combined with a DC offset using a bias-tee and then sent to the microLED/CCFBK driver input on the PCB DC-B daughter card. The signal generated by the signal generator sets the amplitude of the input signal while the bias-tee sets the DC bias operating point for the driver. The Si-Photodetector was aligned to the pixel driver. The optical power response of the pixel is detected by the Si-Photodetector and the electrical output of the detector was fed into the Digital Signal Analyser. The experimental setup is shown in Figure 4-31.

For this measurement, the LED_GND node was biased at –3V. A sine wave of very low frequency was generated by the Signal Generator and the peak-to-peak response of the Si-Photodiode displayed on the Digital Signal Analyser was recorded. The frequency of the sine wave input signal was then swept from a low to a higher value and the Si-Photodiode peak-to-peak responses were recorded. Figure 4-32 shows the frequency response of the microLED/CCFBK driver driven with 1V peak-to-peak input signal biased at 1V DC. From the figure, the –3dB bandwidth was found to be 49MHz.

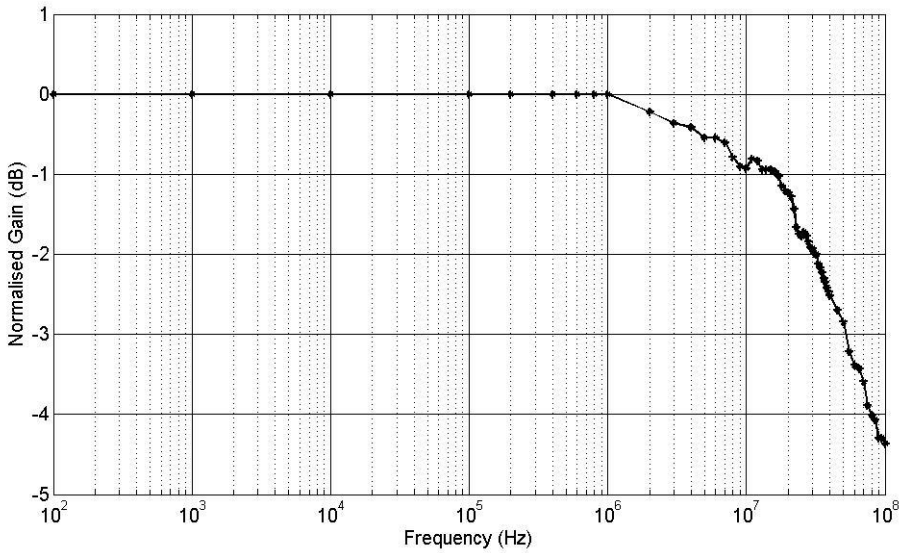

Figure 4-32 – MicroLED/CCFBK driver frequency response with 1V peak to peak input signal biased at 1V DC

The bandwidth, however, depends on the DC bias point and the range of V_{INPUT} peak to peak (p-p) as mentioned in Section 4.5.4. Two experiments were conducted. In the first experiment, the V_{INPUT} range was fixed and the DC bias point varied at 0.6V, 1V, 1.2V, 1.5V and 1.65V. In the second experiment, the DC bias point was fixed and the V_{INPUT} range was set at 200mV, 400mV, 600mV, 800mV and 1V peak to peak. Figure 4-33 shows how the DC bias point and the range of the input signal affected the bandwidth of the microLED/CCFBK driver. There are two trends shown in the figure:

1) The bandwidth of the microLED/CCFBK driver increases with the DC input bias voltage. Taking the V_{INPUT} = 0.8V p-p as an example, the bandwidth increases from 32MHz when it is biased at 0.6V to 65MHz as the DC bias is increased to 1.65V.
2) The bandwidth also increases as the V_{INPUT} p-p is reduced. Taking when the driver is biased at 1V for example, the bandwidth of the driver is 49MHz when the input signal is 1V peak-to-peak. The bandwidth increases to 60MHz when the input signal is reduced to 0.2V peak-to-peak.

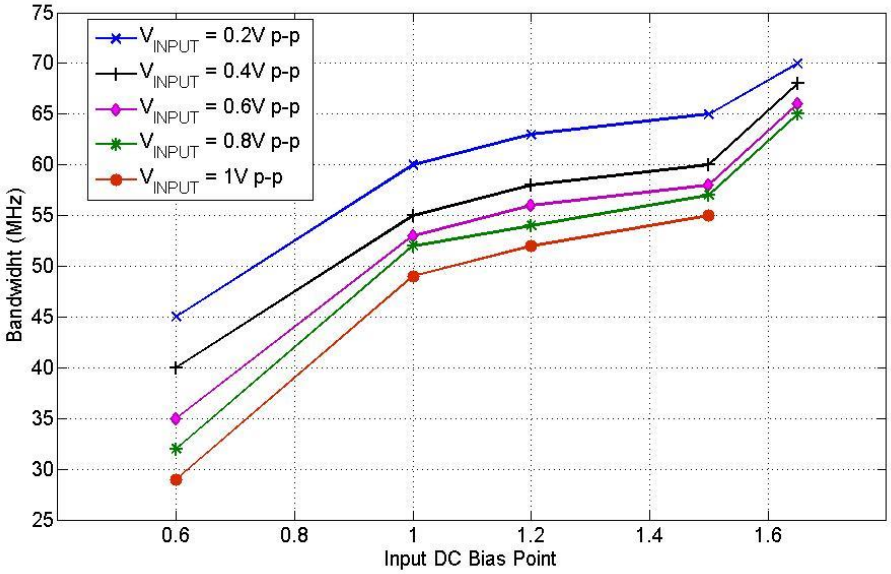

Figure 4-33 – Bandwidth trend with DC bias point for different input voltage swing (peak-to-peak)

The effect seen when changing the DC bias is caused by the bandwidth of OP1 in the CCFBK driver. For all V_{INPUT} range, the bandwidth difference between the lowest and highest DC bias in Figure 4-33 is about 30MHz. As explained in Section 4.5.1, the gain-bandwidth product of OP1 is lowest at the low and high bias point. This was clearly seen in Figure 4-33 where there is a large reduction in bandwidth for all V_{INPUT} range when the input bias is reduced from 1V to 0.6V. When the DC bias is 0.6V, transistor N4 (Figure 4-14) is at the edge of saturation and

therefore OP1 lost its gain-bandwidth product. As the DC bias increases, the bandwidth of OP1 also increases. The bandwidth of OP1 reduces again when DC bias is above 2.3V when P2 and P4 (Figure 4-14) at the edge of saturation. However, because the DC response of the microLED/CCFBK driver does not exceed 2.05V, the effect of reduction at the high DC bias point is not shown in Figure 4-33.

The difference in bandwidth between a small and wide range V_{INPUT} arises because of the slew rate of the driver. The slew rate is limited by the amount of current generated by the CCFBK driver and the total capacitance driven by the circuit which includes the load capacitance of the microLED. For a given slew rate, as the range of input signal decreases, the large signal bandwidth of the driver increases as explained by Equation 4-14. For all DC bias points, the difference in bandwidth between the smallest and the largest V_{INPUT} is about 10MHz, except for when the DC bias point is 0.6V which shows a difference of approximately 15MHz. This is because, at 0.6V DC bias, OP1 has the lowest gain-bandwidth product, thus the slew rate is also at its lowest. Therefore, driving a large signal causes the driver to lose more bandwidth than other DC bias points. The measured large signal bandwidth of the microLED/CCFBK driver, however, is lower than simulated, as shown in Figure 4-22. Further analysis is discussed in the next section

4.8. Measurement vs. Simulation

This section studies the causes of the shortfalls in performance of the measured results in comparison to the simulated results. To understand the causes, the microLED/CCFBK driver was re-simulated. Figure 4-34 shows the schematic circuit diagram of the re-simulation. R_{IN} and C_{IN} are the parasitic resistance and capacitance of the input signal which include connector wires, PCB tracks, and wire-bonds. The bond-pad model (provided by AMS) and the addressing logic circuits are also included in the simulations. R_{Rail} denotes the resistance of the power supply, connector wires, PCB tracks and metal rails that carries the current to M1 and M2. R_{OUT} and C_{OUT} are the output parasitic components which represent the resistance and the capacitance of the gold bump-bond and the metal contacts on CCFBK driver and microLED. The post-layout extraction of CCFBK driver was used for this simulation. Table 4-8 summarises the definition of the added parasitic and the values used.

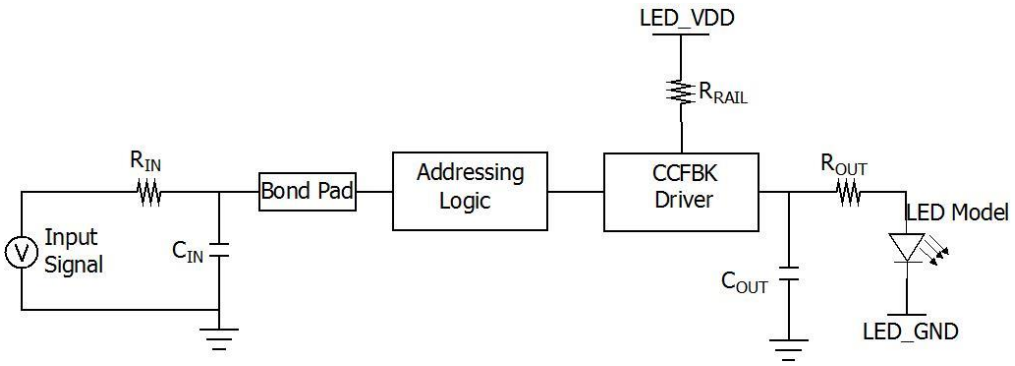

Figure 4-34 – Schematic of the re-simulation

Component	Description	Value
R_{IN}	Resistance of the signal wire, PCB tracks and gold wire bond	10Ω
C_{IN}	Capacitance of the signal wire, PCB tracks and gold wire bond,	5pF
Bond Pad	Resistive and capacitive value of the bond pad	Value determined by model from AMS
R_{RAIL}	Resistance of the Voltage supply, wire and Multimeter	4Ω
R_{OUT}	Resistance of Metal contacts of CCFBK driver and gold bump-bond	2Ω
C_{OUT}	Capacitance of Metal contacts of CCFBK driver and gold bump-bond	5pF

Table 4-8 – Description and values of parasitic components used in the simulation

From simulations, the input parasitic components ($R_{IN,}$ C_{IN}, Bond pad and addressing logic) do not have any effect on the performance. This is demonstrated by comparing the input signal and the signal at the input of the CCFBK driver which shows no difference at DC to frequency beyond 200MHz. Therefore, only R_{RAIL}, C_{OUT}, R_{OUT} affected the microLED/CCFBK driver and are discussed in this section.

4.8.1. DC Characteristics

Figure 4-35 shows the DC response comparison between ideal simulation, parasitic simulation and the measured result. As V_{INPUT} is swept from 0 to 3.3V, the ideal simulation shows I_{M1} response immediately with the increase of V_{INPUT} whereas in both parasitic simulation and measured results, I_{M1} only increases at about 0.07V. This effect occurs because of voltage offset between the differential pair input of the amplifier, which is caused by a mismatch in the layout.

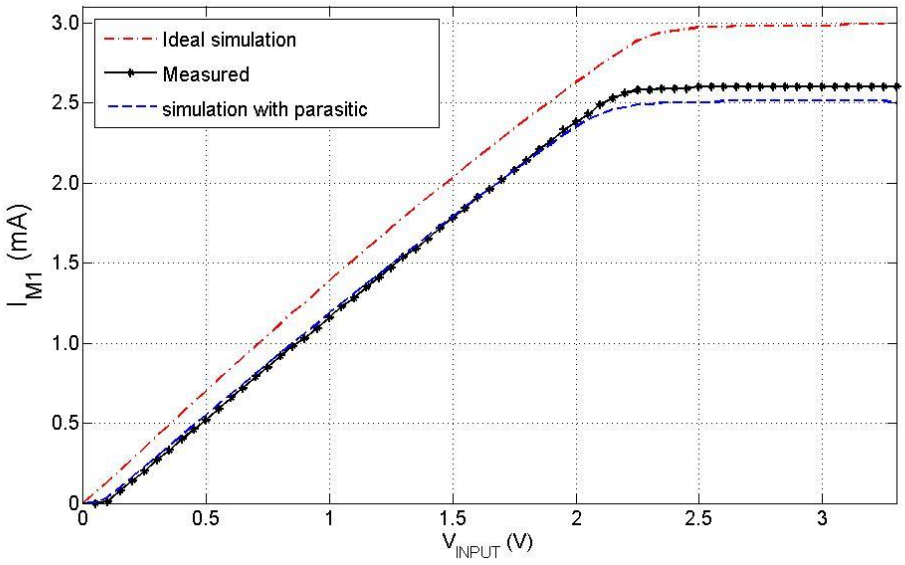

Figure 4-35 – I_{M1} response comparison between ideal simulation, simulation with parasitic and Measurement

Another shortfall seen in the measurement is the reduction in the total current. I_{M1} of the ideal microLED/CCFBK driver was expected to be about 2.95mA. However, the measured result only shows 2.67mA. Furthermore, the V_{INPUT} range has also reduced from 2.4V in the ideal simulation to about 2.2V in the measurement. The cause of the current and V_{INPUT} range reduction is due to the series resistance, R_{RAIL} (Figure 4-34) which causes an additional voltage drop across M1 current route and hence reduces the current sourced by M1. The maximum V_{INPUT} range is then given by Equation 4-18, showing an additional $V_{R_{RAIL}}$ drop from Equation 4-8.

$$V_{INPUT} = V_F = 3.3 - (V_{DS_{M1}} + V_{R_{RAIL}}) \qquad \textbf{Equation 4-18}$$

The same effect is also seen in I_{M2}. There are two parasitic resistances that affect I_{M2}, which are R_{RAIL} and R_{OUT} (Figure 4-34). The R_{RAIL}, as explained earlier, reduces I_{M1} and also the range of V_{INPUT} which is then mirrored by M2. The I_{M2} and V_{INPUT} range of M2 are further reduced by parasitic resistances at the drain of M2, which causes a further voltage drop that pushes M2 to the edge of the saturation region. The parasitic resistances include R_{OUT} and the resistance of the microLED. Figure 4-36 shows the simulation of the I_{M2} response of the CCFBK driver with parasitic components in comparison with the 'ideal' simulation and measured result.

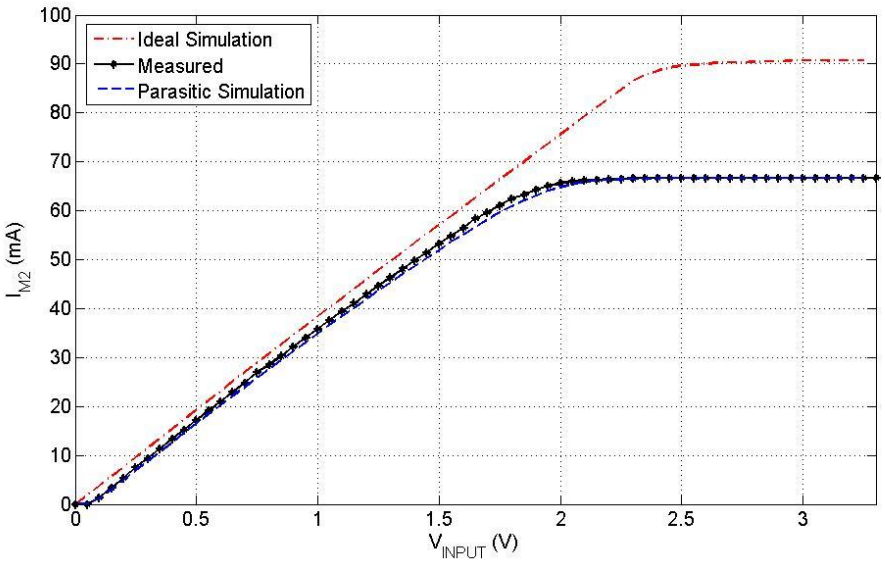

Figure 4-36 – I_{M2} response comparison between ideal simulation, simulation with parasitic and measurement

4.8.2. AC Characteristics

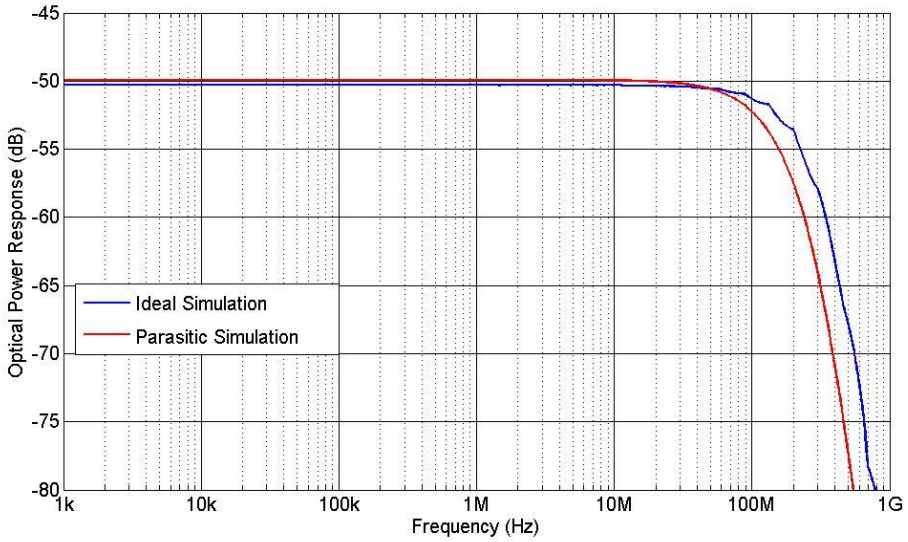

Figure 4-37 – Small signal bandwidth between ideal simulation and simulation with parasitic

The bandwidth of the microLED/CCFBK driver was shown that it varies depending on the range of V_{INPUT} and its bias point (Section 4.7.3). To illustrate the difference between the simulated and measured result, V_{INPUT} of 1V peak-to-peak and 1V bias point was chosen in this section. The small signal bandwidth of the microLED/CCFBK driver was re-simulated.

The difference between the ideal simulation and parasitic simulation was studied. This is shown in Figure 4-37 where the frequency response of the optical power of the microLED/CCFBK driver is plotted. The figure shows that the small signal bandwidth drops from 190MHz in the ideal simulation to 135MHz. This is as expected as the load capacitance at the output of the driver increases due to the additional parasitic capacitance.

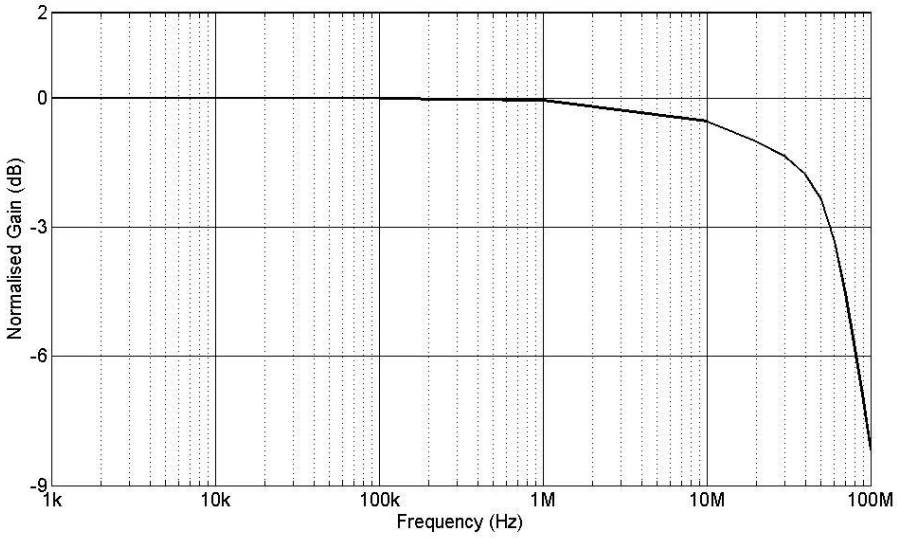

Figure 4-38 – Simulated large signal bandwidth of microLED/CCFBK driver (with parasitic)

The large signal bandwidth on the other hand, was expected to be lower than the small signal bandwidth, as discussed in Section 4.5.4. Figure 4-38 shows the simulated large signal bandwidth of the parasitic microLED/CCFBK driver which shows a bandwidth of 58MHz. This is higher than the measured result of 49MHz, which suggests that the output parasitic capacitance is higher than the chosen estimated value, as shown in Table 4-8. To model the uncertainty parasitic capacitance value, additional capacitance was added to the output of the CCFBK driver, in parallel with the microLED. With the additional capacitance, the parasitic simulation shows a large signal bandwidth of 50MHz, which is similar to the measured results. Possible causes for the additional output parasitic capacitance include:

1) Gold bumps have higher capacitance than expected
2) MicroLED exhibits higher capacitance due to process variations
3) Additional capacitance between the metal contact on CMOS driver to the gold bump and microLED contacts

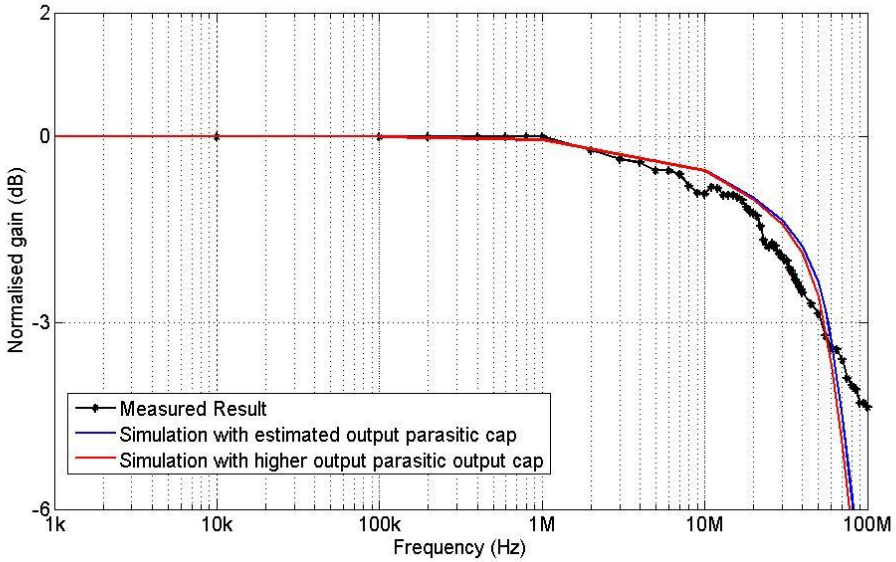

Figure 4-39 – Large signal bandwidth comparison between simulation and measured result

4.9. Summary

The microLED/CCFBK driver was presented in this chapter. The purpose of the driver was to implement the OFDM scheme to increase data transmission rate. The chapter discussed the negative feedback theory, the macromodel and transistor level of the driver. An 80µm diameter round microLED was bump-bonded with the CCFBK driver. The driver was capable of driving the microLED with current up to 67mA. The bandwidth of the driver was measured to be about 30 MHz to about 70 MHz depending on the input voltage peak-to-peak and the bias point.

The main aim of the design was to supply the microLED with a linear current response to the input signal. This was achieved with non-linearity of the current produced by the microLED/CCFBK driver which was found to be only 3.98%. Although the linearity of the current produced by the microLED/CCFBK driver was good, the optical power was still inherited by the non-linearity of the microLED L-I characteristic. The linearity, however, can be improved by reducing the V_{INPUT} peak-to peak-signal. The non-linearity of the optical power was shown to reduce from 12.18% with an optical power range of 3.3mW to 1.46% with an optical power range of 1mW. Further measurement of the microLED/CCFBK characterisation, including its performance in transmitting data, will be discussed in Chapter 6.

Chapter 5 : MicroLED/CMOS Optical Feedback Driver

5.1. Introduction

An analogue microLED/CMOS driver was presented in Chapter 4. The driver, called the CCFBK driver, was designed to supply the microLED with current linearly proportional to the input voltage signal. As discussed in the previous chapter, even though the CCFBK driver exhibits a linear current response with respect to the input voltage signal, the optical power output response does not. Chapter 2 discusses the importance of a linear output (optical power in an optical transmitter) if a high quality OFDM is to be implemented. A 'linear optical driver' in turn, would offer a lower BER than its 'non-linear optical driver' counterpart. This chapter presents the second analogue driver that was designed during the project which was aimed to improve the performance of the previous driver by linearizing the optical power instead of current. The optical power linearization concept, macromodel and transistor level design of the driver, together with simulations, are presented in this chapter. The measured results are presented, compared with simulations and discussed at the end of the chapter.

5.2. Overview

The microLED/CCFBK driver was presented in Chapter 4 which has shown that the optical power output of the driver was not linear due to the inherent non-linear current-to-optical power conversion by the microLED as discussed in Chapter 3. While reducing the output range of the microLED/CCFBK driver showed improvement on linearity, it also decreases the PAPR which is also required to be high for a good OFDM. To overcome the problem, a technique called 'optical feedback' was proposed to linearize the optical power of the microLED without sacrificing PAPR.

The CMOS Optical Feedback (COFBK) driver was aimed to linearize the optical power output proportionally to the input voltage signal. As with 'current feedback', the name 'optical feedback' refers to the technique of driving the microLED where a small proportion of the light produced by the microLED is fed back to the input for linearization correction. Figure 5-1 shows a simple flow chart illustrating the main difference in operation between CCFBK

and COFBK driver, where the negative feedback network is formed by sending a portion of the emitted light signal (rather than current) back to the input.

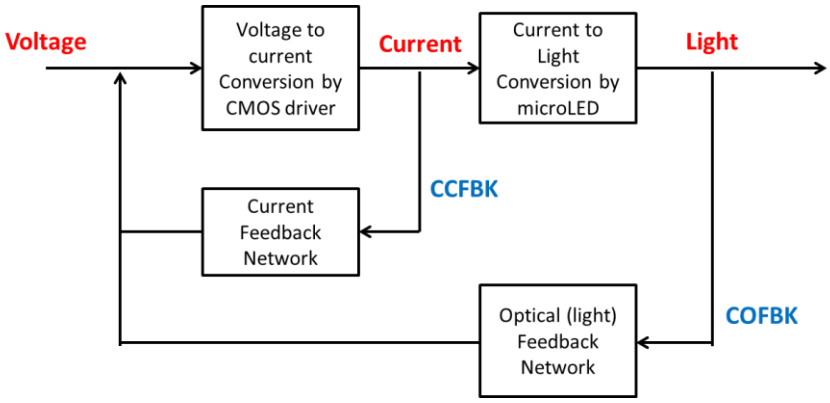

Figure 5-1 – Flow chart operation of CCFBK driver and OFBK driver

5.2.1. Target Specification

The target specification of the microLED/COFBK driver is given as below and is summarised in Table 5-1

1. **Analogue Modulation** – The driver should perform analogue modulation in order to implement OFDM. Optical power output from the microLED/COFBK driver was expected to be linearly proportional to the input voltage signal.
2. **Pixel pitch** – The pixel area (not including photodiode) was specified to be 100µm by 100 µm, the same as the digital driver and the microLED/CCFBK driver.
3. **Driving Current**– Driving current up to 100mA was specified. This decision was made based on two factors:
    a. Pixel area constraint due to the need for extra circuitry for the feedback light detection.
    b. CCFBK driver was also specified to drive up to 100mA. The same driving current was specified for the COFBK driver to serve as a performance comparison specifically in the linearity of the optical power output.
4. **Bandwidth** – A bandwidth of 100MHz was specified for the COFBK driver. This is the same as the CCFBK driver.
5. **BER** – BER is specified to be less than 10^{-3}. This is in accordance with the FEC limit for standard correction mechanism.
6. **Optical Power Dynamic Range** – A microLED driven with 100mA current is expected to produce about 4.5mW of optical power (Section 3.4.2). Unlike the

CCFBK driver where linearity can be improved by reducing the optical power range, the COFBK driver is expected to produce high linearity over a wider range.

Parameter	Value
Signal type	Analogue
Pixel Pitch (not including photodiode)	100µm x 100µm
Driving current	100mA
Optical Power	4.5mW
Bandwidth	100MHz
BER	$< 10^{-3}$
MicroLED optical power dynamic range	0 - 4.5mW

Table 5-1 – Summary table of the target specifications for microLED/COFBK driver

5.3. Optical Feedback Concept

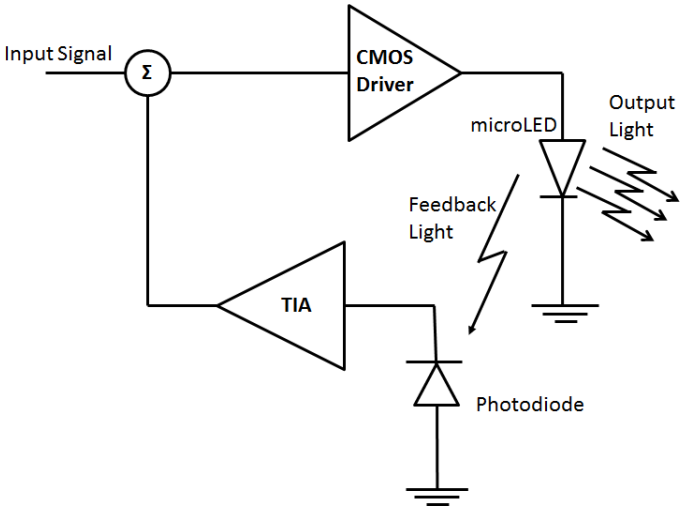

Figure 5-2 – Optical feedback driver concept

Figure 5-2 illustrates the concept of an optical feedback driver which is based on a negative feedback technique (Section 4.3, Figure 4-1). The CMOS driver and microLED in Figure 5-2 represent the feedforward network while the photodiode and Transimpendace Amplifier (TIA) represent the sensing and feedback network. Therefore the optical feedback is a Light Voltage Feedback topology. Moreover, the Light Voltage Feedback topology was chosen because of the availability of a wide bandwidth voltage signal generator. Thus, the microLED/CMOS driver can itself be driven without any signal conversion which would require extra circuitry that could affect the linearity of the input signal.

5.3.1. Light Detection Mechanism

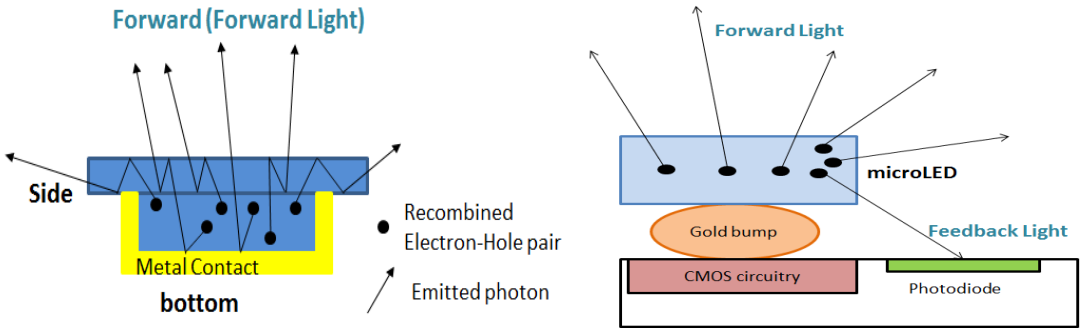

(a) (b)

Figure 5-3 – Schematic cross-section illustration of (a) light radiated from microLED and (b) microLED, CMOS and photodiode integration in a single pixel

The generation of light by microLED was explained in Chapter 2 where the recombination of an electron-hole pair emits a photon. These photons are emitted in all directions. Figure 5-3(a) shows a simple illustration of the emission of the photons generated by a microLED. A metal layer is added around the microLED for two purposes; primarily as a contact with the bump-bond and also as a reflector to direct photons "forward". A Measurement was conducted by Dr. Jonathan McKendry of the IoP to quantity the ratio of the "forward" light to the total light produced $\left(\frac{\text{Forward Light}}{\text{Total Light}}\right)$ by a bare microLED die [106]. It was found that 65% of light was emitted "forward" while the other 35% was "leakage" either to the side or bottom of the die. The distribution of the "leakage" light from the side or bottom of the microLED was not measured due to limitations of the measuring equipment.

The optical feedback is achieved by directing a small sample of the light emitted by the microLED towards the photodiode. Taking advantage of the "leakage" light (Feedback light), the light feed-back is done on-chip by integrating the microLED, CMOS circuitry and photodiode within a single pixel as shown schematically in Figure 5-3(b). The COFBK driver described here is the first CMOS drive IC for the microLED that integrates a CMOS photodiode within the pixel to improve the linearity of the microLED optical power output response by means of optical feedback in order to achieve greater OFDM performance for VLC applications.

The optical characteristics (microLED and photodiode) of the feedback system contribute significantly to the performance of the microLED/COFBK driver. These parameters are:

1. **MicroLED responsivity (L-I Characteristic)** - The microLED L-I characteristic, as presented in Chapter 3, is not linear. Because the microLED was still in fabrication during the design of the COFBK driver, the non-linearity of the microLED L-I characteristic was modelled based on the results obtained from measurements conducted on the previous batch of microLED that was fabricated for the Generation IV CMOS driver (Figure 3-7).
2. **Feedback Light detection**- Or the leakage light was the main uncertainty parameter in the optical feedback design. The detection of the leakage light depends on the geometrical location and structural design of the photodiode. Further details are discussed in Section 5.5.2.
3. **Responsivity of the photodiode** –Defined as the current output per optical power. The responsivity depends on the structure of the photodiode and process technology.

The microLED was fabricated at the IoP, therefore the microLED L-I characteristic and responsivity are determined by the process parameters and structure chosen and implemented by the IoP. As discussed in Chapter 3, the responsivity of the microLED was predicted to be two times greater than its predecessor. Therefore, for a 100mA driving current, the maximum optical power output was expected to be around 4.5mW (Figure 3-7). The photodiode on the other hand, while the responsivity mainly depends on the foundry process parameters, the type chosen and its layout also provide significant effects. Furthermore, the geometrical location of the photodiode also determines how much of the "leakage" or the feedback light from the microLED can be captured. Table 5-2 summarises the optical parameters and its dependencies that could affect the performance of the microLED/COFBK driver.

Parameter	Dependencies	Controllable parameter?
MicroLED responsivity and L-I characteristic	MicroLED design structure and process	No. Determined by IoP
Photodiode Responsivity	Foundry Silicon parameters and structural design	Parameters determined by the foundry. However, the design structure can have a significant effect
Leakage Light detection	Geometric location and structural design of photodiode	Yes

Table 5-2 – Summary of optical parameters for the microLED/COFBK driver

5.4. Proposed CMOS Optical Feedback Driver

5.4.1. Design Overview

Figure 5-4 illustrates the proposed microLED/COFBK driver. An input voltage signal (V_{INPUT}) is applied to the non-inverting input of the operational amplifier (OP1). The output of OP1 sets the gate voltage of n-channel MOSFET (M1), which is biased to operate in the saturation region. The current produced by M1 feeds the microLED hence, light is emitted. The majority of the light is emitted in the "forward" direction while some of the light is emitted in other directions. A portion of the "leakage" light is detected by the photodiode hence producing photogenerated current. The current produced by a photodiode, in general, can be said as linearly proportional to the received light [107, 108, 109] and is converted to a voltage by the TIA where the gain of the TIA is set by R_{TIA}. The output voltage from the TIA is passed through R_F into the inverting input (V_{FB}) of OP1. The high gain of OP1 regulates the gate voltage of M1, pre-distorting the current produced by M1, so that the light produced by the microLED tends to drive the error voltage between the V_{INPUT} and V_{FB} to zero. This consequently causes the microLED to produce light which is linearly proportional to V_{INPUT}. M1 is designed so that it is able to produce drive current up to 100mA. Like the digital driver and CCFBK driver (Section 3.4.3 and Section 4.4.1), the microLED cathode is connected to a separate DC supply (LED_GND) to bias the microLED above its threshold voltage.

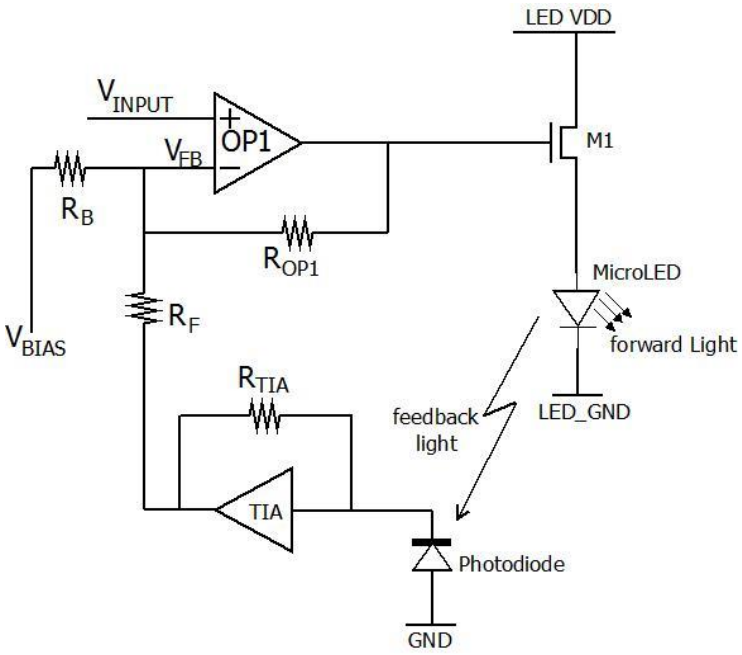

Figure 5-4 – Proposed microLED/CMOS Optical Feedback (COFBK) driver

Figure 5-5 sketches the expected difference between the current response and optical power response between the microLED/CCFBK driver and the microLED/COFBK driver. In the CCFBK driver (Figure 5-5 (a)), the current is linear to V_{INPUT}, but produces a distorted optical power response due to the inherently non-linear L-I characteristic of the microLED. The COFBK driver (Figure 5-5 (b)), on the other hand, pre-distorts the current supplied to the microLED so that it linearizes the optical power response.

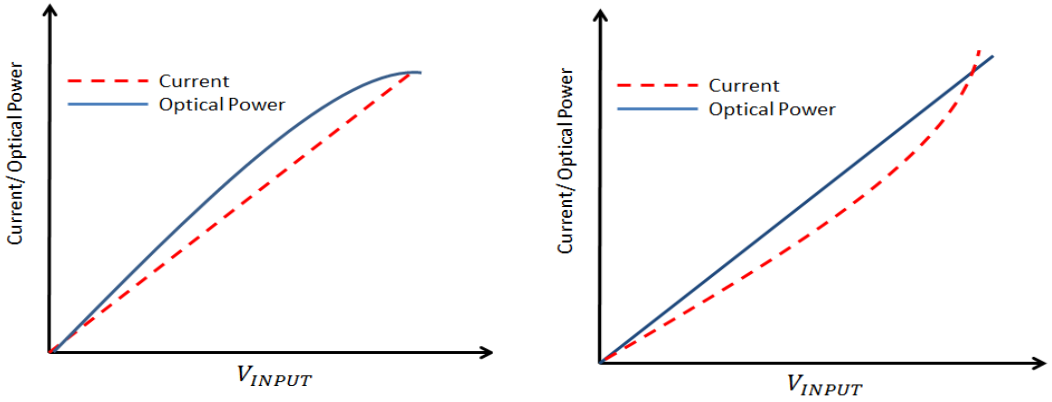

(a) **(b)**

Figure 5-5 – Expected current and optical power response of (a) CCFBK driver and (b) COFBK driver

5.4.2. Optical Feedback Node Analysis

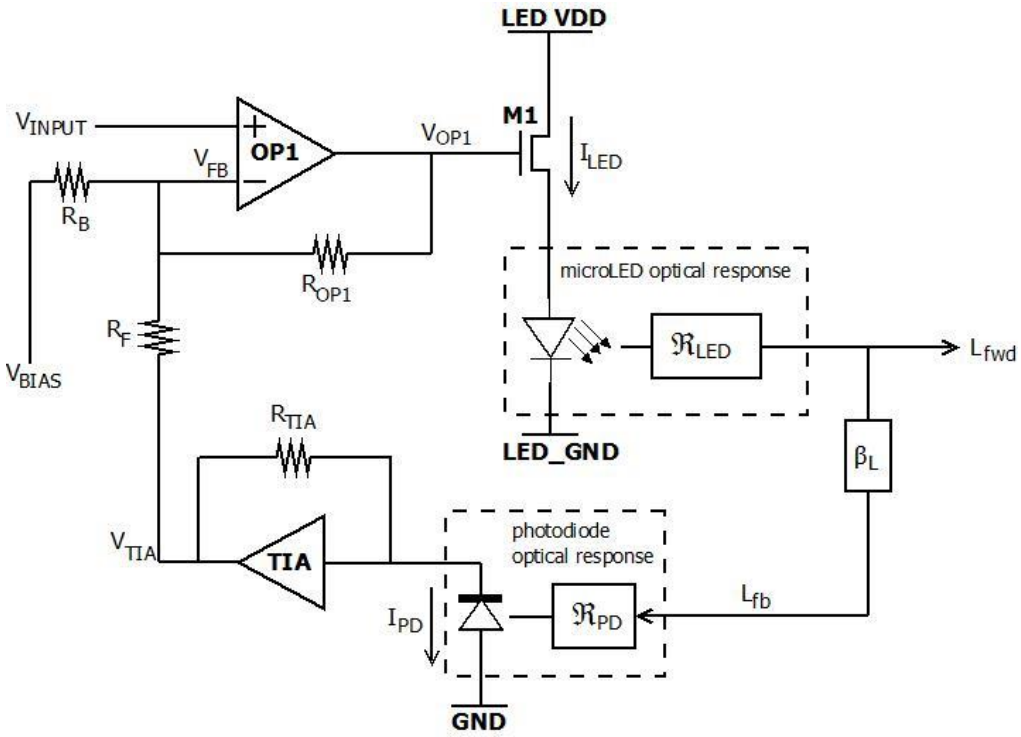

Figure 5-6 – Optical feedback analysis

The feedback operation can be analysed using the configuration shown in Figure 5-6. $R_B$and V_{BIAS} are excluded to simplify the circuit analysis. The optical channel is represented by three parameters:

- $\mathfrak{R}_{LED}$ - The microLED current-to-optical power response for the "forward" light (L_{fwd}), represented by the non-linear transfer function of the microLED L-I characteristic.
- β_L - The ratio of the "feedback" light (L_{fb}) to L_{fwd}. Therefore, $\beta_L$is a constant value of less than 1.
- $\mathfrak{R}_{PD}$ - The responsivity of the photodiode which is represented by the linear transfer function of the optical power-to-current (I-L) characteristic of the photodiode [107, 108, 109]

Using Kirchhoff's Current Law, V_{FB} node can be written as

$$\frac{V_{OP1} - V_{INPUT}}{R_{OP1}} + \frac{V_{TIA} - V_{INPUT}}{R_F} = 0 \qquad \textbf{Equation 5-1}$$

where V_{OP1} is the output voltage of OP1 and V_{TIA} is the output voltage of the TIA. R_F and R_{OP1} are the feedback resistance of OP1. Rearranging Equation 5-1 then

$$V_{INPUT}\left(\frac{R_{OP1} + R_F}{R_{OP1}R_F}\right) = \frac{V_{OP1}}{R_{OP1}} + \frac{V_{TIA}}{R_F} \qquad \textbf{Equation 5-2}$$

V_{OP1} sets the gate voltage of M1 which produces current I_{LED} that drives the microLED. I_{LED} can be approximated as

$$I_{LED} = V_{OP1}.g_{m\_M1} \qquad \textbf{Equation 5-3}$$

where g_{m_M1} is the transconductance of M1. The optical power (L_{fwd}) produced by the microLED is estimated by $\mathfrak{R}_{LED}$, as shown in Equation 5-4

$$L_{fwd} = \mathfrak{R}_{LED}I_{LED} \qquad \textbf{Equation 5-4}$$

L_{fb} is a portion of L_{fwd} ($L_{fb} = \beta_L L_{fwd}$, where $\beta_L < 1$), sensed by a photodiode, generating photogenerated current (I_{PD}), which is then amplified and converted into a voltage by TIA. Therefore, the optical to voltage conversion at the feedback network can be described by Equation 5-5 and Equation 5-6

$$I_{PD} = \Re_{PD} L_{fb} = (\Re_{PD}\beta_L) L_{fwd} \quad \textbf{Equation 5-5}$$

$$V_{TIA} = I_{PD} R_{TIA} \quad \textbf{Equation 5-6}$$

where R_{TIA} is the feedback resistor, which also represents the transimpedance gain of the TIA. Combining Equation 5-2 with Equation 5-3, Equation 5-5 and Equation 5-6, the output of the feedback system (L_{fwd}) can be written with respect to V_{INPUT} as

$$V_{INPUT}\left(\frac{R_{OP1} + R_F}{R_{OP1} R_F}\right) = \frac{L_{fwd}}{R_{OP1}\left(g_{m\_M1} R_{LED}\right)} + \frac{R_{TIA}(\Re_{PD}\beta_L)\left(L_{fwd}\right)}{R_F} \quad \textbf{Equation 5-7}$$

Rearranging Equation 5-7 and assuming $\frac{R_{OP1}}{R_F} \gg 1$, the transfer function of the feedback system can be defined as

$$\frac{L_{fwd}}{V_{INPUT}} = \frac{\left(\frac{R_{OP1}}{R_F}\right) g_{m\_M1} \Re_{LED}}{1 + \left[\left(\left(\frac{R_{OP1}}{R_F}\right) g_{m\_M1} \Re_{LED}\right)(R_{TIA} \Re_{PD} \beta_L)\right]} \quad \textbf{Equation 5-8}$$

Comparing Equation 5-8 and the feedback system closed loop transfer function (Equation 4-2), the feedforward gain, feedback factor and the loop gain of the system is defined by Equation 5-9, Equation 5-10, and Equation 5-11 respectively.

$$\text{Feedforward gain, } \alpha = (A_V) g_{m\_M1} \Re_{LED} \quad \textbf{Equation 5-9}$$

Where $A_v = \left(\frac{R_{OP1}}{R_F}\right)$, represents the gain of OP1

$$\text{Feedback factor, } \beta = R_{TIA}(\Re_{PD}\beta_L) \quad \textbf{Equation 5-10}$$

$$\text{Loop gain, } \alpha\beta = \left((A_V) g_{m\_M1} \Re_{LED}\right)\left(R_{TIA}(\Re_{PD}\beta_L)\right) \quad \textbf{Equation 5-11}$$

Assuming that $\alpha\beta \gg 1$, the closed loop gain can be approximated as

$$\text{Closed loop gain} \approx \frac{1}{\beta} \approx \frac{1}{R_{TIA}(\Re_{PD}\beta_L)} \qquad \textbf{Equation 5-12}$$

The feedback transfer function (Equation 5-8) includes OP1, M1, microLED, photodiode and TIA in the equation. These components have their own associated bandwidth and therefore, they contribute to the frequency characteristic of the feedback system. In order to understand the influence of these components, Equation 5-8 is rewritten as

$$H = \frac{A_{ff}}{1 + A_{ff}\beta_{fb}} \qquad \textbf{Equation 5-13}$$

where A_{ff} is the gain in the feedforward network (OP1, M1 and microLED) and β_{fb} is the gain in the feedback network (photodiode and TIA). The bandwidth of the feedforward network is limited by OP1 while in the feedback network, the bandwidth is limited by the TIA. To simplify the analysis, only the dominant pole for each of the feedforward and feedback network is considered. Therefore, Equation 5-13 can be re-written as

$$H = \frac{\dfrac{A_{ff}}{1 + \dfrac{s}{\omega_{ff}}}}{1 + \left(\dfrac{A_{ff}}{1 + \dfrac{s}{\omega_{ff}}}\right)\left(\dfrac{\beta_{fb}}{1 + \dfrac{s}{\omega_{fb}}}\right)} \qquad \textbf{Equation 5-14}$$

Where $1 + \frac{s}{\omega_{ff}}$ and $1 + \frac{s}{\omega_{fb}}$ are the cut-off frequencies of the feedforward network and the feedback network respectively. Rearranging Equation 5-14 gives

$$H = \frac{A_{ff}\left(1 + \dfrac{s}{\omega_{fb}}\right)}{\left(1 + s\left(\dfrac{1}{\omega_{ff}} + \dfrac{1}{\omega_{fb}}\right) + \dfrac{s^2}{\omega_{ff}\omega_{fb}}\right) + A_{ff}\beta_{fb}} \qquad \textbf{Equation 5-15}$$

$$H = \frac{A_{ff}}{1 + A_{ff}\beta_{fb}}\left(\frac{\left(1 + \dfrac{s}{\omega_{fb}}\right)}{1 + \dfrac{1}{1 + A_{ff}\beta_{fb}}\left(s\left(\dfrac{1}{\omega_{ff}} + \dfrac{1}{\omega_{fb}}\right) + \dfrac{s^2}{\omega_{ff}\omega_{fb}}\right)}\right) \qquad \textbf{Equation 5-16}$$

Equation 5-16 shows two parts where the left part of the equation (outside the main bracket) is the closed loop gain at low frequencies (as predicted in Equation 5-8) while the right part (within the main bracket) shows the frequency response of the transfer function. Equation 5-16 also shows that there exists a zero in the feedback system due to the pole in the feedback network. Therefore, the bandwidth of the feedback network needs to be greater than that of the feedforward network in order to minimise any gain-peaking in the frequency response.

5.5. Macromodel

5.5.1. Photodiode and Transimpedance Amplifier

The photodiode, as illustrated in Figure 5-7, is modelled by a VCCS, which represents the photogenerated current (I_{PD}) due to the impingement of photons on the photodiode active area. The optical power level is represented as a voltage level in the model. Dark current is the leakage current that flows through a photodiode under the no-light condition which is produced by thermally generated carriers in the diode and is modelled here by a parallel resistor R_{SH}. R_{SH} is very large and usually has little effect on the bandwidth of the photodiode [77]. R_S is the series resistance and is usually very small compared to the feedback resistance of the TIA (R_{TIA}). Therefore, R_{TIA} normally dominates the input resistance of a photodiode.

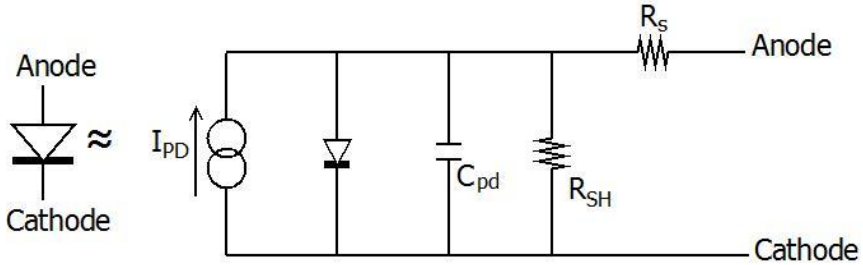

Figure 5-7 – Photodiode model

From Equation 2-15, the –3dB bandwidth of the photodiode can be estimated as

$$f_{3dB\_photodiode} = \frac{1}{2\pi(C_{PD} + C_{in\_A})R_{in\_A}} \qquad \textbf{Equation 5-17}$$

where C_{in_A} and R_{in_A} are the input capacitance and resistance of TIA respectively and C_{PD} is the photodiode junction capacitance. C_{PD} can be estimated by calculating the junction potential across the p-n junction (ϕ_i in Equation 2-18), the depletion width of the p-n junction (X_d in Equation 2-17) and the photodiode area.

A semiconductor photodiode relies on the absorption of incident photons with energy greater than the semiconductor bandgap energy. Light energy is absorbed and decays as they travel in the semiconductor. The decay is determined by the absorption coefficient, α, which is a material property and is different for different wavelengths and materials, as shown in Figure 5-8 [77, 110]. Short wavelength light, which is the case for a microLED with a 450nm wavelength, exhibits stronger absorption, so is absorbed closer to the photodiode surface. Because of the shallow penetration depth, a shallow junction n+/p-substrate type photodiode was chosen for the COFBK driver. The n+ junction depth in the AMS 0.35µm process is 0.2 µm, which is greater than the penetration depth of light with a 450nm wavelength [111].

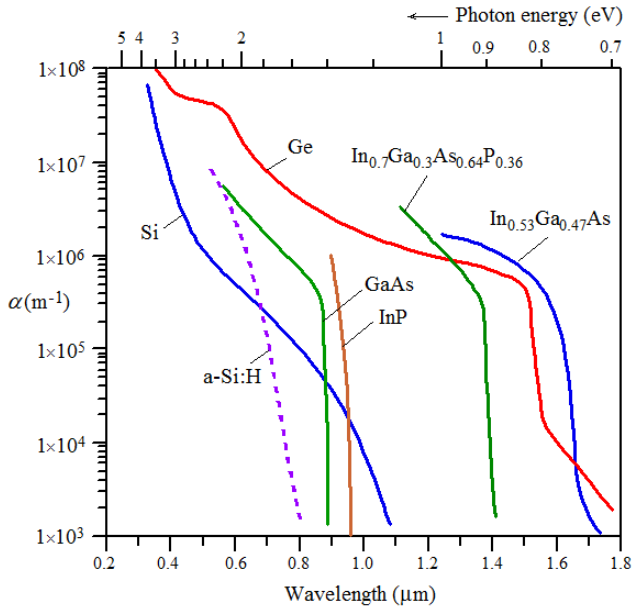

Figure 5-8 – Absorption coefficients for different materials [77, 110]

For the AMS 0.35µm process technology, the p-substrate doping level (N_P) is 212 x 10^{15} cm^{-3} and the shallow n+ has an impurity concentration (N_N) of around 3.3 x 10^{19} cm^{-3} [89, 112]. Using this information, ϕ_i was estimated to be 0.99V. With the ϕ_i known, and the applied reserve bias voltage (ΔV) of 0.9V was chosen, X_d was then calculated using Equation 2-17 to be ≈ 108nm.

The photodiode layout is designed as a rectangular with dimensions of 100µm x 30µm. The selection of these dimensions is discussed later in Section 5.7.1. For the chosen photodiode dimension, C_{PD} was estimated to be 2.8pF using Equation 2-16. To reserve some margin, C_{PD} of 3pF was used in the model for simulation. The responsivity of a CMOS photodiode ($\Re_{PD}$) is low for shorter wavelength (< 600nm), which is again due to lower α in silicon. The

theoretical maximum responsivity for a 450nm wavelength light is 0.23A/W. For N+/p-substrate type photodiode, reports have shown that the responsivity varies from 0.05A/W to 0.15A/W, depending on the process technology and the implemented structure [113, 114]. $\Re_{PD}$ of 0.1A/W was chosen for the model and used in the simulation.

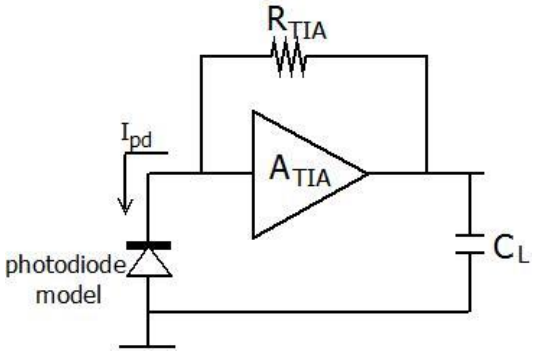

Figure 5-9 – TIA structure

A schematic structure of the TIA is illustrated in Figure 5-9. The TIA is based on an inverting voltage amplifier with open-loop gain (A_{TIA}) and a feedback resistor(R_{TIA}) is connected in shunt configuration. The TIA is a voltage-voltage feedback type, therefore the actual current to voltage conversion occurs on R_{TIA}. The advantage of using this type of TIA is that it reduces the input and output impedances of the voltage amplifier by A_{TIA} [115]. Therefore, the voltage amplifier does not load the photodiode and higher bandwidth can be achieved.

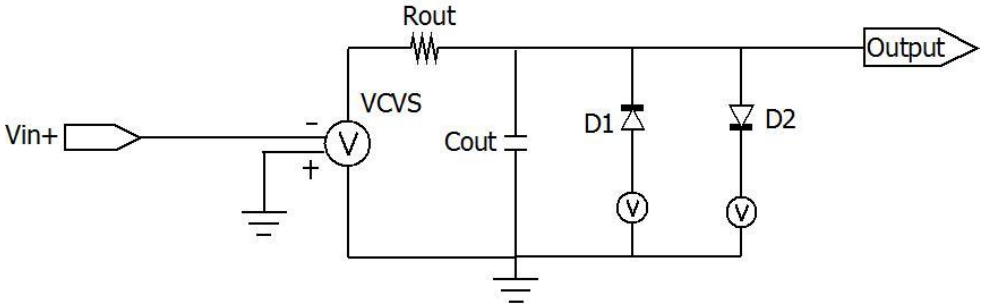

Figure 5-10 – Voltage amplifier macromodel

A macromodel of the voltage amplifier is shown in Figure 5-10. Connected to the input amplifier is the VCVS, representing A_{TIA} of the voltage amplifier. R_{out} and C_{out} creates a low pass filter at the output, representing the voltage amplifier output impedance, and sets the bandwidth. Diode D1 and D2 set the minimum and maximum output voltage from the amplifier respectively. The minimum output voltage is set to be 0 and the maximum is 3.3 as appropriate for the chosen process technology.

The junction capacitance of the photodiode plays an important role in determining the bandwidth of the TIA. For a voltage amplifier with high A_{TIA} and small R_{out}, the closed loop gain of the TIA can be written as [107]

$$\frac{V_{out}}{I_{PD}} = \frac{R_{TIA}}{1 + s\left(\frac{R_{TIA}.C_{in}}{A_{TIA}} + \frac{R_{out}C_{out}}{A_{TIA}}\right) + s^2\left(\frac{R_{TIA}C_{in}R_{out}C_{out}}{A_{TIA}}\right)} \qquad \textbf{Equation 5-18}$$

where C_{in} is the total capacitance at the input of the TIA including C_{PD} while C_{out} is the total capacitance of the output of the TIA including the load capacitance C_L. Equation 5-18 above can be manipulated in order to separate the poles from the input and output impedance. This is written as

$$\frac{V_{out}}{I_{PD}} = \frac{R_{TIA}}{\left(1 + s\frac{R_{TIA}C_{in}}{A_{TIA}}\right)\left(1 + s(R_{out}C_{out})\right)} \qquad \textbf{Equation 5-19}$$

Based on Equation 5-19, the input or output impedance can be the dominant pole in the frequency response. In this case, C_{in} is larger compared to C_{out} as it includes the relatively large C_{PD}. Furthermore, R_{TIA} (which determines the gain of the TIA) is also much larger thanR_{out}. Therefore, the output pole is placed at a much higher frequency than the input pole. Thus, the bandwidth of the TIA is determined by the input pole of the closed loop transfer function and can be estimated as

$$BW_{TIA} = \frac{A_{TIA}}{2\pi(R_{TIA}C_{in})} \qquad \textbf{Equation 5-20}$$

From Equation 5-20, it can be concluded that the bandwidth of the TIA is mainly limited by C_{PD} and R_{TIA}. The bandwidth, however, can be improved by having a voltage amplifier with a larger A_{TIA}. Figure 5-11 shows an AC simulation of the TIA with A_{TIA} of 1000, driving a 100fF load and varying R_{TIA}. R_{TIA} values of 10kΩ, 20kΩ, and 50kΩ were chosen, showing a mid-band gain of 80 dB, 86 dB, and 94 dB respectively. From the simulations, the bandwidth was found to be 1.06GHz, 751MHz, and 469MHz respectively. As expected, the gain of the amplifier is equal to R_{TIA} and the bandwidth decreases as R_{TIA} increases, as predicted in Equation 5-20. An important point to note in Figure 5-11 is the gain peaking which occurs for all TIA gain configurations.

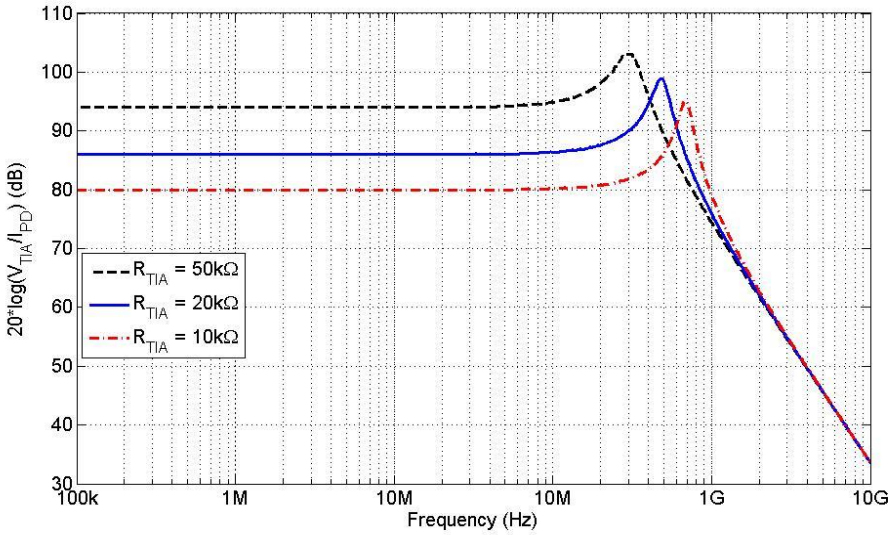

Figure 5-11 – Changing the gain of TIA by sweeping R_{TIA}

The gain peaking occurs because the phase margin of the loop gain of the TIA may be less than 60° (as explained in Section 4.4.3), which indicates that the TIA is either marginally stable or unstable. The gain peaking effect can be reduced by including a feedback capacitor (C_{TIA}) in parallel with R_{TIA}. Figure 5-12 shows the effect of increasing C_{TIA} on the gain peaking response. Note that the peaking is reduced as C_{TIA} is increased. However, this comes at a cost of reducing the overall bandwidth of the TIA. In Figure 5-12, the gain-peak is eliminated when C_{TIA} of 18fF was inserted into the TIA with R_{TIA} of 20kΩ. The overall TIA bandwidth was reduced from 751MHz to 514MHz. Table 5-3 summarises the value of the TIA macromodel in this thesis.

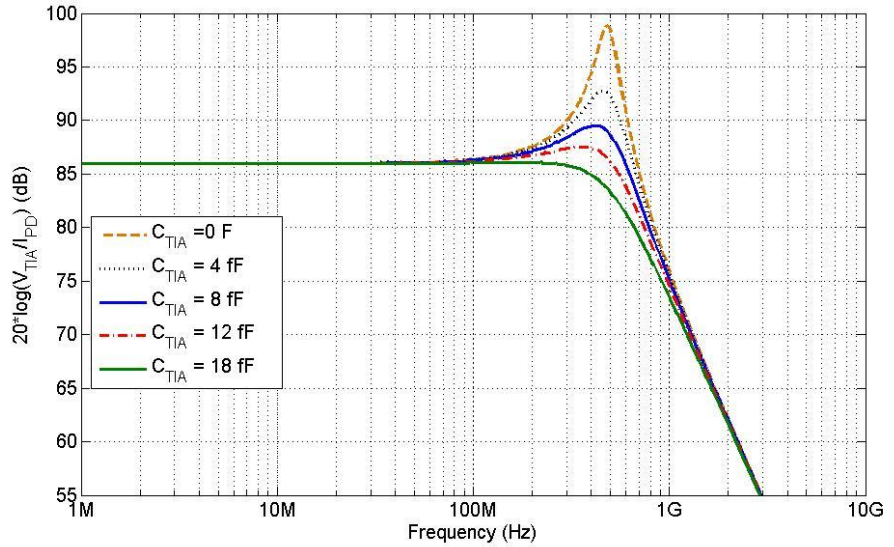

Figure 5-12 – Effect of C_{TIA} on the gain peaking

Description	Value
Photodiode junction capacitance , C_{PD}	3pF
Voltage amplifier gain, A_{TIA}	1000
TIA feedback resistor , R_{TIA}	20kΩ
TIA feedback capacitor, C_{TIA}	18fF
TIA gain	20 000
TIA Bandwidth	514MHz

Table 5-3 – Summary of parameters used in the TIA macromodel

5.5.2. CMOS Optical Feedback Driver

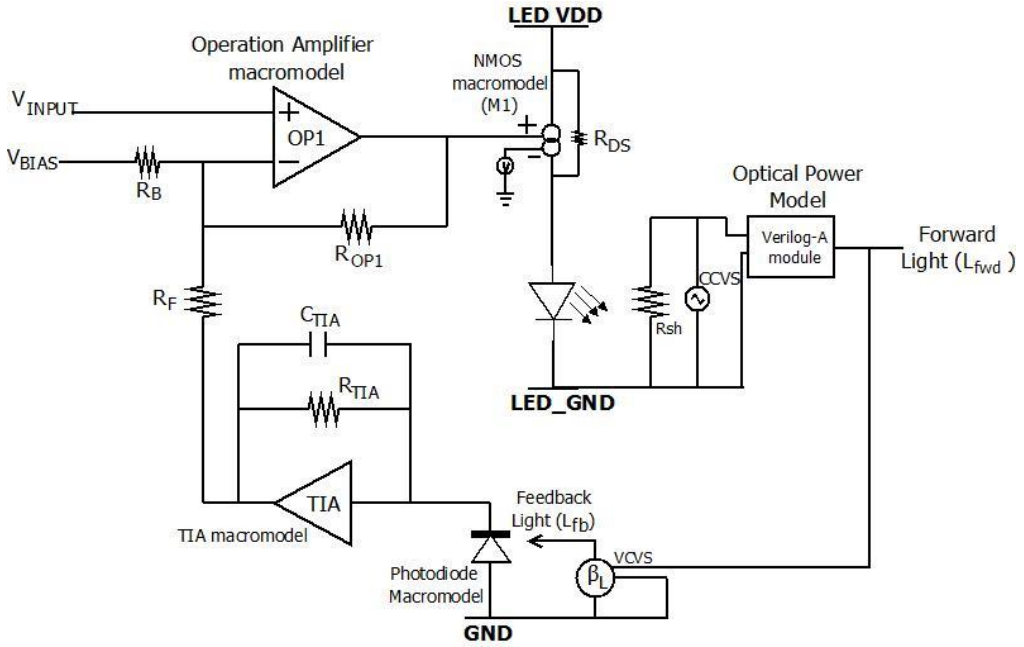

Figure 5-13 – Macromodel of CMOS Optical Feedback (COFBK) driver

Figure 5-13 shows the macromodel of the microLED/COFBK driver used in the simulation which consists of:

- Operational amplifier macromodel (OP1)
- n-channel MOSFET macromodel (M1)
- microLED model
- Optical power (current to light) conversion Verilog-A model
- Photodiode model
- And TIA macromodel

The macromodel for OP1 and MOSFET M1 were discussed in Section 4.4.2 while the microLED model and optical power conversion Verilog-A model were discussed in Section 3.4.2. The photodiode model and TIA macromodel were discussed earlier in this chapter

(Section 5.5.1). The COFBK driver is expected to be able to produce current driving the microLED up to 100mA. With this information, g_{m_M1} is calculated to be about 71mS using Equation 4-10. Therefore, from Equation 4-11, g_{m_VCCS} of 35mS is used in the COFBK driver macromodel. The parameters for OP1 are the same as presented in Section 4.4.2.

Figure 5-6 and Equation 5-8 show that $\Re_{LED}$ and β_L are important in determining the closed loop gain of the feedback system. $\Re_{LED}$ is presented in the macromodel by the Optical power conversion Verilog-A model. The Verilog-A model is essential in the microLED/COFBK driver macromodel simulation for two reasons:

1. It provides an estimated gain coefficient of the current to optical power conversion
2. It inserts the estimated non-linear characteristic of the microLED into the model

β_L, on the other hand, is represented by a VCVS and is modelled based on an assumption that the ratio of $\frac{L_{fb}}{L_{fwd}}$ is constant at any optical power level. This implies that L_{fb} would increase proportionally as L_{fwd} increases. Therefore the light in the feedback path (L_{fb}) that impinges on the photodiode is β_L times lower than L_{fwd}. For a microLED with 100mA driving current, L_{fwd} is expected to be about 4.5mW. As mentioned in Section 5.3.1, L_{fwd} is only 65% of the total optical power produced by the microLED, while the other 35% is "leaked" to the sides. Therefore, the side emitting "leakage" light (L_{side}) can be estimated as

$$L_{side} = \frac{0.35 \times L_{fwd}}{0.65} \approx 2.42\ mW \qquad \textbf{Equation 5-21}$$

A square microLED is bonded onto the COFBK driver. Assuming that the amount of light leaked to each side is equal, then L_{fb} can be written as Equation 5-22

$$L_{fb} = \frac{L_{side}}{4} \approx 605\mu W \qquad \textbf{Equation 5-22}$$

Therefore, the ratio of feedback light to feedforward light can be estimated as

$$\beta_L = \frac{L_{fb}}{L_{fwd}} \approx 0.13 \qquad \textbf{Equation 5-23}$$

For the macromodel simulation, a slightly conservative value of 0.1 was chosen for β_L to reserve some margin for overestimation.

The input of the TIA is biased at 0.9V and the output of the TIA is forced to be equal to its input by R_{TIA}. Assuming that L_{fb} is 605µW and $\Re_{PD}$ of 0.1A/W (Section 5.5.1) is chosen, the current generated by the photodiode (I_{PD}) can be estimated to be 60.5µA. Supposing that V_{TIA} increases by 1V for I_{PD} of 60µA, than R_{TIA} can be calculated to be

$$R_{TIA} = \frac{\Delta V_{TIA}}{I_{PD}} \approx 16.5\ k\Omega \qquad \textbf{Equation 5-24}$$

For the macromodel simulation, R_{TIA} of 20kΩ is chosen. This is again to "boost" V_{TIA} supposing that the calculated β_L and $\Re_{PD}$ were overestimated.

The combination of R_B and R_F shifts the DC output point of the TIA, which is controlled by V_{BIAS} node. This allows the DC operating point of the microLED/COFBK driver to be biased at its optimum point. R_{OP1}, together with R_B and R_F set the forward gain of OP1. Table 5-4 summarises the parameter values used in the macromodel simulation. Using these values (as summarised in Table 5-3 and Table 5-4), DC and AC simulations were conducted to investigate how the parameter values influence the performance of the microLED/COFBK driver.

Parameter	Description	Value
A_V	Operational amplifier open loop gain	1000
GBW_{TIA}	Operational Amplifier Gain-Bandwidth product	160MHz
g_{m_VCCS}	Transconductance of transistor M1	35mS
$\Re_{LED}$	microLED responsivity (current to light conversion)	Polynomial regression equation (Chapter 3)
β_L	Feedback light to forward light ratio $\left(\frac{L_{fb}}{L_{fwd}}\right)$	0.1
$\Re_{PD}$	Photodiode responsivity	0.1A/W
R_{TIA}	TIA feedback resistor (also represent the gain of TIA)	20kΩ
BW_{TIA}	Bandwidth of TIA	514MHz
R_F , R_B	DC level shifter to set the bias of COFBCK driver	10kΩ
R_{OP1}	The feedback resistor of the operational amplifier. $\frac{R_{OP1}}{R_F}$ is the closed loop gain of the feedforward path	1MΩ

Table 5-4 – Summary of the parameters used in the COFBK driver macromodel simulation

5.5.2.1. DC simulation

The microLED/COFBK driver macromodel DC characteristic was simulated by biasing the LED_GND node at –3V. V_{BIAS} is set at 2V which sets OP1 around mid-rail. Figure 5-14(a) and Figure 5-14(b) show the macromodel simulation results of current response (I-V characteristic) and the optical power response (L-V characteristic) respectively. From the figure, the maximum current and optical power produced by the macromodel were found to be 105mA and 4.8mW respectively.

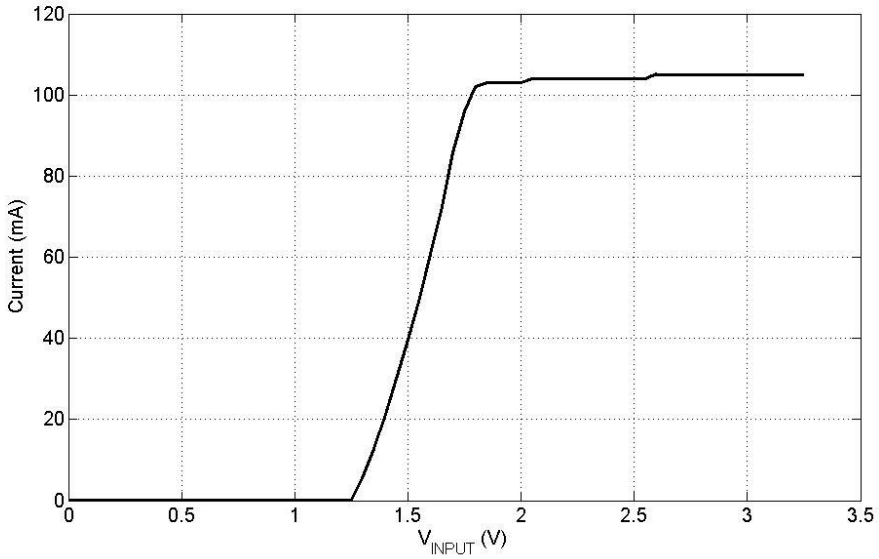

(a)

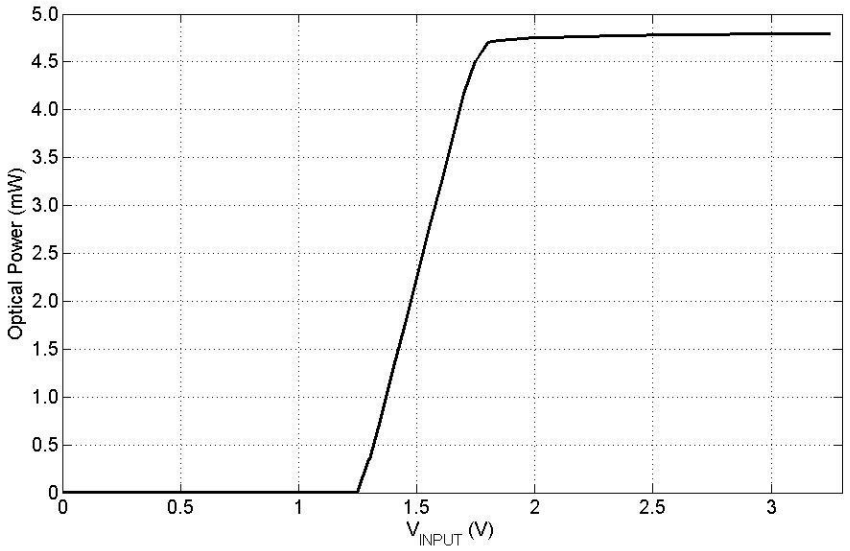

(b)

Figure 5-14 – DC simulation of COFBK driver showing (a) I-V characteristic and (b) L-V characteristic

The aim of the microLED/COFBK driver is to linearize the optical power output by pre-distorting the current driving the microLED (Section 5.4.1). To demonstrate this, The I-V and L-V characteristics are magnified in the x-direction and plotted together with a linear regression fitted line, as shown in Figure 5-15. The non-linearity of the I-V characteristic is emphasized, where the current response is shown to be pre-distorted and behaving in a 'concave up' manner. As a result of the pre-distorted current response, the optical power response of the microLED/COFBK driver follows the linear regression fitted line closely. The simulated I-V and L-V characteristics were as predicted, as previously shown in Figure 5-5(b). This proves that the optical feedback technique applied in the microLED/COFBK driver is able to improve the linearity of the microLED optical power response in comparison to the bare microLED die and microLED/CCFBK driver counterparts.

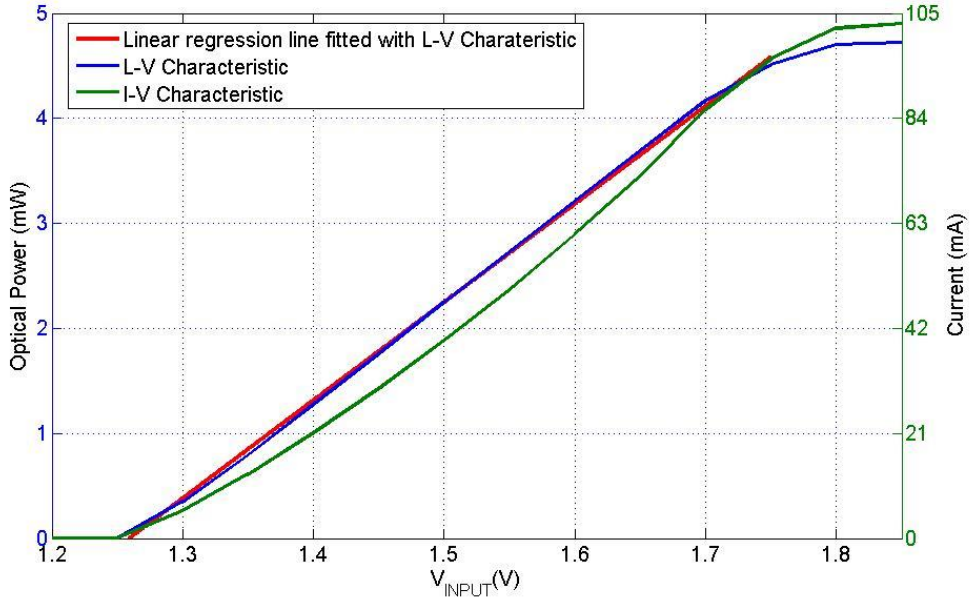

Figure 5-15 – Magnified portion of in the x-direction response of I-V characteristic and L-V characteristic with linear regression fitted line

Figure 5-15 also shows that V_{INPUT} is biased approximately at 1.52V and with a range of about 500mV peak-to-peak. The range of operation (V_{INPUT} range) is determined by the gain in the feedback path. Equation 5-24 predicts that the TIA would produce a signal of about 1V peak-to-peak, ranging from 0.9V to 1.9V. The V_{INPUT} range can be predicted by analysing the COFBK driver biasing circuit. R_B and R_F form a voltage divider between V_{BIAS} and V_{TIA} into the non-inverting input of OP1 (V_{FB} in Figure 5-4). R_B is designed to be equal to R_F, therefore V_{INPUT} range can be calculated as

$$\Delta V_{INPUT} = \Delta V_{FB} = \left(\frac{V_{TIA\_max} - V_{BIAS}}{2}\right) - \left(\frac{V_{TIA\_min} - V_{BIAS}}{2}\right) = \frac{V_{TIA\_max} - V_{TIA\_min}}{2}$$

Equation 5-25

where V_{TIA_max} and V_{TIA_min} are the maximum and minimum output signal from the TIA respectively. Using Equation 5-25, the V_{INPUT} range is calculated to be 500mV peak-to-peak (ranging from 1.275V to 1.775V), in line with Figure 5-14. This establishes that the V_{INPUT} range is determined by the gain in the feedback path ($\beta_L, \Re_{PD}$ and R_{TIA}), where a higher feedback gain gives a wider V_{INPUT} range.

5.5.2.2. AC Simulation

AC simulation was performed using the parameter values from Table 5-3 and Table 5-4, the simulated result is shown in Figure 5-16, showing a closed loop gain of –46 dB with a bandwidth of 73MHz. The closed loop gain can be predicted from, and is consistent with, Equation 5-12, which also suggests that the closed loop gain is inversely proportional to the feedback gain, β. Therefore, the bandwidth of the microLED/COFBK driver can be increased by reducing the closed loop gain, i.e. increasing β.

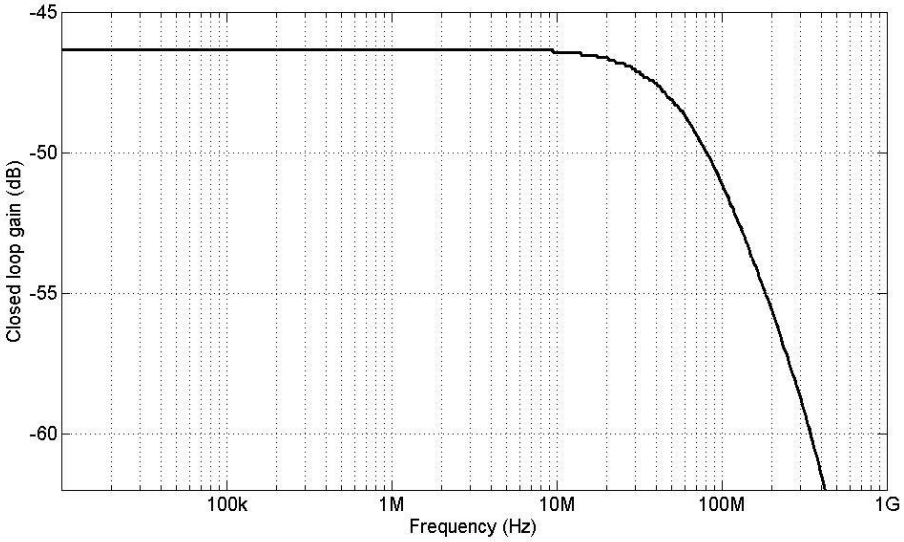

Figure 5-16 – Frequency response of the L_{fwd} of the microLED/COFBK model

Figure 5-17 shows an example of increasing the feedback gain of the amplifier, by varying β_L from 4% to 18%, showing that the bandwidth increases from 26MHz to 151MHz. Therefore,

a high feedback gain is desirable in order to increase the bandwidth of the system. The feedback gain can be increased by raising one or more of the

- ratio of the feedback light (β_L)
- photodiode responsivity ($\Re_{pd}$)
- gain of the TIA

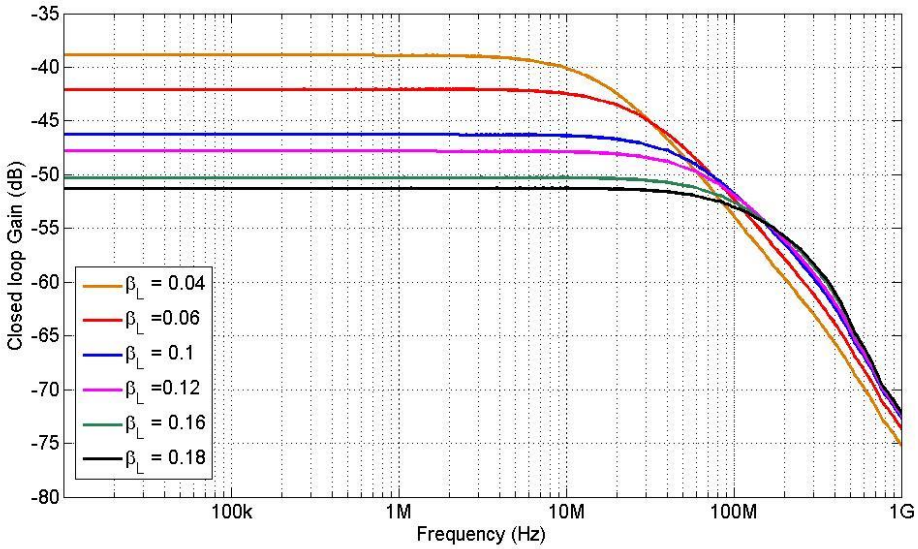

Figure 5-17 – Frequency response of the COFBK driver by varying the feedback gain (β)

Both β_L and $\Re_{PD}$ are process dependent, therefore, they are harder to control. On the other hand, the gain of the TIA can be controlled and set during the design. Moreover, having a high gain TIA is also an advantage if β_L and $\Re_{PD}$ turn out to be lower than expected (which could further reduce the bandwidth of the microLED/COFBK driver). However, it is also important to note that the bandwidth of the TIA decreases as its gain increases. As suggested by Equation 5-16, the closed loop function exhibits a zero due to the pole in the feedback network, which causes gain-peaking in the frequency response. To minimize such event, the bandwidth of the feedback network has to be greater than the gain-bandwidth product of the feedforward network. Figure 5-18 shows the effect of the bandwidth of TIA on the feedback system. Three cases were considered:

1. The bandwidth of the TIA is lower than the gain-bandwidth product of OP1 ($BW_{TIA} < GBW_{OP1}$)
2. The TIA bandwidth and gain-bandwidth product OP1 is equal ($BW_{TIA} = GBW_{OP1}$)
3. The bandwidth of the TIA is greater than the gain-bandwidth product of OP1 ($BW_{TIA} > GBW_{OP1}$)

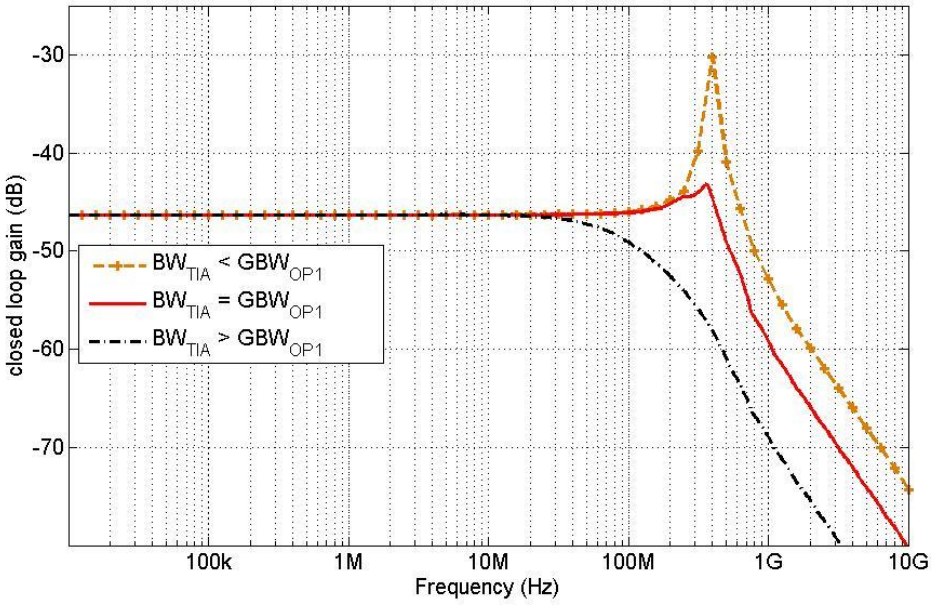

Figure 5-18 – Effect of feedback network bandwidth (BW_{TIA}) on the COFBK driver frequency response

In case 1, very high gain-peaking occurs (about 17dB) which suggests that the feedback system is unstable. The same can be said for case 2 even though the gain-peaking is reduced to 3dB. No gain-peaking is shown in case 3 where the bandwidth of the TIA is greater. However, this comes at a price of reduced overall bandwidth. Because of this, in order to ensure the stability of the feedback loop, the bandwidth of the TIA has to be designed to be greater than the gain-bandwidth product of OP1. To allow a safety margin, the gain-bandwidth product of OP1 is designed for no more than 65% that of the TIA bandwidth

5.6. Transistor Level Design

The ideal macromodel as described in Section 5.5 is replaced with a MOSFET and resistor model provided by the AMS 0.35µm BiCMOS process HIT-KIT. This is the first time that the microLED and CMOS photodiode are integrated in a single pixel, so until it is measured, there is a high level of uncertainty in the level of the feedback light captured by the photodiode. Therefore, the TIA is equipped with 3 different gain options to accommodate this uncertainty.

5.6.1. Voltage Amplifier

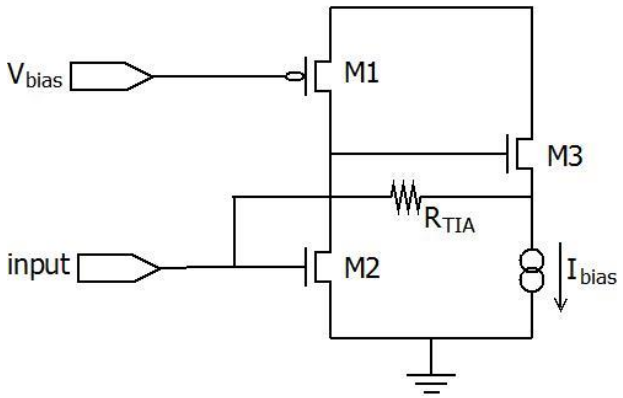

Figure 5-19 – Common voltage amplifier for transimpedance amplifier

As shown in Equation 5-20, a high gain voltage amplifier is favoured to achieve a high bandwidth TIA. A common TIA is based on a single-stage buffered voltage amplifier type, as shown in Figure 5-19. The gain of the voltage amplifier in this configuration corresponds to the intrinsic gain of a MOSFET, which has a typical gain of 10, depending on the process technology parameters (and tends to be smaller with downscaling of technology [107]). Furthermore, the voltage amplifier structure also requires additional biasing circuitry.

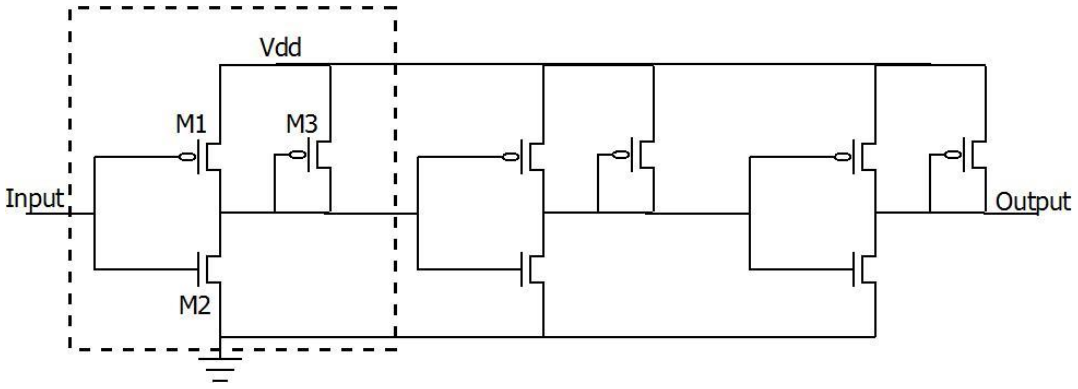

Figure 5-20 – 3-stage voltage amplifier consisting of 3 identical voltage amplifier stages connected in series. Dotted box represents a single stage

Figure 5-20 shows the voltage amplifier used in this project. This voltage amplifier consists of three identical basic voltage amplifier stages connected in series. P-channel MOSFET M1 and M3 and n-channel MOSFET M2 form a single stage voltage amplifier (highlighted in the dotted bracket). The multiple-stage amplifier is used to obtain a large open-loop gain where the total gain of the voltage amplifier is the gain of a single stage to the power of three (A_{V_total}

= $\left(A_{V\_1stage}\right)^3$). Furthermore, the voltage amplifier shown in Figure 5-20 is a self-biased amplifier. The bias voltage is set by the width to length ratio $\left(\frac{W}{L}\right)$ of M1, M2 and M3 respectively. Therefore, no additional circuitry is needed. This is an advantage as the COFBK driver is limited by the pixel area available.

The voltage gain of the single stage voltage amplifier (A_{V_1stage}) can be found using Equation 5-26

$$A_{V\_1stage} = \frac{g_{m\_M1} + g_{m\_M2}}{g_{m\_M3} + g_{DS1} + g_{DS2} + g_{DS3}} \approx \frac{g_{m\_M1} + g_{m\_M2}}{g_{m\_M3}} \qquad \textbf{Equation 5-26}$$

where g_{m_M1}, g_{m_M2} and g_{m_M3} are the transconductances while g_{DS1}, g_{DS2}, and g_{DS3} are the drain or output conductance of M1, M2 and M3 respectively. In this case, $g_m \gg g_{DS}$ is assumed.

The voltage amplifier is biased such that the voltage at the output is equal to the input, thus the voltage drops across the drain-source of M1 and M3 are always identical. Equation 5-26 above can be re-written as

$$A_{V\_1stage} = \frac{\frac{2I_{M1}}{(V_{gs} - V_{tp})_{PMOS}} + \frac{2I_{M2}}{(V_{gs} - V_{tn})_{NMOS}}}{\frac{2I_{M3}}{(V_{gs} - V_{tp})_{PMOS}}} \qquad \textbf{Equation 5-27}$$

where I_{M1}, I_{M2} and I_{M3} are the drain source currents through M1, M2 and M3 while $\left(V_{gs} - V_{tp}\right)_{PMOS}$ and $\left(V_{gs} - V_{tn}\right)_{NMOS}$ are the drain source voltage drops across the p-channel and n-channel MOSFET respectively. Looking at Figure 5-20, using Kirchhoff's current law at the output node of a single stage, it can be found that

$$I_{M1} + I_{M3} = I_{M2} \qquad \textbf{Equation 5-28}$$

Therefore, by applying Equation 5-28, Equation 5-27 can be simplified further into Equation 5-29

$$A_{V\_1stage} = \frac{I_{M1}}{I_{M3}} + \left(1 + \frac{I_{M1}}{I_{M3}}\right)\frac{(V_{gs} - V_{tp})_{PMOS}}{(V_{gs} - V_{tn})_{NMOS}} \quad \textbf{Equation 5-29}$$

Assuming that the $\left(\frac{W}{L}\right)$ ratio between M1-M3 and M2-M3 is written as X and Y respectively, Equation 5-28 also can be written as

$$\frac{K_p'}{2}(V_{gs} - V_{tp})^2_{PMOS}(X + 1) = \frac{K_n'}{2}(V_{gs} - V_{tn})^2_{NMOS}(Y) \quad \textbf{Equation 5-30}$$

$$\frac{(V_{gs} - V_{tp})^2_{PMOS}}{(V_{gs} - V_{tn})^2_{NMOS}} = \frac{K_n'}{K_p'}\left(\frac{Y}{X + 1}\right) \quad \textbf{Equation 5-31}$$

Inserting Equation 5-31 into Equation 5-29, A_{V_1stage} and the ratio of M1-M3 and M2-M3 then can be estimated. This is shown in Equation 5-32

$$A_{V\_1stage} = X + \sqrt{(X + 1).Y}\sqrt{\frac{K_n'}{K_p'}} \quad \textbf{Equation 5-32}$$

From equation 5-7 above, it can be seen that A_{V_1stage}depends on the gain factor of the p-channel and n-channel MOSFET (K_p' and K_n') and the ratio between M1-M3 and M2-M3 (X and Y).The typical value of K_p' and K_n' are given as 58 µA/V^2 and 170 µA/V^2 respectively [89] and are technology dependent. From the equation, to achieve high A_{V_1stage}, X and Y are to be maximised. However, this is limited by the pixel area available. Furthermore, the ratio between M1 to M2 will determine the DC point of the voltage amplifier where it was chosen to be 0.9V. To maximise speed, minimum length transistor of 0.35µm is used. Thus, the width of M1, M2 and M3 are chosen as 2.3µm, 26µm and 2.2µm respectively. Using Equation 5-32, the gain of a single stage voltage amplifier can be estimated to be about 9.

The simulated frequency response of the single stage voltage amplifier is shown in Figure 5-21. From Figure 5-21, A_{V_1stage} was found to be 8.71 (18.8 dB). This is slightly lower than the predicted gain of 9 using Equation 5-32. The bandwidth of the single stage voltage amplifier was shown to be 400MHz. From the gain obtained in Figure 5-21, the total gain of the 3-stage voltage amplifier (A_{V_total}) is predicted to be 660 (56.4 dB).

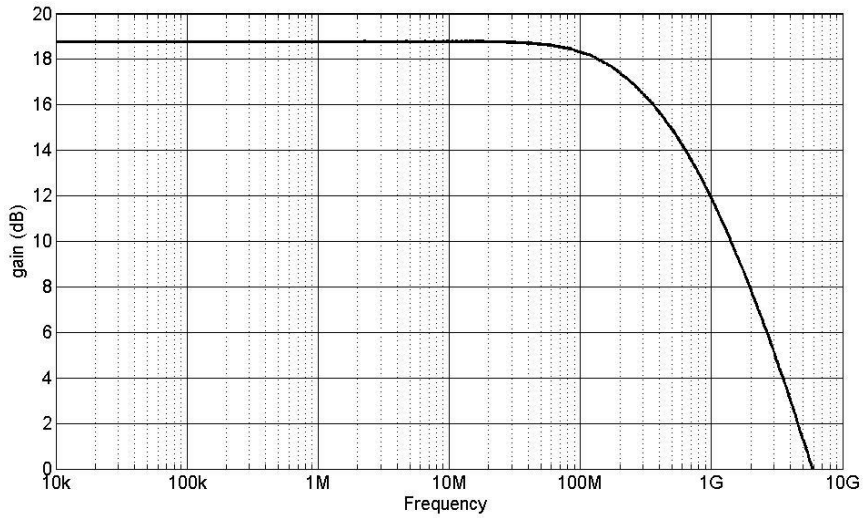

Figure 5-21 – Simulated frequency response of a single stage voltage amplifier

Figure 5-22 shows the frequency response of the 3-stage amplifier driving a 100fF load capacitance showing A_{V_total} of 660 (56.4 dB), which is as expected. The bandwidth of the voltage amplifier was found to be 220MHz.

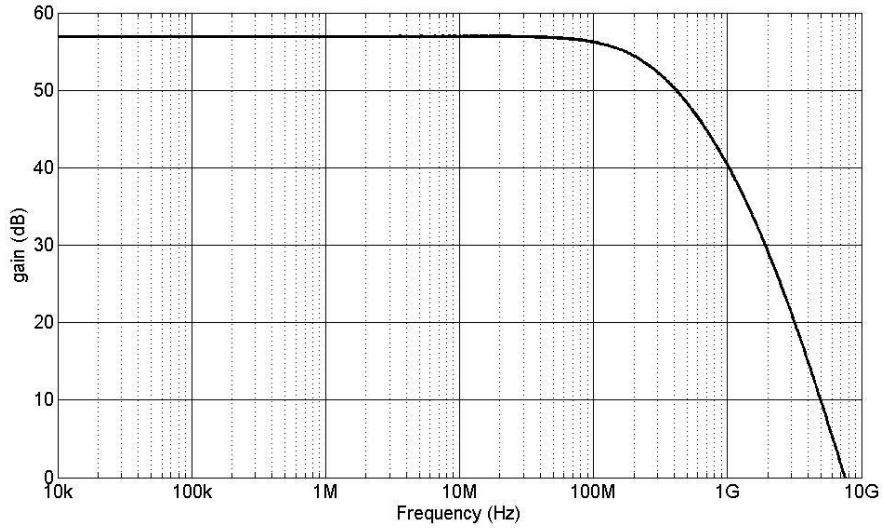

Figure 5-22 – Simulated frequency response of the 3-stage voltage amplifier

5.6.2. Transimpedance Amplifier

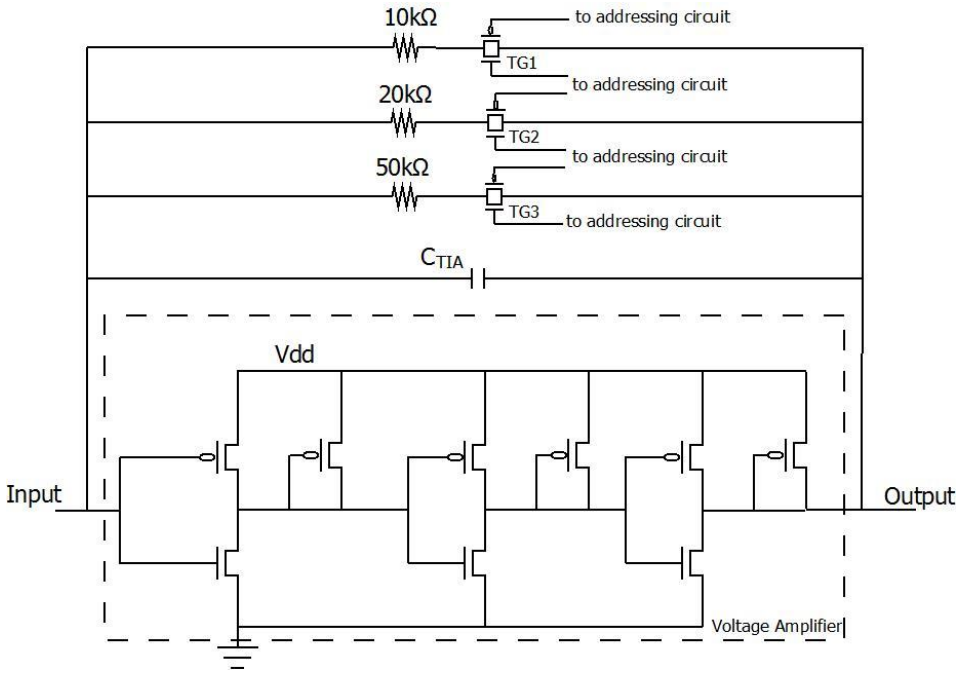

Figure 5-23 – Transimpedance Amplifier with 3 selectable feedback operation

Figure 5-23 shows the schematic circuit diagram of the TIA designed for the COFBK driver. The dotted box is the 3-stage amplifier as presented in Section 5.6.1. A selectable gain is provided in the TIA in order to accommodate the combined uncertainty of β_L and $\Re_{PD}$. Feedback resistors (R_{TIA}) of 10kΩ, 20kΩ and 50kΩ are connected between the input and the output node as shown in Figure 5-23. Therefore, the feedback network gain (gain of the TIA) can be switched between a gain of 10 000, 20 000 or 50 000. C_{TIA} is connected in parallel with R_{TIA}. C_{TIA} reduces the gain-peaking in the frequency response of the TIA (as discussed in Section 5.5.1). Transmission gates (TG1, TG2 and TG3) are connected in each branch to allow the selection of R_{TIA}. The transmission gates are controlled by an addressing circuit (not shown in Figure 5-23), where only one gate can be selected at any given time.

Section 5.5.2 discussed that the optical power of the feedback path is estimated to be around 605µW. With the assumption that the photodiode responsivity is 0.1A/W; the photocurrent generated by the photodiode is estimated to be up to 60µA. Figure 5-24 shows the simulated DC response of the TIA with current generated by the photodiode up to 60µA. Under no (feedback) light condition, the output of the TIA (V_{TIA}) is biased at 0.9V as discussed in Section 5.6.1. Figure 5-24 also shows the comparison when different values of R_{TIA} are selected. As expected, V_{TIA} is higher with larger R_{TIA}, and can be predicted using Equation 5-33

$$V_{TIA} = 0.9V + (I_{PD}R_{TIA})$$ **Equation 5-33**

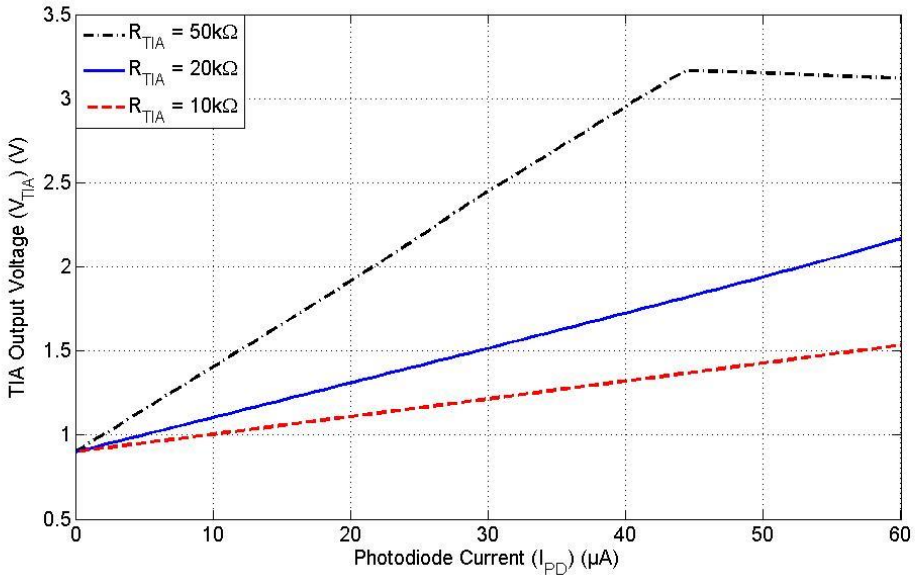

Figure 5-24 – Simulated DC response of TIA with different R_{fb}selected

Figure 5-25 shows the frequency response of the TIA for R_{TIA} of 10kΩ, 20kΩ and 50kΩ, with and without C_{TIA}, driving a 100fF load. C_{TIA} value of 20fF was used for the TIA. Figure 5-25 clearly shows the effect of inserting C_{TIA}, where the gain-peaking for all configurations was significantly reduced, hence putting the TIA in a more stable state. Table 5-5 summarises the bandwidth of the TIA with different R_{TIA} (with C_{TIA})

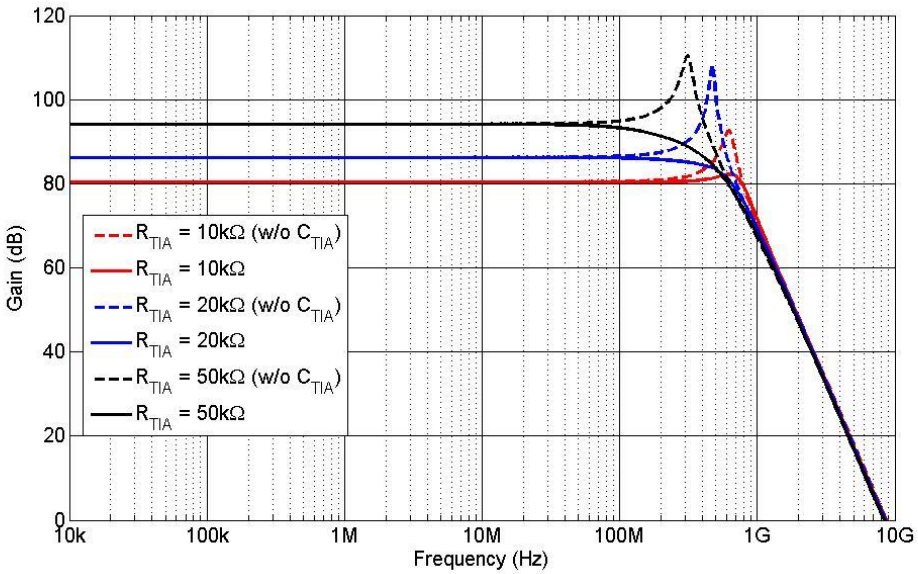

Figure 5-25 – Frequency response of the TIA with and without C_{TIA} for different R_{TIA}

Feedback gain (R_{TIA})	Bandwidth
10kΩ	845 MHz
20kΩ	505 MHz
50kΩ	205 MHz

Table 5-5 – TIA bandwidth with different R_{fb}

5.6.3. Forward Network

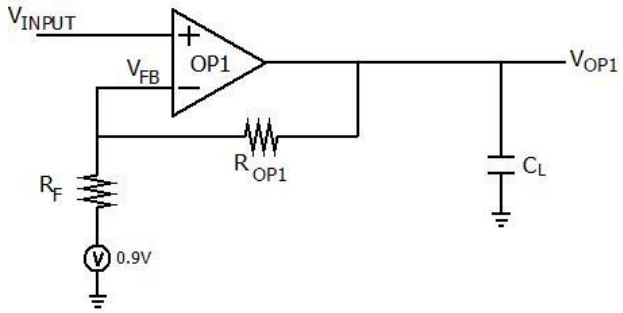

Figure 5-26 – Operational amplifier in the forward network

Figure 5-26 shows the operational amplifier (OP1) in the feedforward network driving a load capacitance (C_L) of 500fF which represents the gate capacitance of the n-channel MOSFET M1 (Figure 5-4). OP1 has the same architecture as that used in the CCFBK driver (single stage telescopic amplifier), but with reduced dimensions. A detailed description of the amplifier can be found in Section 4.5.1. The inverting input (V_{FB}) is connected to feedback resistors R_{OP1} and R_F, which is biased at 0.9V to represent the output of the TIA. The small signal closed loop gain of OP1 is given by the ratio of $\frac{R_{OP1}}{R_F}$. In this case, R_{OP1} and R_F are designed to be 1MΩ and 10kΩ respectively, hence giving a closed loop gain of 100.

R_F is implemented using a high resistivity poly layer (*RpolyH* layer), which is available in the AMS 0.35µm BiCMOS process technology. R_{OP1} on the other hand, is designed using a p-channel MOSFET biased in the linear region. This is because, even with a high resistive poly layer, the footprint of a 1MΩ resistor would be very large and area inefficient, which is a problem for an area-limited pixel. The R_{OP1} MOSFET is biased in the linear region with the gate of the MOSFET is tied to ground. The width and length of R_{OP1} can be calculated using Equation 5-34

$$R_{OP1} = \frac{1}{K_p' \left(\frac{W_{R_{OP1}}}{L_{R_{OP1}}}\right)(V_{gs} - V_t)}$$ **Equation 5-34**

where, in order to achieve high resistance, a large $L_{R_{OP1}}$ is required. The effective voltage across R_{OP1} was designed to be 0.55V to ensure it operates in the linear region and $W_{R_{OP1}}$ was chosen to be 0.5µm. $L_{R_{OP1}}$ is then calculated to be 16µm.

Referring to Figure 5-4, M1 is the driving MOSFET that supplies current to the microLED. Therefore, M1 is expected to able to drive the microLED up to 100mA. The width of M1 can be estimated using Equation 4-13. The nominal value of K_n' and V_T of n-channel MOSFET is given as 170µA/V^2 and 0.46V respectively. For the chosen process, the minimum length of a transistor is 0.35µm. Therefore, the length of M1 (L_{M1}) was chosen to be 0.35µm. Assuming the effective voltage across the transistor is 1V, the width of M1 is calculated to be 300µm.

$$I_{D\_M1} = 100mA = \frac{K_n'}{2}\left(\frac{W_{M1}}{L_{M1}}\right)(V_{GS} - V_T)^2$$ **Equation 5-35**

Figure 5-27 shows the simulated frequency response of OP1 in the forward network, giving a gain of 102 (40.2 dB) and gain-bandwidth product of 140MHz, which is about two-thirds (2/3) of the smallest bandwidth of the TIA (R_{TIA} of 50kΩ TIA gain configuration in Table 5-5). This difference is important to ensure the stability of the optical feedback system, as discussed in Section 5.5.2.2.

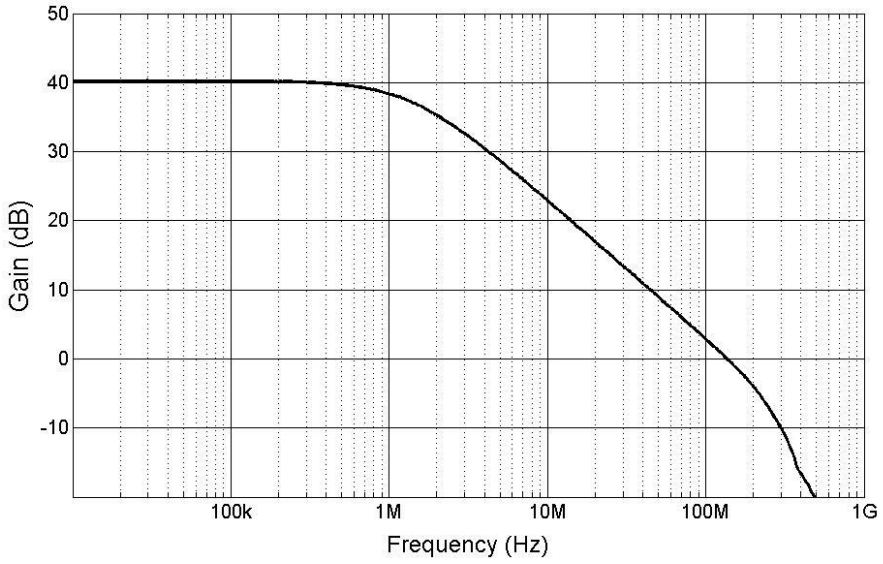

Figure 5-27 – Closed loop frequency response of the OP1 in the feedforward network

5.6.4. CMOS Optical Feedback Driver

The transistor level circuit for the TIA and forward network is connected, as shown in Figure 5-4 to form the COFBK driver. The microLED model and the photodiode model, as presented in Section 3.4.2 and Section 5.5.1 respectively, are used in the design simulation. The simulations are performed by biasing the LED_GND at –3V.

5.6.4.1. DC Performance

Figure 5-28 shows the simulated I-V characteristics of the microLED/COFBK driver for all TIA configurations. From the figure, the driver is able to produce current up to 102mA. However, it is important to note that the current produced by the driver begins to saturate at about 90mA. This is true for all configurations. Therefore, it is fair to say that the driving current "pseudo-linear" region of the microLED/COFBK driver is from 0 to 90mA.

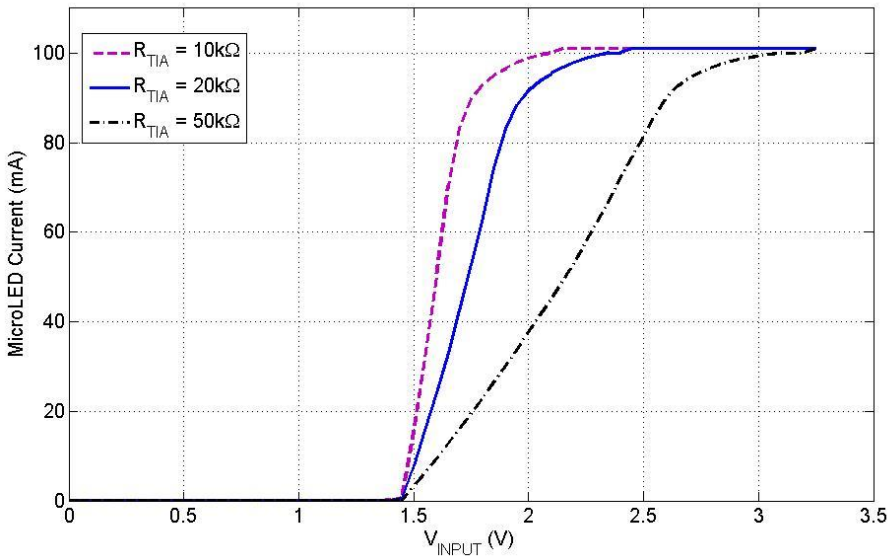

Figure 5-28 – MicroLED/COFBK driver simulated I-V characteristic

Figure 5-29 shows a magnified version of the I-V characteristic. An example of the linear fitted line is shown for the COFBK driver with 50kΩ TIA gain configuration from 0 to approximately 90mA. Notice that the figure demonstrates a concave-up response. Thus, the simulated I-V characteristic of the microLED/COFBK driver is as expected, as from the analysis in Section 5.5.2.1. From this non-linear I-V characteristic, the optical power response (L-V characteristic) of the microLED/COFBK driver is expected to produce a linear output with respect to the input voltage (V_{INPUT}).

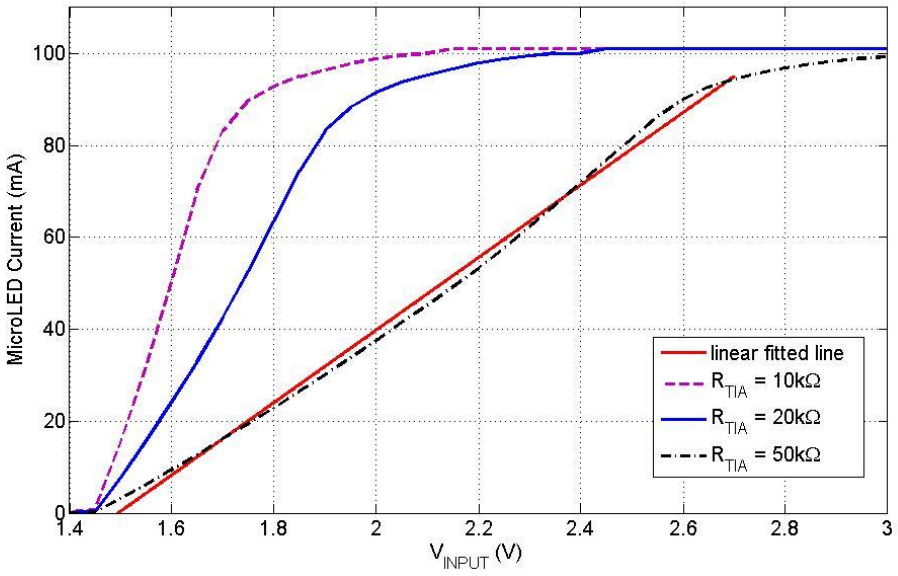

Figure 5-29 – Magnified version of the simulated microLED/COFBK driver I-V characteristic

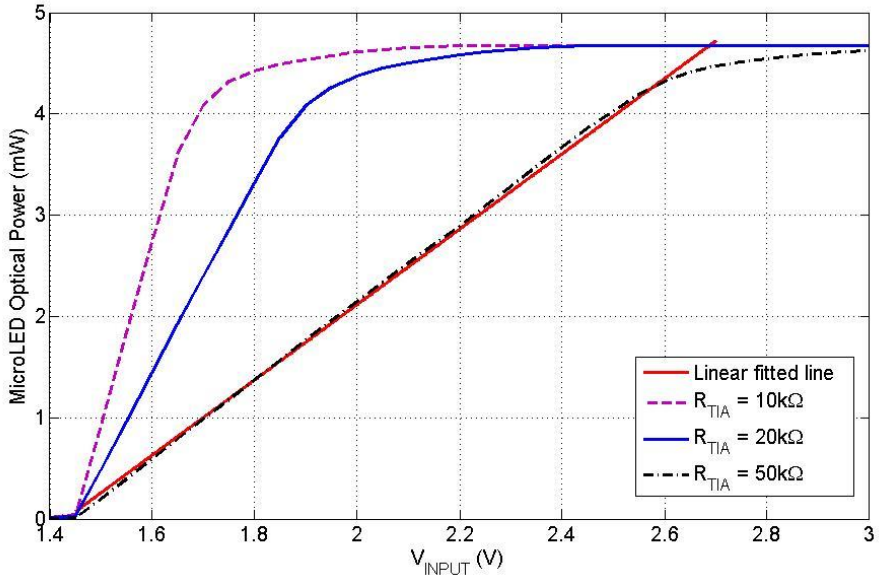

Figure 5-30 – Magnified version of the simulated MicroLED/COFBK driver L-V characteristic

Figure 5-30 shows the L-V characteristic of the microLED/COFBK driver with the same V_{INPUT} range as Figure 5-29, which demonstrates that the driver produces up to 4.5mW of optical power, which is as expected at 100mA driving current. Again, due to the saturation of the current response around 90mA, the optical power saturates around 4.2mW for all TIA configurations. However, the most important thing to note here is the marked improvement in

the degree of linearity of the optical response from 0 to 4.2mW. This is shown in Figure 5-30, using the COFBK driver with 50kΩ TIA gain configuration as an example, the linear regression fitted line matches closer with the optical power response than the current response shown in Figure 5-29. Therefore, from the simulation of the I-V and L-V characteristics of the microLED/COFBK driver, it can be said that the driver is able to substantially correct the non-linearity of the inherited microLED L-I response.

5.6.4.2. AC Simulation

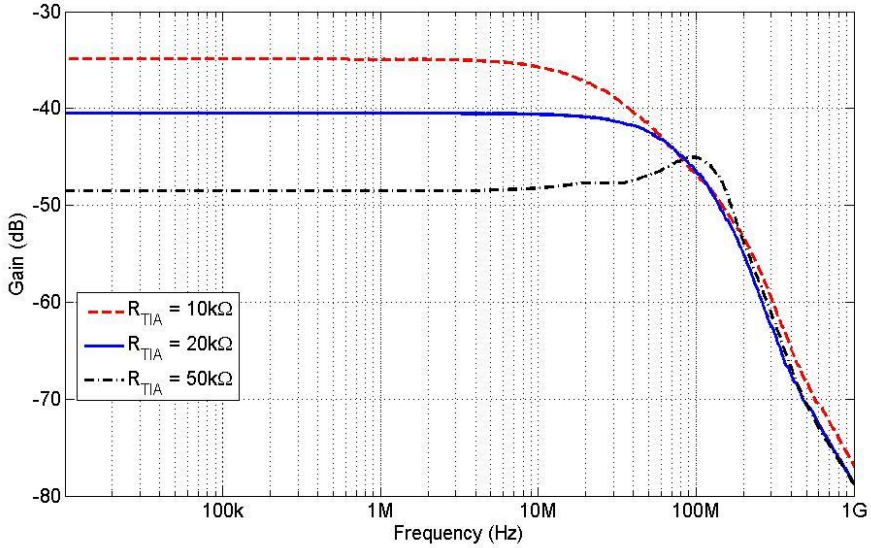

Figure 5-31 – Simulated frequency response of the MicroLED/COFBK driver for all TIA gain configurations

The frequency response of the microLED/COFBK driver for all TIA gain configurations is shown in Figure 5-31. The driver configuration with the highest TIA gain gives the highest bandwidth. This is as expected and discussed in Section 5.5.2.2. For the microLED/COFBK driver with 50kΩ TIA gain configuration, the bandwidth was found to be 157 MHz, while for the 20kΩ and 10kΩ TIA gain configurations, the bandwidth was found to be 77 MHz and 29 MHz respectively. From Figure 5-31, it can be noted that while the 50kΩ TIA gain configuration gives the highest bandwidth, the frequency response exhibits gain peaking which occurs around 100 MHz. This suggests that the feedback loop could be unstable. The stability of the microLED/COFBK driver system can be investigated by breaking the feedback loop and applying an input signal into the feedback path (V_{LFB}). The output signal (L_{fwd}) is plotted to show the loop gain of the feedback operation. The schematic diagram of the loop gain simulation is shown in Figure 5-32.

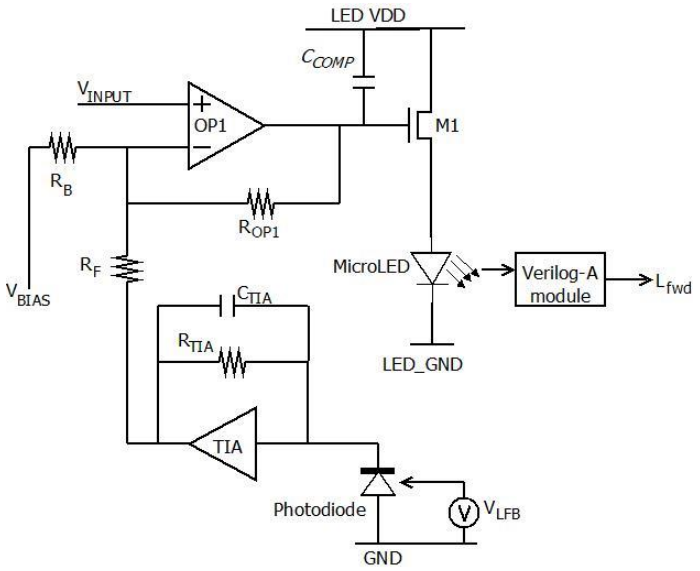

Figure 5-32 – Configuration for simulated loop gain analysis

Figure 5-33 shows the simulated loop gain frequency response of the microLED/COFBK driver with 50kΩ TIA gain configuration. The phase margin, when the gain is unity, for this configuration is 44.3°, indicating that the driver is marginally stable. As a rule of thumb, a phase margin has to be greater than 45° for it to be considered stable. To increase the phase margin, a compensation capacitor (C_{COMP}) with a value of 150fF is added to the output of OP1. The additional capacitor at the output of OP1 reduces the gain-bandwidth product and hence improves the phase margin of the system. With the added C_{COMP}, the phase margin for the 50kΩ increases slightly to 48.1°.

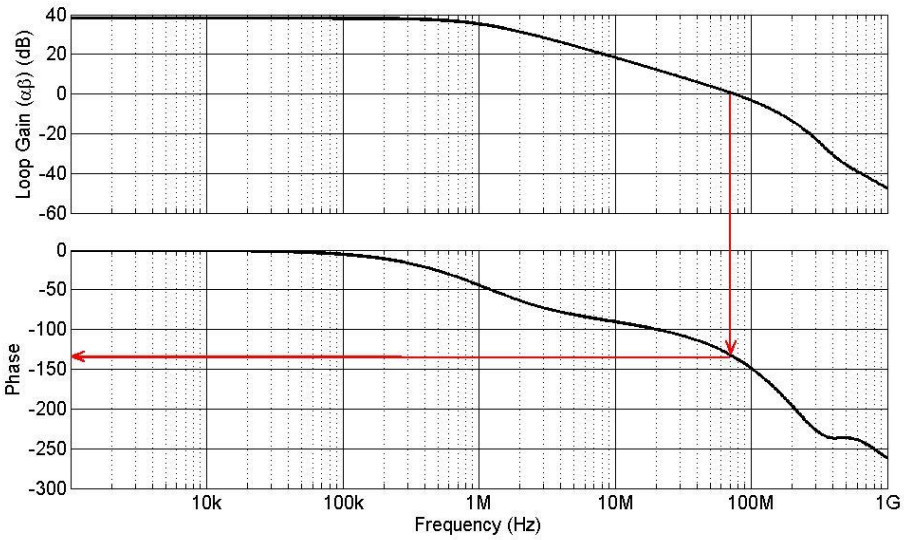

Figure 5-33 – Simulated frequency response of loop gain analysis of the microLED/COFBK driver with 50kΩ gain TIA configuration

Although the additional C_{COMP} increases the phase margin of the 50kΩ gain TIA configuration to above 45°, the driver is still considered 'in danger' of becoming unstable. It is important to remember that the purpose of adding the 50kΩ TIA gain configuration is to overcome the uncertainty of β_L and $\Re_{PD}$. Assuming that β_L or $\Re_{PD}$ or both are less than estimated, the loop gain of the feedback system will also decrease. Any decrease in the loop gain will in turn improve the phase margin for the 50kΩ TIA gain configuration. For example purposes, a comparison was made for the 50kΩ TIA gain configuration where β_L is reduced from 10% to 8%. Figure 5-34 shows that the loop gain decreases from 38 dB to 35.8 dB when β_L is reduced from 10% to 8%. As predicted, the phase margin improved from 48.1° to 56° putting the feedback system in a more stable state. The same explanation is applied to the 10kΩ TIA gain configuration. Using the estimated β_L and $\Re_{PD}$ value, the phase margin for the 10kΩ TIA gain configuration was found to be 72.1°, so it can be considered to be in an overdamped state which causes slow settling time. The phase margin will improve if either β_L or $\Re_{PD}$ (or both) is higher than estimated.

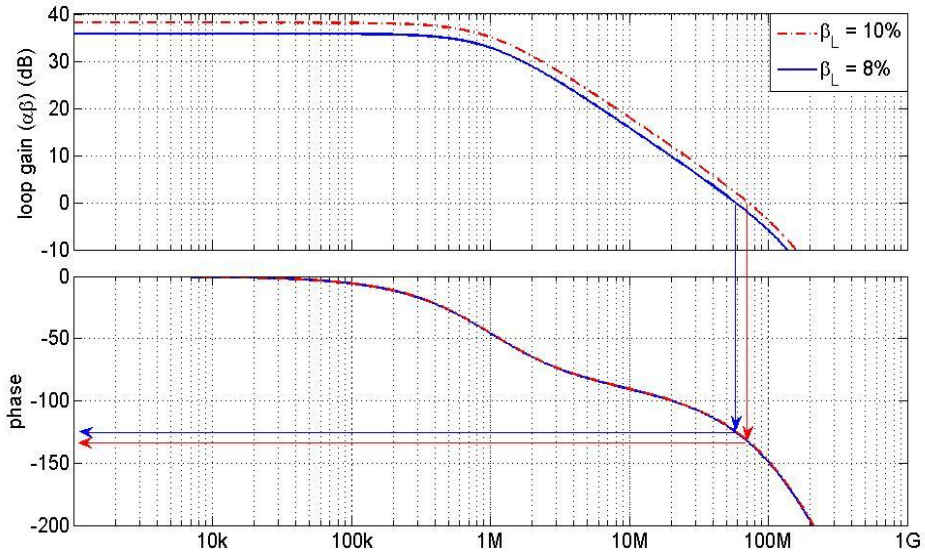

Figure 5-34 – Effect of the β_L on the loop gain and feedback stability

In conclusion, the stability of the microLED/COFBK driver depends on the gain in the feedback loop. The driver is designed so that it is stable with the estimated gain from the chosen design values. The loop gain, phase margin and the bandwidth of the microLED/COFBK driver for all the TIA gain configurations using the estimated β_L and $\Re_{PD}$ are summarised in Table 5-6.

	TIA Gain Configuration		
	10kΩ	**20kΩ**	**50kΩ**
Loop gain	24 dB	30 dB	38 dB
Phase margin	72.1°	64°	48.1°
Bandwidth	29 MHz	77 MHz	157 MHz

Table 5-6 – Summary of the loop gain, phase margin and bandwidth of the microLED/COFBK driver with the estimated β_L and $\Re_{PD}$

5.7. Layout and Post-Processing

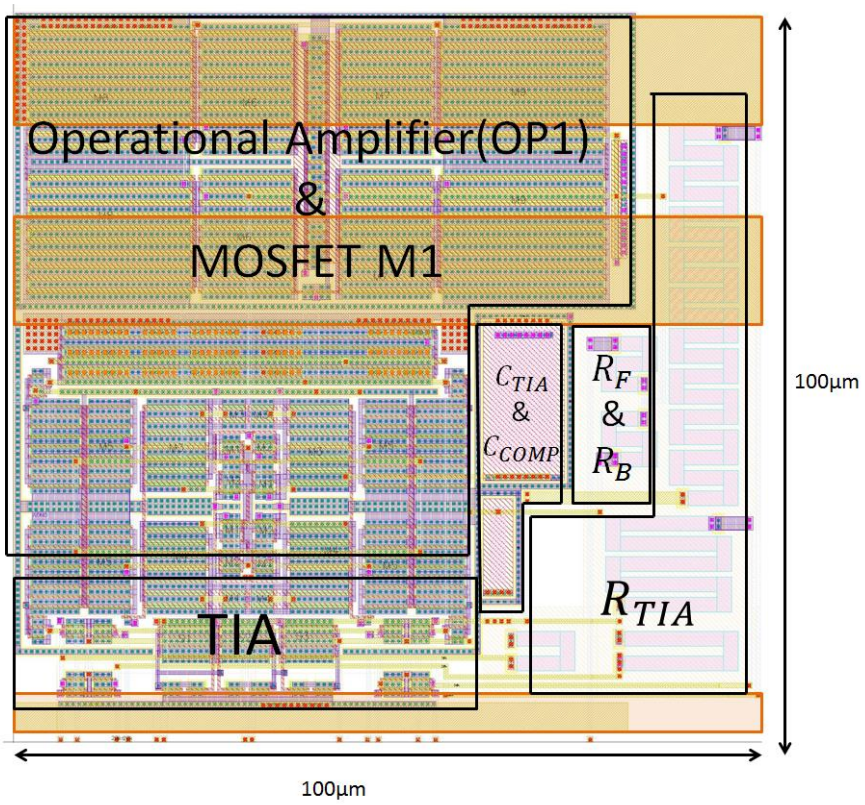

Figure 5-35 – Schematic layout of COFBK driver

The pixel pitch of the microLED/COFBK driver (not including the photodiode) is specified to be 100µm x 100µm, keeping the area the same as the digital driver and CCFBK driver. As with the digital driver and CCFBK driver, there are four metal layers available and the microLED is bump-bonded on top of the CMOS pixel. The top metal layer (Metal4) is used as an intermediate electrode and mechanical protection layer for the underlying CMOS circuitry as explained in Chapter 3 and Chapter 4. The schematic layout of the COFBK driver pixel is shown in Figure 5-35, which excludes Metal4, highlighting OP1, TIA, R_{TIA} of 10kΩ, 20kΩ and 50kΩ and R_F and R_B of the biasing network and capacitors of C_{TIA} and C_{COMP}.

Circuit interconnections are mainly run in Metal1 and Metal2 while Metal3 is used as a power supply rail. Metal4 is used exclusively for the "vertical" connection between the CMOS driver output and the microLED within each pixel. The area of Metal4, as for the CCFBK driver, is 95µm x 95µm with a passivation window opening of 80µm x 80µm, which was determined by the bump-bonding specification (Section 3.5). All resistors in the COFBK driver pixel (except for R_{OP1}) were implemented in the high resistivity polysilicon (*RpolyH*) layer as described in Section 5.8.1. The area of *RpolyH* was found using Equation 4-15 and Equation 4-16 and is summarised in Table 5-7. The capacitors on the other hand, are polysilicon-oxide-polysilicon (poly-poly) type capacitors with effective area capacitance of 0.86fF/µm2 [89]. Using this value, the area of C_{TIA} and C_{COMP} were calculated and are compiled in Table 5-7.

	Width	**Length**
R_{TIA} = 10kΩ	2 µm	15 µm
R_{TIA} = 20kΩ	2 µm	30 µm
R_{TIA} = 50kΩ	2 µm	75 µm
R_1	2 µm	15 µm
R_2	2 µm	15 µm
C_{TIA}	2 µm	10.4 µm
C_{COMP}	9 µm	18.75 µm

Table 5-7 – Summary of the area of resistors and capacitors in COFBK driver

5.7.1. Photodiode

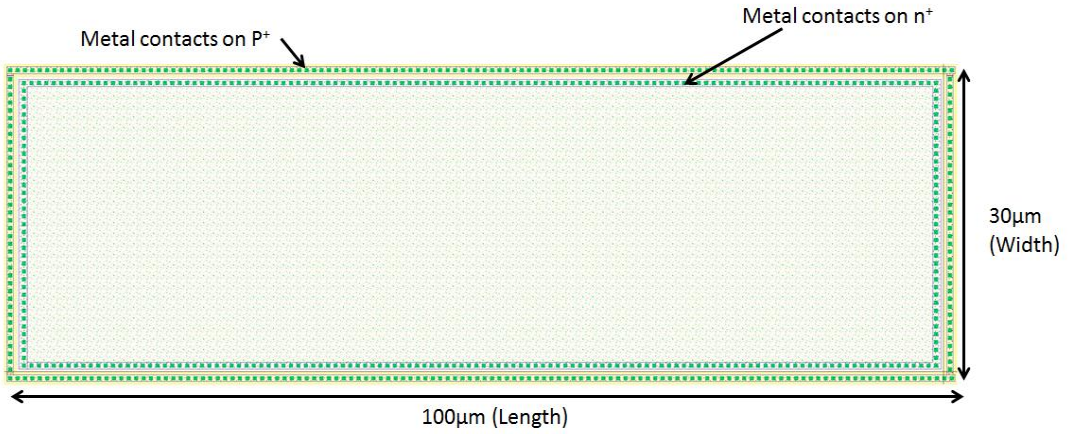

Figure 5-36 – Layout of the n+/p-substrate photodiode

The schematic layout of the n+/p-substrate photodiode is shown in Figure 5-36. The area of the photodiode was chosen to be 100µm x 30µm. The length of the photodiode was chosen to be the same as the length (or width) of the microLED, which is 100 µm, to maximise the

amount of light captured on the feedback path. Although it is desirable to have the photodiode as large as possible to maximise the detection of the feedback light, the area of the photodiode has a significant effect on the bandwidth of the TIA (Equation 5-26). Therefore, the chosen width of the photodiode represented a trade-off between maximising light detection and maximising bandwidth.

5.7.2. MicroLED and COFBK Driver Integration

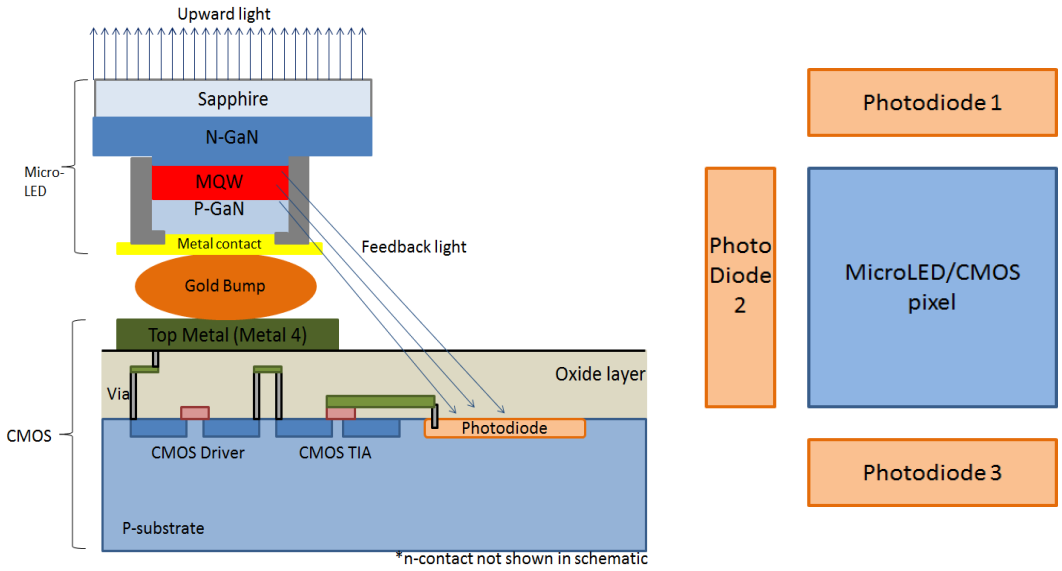

(a) **(b)**

Figure 5-37 – (a) Schematic cross section of the microLED-CMOS-photodiode device (b) Layout view of the photodiodes placement around the driver pixel

To ensure sufficient light to be fed into the photodiode, some considerable steps were taken:

1. **Modification to the microLED** – As mentioned in Section 5.3.1, the microLED is surrounded by a metal layer which acts not only as a contact, but also as a mirror to guide photons "forward". Due to the uncertainty of β_L, the metal contact on the sides of the microLED is removed. This should increase the amount of feedback light, but may come at a cost of reducing the forward light.
2. **Bonding placement** – The microLED and the CMOS driver have the same pitch dimensions. The microLED is bump-bonded directly on top of the CMOS driver. The feedback light is expected to leak from the sides of the microLED, and detected by a photodiode which is placed at the side of the pixel. A schematic cross section of the microLED-CMOS driver-photodiode arrangement is shown in Figure 5-37(a).

3. **Multiple photodiodes** – Again, due to the uncertainty of the amount leakage light on the sides of the microLED, the CMOS driver is equipped with three photodiodes, which are placed on three of the four sides of the pixel, as shown in Figure 5-37(b). The purpose of the three photodiodes option is to allow the driver to select the photodiode channel that captures the most suitable amount of feedback light. It is designed so that only one photodiode can be selected at a given time.

5.7.3. Polyimide Stripping

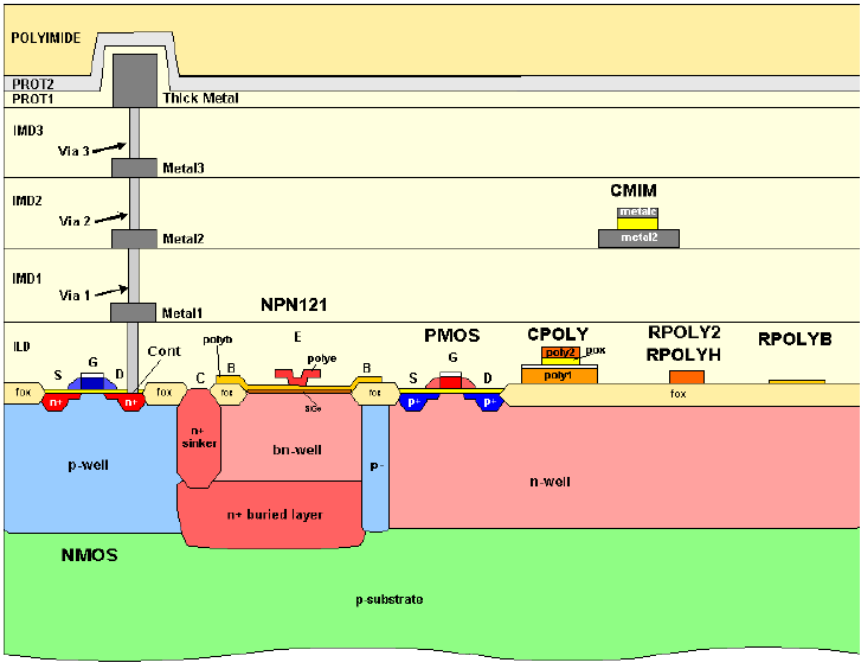

Figure 5-38 – Schematic cross section of AMS 0.35µm CMOS wafer. Image adapted from the original presented in Austria Microsystems 0.35µm BiCMOS process parameters document [89]

Figure 5-38 shows a schematic cross section of a device fabricated on the AMS 0.35µm BiCMOS process. Under this process, there are three layers that make the passivation layer. One of the layers is the polyimide layer, which is about 4.5µm thick. [116, 82] discussed that the polyimide layer reduces the amount of light detected by a photodetector in a CMOS chip. The stripping of the polyimide layer improves the detection by a factor of 2 to 3 [116, 82]. The polyimide stripping is conducted at the Scottish Microelectronics Centre (SMC), University of Edinburgh. The polyimide stripping is made before the microLED is bump-bonded onto the CMOS chip and is conducted by performing oxygen plasma etching on the CMOS chip for 6 hours.

5.8. Measurement

The same bump-bonding technique (as discussed in detail in Section 3.6) was implemented where a 100µm square microLED was bump-bonded onto the COFBK driver. The IMNS generic test board and DC-B daughter card (Section 3.7) were used for all conducted measurements. This section discusses the DC and AC performance of the microLED/COFBK driver.

5.8.1. TIA Responsivity

To measure the responsivity of the photodiode (and TIA), one of the driver chips was wire-bonded into a package without a microLED die bump-bonded onto it. An external light source was used for this experiment. This allowed the light from the external source to reach the photodiode on the COFBK driver array without any obstruction from the microLED die. An LED (OSRAM OSLON SSL [117], Figure 5-39(a)) was used as the external light source. The LED has a peak wavelength of 455nm, which is similar to the microLED. The external LED was connected to a Keithley picoammeter which was used to bias the external LED above its threshold voltage and to supply current

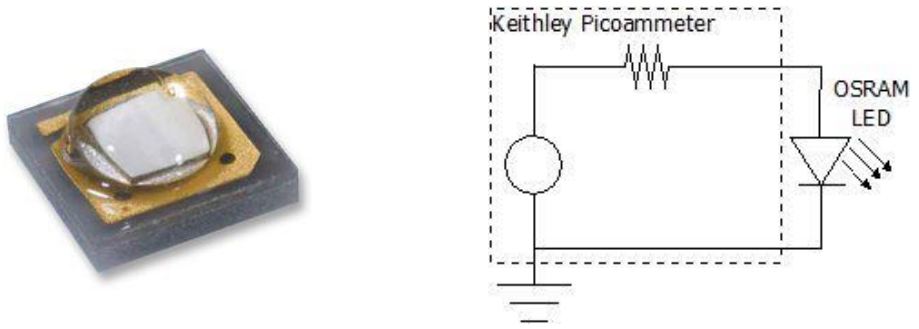

(a) **(b)**

Figure 5-39 – (a) Photograph of OSRAM LED and (b) Schematic circuit diagram of the external LED driver used in COFBK driver's TIA responsivity experiment

Figure 5-40 shows a schematic diagram of the optical bench setup for the TIA responsivity experiment. The optical bench consists of two types of bi-convex lens with a focal length of 25mm (F25) and 50mm (F50) respectively, a 50-50 beam-splitter and a Thorlabs' photodiode power sensor (SC130+PM100D) with a sensor diameter of 8mm. Light from the external LED driver is collimated by the F25 bi-convex lens and passes through the beam splitter which

splits the light into two with a power ratio of 1 to 1. Light exits at both faces of the beam splitter passes through an F50 lens which focuses the light into a small beam ≤ 1mm in diameter. The photodiode sensor is placed at one focal point and the COFBK driver is placed at the other. Therefore, the light received by the photodiode power sensor is the same as the light received by the photodiode on the COFBK driver chip.

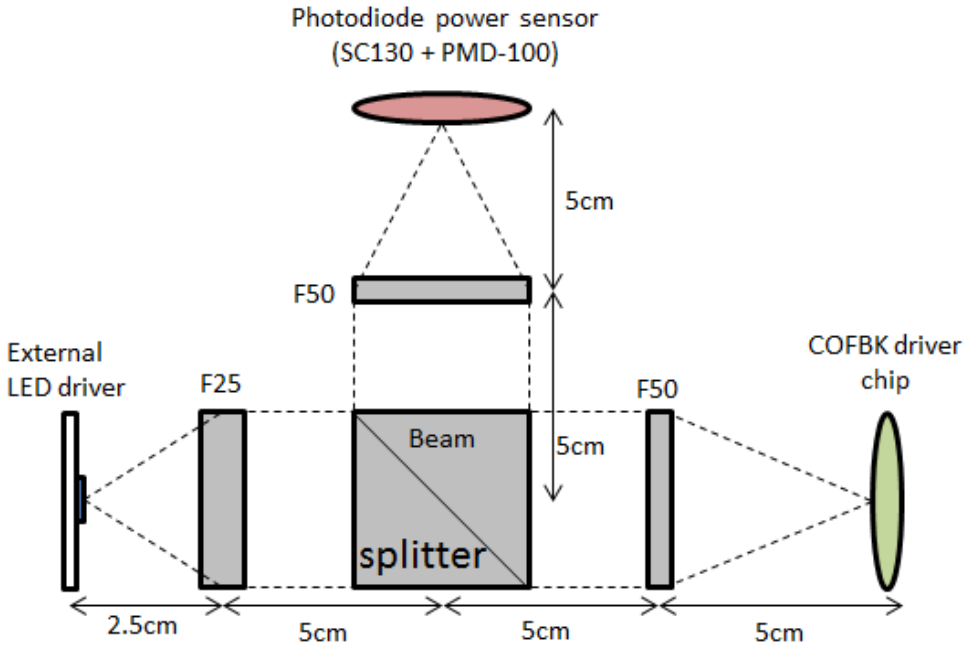

Figure 5-40 – Optical Bench setup for the COFBK' photodiode responsivity experiment

For calibration purposes, the photodiode power sensor was placed consecutively at one focal point, then the other to measure the splitting light ratio. From the measurement, the ratio of $\frac{P_{COFBK}}{P_{PMD}}$ is approximately $\frac{51}{49}$, where P_{COFBK} is the optical power on the COFBK driver chip's side and P_{PMD} is the optical power on the photodiode power sensor's side. With the ratio known, P_{COFBK} can be calculated as

$$P_{COFBK} = 1.04 P_{PMD} \qquad \textbf{Equation 5-36}$$

The actual optical power received by the COFBK driver's photodiode however, is less than P_{COFBK} due to the size of the photodiode being 100µm x 30µm, as mentioned in 5.7.1. Therefore, the optical power received by the photodiode is just a fraction of the total of P_{COFBK}, which can be approximated by

$$P_{PD} = \left(\frac{A_{PD}}{A_{beam}}\right) \times P_{COFBK} \qquad \textbf{Equation 5-37}$$

where P_{PD} is the optical power received by the COFBK driver's photodiode, A_{PD} is the area of the photodiode and A_{beam} is the area of the beam from the optical set-up.

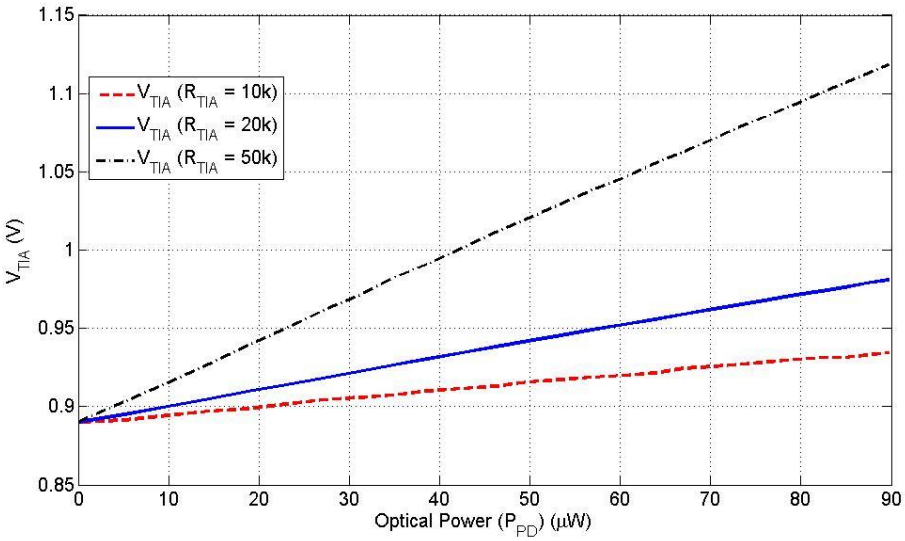

Figure 5-41 – TIA response with optical power received

On the COFBK driver side, the output voltage of the TIA (V_{TIA}) was measured using a digital multimeter. Figure 5-41 shows the photodiode and TIA response with increasing optical power. From Figure 5-41, it is shown that the TIA is biased at 0.89V and V_{TIA} increases linearly with increasing P_{PD}. As expected, the configuration of R_{TIA} of 50kΩ gives the highest response. From the measurement, R_{TIA} of 50kΩ and 20kΩ gives a gain of about five and two times higher with respect to the R_{TIA} of 10kΩ response, which is also as expected. The rightmost three columns of Table 5-8 summarises the ratio between each configuration.

P_{PD}	V_{TIA_10k}	V_{TIA_20k}	V_{TIA_50k}	$\frac{V_{TIA\_50k} - V_{BIAS}}{V_{TIA\_10k} - V_{BIAS}}$	$\frac{V_{TIA_{20k}} - V_{BIAS}}{V_{TIA_{10k}} - V_{BIAS}}$	$\frac{V_{TIA\_50k} - V_{BIAS}}{V_{TIA\_20k} - V_{BIAS}}$
38.7µW	0.910V	0.930V	0.991V	5.05	2.02	2.50
53.4µW	0.919V	0.947V	1.034V	5.06	2.01	2.51
73.5µW	0.930V	0.971V	1.093V	5.08	2.03	2.50

Table 5-8 – Summary of ratio of TIA with difference TIA gain configurations

Using the measured V_{TIA}, I_{PD} can be calculated using Equation 5-38

$$I_{PD} = \frac{V_{TIA\_P_{PD}} - V_{TIA\_0}}{R_{TIA}}$$ **Equation 5-38**

where $V_{TIA\_P_{PD}}$ is V_{TIA} at a certain P_{PD} and V_{TIA_0} is V_{TIA} when P_{PD} = 0W. Figure 5-42 shows the I_{PD} generated in each TIA gain configurations. For the 50kΩ and 20kΩ TIA gain, the current generated overlapped each other. For the 10kΩ gain however, the current generated is slightly lower and fluctuates. This is due to the limitation of the measuring equipment, where the received optical power (P_{PD}) in Figure 5-41 only causes a small increase in the V_{TIA} reading

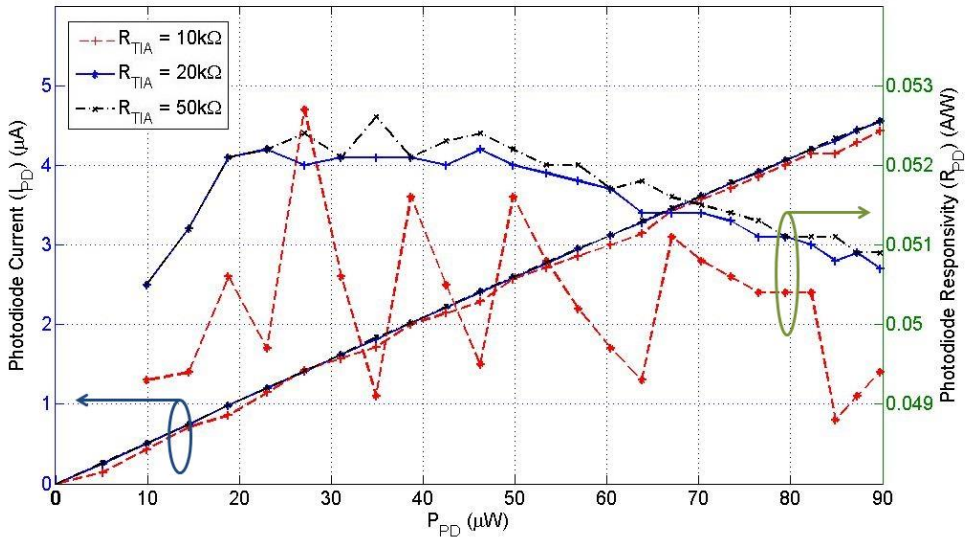

Figure 5-42 – I_{PD} response and R_{PD}

$$\Re_{PD} = \frac{I_{PD}}{P_{PD}}$$ **Equation 5-39**

Figure 5-42 also shows $\Re_{PD}$ for all different TIA gain configurations where $\Re_{PD}$ can be calculated using Equation 5-39. For the 10kΩ TIA gain configuration, it can be seen that $\Re_{PD}$ fluctuates due to the measuring limitation, as mentioned above. From the figure, the average $\Re_{PD}$ is calculated to be approximately 0.051. The fluctuate reading of the 10kΩ TIA gain configuration gives more than 2% variation from the average $\Re_{PD}$ value while both 50kΩ and 20kΩ TIA gain configurations give variation less than 2%. Therefore, it is fair to say that the I_{PD} measurement is more accurate using R_{TIA} of 50kΩ and 20kΩ. The calculated value of $\Re_{PD}$ however, is about half of the estimated $\Re_{PD}$ used in simulations.

5.8.2. Feedback Light Ratio

With the responsivity of the TIA known, the feedback light ratio (β_L) can be measured using the COFBK driver chip with microLED. This was done by measuring the L_{fwd} and V_{TIA} response. L_{fwd} was measured using Thorlab's photodiode power sensor (SC130 + PM100D), which was aligned with the microLED/COFBK driver pixel. The V_{TIA} output response was measured using a digital multimeter. Figure 5-43 shows the measured result from the experiment for all TIA gain configurations. The increment in V_{TIA} for 50kΩ TIA gain configuration is higher than 20kΩ and 10kΩ as expected. The average increment ratio for 50kΩ TIA gain configuration to 20kΩ and 10kΩ was calculated to be 2.47 and 4.97 respectively.

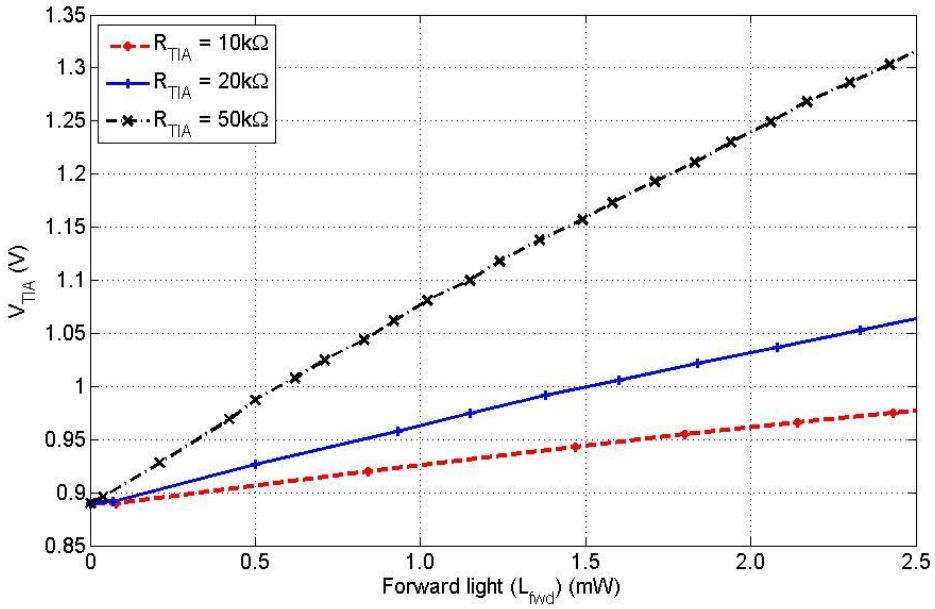

Figure 5-43 – TIA response of the microLED/COFBK driver

The generated I_{PD} depends on $\Re_{PD}$ of the TIA and the amount of feedback light (L_{fb}), which is a portion (β_L) of L_{fwd}. Therefore, the increment in the V_{TIA} (ΔV_{TIA}) can be calculated using Equation 5-40

$$\Delta V_{TIA} = [\Re_{PD} L_{fb}] R_{TIA} = [\Re_{PD} (\beta_L L_{fwd})] R_{TIA} \qquad \textbf{Equation 5-40}$$

Thus, the ratio of the feedback light to the forward light can be written as shown in Equation 5-41

$$\beta_L = \frac{\Delta V_{TIA}}{(L_{fwd}\Re_{PD})R_{TIA}} \qquad \textbf{Equation 5-41}$$

Figure 5-44 shows a plot of the calculated β_L using the data measured in Figure 5-43 with a $\Re_{PD}$ value of 0.051A/W, as measured in Figure 5-42. Figure 5-44 shows that β_L varies from 0.070 to 0.075 for all TIA gain configurations. TIA of 10kΩ gain shows a lower β_L, which is caused by a small ΔV_{TIA} and a measuring equipment limitation as mentioned in Section 5.8.1. The average β_L is then calculated to be 0.073 or 7.3% of the L_{fwd}. This is, again, lower than the expected β_L of 0.1 used in simulation.

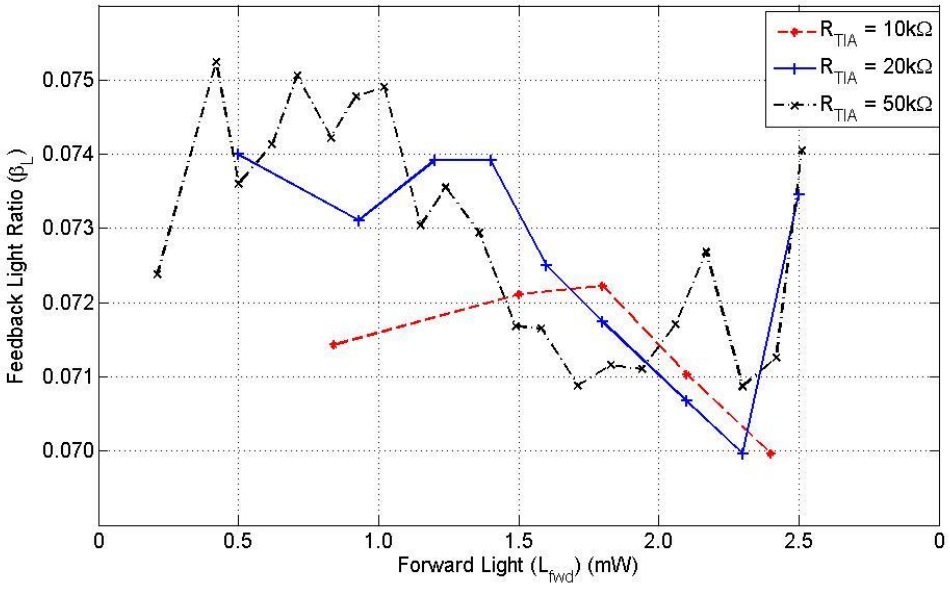

Figure 5-44 – Feedback light ratio (β_L) response

5.8.3. DC Performance

The DC performance of the microLED/COFBK driver was measured by biasing the LED_GND at –3V. The current consumption of the microLED/COFBK driver was measured with a digital multimeter, which is connected between the LED_GND node and the negative bias supply. The optical power was measured using a photodiode power meter sensor (SC130 + PM100D). The sensor was aligned directly with the selected pixel. The experimental setup is shown in Chapter 4 (Figure 4-25). The measurement of the I-V and L-V characteristics were conducted simultaneously.

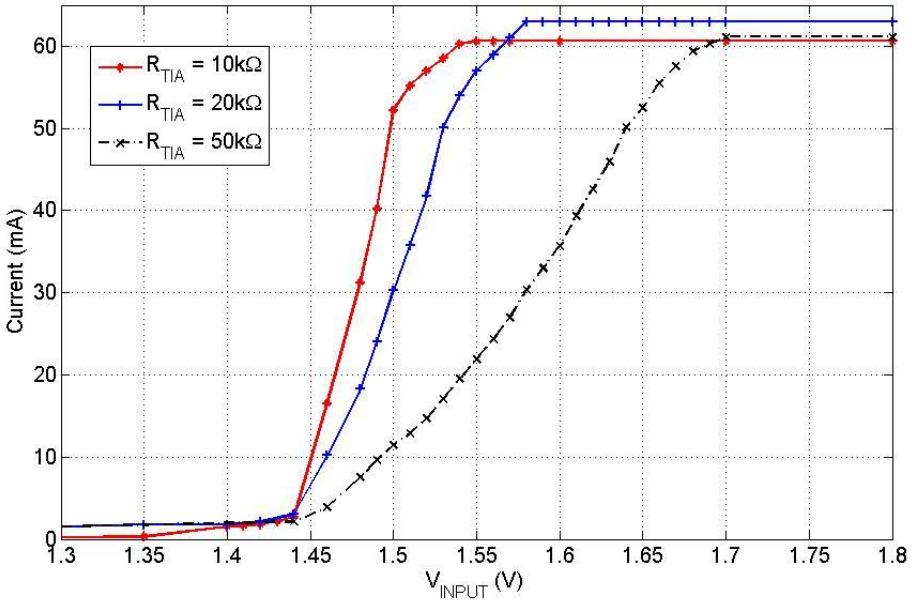

Figure 5-45 – MicroLED/COFBK driver I-V Characteristic for all TIA gain configurations

Figure 5-45 shows the I-V characteristic of the microLED/COFBK driver when the driver is biased at 2V ($V_{BIAS} = 2V$) and V_{INPUT} is swept from 0 to 3.3V for all TIA gain configurations. Note that only a V_{INPUT} ranging from 1.3V to 1.8V is shown in the figure. The results show a wider V_{INPUT} range for the 50kΩ TIA gain configuration, narrowing at the 20kΩ and further at the 10kΩ TIA gain configuration. This is as expected as the feedback gain is the highest in the 50kΩ TIA gain configuration, as discussed in Section 5.5.2.1. The range of V_{INPUT} can be calculated using Equation 5-25 applied to the results shown in Figure 5-43. The current produced by the microLED/COFBK driver increases non-linearly when V_{INPUT} exceeds 1.43V (which is set by V_{BIAS}) and starts to saturate at about 55mA for all configurations. The maximum current produced by the driver is about 60mA, which is lower than the design specification. The cause of the current shortfall is discussed in Section 5.9. Figure 5-46 shows the analysis of the I-V characteristic linearity, using the 50kΩ TIA gain configuration as an example. The I-V characteristic of the 50kΩ TIA gain configuration is compared with a linear regression fitted line to calculate the degree of non-linearity. The procedure of the linearity analysis is the same as explained in Section 4.7.2. Figure 5-46 indicates that the measured result shows a similar trend to the simulated result (as presented in Figure 5-29) where the I-V characteristic behaves in a "concave up" response to compensate for the drop in the microLED optical power at higher current. From the analysis, the I-V characteristic of the microLED/COFBK driver shows an R^2 value of 0.9885 and 12.3% non-linearity. The high

non-linearity percentage is as expected as the current is being pre-distorted to allow linearization of the microLED optical power response, as discussed in Section 5.5.2.1.

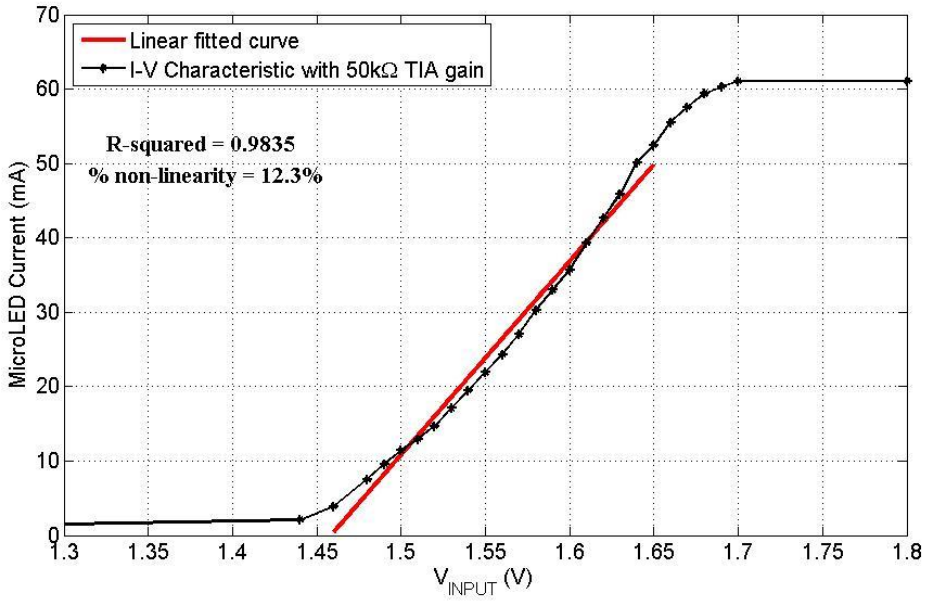

Figure 5-46 – Linearity analysis on the I-V Characteristic of microLED/CMOS driver with 50kΩ TIA gain configuration

The optical power response of the microLED/COFBK driver was investigated next. Figure 5-47 shows the L-V characteristic for the microLED/COFBK driver for all TIA gain configurations. The optical power response, for all configurations, shows a linear increment when V_{INPUT} is greater than 1.43V before it starts to saturate when the optical power is about 2.3mW and settles to a value around 2.5mW when V_{INPUT} is further increased. However, referring to the measurement results obtained with the microLED/CCFBK driver as presented in Section 4.7.1 and the microLED optical power response model (Section 3.4.2), for a microLED driven with about 60mA current, the optical power produced was expected to be approximately 3mW. Therefore, the measured optical power result from the microLED/COFBK driver is lower than the expected optical power value for a given drive current. This suggests that there is a degradation in the optical power performance of the microLED for the COFBK driver. The cause of this shortfall is discussed in Section 5.9.

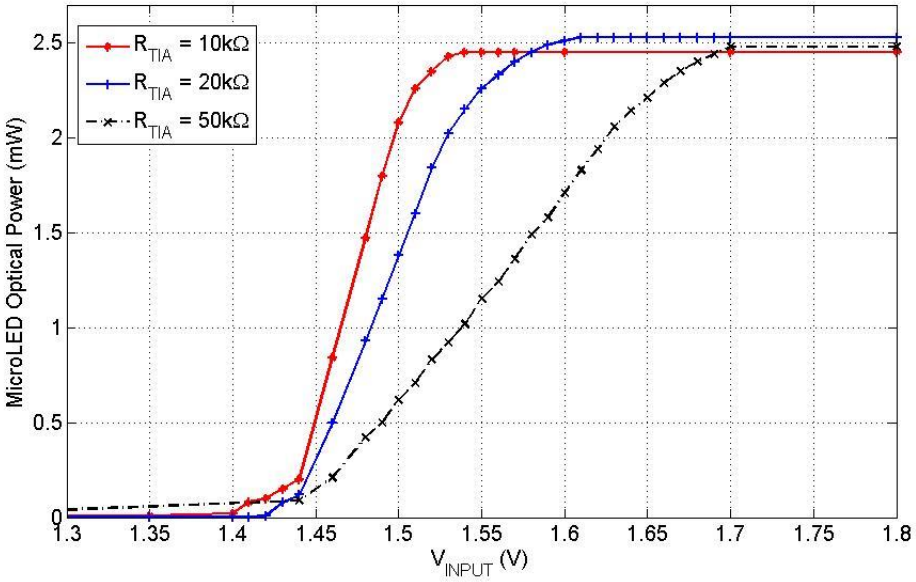

Figure 5-47 – Measured MicroLED/COFBK driver L-V characteristic for all TIA gain

Figure 5-48 (a) to (c) shows the measured optical power response of the microLED/COFBK driver for each TIA gain configuration. For fair comparison, the linearity of the optical power was measured from about 0.1 to 2.3mW for all TIA gain configurations, which is the region at which the optical power is considered to be in linear. The R^2 value was calculated to be 0.9955, 0.9978 and 0.9989 for 10kΩ, 20kΩ and 50kΩ TIA gain configurations respectively. The non-linearity percentage was calculated to be 4.4% for 10kΩ TIA gain configuration and less than 3% for both 20kΩ and 50kΩ TIA gain configurations. One of the reasons why the non-linearity of the 10kΩ TIA gain configuration is measured to be slightly higher is due to the limitation of the measuring equipment. The V_{INPUT} range is about 70mV in the 10kΩ TIA gain configuration and the input signal generator used in the DC measurement can only be increased in 10mV steps. The results of the linearity analysis are summarised in Table 5-9

TIA gain configuration	V_{input} range	Max Optical power output	R^2	Non-linearity percentage	"Linear" optical power range
10kΩ	70mV	2.45mW	0.9955	4.40%	0.13mW to 2.26mW
20kΩ	110mV	2.51mW	0.9978	2.77%	0.12mW to 2.26mW
50kΩ	230mV	2.48mW	0.9989	2.51%	0.09mW to 2.21mW

Table 5-9 – Summary of the MicroLED/COFBK driver linearity analysis

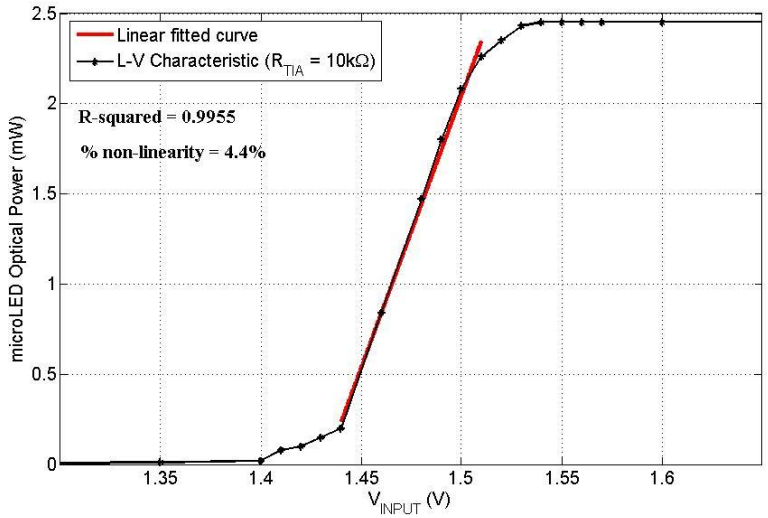

(a)

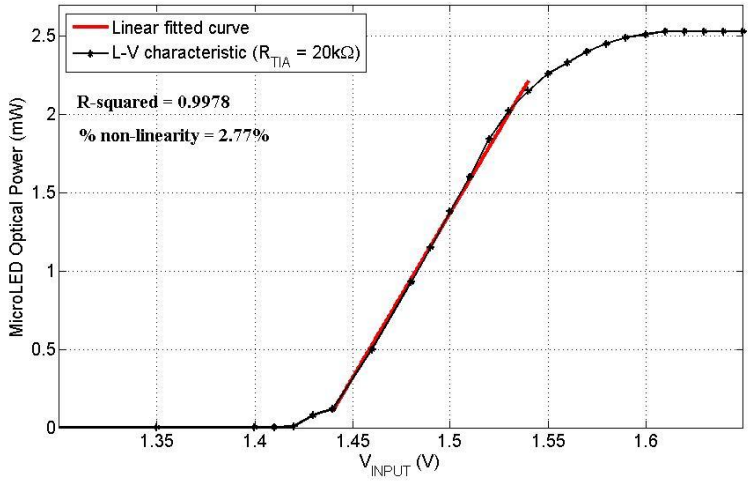

(b)

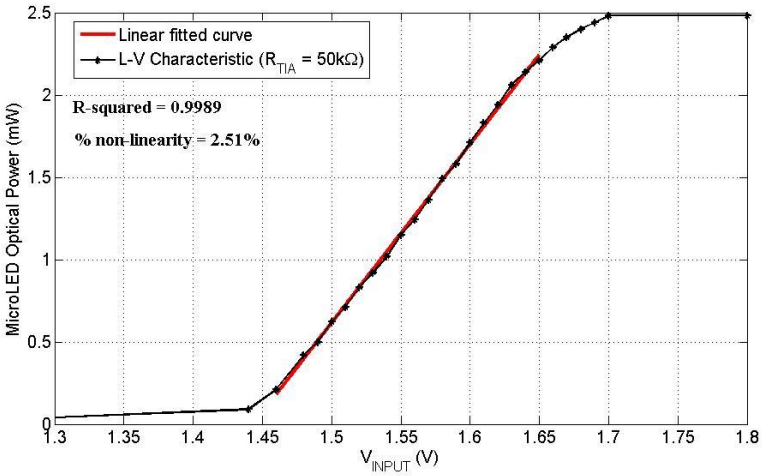

(c)

Figure 5-48 – I-V non-linearity analysis of the (a) 10kΩ TIA gain (b) 20kΩ TIA gain (c) 50kΩ TIA gain configuration

As a conclusion from the DC measurement, the optical feedback technique has proven to linearize the optical power response of the microLED proportionally to V_{INPUT} by pre-distorting the current supplying the microLED. The degree of non-linearity was measured to be only up to 4.4% for about 2.2mW of optical power range. The linearity comparison with microLED/CCFBK driver and further analysis on how the improved linearity affects OFDM performance are discussed in Chapter 6.

5.8.4. Frequency Response

Referring to Figure 5-4, the microLED/COFBK driver operating point can be set by applying a DC voltage to the V_{BIAS} node. V_{BIAS} affects the performance of the microLED/COFBK driver as it allows the user to bias OP1 to operate at its highest gain-bandwidth region. The V_{BIAS} node is set using a DC power supply for all experiments presented in this thesis. Figure 5-49 shows the DC operating point of V_{INPUT} when V_{BIAS} is varied from 0 to 4V and compared with the calculated V_{INPUT} DC operating point using Equation 5-25. Figure 5-49 shows the measured V_{INPUT} DC operating point increase linearly with V_{BIAS} as expected. However, the measured V_{INPUT} DC operating point shows a slightly higher value than calculated due to a mismatch between the two biasing transistors (R_B and R_F in Figure 5-4) and voltage off-set between OP1 inputs. From the simulation, OP1 has the highest gain-bandwidth product when biased around 1.2V to 1.8V. From the figure, this corresponds to V_{BIAS} around 1.2V to 2.8V.

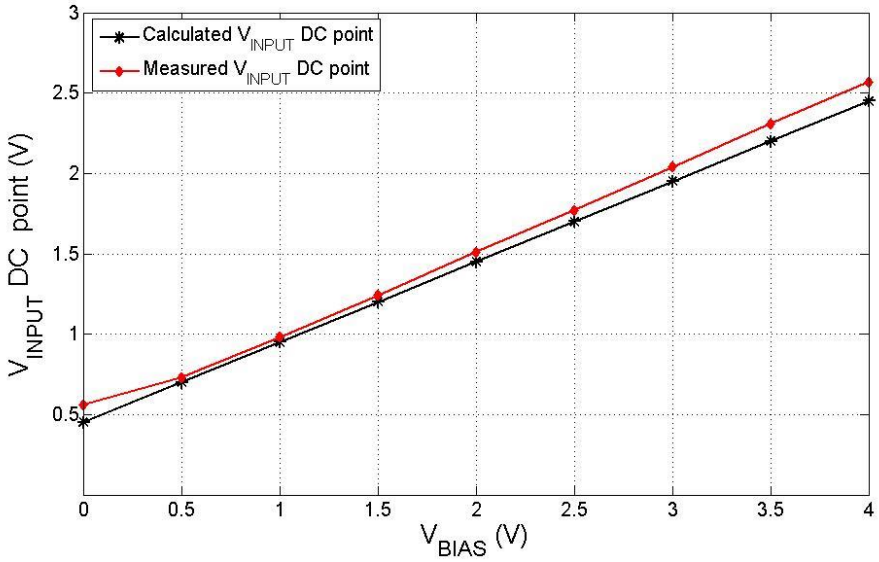

Figure 5-49 – DC operating point at the non-inverting input of OP1 (V_{INPUT}) with varying V_{BIAS}

The frequency response measurement was conducted to find the bandwidth of the microLED/COFBK driver. The experimental setup is the same as the frequency response measurement for the microLED/CCFBK driver, as presented in Section 4.7.3 (Figure 4-31) and was conducted on all TIA gain configurations. Figure 5-50 shows examples of the output from the microLED/COFBK driver captured using a PDA10A photodetector and displayed on the signal analyser (DSA90840A), showing the optical power response of the driver with 20kΩ and 50kΩ TIA gain configurations, with a ramp-signal (triangle wave) driven at V_{INPUT} and V_{BIAS} was set at 2V. Figure 5-50(a) shows that the optical power of the microLED/COFBK driver with the 20kΩ TIA gain configuration producing triangle wave signals.

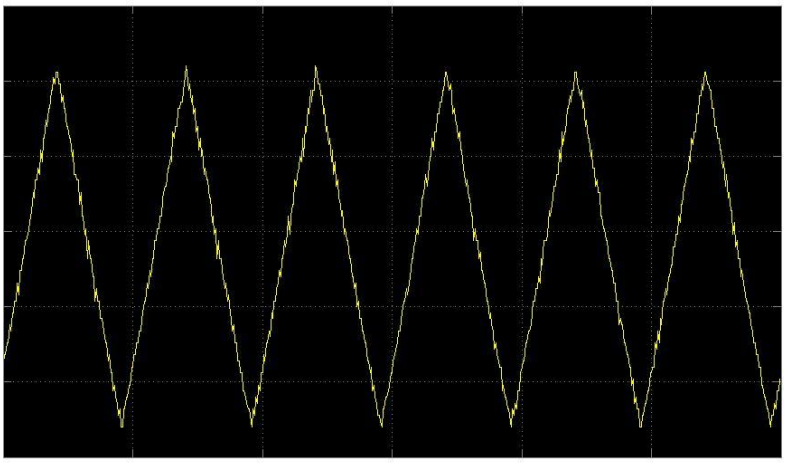

(a)

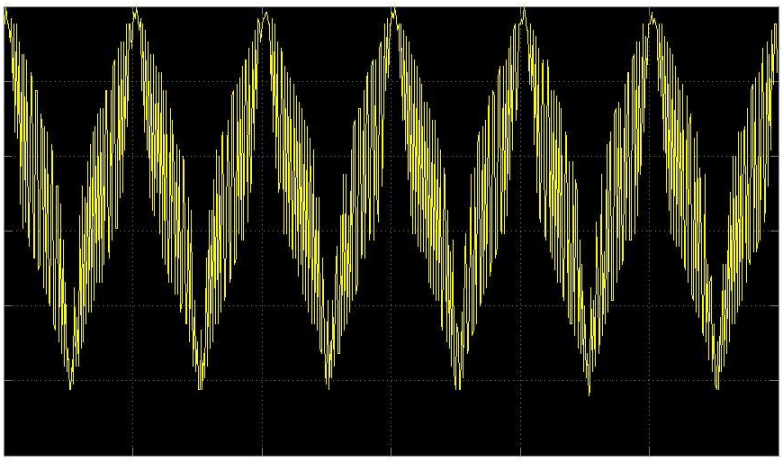

(b)

Figure 5-50 – Example of the microLED/COFBK output captured using PDA10A, driven with a ramp-signal for (a) 20kΩ TIA gain and (b) 50kΩ TIA gain configurations

Figure 5-50(b) on the other hand, shows that the optical power response of the driver with 50kΩ TIA gain configuration, clearly showing that the driver is oscillating, which indicates that the feedback system for said configuration is unstable. The stability of the driver, especially for the 50kΩ TIA gain configuration, changes as V_{BIAS} is varied. This is shown in Table 5-10 where the 50kΩ TIA gain configuration was found to be stable when V_{BIAS} is set to 0V, 0.5V or 4V. As discussed in Section 5.5.2.2, the gain-bandwidth product of OP1 has to be lower than the bandwidth of the TIA to ensure stability. When V_{BIAS} is set to 0V, 0.5V or 4V, the gain-bandwidth product of OP1 has significantly reduced compared to when it is biased at its optimum operating point, thus the loop gain of the feedback system achieved greater stability. The lower gain-bandwidth product in OP1 is due to the cascode transistors (Figure 4-14) operating at the edge of the saturation region or in the linear region. Due to the unstable operation of the microLED/COFBK driver with 50kΩ TIA gain configuration, only the frequency response of the 10kΩ and 20kΩ TIA gain configurations are presented and discussed in this section.

TIA gain configuration	V_{BIAS}								
	0	0.5	1.0	1.5	2	2.5	3	3.5	4
10kΩ	yes	yes	yes	yes	yes	yes	yes	yes	yes
20kΩ	yes	yes	yes	yes	yes	yes	yes	yes	yes
50kΩ	yes	yes	No	No	No	No	No	No	yes

Table 5-10 – Stability state of the microLED/COFBK driver vs. V_{BIAS} for all TIA gain configuration

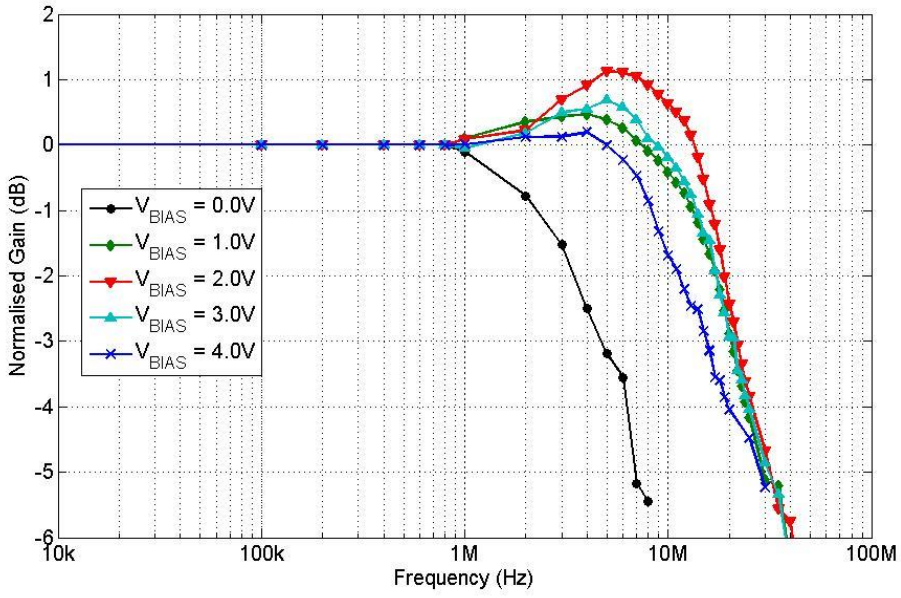

Figure 5-51 – Frequency response of the microLED/COFBK driver with 10kΩ TIA gain configuration

Figure 5-51 shows the frequency response of the microLED/COFBK driver with 10kΩ TIA gain configuration where V_{BIAS} is swept from 0 to 4V in 1V steps and the V_{INPUT} DC point is set according to Figure 5-49. As shown in Figure 5-51, the bandwidth of the driver increases as V_{BIAS} increases from 0V to 2V, but reduces if V_{BIAS} is further increased. This is as expected as OP1 is biased at its optimum operating point when V_{BIAS} is set to be around 2V (Figure 5-49), thus the feedback system produces the highest bandwidth. When V_{BIAS} is further increased, OP1 moves away from its optimum operating point, hence the feedback system loses bandwidth. Another trend highlighted in Figure 5-51 is the gain-peaking in the frequency response when V_{BIAS} is set between 1V to 3V, which suggests that the feedback system is marginally stable within this biasing point. Moreover, the gain peaking was also shown to increase as the bandwidth of the driver increases. This indicates that there is a relationship between the gain-peaking in the frequency response with the gain-bandwidth product of OP1. As V_{BIAS} is increased to 2V, the gain-bandwidth of OP1 increases and therefore the phase margin of the loop gain of the feedback system reduces, hence putting the driver in a less stable state. As a result, the gain-peaking in the frequency response also increased. As V_{BIAS} is further increased, the gain-bandwidth product of OP1 reduces, therefore increasing the phase margin of the feedback system. Consequently the gain-peaking in the frequency response is reduced.

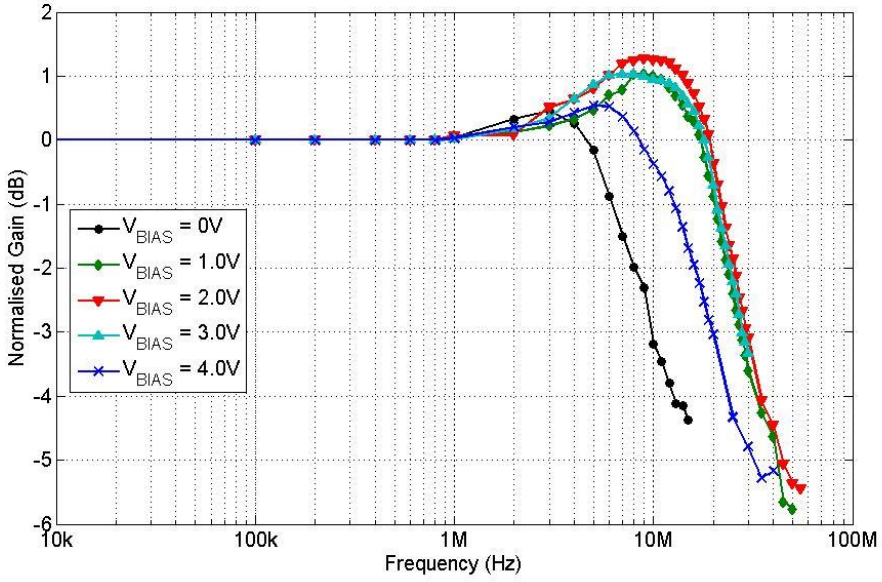

Figure 5-52 – Frequency response of the microLED/COFBK driver with 20kΩ TIA gain configuration

The frequency response for the 20kΩ TIA gain configuration is shown in Figure 5-52, behaving in a similar fashion to the 10kΩ TIA gain configuration. Two important trends are seen in Figure 5-52

1. The bandwidth for each V_{BIAS} point in the 20kΩ TIA gain configuration is higher than that of the same bias point in the 10kΩ TIA gain configuration. This is expected as the gain in the feedback network for the 20kΩ TIA gain configuration is higher. As discussed in Section 5.5.2.2, as the gain in the feedback network increases, the bandwidth of the feedback system also increases. The highest bandwidth measured was 31MHz for the 20kΩ gain configuration compared to 23MHz for the 10kΩ TIA gain configuration.
2. The gain-peaking in the frequency response for the 20kΩ gain TIA configuration is higher than in the 10kΩ gain TIA configuration. The highest peak measured for the 20kΩ gain configuration is 1.26 dB compared to 1.12 dB in the 10kΩ gain TIA. This is because the TIA bandwidth with 20kΩ TIA gain configuration is about two times lower than for the 10kΩ TIA gain configuration. Therefore, the bandwidth of the 20kΩ TIA is closer to the gain-bandwidth product of OP1 hence putting the system in a lesser stable state.

Further analysis and discussion on the cause of the gain-peaking in the frequency response is presented in Section 5.9.3.

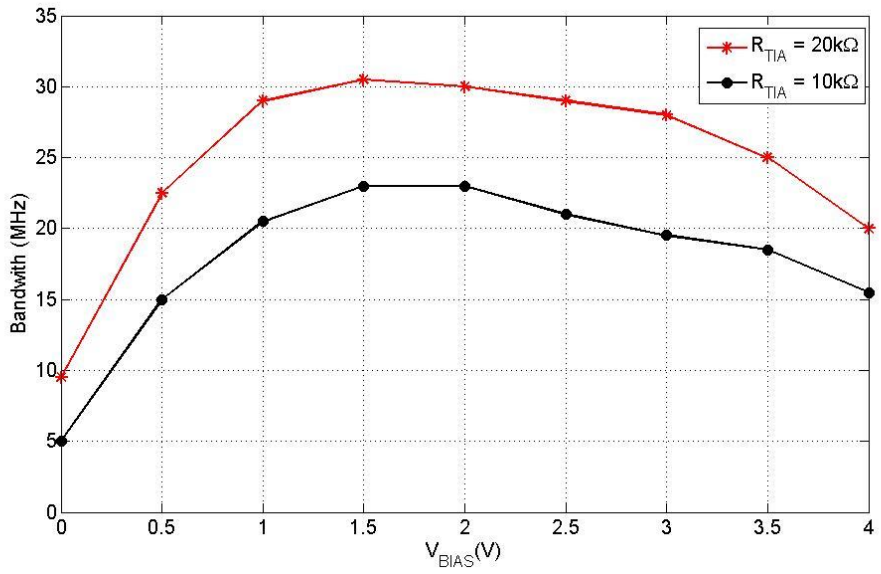

Figure 5-53 – Bandwidth as a function of V_{BIAS} for the 10kΩ and 20kΩ configuration

Figure 5-53 shows the summary of the bandwidth of the microLED/COFBK driver as a function of V_{BIAS} for both 10kΩ and 20kΩ gain TIA configurations. Both configurations show a similar trend where the bandwidth reaches its optimum operating point when V_{BIAS} is biased between 1.5V and 2V and reduces if biased outside this range. The bandwidth of the microLED/COFBK driver with 20kΩ gain TIA configuration shows about 1.3 times higher bandwidth than the 10kΩ gain TIA configuration. This is consistent for all V_{BIAS} points. Table 5-11 summarises the measured frequency response for both configurations when V_{BIAS} is set to 2V.

	V_{BIAS}	V_{INPUT} DC point	Bandwidth	Gain-peaking
20kΩ gain configuration	2	1.6	30.5 MHz	1.26 dB
10kΩ gain configuration	2	1.57	23 MHz	1.12 dB

Table 5-11 – Summary of frequency response comparison between microLED/COFBK driver with 10kΩ and 20kΩ gain TIA configurations.

5.9. Measurement vs. Simulation

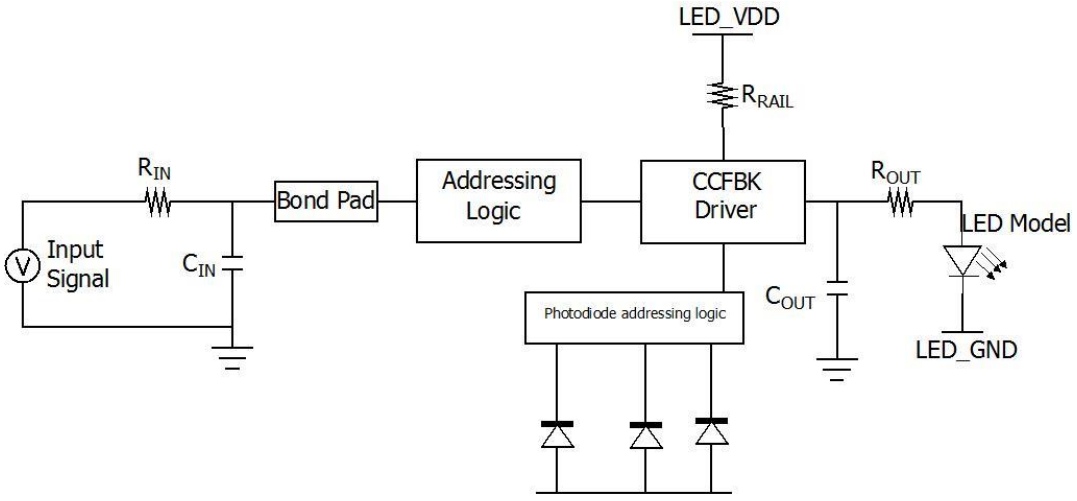

Figure 5-54 – Schematic diagram of the microLED/COFBK driver with parasitic component simulation

The measured results of the microLED/COFBK driver, in general, demonstrate a reduced level of performance compared to those predicted by the simulations. This section investigates the reasons underlying the shortfall. Figure 5-54 shows the schematic circuit diagram for the re-simulation, which also includes the three photodiode options. The microLED/COFBK driver post-layout parameter extraction was used for re-simulations and the microLED Verilog-A

optical power model was adjusted to match the L-V characteristic of the measured microLED/COFBK driver.

The parasitic component values previously used in the CCFBK driver investigation (Section 4.8) are used in the re-simulation. The values of these parasitic components are summarised in Table 4-8. As with the CCFBK driver, the input parasitic components do not have any effect on the microLED/COFBK driver. It is only R_{RAIL}, C_{OUT}, R_{OUT} and the photodiodes that affect the performance of the microLED/COFBK driver.

5.9.1. MicroLED Optical Power Degradation

The maximum current driving capability of the microLED/COFBK driver was measured to be about 60mA, thus producing an optical power of about 2.5mW. The optical power of the microLED/COFBK is, however, lower than the optical power measured from the microLED/CCFBK driver, which produces about 3.5mW from 67mA current. One of the plausible explanations for the degradation in the light produced by the microLED is the modification made to the microLED structure where the metal layer around the microLED was removed. The metal layer acts as a contact layer and more importantly as a mirror which directs the generated lights "forward" (Figure 5-3). The removal of the metal layer around the microLED was made to assist the feedback operation so that there is more light in the feedback path. However, this comes at a cost of reducing the "forward" light.

5.9.2. Feedback Gain and DC Characteristics

The DC characteristic was re-simulated by altering $\Re_{PD}$ and β_L to be the same as the measured value (Section 5.8.1 and Section 5.8.2), where $\Re_{PD}$ is set to be 0.051 (51mA/W) while β_L is set to be 0.073 (7.3%) and only one photodiode is selected. Figure 5-55 shows the L-V characteristic of the re-simulated microLED/COFBK driver with 20kΩ TIA gain configuration. From the simulation, when β_L is set to be equal to 0.073, the re-simulated optical power response has a shallower slope than the measured result, as shown in Figure 5-55. This indicates that the chosen simulated parameters (β_L or $\Re_{PD}$ or both) produces higher gain in the feedback path than the calculated value found in the measurement. To find the cause of the difference between the re-simulated and the measured results, $\Re_{PD}$ is kept the same at 0.051 (51mA/W) while β_L is swept from 0.073 to a lower value. The simulated result with β_L of 0.055 is plotted in Figure 5-55, showing a closer fitted line with the measured result. This

provides some confirmation that the calculated feedback channel gain ($\beta_L \Re_{PD}$) value obtained from the measurements are higher than the actual value. The simulation with β_L of 0.055 was repeated for the 50kΩ TIA gain configuration, and is plotted in Figure 5-56.

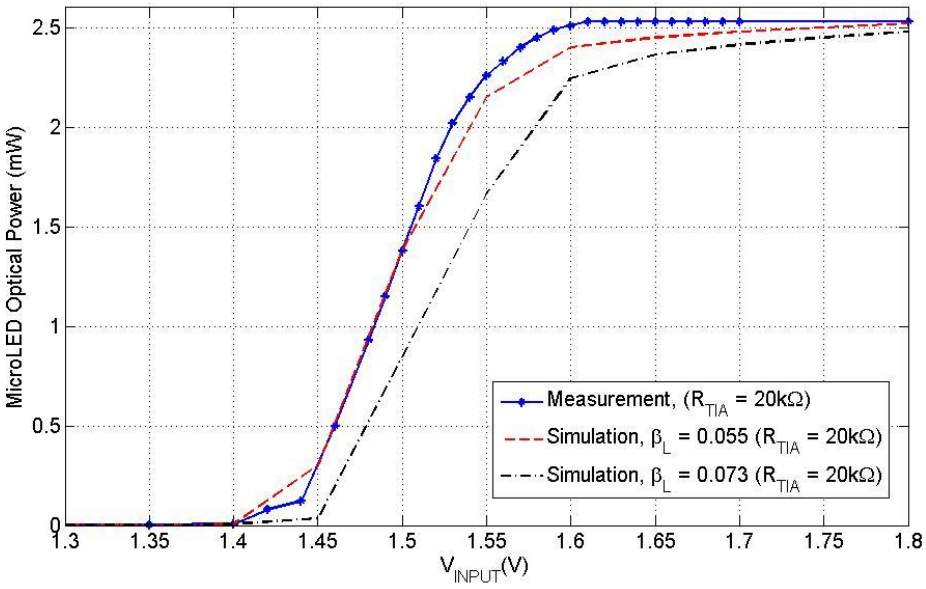

Figure 5-55 – L-V characteristic of the microLED/COFBK driver with 20kΩ TIA gain configuration comparison between measurement and re-simulation ($\Re_{PD}$was set to 0.051A/W)

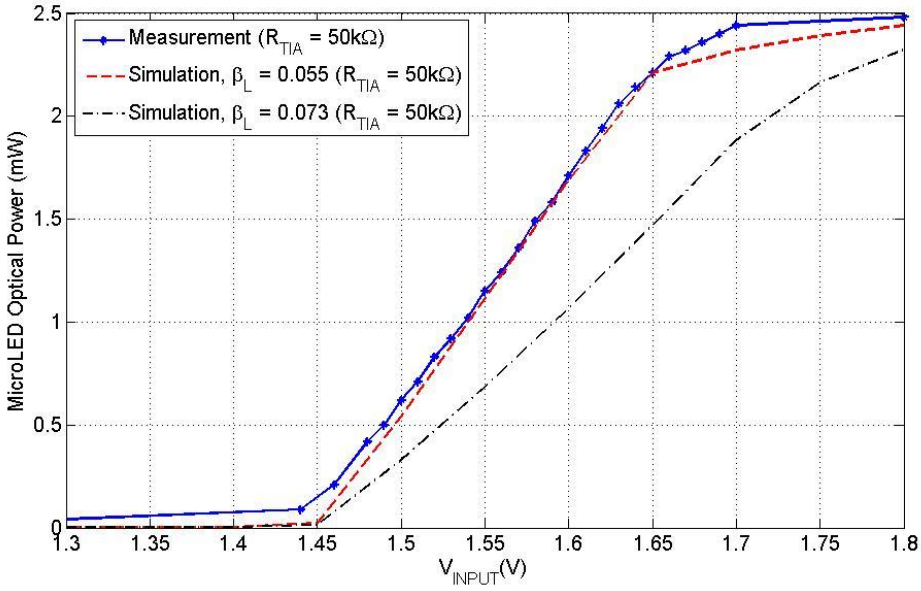

Figure 5-56 – L-V characteristic of the microLED/COFBK driver with 50kΩ TIA gain configuration comparison between measurement and re-simulation

The simulated L-V characteristic of the microLED/COFBK driver with 50kΩ TIA gain configuration shows the same trend as the 20kΩ TIA gain configuration, where when β_L is set to 0.073, the microLED optical power shows a less steep response than the measured result and a closely fitted response was found when β_L is reduced to 0.055. The consistency in the simulated results gives a higher degree confirmation that the actual feedback channel gain is lower than the measured values. One of the possible causes of the differences between the measured and simulated results are the additional current, "leaked" from the other two photodiodes option that were supposedly 'inactive' during the measurement. This is depicted in Figure 5-57.

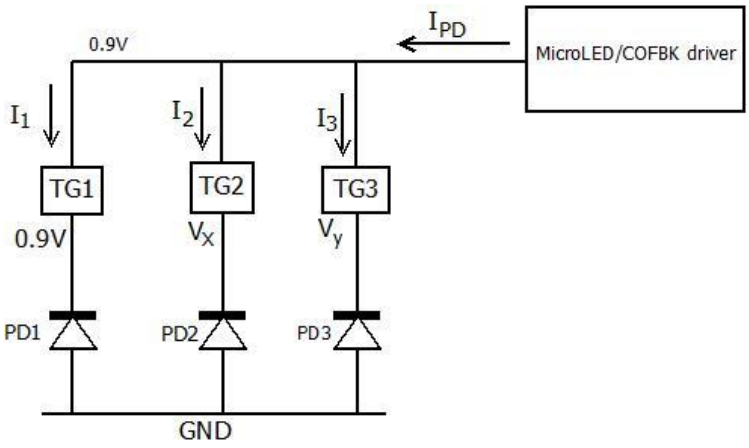

Figure 5-57 – Schematic of the photogenerated current in the three photodiode options

The total current sink by the TIA (I_{PD}) is equal to the sum of the current generated by each photodiodes (PD1, PD2 and PD3). As discussed in Section 5.7.2, the input of the TIA is biased at 0.9V which sets the reverse bias voltage of the chosen photodiode. The photodiodes are selected by addressing the corresponding transmission gate (TG1, TG2 and TG3) and only one photodiode can be selected at a given time. Assuming PD1 is selected, the bias voltage on PD1 will be 0.9V. V_X and V_Y are the bias voltages of the unselected PD2 and PD3 respectively, which in theory should be close to 0V. During the optical feedback operation, as V_{INPUT} increases above the set V_{BIAS}, the optical power increases. The "feedback" light from the microLED is detected by all photodiodes, which are placed at three of the four sides of the COFBK driver pixel (Figure 5-37). Because V_X and V_Y are close to zero, the depletion region in PD2 and PD3 is much smaller than PD1 (Equation 5-5). Therefore, the photocurrent formed by PD2 and PD3 (I_2 and I_3) should be insignificant compared to PD1 (I_1). However, this is not the case even if V_X and V_Y is assumed to be 0 as there is still photocurrent generated due

to the built-in potential (ϕ_i in Equation 2-18), which depends on the chosen process technology doping concentration of the p and n region.

Therefore, the TIA output voltage response measured during the experiment is actually the sum of the photogenerated current in the three photodiodes ($I_1 + I_2 + I_3$), albeit I_2 and I_3 are each much less than I_1. Therefore, the calculated $\Re_{PD}$ and β_L obtained from the measurements in Section 5.9.2 are the values for the three photodiodes; the selected PD1 and the non-selected PD2 and PD3. The "additional" photogenerated current works in favour of the optical feedback as it increases the feedback channel path gain. The actual $\Re_{PD}$ and β_L for a single photodiode unfortunately, cannot be determined.

The total current measured from the microLED/COFBK driver is about 60mA, which is lower than the 100mA, as by design. The cause of the current shortfall is R_{OUT} (Figure 5-54). R_{OUT} is the parasitic resistance, which includes the Metal4 resistance, the bump-bond resistance, and the resistance of the microLED and its metal contact. Referring to Figure 5-54, R_{OUT} causes an 'additional' voltage drop between M1 and the microLED. This additional voltage drop reduces the gate-source voltage of M1 and hence reduces the current. Figure 5-58 shows the simulation of the microLED/COFBK driver with parasitic components, using the 50kΩ TIA gain configuration as an example, and $\Re_{PD}$ and β_L of 0.051 and 0.055 respectively, compared with the 'ideal' simulation and measured result.

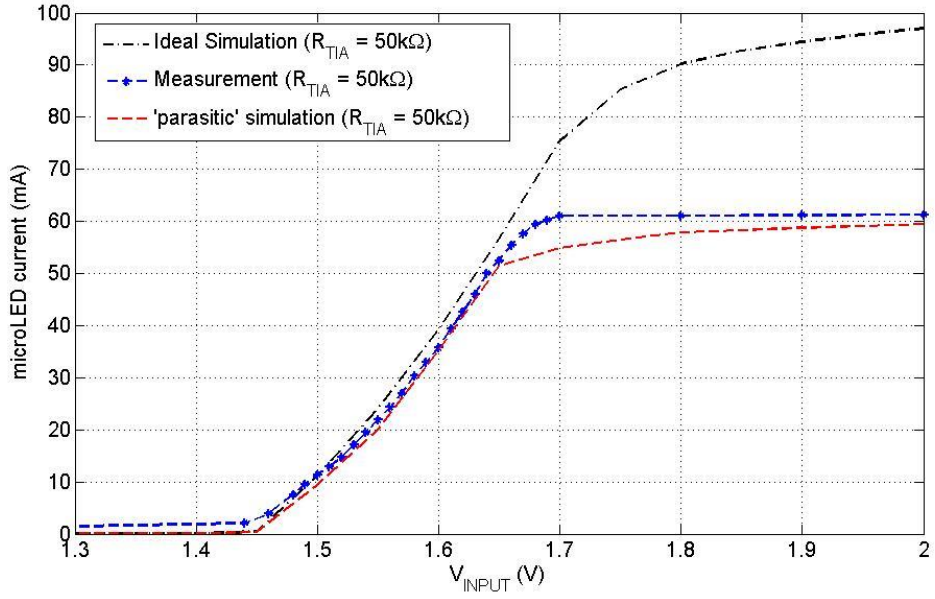

Figure 5-58 – M1 DC current response comparison of COFBK driver with 50kΩ TIA gain between ideal simulation, simulation with parasitic and measurement

5.9.3. Parasitic Frequency Response

The frequency response measurement (Section 5.8.4) shows a gain-peaking for the 10kΩ and 20kΩ TIA gain configurations while the 50kΩ TIA configuration oscillates. This can be explained by investigating the additional photodiodes that were initially added to the driver to provide options to select the photodiode that captures the most "feedback" light. However, the additional photodiodes have caused an increase to the capacitance of the input of the TIA (C_{in}). As shown in Equation 5-20, the bandwidth of the TIA is strongly dependent on C_{in} where, as C_{in} increases, the bandwidth of the TIA decreases. As a result of the reduced TIA bandwidth, as explained in Section 5.5.2.2, the feedback system moves into a less stable state. If the bandwidth of the TIA is approximately equal or lower than the gain bandwidth product of OP1, the feedback system may fall into an unstable state, which causes the oscillation to the output signal. The gain peaking in the frequency response is also related to the reduced TIA bandwidth, where a TIA with a lower bandwidth produces a greater gain-peaking. This was the reason why the optical power output oscillates for the 50kΩ TIA gain configuration while the gain peaking in the frequency response for the 20kΩ TIA gain configuration is greater than the 10kΩ TIA gain configuration (Figure 5-51 and Figure 5-52).

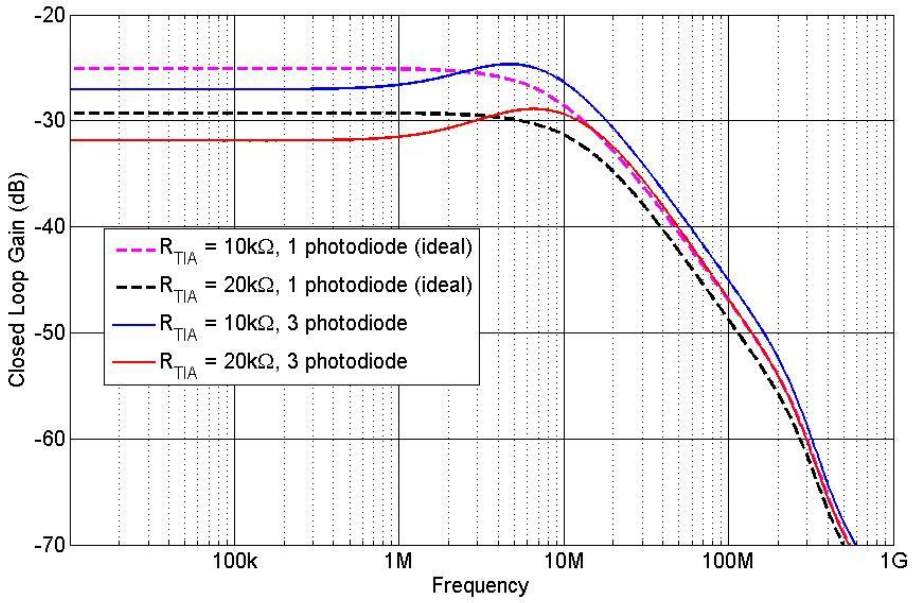

Figure 5-59 – Frequency response of the microLED/COFBK driver simulation comparison between "ideal" (1 photodiode) and "parasitic" (3 photodiodes) loading

Figure 5-59 compares the "ideal" frequency response of the microLED/COFBK driver, with supposedly only one photodiode loading the TIA, and the "parasitic" frequency response in

which all three photodiodes are loading the TIA. The simulated "ideal" frequency response shows a flat band and 20 dB per decade roll off after the cut-off frequency. The simulated "parasitic" frequency response on the other hand, shows a gain-peaking, as seen in the measurements. Additionally, the bandwidth of the driver increases because of the gain-peaking. Another important point to note, taking the 20kΩ configuration as an example, is that the "ideal" frequency response has a higher closed loop gain than that of the "parasitic". The closed loop gain can be approximated as $\frac{1}{\beta}$ (Equation 4-2), where β is the gain in the feedback path. As explained in Section 5.9.2, the 'non-active' photodiodes also contributes to the gain in the feedback channel thus, the closed loop gain of the "parasitic" driver is lower than the "ideal" driver, which then contributes to the slightly higher bandwidth.

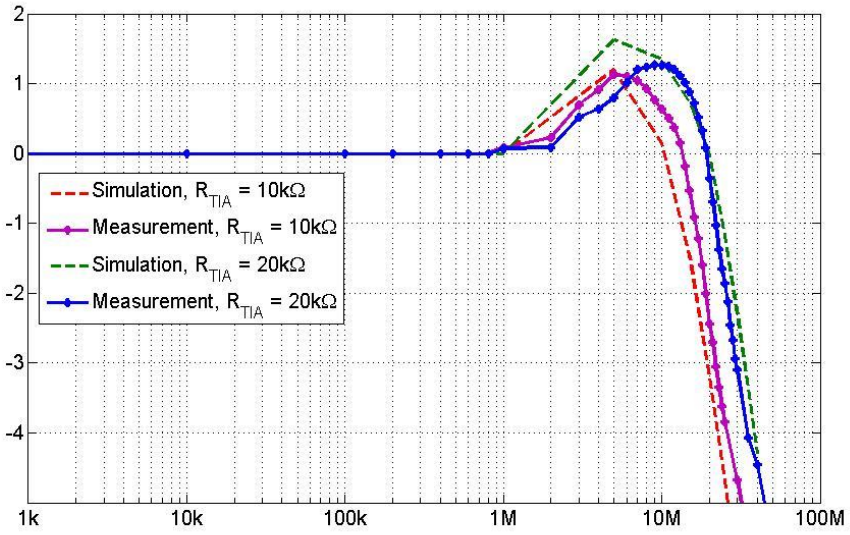

Figure 5-60 – Re-simulated vs. measured result of the frequency response of the microLED/COFBK driver for 10kΩ and 20kΩ TIA gain configurations.

The frequency response simulation (using the chosen $\Re_{PD}$ and β_L, as explained in Section 5.9.2) was re-conducted following the exact same steps performed for the microLED/COFBK driver frequency response measurements (Section 4.7.3(Figure 4-31)) and V_{BIAS} set to 2V. The re-simulated result is compared with the measured result for both the 20kΩ and 10kΩ TIA gain configurations, as shown in Figure 5-60. From the figure, the re-simulated result shows a bandwidth of 32MHz, which is slightly higher than the measured result, which is about 31MHz for the 20kΩ TIA gain. For the 10kΩ configuration, the simulated result shows a bandwidth of 21MHz. This is slightly lower than the measured bandwidth of about 23MHz. From the comparison, it is fair to say that the combination of the chosen $\Re_{PD}$ and β_L in the re-simulation

has produced a similar response as found from the measurement. Therefore the combination $\Re_{PD}$ and β_L ($\Re_{PD}\beta_L$) of the microLED/COFBK driver can be estimated to be 0.0028.

5.10. Summary

The microLED/COFBK driver, which combines a transmitter and a detector within a single pixel, was designed to improve the linearity of the optical power output of the microLED for OFDM transmission purposes. The theory of optical feedback and the light detection method were discussed in this chapter, followed by the macromodel and the transistor level design of the COFBK driver. To cope with the uncertainty of the 'feedback' light, the driver was designed with three TIA gain configurations and the option to choose one from three different photodiodes. A 100µm square microLED was bump-bonded with the COFBK driver. The driver was capable of driving the microLED with current up to approximately 60mA, producing about 2.5mW of optical power. The bandwidth of the microLED/COFBK driver was measured to be up to 31MHz.

The DC measurement results, presented in Section 5.8.3, show that the linearity of the optical power output of the microLED/COFBK driver demonstrated improvement in comparison to the microLED/CCFBK driver counterpart with the degree of non-linearity found to be only up to 4.40% for 2.2mW of optical power range. From the results obtained, it can be said that the optical feedback technique of integrating microLED and photodiode within a pixel has been proven to linearize the microLED optical power output response. Further discussion on the DC performance comparisons between the microLED/CCFBK driver and the microLED/COFBK driver are presented in Chapter 6.

While the DC response of the optical power output of the microLED/COFBK driver exhibits good linearity, the driver faces problem with gain-peaking in its frequency response. The cause of the gain-peaking was due the additional photodiodes that were added in the design, as investigated and presented in Section 5.9.2. As mentioned earlier, the additional photodiodes were added to assist the capturing of the feedback light. However, they increase the input capacitance of the TIA, hence reducing the bandwidth of the TIA, which resulted in a 'peak' in the frequency response. The effect of the gain-peaking on the linearity of the AC response and the performance of the microLED/COFBK driver transmitting OFDM signal are further discussed in Chapter 6.

Chapter 6 : Linearity and BER Performance for VLC Application Comparison

6.1. Introduction

Today, wireless communication has become an essential part of almost everyone's daily life and the number of users has increased exponentially over the last decade [1, 118]. RF channels, as the main method of wireless communication, are becoming more congested as the number of user increases [119, 120, 121]. This has led to numerous efforts to find alternatives to reduce the dependency on RF. One of the proposed solutions is VLC, which uses visible light as the medium of data transmission. OFDM is one of the modulation schemes, which was adopted from RF that was proposed to be implemented in VLC in order to increase the data transmission rate. However, as discussed in Section 2.3.5, the OFDM scheme requires high PAPR to ensure low BER transmission. Because of the high PAPR requirement, the linearity of the driver becomes an important factor. A non-linear transmitter limits the dynamic range, which causes clipping and signal degradation. In VLC, the optical source (microLED in this case) is the main cause of non-linearity. Hence, two analogue modulated drivers (microLED/CCFBK driver and microLED/COFBK driver) were designed in this project with the aim to improve the linearity of the transmitter.

In Chapter 4, a microLED/CCFBK driver was presented where the current produced by the driver is linearly proportional to the input voltage signal. The linearity of the optical power output can be improved by reducing the optical power operating range. In Chapter 5, a microLED/COFBK driver was presented in which, by using an optical feedback technique, the optical power output is linearized with respect to the input voltage signal. The linearity of the DC characteristic of both drivers were presented in Chapter 4 and Chapter 5 respectively. In this chapter, the linearity of the DC and AC characteristics of both the microLED/CCFBK driver and microLED/COFBK driver are compared. The capability of both drivers to transmit an OFDM signal is demonstrated and analysed later in the chapter.

6.2. Linearity of DC Response Comparison

The DC linearity analysis of the microLED/CCFBK driver and microLED/COFBK driver (as presented in Section 4.7.1 and Section 5.8.3 respectively) are compiled in Table 6-1. From Table 6-1, the microLED/CCFBK driver displays non-linearity percentage that varies from 1.49% to 12.18% depending on the selected optical power range. As discussed in Section 4.7.2, the non-linearity of the microLED/CCFBK driver was inherited from the L-I characteristic of the microLED, and from Table 6-1, it is evident that the linearity can be improved by reducing the optical power output range. Furthermore, the linearity can also be affected by the DC bias point of the optical power output. For example, consider entry 2 and 3 of Table 6-1, where the optical power range is similar for both entries with values of 2.23mW and 2.05mW respectively, but entry 2 has a higher DC bias point than entry 3. From the table, the non-linearity of entry 3 is greater than entry 2 even though the optical power is slightly lower. This suggests that the microLED/CCFBK driver exhibits greater linearity at a higher DC bias point compared to the lower DC bias point for a similar optical power range.

	Driver	Optical Power Output Range	R^2	Non-linearity percentage
1	Current feedback	3.31mW (0.3 - 3.61mW)	0.9701	12.18%
2		2.23mW (1.03-3.26mW)	0.9872	7.46%
3		2.05mW (0.3-2.08mW)	0.9875	7.81%
4		1.8mW (1.56-3.36mW)	0.9923	5.78%
5		1mW (2-3mW)	0.9971	1.49%
6	Optical feedback with 10kΩ TIA gain	2.13mW	0.9955	4.40%
7	Optical feedback with 20kΩ TIA gain	2.14mW	0.9978	2.77%
8	Optical feedback with 50kΩ TIA gain	2.12mW	0.9989	2.51%

Table 6-1 – Table of linearity of the DC performance of the microLED/CCFBK driver and the microLED/COFBK driver

The microLED/COFBK driver on the other hand, was aimed to pre-distort the current supplied to the microLED in order to linearize the light output. Table 6-1 shows that the microLED/COFBK driver exhibits lower non-linearity percentage than the microLED/CCFBK driver counterpart (of comparable optical power range), with value varying from 2.51% to 4.40%. The higher non-linearity (of 4.40%) in the 10kΩ TIA gain configuration is due to the very small input voltage range (which is about 70mV). The

measuring equipment is limited by the small input range which reduces the reading accuracy. The non-linearity for the 20kΩ and 50kΩ TIA gain configurations shows similar non-linearity percentage of 2.77% and 2.51% respectively. As a comparison with the microLED/CCFBK driver, consider a similar optical power operating range, the non-linearity percentage has reduced from about 7.8% (entry 3) to about 2.5% (entry 7). Therefore, this proves that the microLED/COFBK driver has reduced the non-linearity of the optical source transmitter by about 5.3 percentage point.

6.3. Linearity of the AC Response

The linearity of the AC response of the two drivers was then investigated. For this experiment, LED_GND is biased at –3V for both drivers. The experimental setup is the same as the bandwidth measurement as mentioned in Section 4.7.3 and shown in Figure 4-31. A sine wave is applied to the driver's input and the optical power response from the microLED is detected by the Si-Photodetector (PDA10A), which is then fed into the digital signal analyser (DSA90804A). FFT is then applied to the output signal and the results are analysed.

The FFT spectrum shows the linearity of the AC response of the driver output signal in the frequency domain. Based on the Fourier Transform principle, any signal can be reconstructed by adding multiple pure sinewaves with appropriate amplitude, frequency and phase [122]. Therefore, in theory, a pure sinewave produced in a linear system should consist of only one sinewave signal with a particular frequency and phase. A schematic representation of the FFT spectrum of the output signal is shown in Figure 6-1. The important elements of the FFT plot are marked with letters A to G and are explained in Table 6-2.

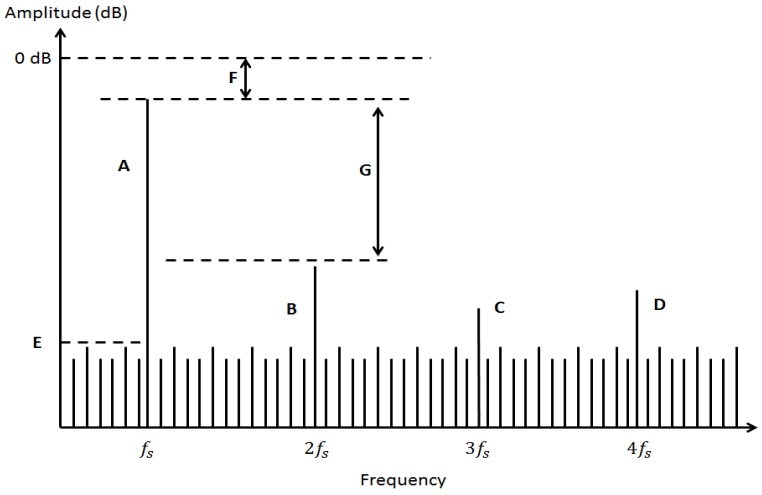

Figure 6-1 – Schematic representation of an FFT spectrum

A	Fundamental signal magnitude at frequency f_s. Measured in decibels (dB)
B, C and D	The 2nd, 3rd and 4th harmonic magnitude. Occurs at $n.f_s$, where n is an absolute number greater or equal to 2
E	Average noise floor of the detector
F	Headroom of the Fundamental Signal. The distance from the fundamental signal (A) to 0 dB
G	The Spurious Free Dynamic Range (SFDR). The distance from the fundamental signal (A) to the highest spur (in dB).

Table 6-2 – Definition of the elements in FFT spectrum

The headroom of the fundamental signal is an important element to ensure that the signal produced by the photodetector is not clipped. If signal clipping occurs, the FFT plot will show distortion in the form of spurs at frequencies other than the fundamental frequency. The linearity of the AC response of the output signal from the driver is quantified by the value of its total harmonic distortion (THD) and SFDR.

$$THD = \frac{\sqrt{V_2^2 + V_3^2 + V_4^2 + V_5^2}}{V_1} \qquad \textbf{Equation 6-1}$$

Harmonic distortion is the ratio of the RMS value of the specified harmonic to the RMS of the fundamental signal. Therefore, THD is the ratio of the sum of the RMS values of all harmonic components to the fundamental signal, as shown in Equation 6-1, where V_1, V_2 , V_3, V_4, and V_5 are the RMS values of the respective harmonic (in general, only the first 5 harmonics are significant and those are used in this thesis).

SFDR, on the other hand, is the ratio of the RMS value of the fundamental signal to the RMS value of the largest spurious signal, regardless of where it falls in the frequency spectrum, which quantifies the amount of distortion in the system. In general, harmonic spurs are caused by distortion in the fundamental signal. Spurs resulting from the non-linearity of the output signal will appear as multiples of the output signal frequency (B, C and D). Non-harmonics spurs are the result of other devices or external noise sources. In this analysis, SFDR is quantified as the distance of the fundamental signal to the highest harmonic spur (G in Figure 6-1) unless otherwise stated.

6.3.1. MicroLED/CCFBK Driver

An FFT analysis was conducted on the microLED/CCFBK driver with varying optical power and frequency. By varying optical power, the AC linearity of the signal is expected to improve as the optical power output range is reduced. The linearity is also investigated as the frequency increases.

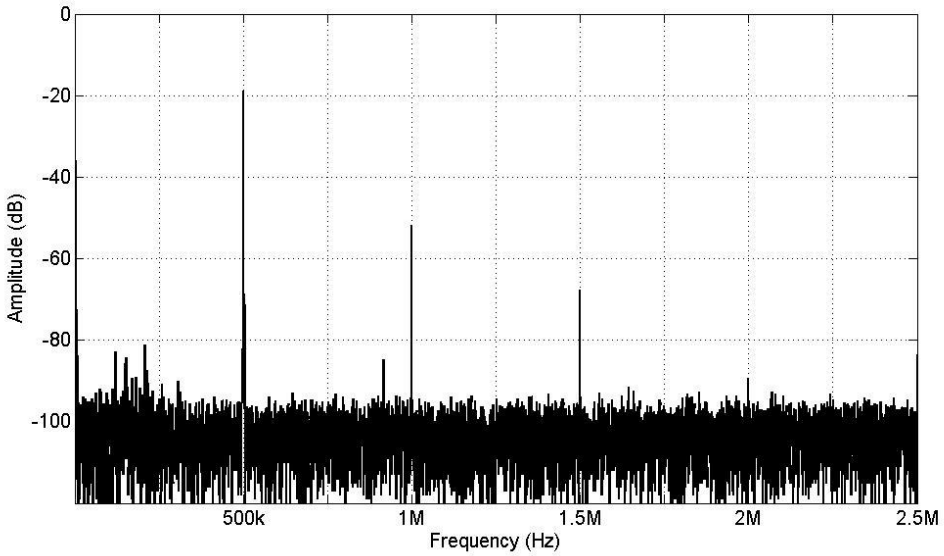

Figure 6-2 – FFT spectrum of microLED/CCFBK driver producing optical power of 2.23mW with sinewave input of 500 kHz

Figure 6-2 shows an example of the FFT spectrum captured from the microLED/CCFBK driver output, producing about 2.23mW of optical power when a 500 kHz sine wave is applied to the input. The fundamental spur is found at 500 kHz, which is to be expected from a 500 kHz input sinewave signal. The amplitude of the fundamental component is recorded to be –18.8 dB. The worst spur was found at 1MHz, showing the amplitude of –51.87 dB. The SFDR of the signal is then calculated to be 33.04 dB. Other spurs occur at 1.5MHz, 2MHz and 2.5MHz, but with a much lower amplitude. The spurs occur at the signal's harmonics, which indicate that some degree of distortion take places in the fundamental signal. Using the values obtained, the THD of the signal is calculated to be 2.26%.

To assist with explanation and comparison purposes, four optical power ranges are chosen and labelled as Range A, B, C, and D respectively, as summarised in Table 6-3. The maximum optical power output range chosen is approximately 2.2mW (A and B). This value was chosen to serve as a comparison to the microLED/COFBK driver, which can produce around 2.2mW

of optical power. The maximum optical power that can be produced by the microLED/CCFBK driver is 3.6mW. This value, however, is excluded in this analysis as the R^2 value and the non-linearity percentage is higher. Therefore, the SFDR and THD are expected to be worse than the chosen values in Table 6-3.

	Optical Power Range	R^2	Non-linearity percentage
Range A	2.05mW (0.3 - 2.08mW)	0.9875	7.81%
Range B	2.23mW (1.03 - 3.26mW)	0.9872	7.46%
Range C	1.8mW (1.56 - 3.36mW)	0.9923	5.78%
Range D	1mW (2 - 3mW)	0.9971	1.49%

Table 6-3 – Summary of chosen optical range for SFDR and THD measurement

Figure 6-3 shows the SFDR of the selected optical power range with a frequency up to 50MHz. At lower frequencies, Range D shows the highest SFDR. This is as expected as the optical power range for Range D is lower than others; hence producing higher linearity than Range A to Range C. Furthermore, as discussed in Section 6.2, higher linearity can be obtained by biasing at the upper half of the L-V characteristic. This can be seen as a comparison in Range A and Range B. Range B exhibits higher optical power than Range A, but has higher SFDR than Range A. Therefore, The SFDR obtained in the FFT experiment is consistent with the DC measurement, where the SFDR increases as the optical power range is decreased and also depends on the biasing point on the optical power output curve.

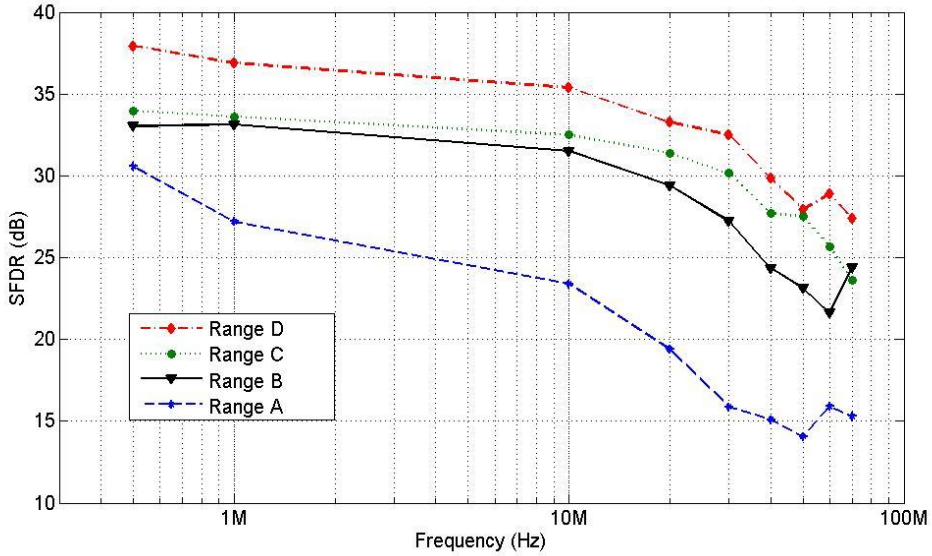

Figure 6-3 – MicroLED/CCFBK SFDR for different optical power range with varying frequency

The reduction of the SFDR is also related to the bandwidth of the microLED/CCFBK driver. As presented in Section 4.7.3, the bandwidth of the microLED/CCFBK driver depends on the DC bias and the amplitude of the signal. This can be seen in Range A, where the bandwidth of the selected range is about 35MHz (Figure 4-33), which is lower than the bandwidth of 50 to 55 MHz for Range B, C and D. Consequently, the SFDR for Range A drops more steeply with frequency than the SFDR of Range B, C and D.

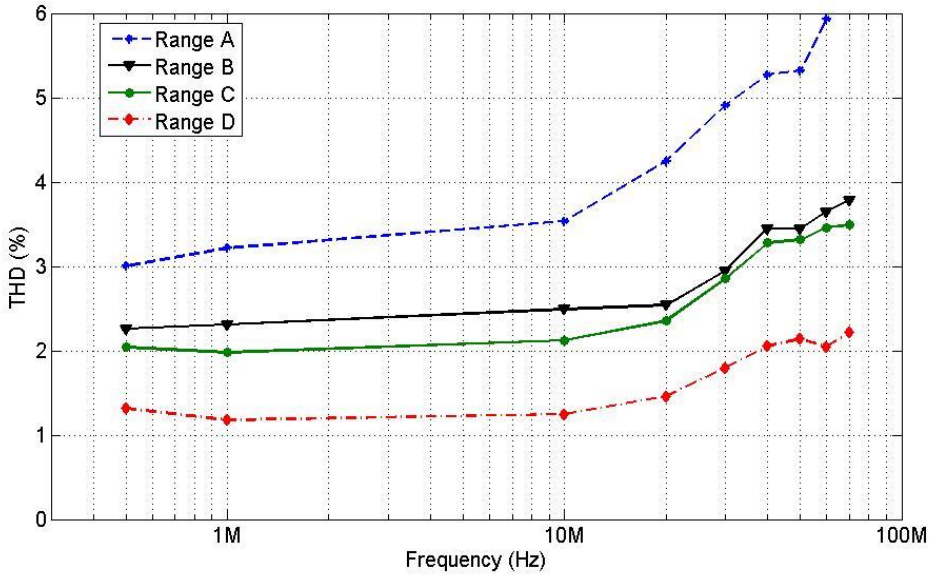

Figure 6-4 – MicroLED/CCFBK THD for different optical power range with varying frequency

Figure 6-4 shows the THD measurement for the same optical range and a similar trend is obtained for all the ranges where the THD deteriorates as the frequency increases. This indicates that the SFDR are correlated to THD. The summary of the obtained SFDR and THD are compiled in Table 6-4

	Optical Power Range	SFDR in pass band	SFDR at 3dB Bandwidth	THD in pass band	THD at 3dB Bandwidth
Range A	2.05mW	30.6 dB	15.9 dB	3.05%	4.90 %
Range B	2.23mW	33.1 dB	23.1 dB	2.26%	3.45 %
Range C	1.8mW	34.0 dB	25.7 dB	2.03%	3.46 %
Range D	1mW	37.9 dB	28.9 dB	1.32%	2.14 %

Table 6-4 – Summary of SFDR and THD results

6.3.2. MicroLED/COFBK Driver

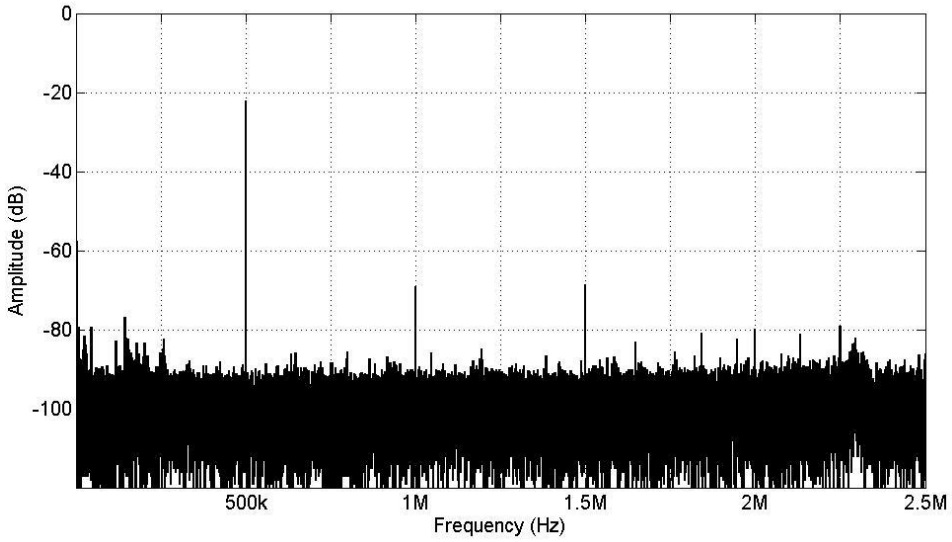

Figure 6-5 – FFT spectrum of microLED/COFBK driver with 20kΩ TIA gain configuration producing optical power of 2.2mW with sinewave input of 500 kHz

Figure 6-5 shows an example of the FFT spectrum captured from the microLED/COFBK driver with 20kΩ TIA gain configuration with V_{BIAS} set to 2V which shows improvement in both the SFDR and THD in comparison to the microLED/CCFBK driver counterpart. The driver produces about 2.14mW of optical power when a 500 kHz sine wave is applied to the input. The fundamental component was found at 500 kHz, as expected, with an amplitude of –22.15 dB. The worst spur was found at 1.5 MHz, showing the amplitude of –68.5 dB, which is also the signal's third harmonic. The SFDR is calculated to be 46.4 dB. Although there is some degree of distortion detected in the signal, the SFDR of said microLED/COFBK driver is greater than the microLED/CCFBK driver (as shown in Figure 6-2) where the SFDR value was found to be 33.04 dB. The THD of the microLED/COFBK driver, on the other hand, was calculated to be 0.67%, showing an improvement over the 2.26% which was achieved from microLED/CCFBK driver.

Figure 6-6 shows the SFDR of the microLED/COFBK driver for the 10kΩ and 20kΩ TIA gain configurations with varying V_{BIAS} (Figure 5-4) at an input signal frequency of 500 kHz with both producing approximately similar optical power. The 50kΩ TIA gain configuration is excluded in this analysis because of its signal oscillation (As presented in Section 5.8.4). The 20kΩ TIA gain configuration shows a greater SFDR of around 46 dB compared to approximately 40 dB for the 10kΩ gain configuration. The limitation of the measuring equipment contributes to the lower SFDR for the 10kΩ TIA gain configuration (as presented

in Section 5.8.3). Variations in V_{BIAS} have no substantial systematic influence on the SFDR for both TIA configurations. This is as expected as V_{BIAS} is used to bias the microLED/COFBK driver at its optimum operating point. Therefore the linearization of the signal at lower frequency is not affected by the biasing point.

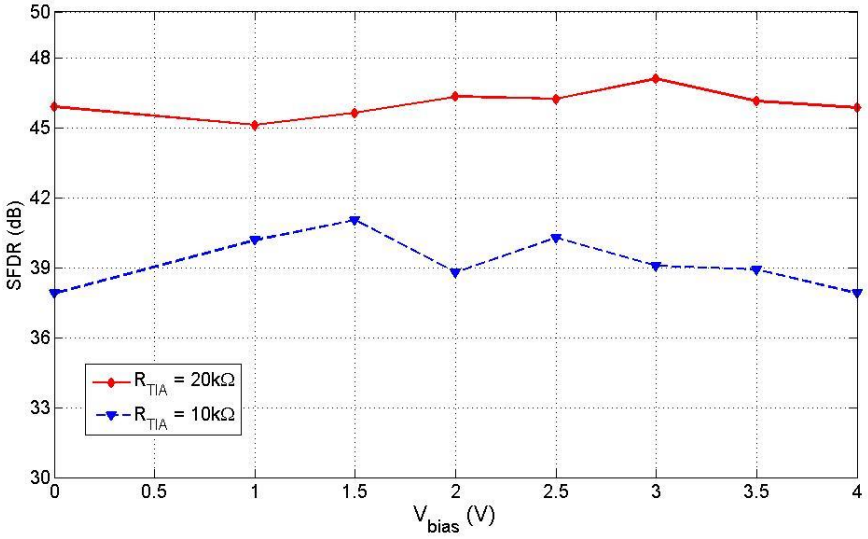

Figure 6-6 – SFDR of microLED/COFBK driver with different TIA gain configuration by varying V_{BIAS} at fundamental frqeuency of 500 kHz

The linearity analysis of the microLED/COFBK driver output signal at higher frequency is shown in Figure 6-7, showing both SFDR and THD up to 30MHz for both TIA gain configurations. V_{BIAS} was set to be 2V for this experiment. From Figure 6-7, several observations can be made:

1. The SFDR reduces as the frequency increases up to 10MHz before it starts to increase again. This is true for both the 10kΩ and 20kΩ TIA gain configurations. The drop in the SFDR for both configurations can be explained by looking at the frequency response of the microLED/COFBK driver shown in Section 5.8.4 (Figure 5-51 and Figure 5-52). As discussed in Section 5.9.4, the frequency response exhibits gain-peaking, which causes the output signal to be distorted. This effect is evident in the SFDR measurement, indicating that the output signal produced by the microLED/COFBK driver loses its linearity with increasing frequency due to the gain-peaking. The worst SFDR was recorded at a frequency around 10MHz where the highest gain-peak in the frequency response for both configurations occurred. Beyond this frequency, the gain peaking reduces and therefore the SFDR improves.
2. The SFDR of the 20kΩ TIA gain configuration is greater than 10kΩ TIA gain configuration up to 5MHz. Above this point, the 10kΩ configuration has a higher

SFDR value. The lower SFDR value in the 20kΩ TIA gain configuration is contributed by the amplitude of the gain peaking. Referring to the Figure 5-51 and Figure 5-52, the 20kΩ TIA gain configuration exhibits greater gain-peak amplitude than the 10kΩ TIA gain configuration. This in turn resulted in a lower SFDR for the 20kΩ TIA gain configuration.

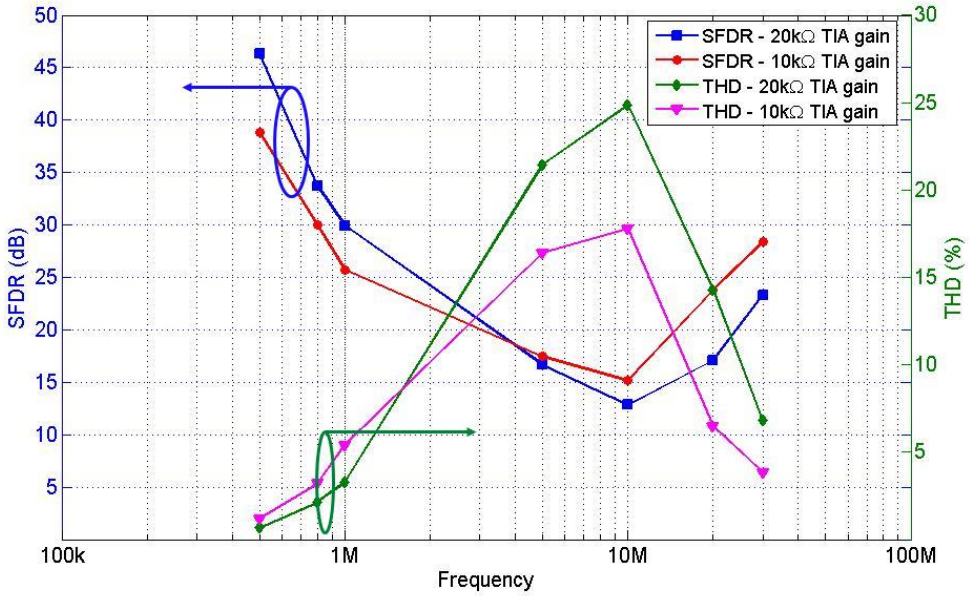

Figure 6-7 – MicroLED/COFBK driver SFDR for different TIA gain configuration range with varying frequency

3. The drop in SFDR is not directly translated into the THD, i.e. a higher SFDR value is not translated into a lower THD value. This can be seen at a frequency around 2MHz where the SFDR for the 20kΩ TIA gain configuration is greater, but the THD is worse than the 10kΩ TIA gain configuration. Again, this is caused by the amplitude of the gain-peaking. As the amplitude of the gain-peak for the 20kΩ TIA gain configuration is greater, the harmonics spurs increase more with the increasing frequency and therefore produces higher THD. The effect becomes more evident at a frequency of 10MHz where the amplitude of the gain peak is at the highest for both configurations. The difference of ratio in the THD between the 10kΩ and 20kΩ TIA gain configurations is greater than in the SFDR. This suggests that the harmonics of the signal increases more with gain-peaking amplitude, which in turn results in a higher THD reading.

The SFDR and THD results presented in Figure 6-7 are summarised in Table 6-5.

TIA gain	Optical Power Range	SFDR @ 500kHz	THD @ 500kHz	SFDR @ 10MHz	SFDR @ 10MHz	SFDR @ 3 dB BW	SFDR @ 3 dB BW
10kΩ	2.14mW	38.18 dB	1.18%	15.16 dB	17.79%	22.2 dB	6.4%
20kΩ	2.13mW	46.35 dB	0.67%	12.85 dB	24.8%	23.2 dB	6.82%

Table 6-5 – Summary of SFDR results for microLED/COFBK driver

6.3.3. AC Linearity Comparison

The comparison of the linearity of the DC response was made in Section 6.2. From this comparison, the microLED/COFBK driver shows an improved linearity compared to the microLED/CCFBK driver. In this section, the linearity of the AC response of the two drivers is summarised and presented in Table 6-6. For fair comparison, the optical power range for the two drivers was chosen to be approximately equal, producing about 2 to 2.2mW of optical power.

From Table 6-6, it is clear that at a low frequency, the linearity of the AC response of the microLED/COFBK driver (for both configurations) is superior to the microLED/CCFBK driver. The highest SFDR was found using the COFBK driver with a 20kΩ TIA gain configuration at 46.35dB, and the lowest was the CCFBK driver where the microLED optical power was biased at a low DC bias point with 30.6dB. The same trend is seen for the THD at low frequencies, where the lowest THD was found to be 0.67% with the microLED/COFBK driver with a 20kΩ gain configuration and the highest was 3.05% from the microLED/CCFBK driver. This clearly demonstrates that the optical feedback technique improves the linearity of the optical power signal. However, it is important to remember that this comparison was made in the low frequency range below the frequency range where the gain-peaking distorts the output signal of the microLED/COFBK driver, which produces lower SFDR and higher THD. Therefore, it is fair to conjecture that a microLED/COFBK driver designed to exhibit zero gain peaking would have superior linearity in an AC response across a broader frequency range.

Driver	Optical Power Range	SFDR at low frequency	THD at low frequency	SFDR at 3dB Bandwidth	THD at 3dB Bandwidth
CCFBK	2.05mW	30.6 dB	3.05%	29.9 dB	4.90 %
CCFBK	2.23mW	33.1 dB	2.26%	23.1 dB	3.45 %
COFBK with 10kΩ TIA gain	2.13mW	39.18 dB	1.18%	22.2 dB	6.4%
COFBK with 20kΩ TIA gain	2.14mW	46.35 dB	0.67%	23.2 dB	6.82%

Table 6-6 – AC linearity data for microLED/CCFBK driver and microLED/COFBK driver

6.4. VLC Performance

6.4.1. Experimental Setup

In communications, the ratio of the number of error bits to the number of bits transmitted (BER) in a channel provides a performance metric of the channel from the transmitter to the receiver. Depending on the performance limit set for a specific application, the channel performance may or may not be acceptable. For a VLC application, BER is typically set to be 10^{-3}. While it is impossible to determine if a particular bit is received correctly or not, the BER test gives a statistical prediction with good confidence of the performance if the parameters of the channel link are known. Thus, the BER experiment indicates the performance which includes the performance of the transmitter, the link channel from the transmitter to the receiver as well as the performance of the receiver.

In this thesis, however, only the performance of the transmitters, i.e. microLED/CCFBK driver and microLED/COFBK driver, are investigated. In order to eliminate any errors caused by the link channel and the receiver, the experimental setup for the two designed drivers is kept unchanged. Therefore, errors that are caused by the link channel and photodetector are constant while only the performance of the drivers ultimately contributes to any measured difference in the BER performance. The experimental setup includes a MATLAB controlled arbitrary waveform generator (Agilent 81180A), the microLED/CMOS driver generic test board with daughter card (DC-B), a fast Si-photodetector (PD10A) and a digital signal analyser (Agilent DSA9084A). The distance between the microLED driver and the photodetector is set to 1 cm. The experimental setup is shown in Figure 6-8 and Figure 6-9.

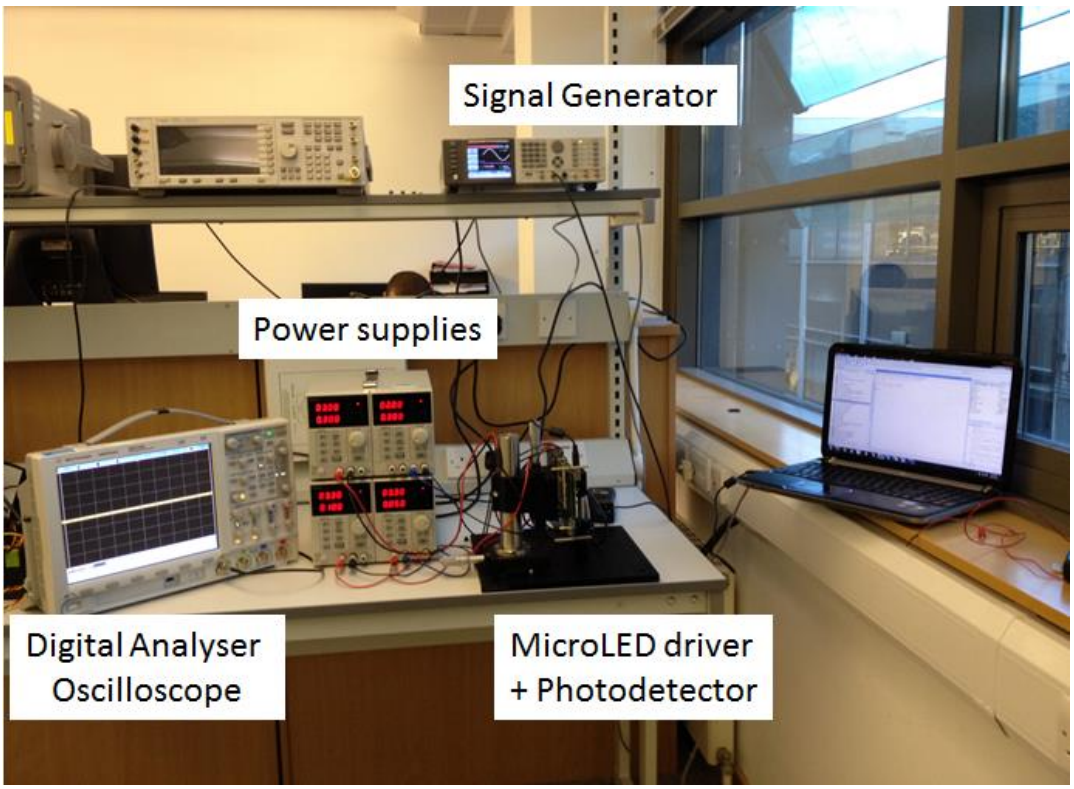

Figure 6-8 – Experiment setup for BER performance test

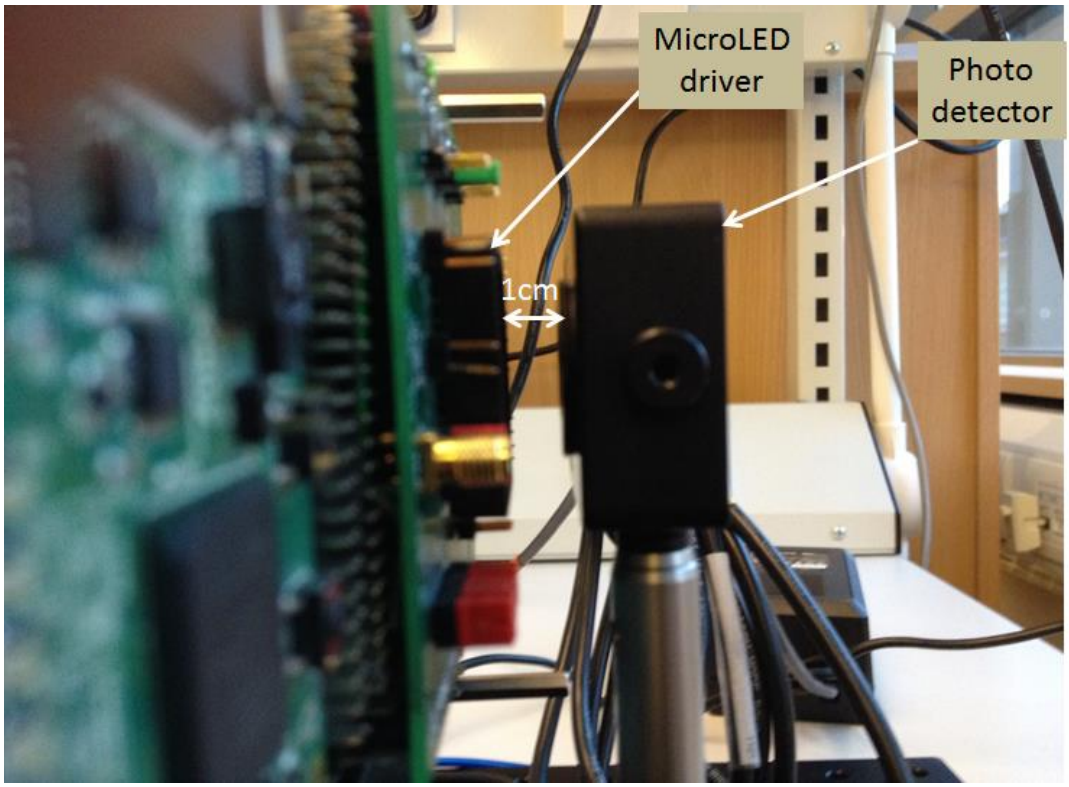

Figure 6-9 – Distance between microLED driver and photodiode

6.4.2. OFDM MATLAB Code

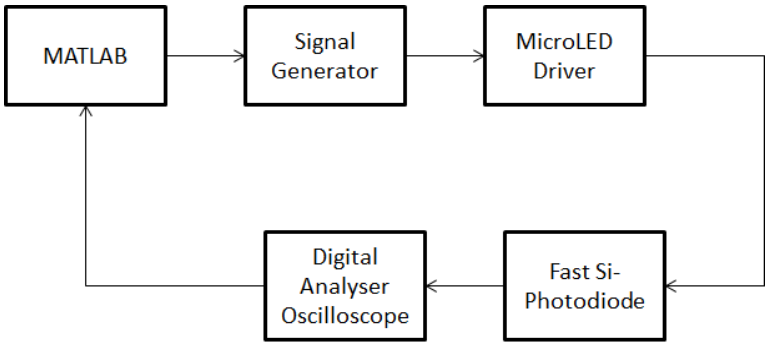

Figure 6-10 – BER test flow

Figure 6-10 shows the flow of the conducted BER test. A random sequence of OFDM signal with n-number of frames is generated by MATLAB code where it is passed to the signal generator that is also controlled by MATLAB via the Agilent I/O Control Suite. The signal is then passed to the microLED/CMOS driver (CCFBK driver or COFBK driver). The light generated by the microLED is detected by the fast-Si photodiode at a distance of 1cm. The fast Si-Photodiode is connected directly to the Digital Analyser Oscilloscope where the output signal generated by the microLED driver can be observed in real time. Therefore, the OFDM signal observed is comprised of loops of n-number of frames that were generated by MATLAB. These n-number of frames are then captured by identifying the preamble frame and are inserted back into MATLAB to be compared with the generated signal thus allowing the BER to be determined.

Parameters	Symbol	Description	Value
Constellation	M	Size of constellation points	64,128,256,512
Number of frames		Number of Frames generated by the MATLAB code	72
FFT size	$nFFT$	Size of the FFT. IFFT is performed on the transmitter side and FFT on the receiver's end	1024
Omitted Carriers	C_O	The number of low frequency carriers that are set to zero (not including DC carrier).	Equation 6-2
Cyclic prefix length	C_P	Size of the cyclic prefix. Therefore the OFDM signal frame has an effective length of $nFFT - C_P$	5
Preamble length	C_I	Length of preamble to indicate the start of each OFDM transmission	1500

Figure 6-11 – Summary of parameters used in generating OFDM signal

The OFDM MATLAB code used in the BER experiment was written by Dobroslav Tsonev, a Ph.D. student from the University of Edinburgh, as part of this Ph.D. research. The generated signal is DCO-OFDM type. Therefore a bias voltage must be applied to the input voltage signal generated by the MATLAB code. The DCO-OFDM was discussed briefly in Section 2.3.4 and in more detail in [123]. Some of the important parameters and their values are summarised in Table 6-5. The MATLAB code also performs post-signal processing, including Forward Error Correction (FEC) and Channel link estimation

The constellation points (M) constitute a representation of a signal modulated by a digital modulation scheme such as quadrature amplitude modulation (QAM) or Phase-Shift Keying (PSK). It represents the possible symbols that may be selected by a given modulation scheme as points. In the BER experiment for the microLED/CMOS drivers, QAM is used in which the constellation points are arranged in a square grid. Since in digital telecommunications the data are binary, the number of points in the grid is a power of 2 and each constellation represents a symbol. By moving to higher-order constellation, a higher number of bits can be inserted into a symbol. For example, 64-QAM has 6 bits per symbol (2^6) while a 256-QAM has 8 bits per symbol (2^8). There are a number of reasons limiting the use of higher M and SNR is usually the main limiting factor. In order to keep BER low when higher M is used, SNR must be improved. From the transmitter point of view, this can be done by increasing the signal strength; i.e. increasing the amplitude of the light output signal from the microLED driver. By doing this, therefore, the PAPR of the transmitter increases. Furthermore, to ensure the accuracy of the constellation mapping and avoid signal clipping, the transmitter is required to have high linearity. Thus, for a transmission with equal SNR, a transmitter with higher linearity will produce a lower BER. For the BER experiment, M of 64, 128, 256 and 512 were used. The BER results obtained from the microLED/CCFBK driver and microLED/COFBK driver are compared and discussed later in Section 6.4.3.

$nFFT$ determines the bandwidth of each of the transmitted carrier symbol. Due to Hermittian symmetry, the effective number of FFT is $\frac{nFFT}{2}$. Therefore, only $\frac{nFFT}{2} - C_p$ carriers are modulated with QAM symbols. $nFFT$ of 1024 was used in his experiment thus the effective FFT is 512. $nFFT$ also determines C_O, where few of the lower frequency carriers are omitted due to the limitation of the signal generator which is unable to produce a signal below a frequency of 100 kHz. Therefore, C_O can be calculated as

$$C_O = \frac{\left(\frac{nFFT}{2} - C_p\right)(100 \times 10^3)}{BW_t}$$ **Equation 6-2**

where BW_t is the total bandwidth of the OFDM signal.

C_P, as discussed in detail in Section 2.3.4, is added at the beginning of each symbol to reduce ISI. The number of frames determines the number of bits transmitted in the BER experiment. Ideally, an infinite number of frames are desired for BER calculation. However, this is limited by the memory available on the digital analyser that is used to record the transmitted data. Two methods were considered in choosing the number of frames:

1) Using a large number of frames so that more data is transmitted in each transmission loop, and reduce the sampling rate per symbol in the digital analyser. However, this comes at a cost of reduced BER because error is introduced due to the downsample by the digital analyser.
2) Using a small number of frames and high sampling rate per symbol by the digital analyser. This gives a more precise reading of BER. However, a transmission with BER less than 10^{-5} is calculated as 0 error bits by the MATLAB code.

In this experiment, method 2 was chosen. In order to achieve a more accurate reading, 10 samples of the transmission were taken each time and the average BER was recorded. Using this method, the minimum BER achievable is in the range of 5 x 10^{-7}. C_I is the gap between each of transmitted data loop which is used in MATLAB to identify the beginning of the received data transmission for BER calculation. A screen shot of the generated OFDM signal by the signal generator and the OFDM signal received by the photodector is shown in Figure 6-12 (a). Figure 6-12 (b) shows the magnified version of the same signal in the x-direction.

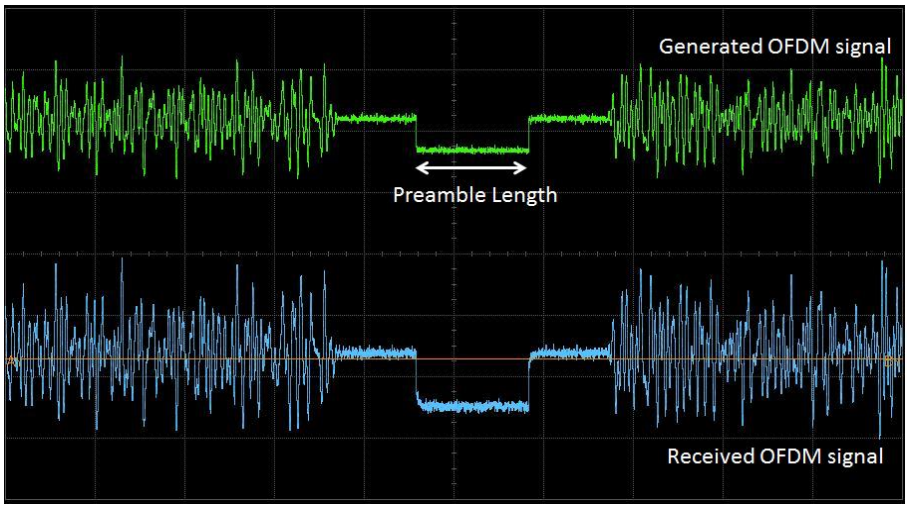

(a)

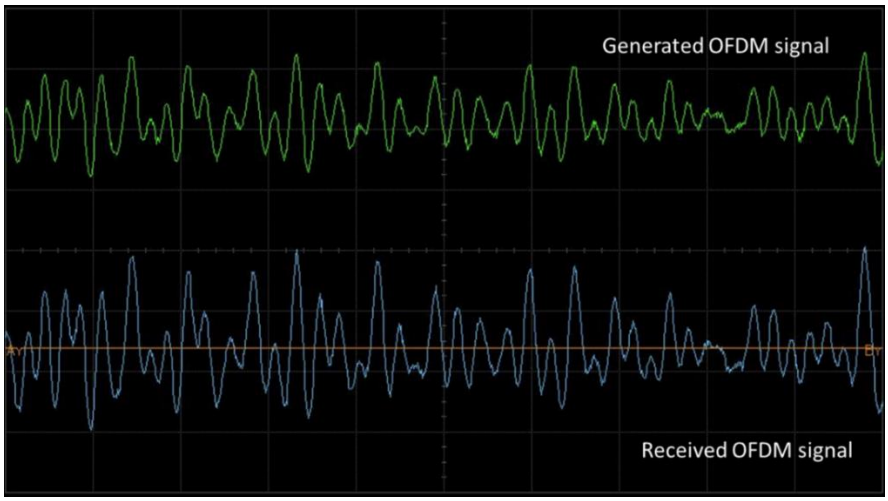

Figure 6-12 – (a) Screenshot of generated and received OFDM signal with Preamble and (b) magnified section of (a)

6.4.3. Bit Error Rate Experiment

The first BER experiment was conducted using the microLED/CCFBK driver with LED_GND biased at –3V. The experiment looked at the relationship between BER and the driver's input signal (V_{INPUT}) range of four different constellation points (64-QAM, 128-QAM, 256-QAM, and 512-QAM). In this experiment, the total bandwidth of the OFDM signal was set to 800 kHz. V_{INPUT} was biased at 1.1V and the range was varied from 0.2V to 1.8V. As mentioned in the Section 6.4.2, due to the limitation of the measuring equipment, BER lower than 5 x 10^{-7} could not be measured and therefore not plotted on the graph. This is seen on the 64-QAM curve in Figure 6-13 where the middle part of the curve is not plotted, indicating that the BER is lower than 5 x 10^{-7}. As seen in Figure 6-13 there is a general trend for all four constellation

points. BER is high at V_{INPUT} range of 0.2V and initially decreases as V_{INPUT} range increases. After V_{INPUT} range increases above 1.3V, BER starts to increase again and the highest BER was recorded at V_{INPUT} range of 1.8V. At the lowest V_{INPUT} range of 0.2V, in theory, the output signal of the microLED/CCFBK driver has the highest linearity. However, BER recorded was higher the medium V_{INPUT} range. The high BER is contributed by the low optical power detected at the receiver end, thus producing low SNR. As the V_{INPUT} range is increased, BER starts to decrease as the SNR improves. BER value of lower than 5 x 10^{-7} was recorded when the V_{INPUT} range is increased above 0.4V for the 64-QAM transmission. As the V_{INPUT} range increases above 0.9V, the non-linearity of the output signal starts to increase. As a result, the OFDM output signal starts to clipped, resulting in an increase of BER.

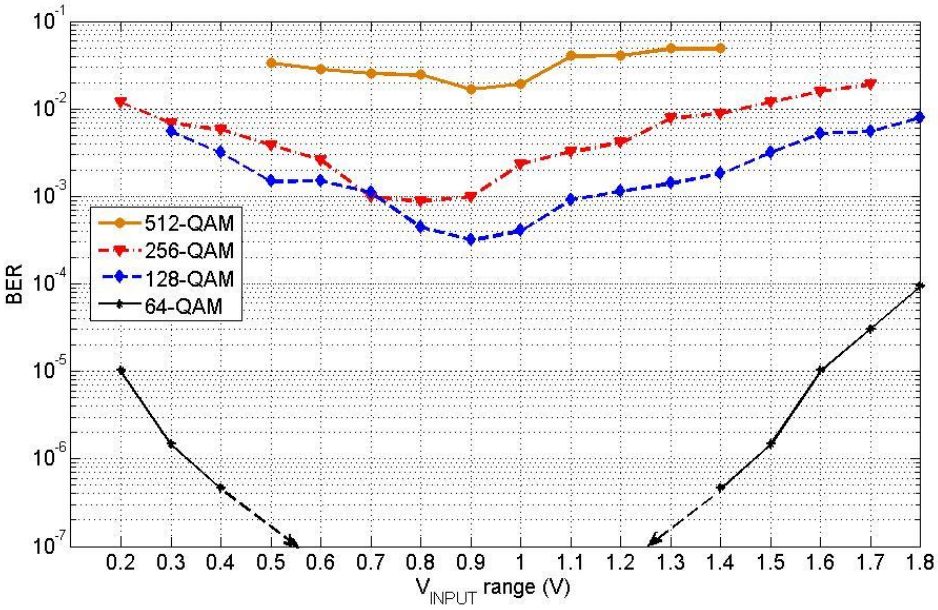

Figure 6-13 – BER as a function of the OFDM input signal range. Different number of QAM are considered.

The effect of the OFDM non-linearity is further shown by increasing the number of QAM. As the number of QAM is increased, the number of distinct states in OFDM signal also increased. Therefore, a high linearity output signal is required to address the states. As seen in Figure 6-13, BER increases as the number of QAM is increased. Only 64-QAM and 128-QAM have recorded BER less than 10^{-3}. The lowest BER was recorded when V_{INPUT} range is 0.9V for all numbers of QAM. This translates to an optical power range of 1.83mW (1.56mW to 3.39mW).

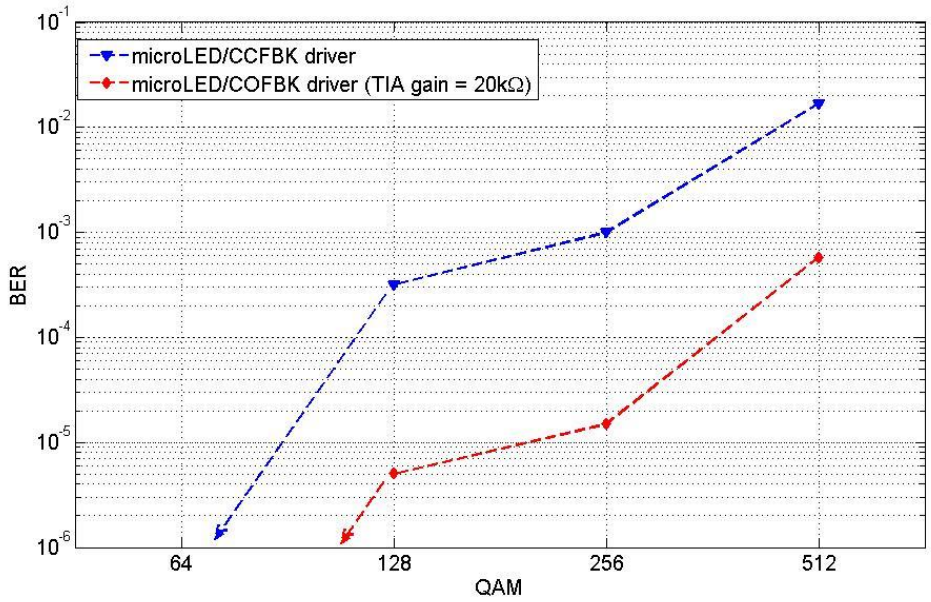

Figure 6-14 – QAM comparison between microLED/CCFBK driver and microLED/COFBK driver

The second BER experiment compares the performance of the microLED/CCFBK driver with the microLED/COFBK driver (with 20kΩ TIA gain configuration) for 64-QAM, 128-QAM, 256-QAM and 512-QAM OFDM signal. Using the V_{INPUT} range which gives the best BER for microLED/CCFBK driver (as discussed above), the microLED/CCFBK driver produces an optical power of 1.83mW while the optical power produced by the microLED/COFBK driver is 2.14mW, as stated in Table 6-6. The bandwidth of the OFDM signal was set to be 800 kHz for this experiment and the result is shown in Figure 6-14. For 64-QAM OFDM, the BER was recorded to be less than 10^{-6} for both drivers. For 128-QAM, 256-QAM and 512-QAM, the BER for the microLED/COFBK driver was found to be lower that of the microLED/CCFBK driver. Furthermore, the microLED/COFBK driver produces a higher optical power. This clearly shows the advantage of linearizing the microLED driver output signal where a lower BER can be achieved for an OFDM signal with the same number of QAM points. The BER of 256-QAM OFDM using the microLED/CCFBK driver was recorded to be $1.7\text{x}10^{-3}$ and this is outwith the performance limit of 10^{-3} for a VLC application. For the microLED/COFBK driver, a 512-QAM OFDM gives a BER error of $5.8\text{x}10^{-4}$ which is still within the performance limit. So, it can be said that the improved linearity of the output signal has increased the data rates approximately by a factor of four. Therefore, it can be concluded that higher quality data transmission can be conveyed by having a higher linearity microLED driver.

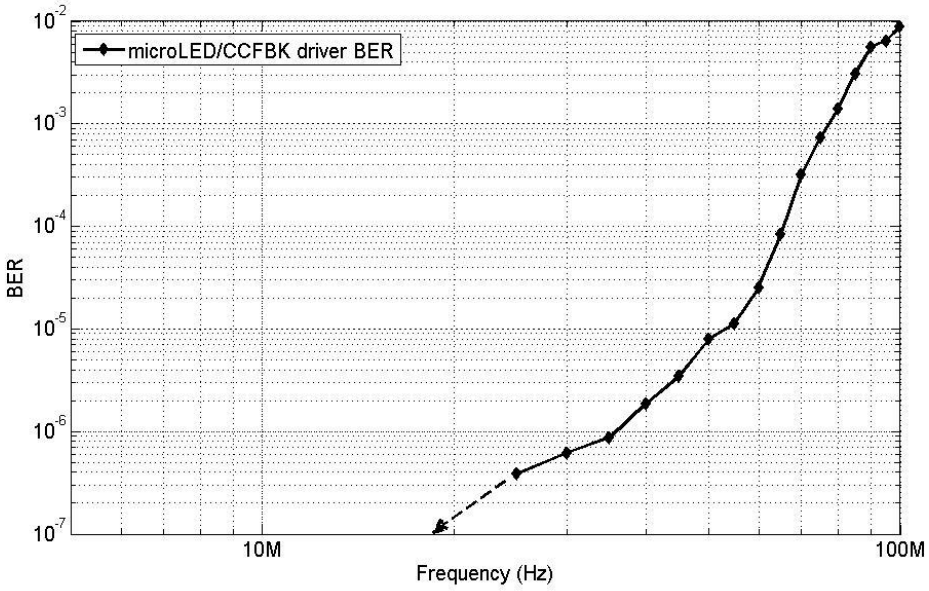

Figure 6-15 – Frequency Sweep BER for the microLED/CCFBK driver

In the third experiment, the bandwidth of the OFDM transmission is swept for the microLED/CCFBK driver. In this experiment, a 64-OFDM signal was transmitted with bandwidth in the range from 500 kHz up to 100MHz. V_{INPUT} is biased at 1.1V with a range of 0.9V. A 64-QAM OFDM signal was chosen for the experiment because, as seen in the previous two experiments, it produces the lowest BER. The result of this experiment is shown in Figure 6-15. As the bandwidth of the OFDM signal increases, BER also increases. Approximately when the OFDM bandwidth is below 35MHz, BER of the transmission was found to be less than 10^{-6}. BER of 10^{-3} was recorded when the bandwidth of the OFDM signal is about 78MHz. This is beyond the bandwidth of the microLED/CCFBK driver itself. There are two reasons that allow low BER transmission beyond the bandwidth of the driver:

1. The system (driver + receiver) exhibits a high SNR. In theory, the OFDM signal can have infinite bandwidth as long as the SNR is high enough to keep the BER low.
2. The inclusion of FEC in the receiver's signal processing. FEC is used to detect, predict and correct a limited number of errors in the transmission. This is done by taking samples of the first few frames of the OFDM signal and the channel link was predicted. In this case, a sample of 5 frames was used.

$nFFT$ of 1024 was used in this experiment. C_O was calculated using Equation 6-2 and only one carrier was omitted. Therefore, the effective number of carriers available for transmission is 506. The maximum data rate achieved within the performance limit of VLC is approximately 468Mb/s.

The same experiment for microLED/COFBK driver, however, was not included in this thesis. As mentioned before, the BER depends on the transmission system which includes the transmitter, the channel link and the receiver. From the transmitter point of view, it was shown that it is possible to reduce the BER using the microLED/COFBK driver, which improves the linearity of the optical power response of the microLED. Furthermore, because of the improved linearity, higher data rate can be achieved by transmitting the OFDM signal with higher QAM points as presented in Figure 6-14. The implementation of the driver presented in this thesis, however, suffers from gain-peaking in the frequency response which distorts the signal at higher frequencies as discussed in Section 6.3.2 thus, the BER for the microLED/COFBK driver is expected to be higher than the microLED/CCFBK driver as the frequency increases. Nonetheless, it is fair to speculate that a microLED/COFBK driver designed to exhibit zero gain peaking would be able to transmit higher data rate than a microLED/CCFBK driver for the same transmission bandwidth.

The cause of the gain peaking was investigated in Section 5.9, which concludes that the additional photodiodes that were added to the pixel cause the bandwidth of the TIA to drop lower than the gain-bandwidth product of the feedforward network in the COFBK driver which resulted in instability in the closed loop function. The gain-peaking in the frequency response could be minimized or eliminated in a future design by using only one photodiode to ensure that the bandwidth of the TIA is greater. However, it is important to note that the additional photodiodes were added to the driver to assist the detection of the feedback light. Thus, if only one photodiode is to be used, a further study of the feedback path characteristic is needed. This is discussed in further detail in Section 7.2.

The distance between the microLED/CMOS driver and optical receiver in the experimental setup reported in this thesis was 1 cm. In practice, this distance is too short for useful VLC applications. Because the light produced by the microLED propagated in an approximately Lambertian pattern, the actual light that was captured by the optical receiver is only a portion. Thus the distance of the link channel can be improved with the help of a well-designed optical system. This can be done by collimating the lambertian pattern of the microLED into a tighter beam. As seen in Figure 6-13, the SNR plays a significant part in determining the BER of the system. From the detector point of view, the SNR can also be improved with the help of an optical system by constraining the light into a narrower beam thus increasing the signal strength. Another way of improving SNR is by using a more sensitive and lower noise photodetector.

6.5. Summary

The linearity of the DC and AC response of the microLED/CCFBK driver and the microLED/COFBK driver is presented and compared in this chapter. For the DC response, V_{INPUT} of both drivers were swept from 0V to 3.3V and the optical power response of both drivers was compared. For a similar optical power output range, the microLED/COFBK driver has shown greater linearity performance with the degree of non-linearity is 5.3% lower over that of the microLED/CCFBK driver. For the AC response, a sinewave signal was applied to V_{INPUT} and an FFT was performed to the output signal from the microLED. The optical power was set to give a similar range for both CCFBK driver and COFBK driver. The linearity of the output signal was quantified by SFDR and THD. In the low frequency, the microLED/COFBK driver again has shown greater FFT performance than the microLED/CCFBK driver with an improvement of 16 dB in SFDR. The THD of the microLED/CCFBK was found to be around 2.2% while that of the microLED/COFBK driver was around 0.66%. This indicates that the AC response of the microLED/COFBK driver performs greater linearity than that of the microLED/CCFBK driver. However, the linearity performance of the microLED/COFBK driver drops as the frequency increases, caused by the gain-peaking in the frequency response (an artefact of this particular implementation).

The data transmission performance using OFDM scheme for both drivers was also presented and compared in this chapter. For a fair comparison, due to the gain-peaking exhibited by the microLED/COFBK driver at high frequencies, the bandwidth of the OFDM transmission was kept below 800 kHz. The experiments were conducted using 64-QAM, 128-QAM, 256-QAM and 512-QAM. The results showed that the microLED/COFBK driver produced lower BER than the microLED/CCFBK driver for all QAM cases. This experiment highlights the advantage of improving the linearity of the microLED/CMOS driver output signal where higher QAM can be transmitted with lower BER thus increasing the data rate. From the result shown in Figure 6-14, the 512-QAM OFDM transmission using microLED/COFBK driver gave a BER less than 10^{-3}, which is within the specification of VLC application, whereas a comparable BER was found in microLED/CCFBK driver using 128-QAM OFDM transmission. Thus, it can be said that the improved linearity of the output signal has increased the data rates by a factor of four.

A Further experiment was conducted to find the maximum transmission data rate performed by the microLED/CCFBK driver. The microLED/COFBK driver was not included due to the

gain-peaking response exhibited in its higher frequency. The experiment using 64-QAM OFDM transmission has shown a data rate up to 468 Mbit/s with the distance between the transmitter and receiver is 1cm. The transmission data rate and distance can be improved with the help of a well-designed optical system to focus the microLED optical power output into a narrower beam.

Table 6-7 summarises the pros and cons of the microLED/CCFBK driver compared to the microLED/COFBK driver. The design of the microLED/COFBK driver is more complicated than the design of the microLED/CCFBK driver because of the integration of the microLED and photodiode within a pixel. Furthermore, the addition of the photodiode and TIA in the feedback network add an extra pole in the feedback path, thus more attention is needed to ensure the stability of the feedback loop. Also, the design of the photodiode is process dependent and together with its integration method with microLED, determines the gain in the feedback network which also affect the driver's operating range and bandwidth. The feedback network gain of the microLED/CCFBK driver on the other hand, can be designed with conventional CAD tools with higher precision and confidence. Despite the complicated design of the microLED/COFBK driver, it has been proved that it produces greater linearity performance than the microLED/CCFBK driver. Because of this, PAPR is not sacrificed to achieve higher linearity. As presented in Figure 6-14, the improvement in linearity allows the implementation of OFDM with higher QAM thus increasing the transmission data rate.

	CCFBK Driver	**COFBK Driver**
Design	Simple	Complex integration between microLED and photodiode
Stability	Stable	Additional poles introduced by TIA means more attention is needed for stability
Feedback network gain	Can be estimated with higher accuracy during design	Highly dependent on $\Re_{PD}$ which is process dependent and not yet well characterised. The photodiode's shape and position also contribute to the feedback network's gain
Input Range	Can be determined during design	Can be determined during design, but also depends on the feedback network gain
Bandwidth	Can be determined during design	Highly dependent on the feedback network gain
Optical power Linearity	Inherit the Current to optical power (L-I) response non-linearity of the microLED	Linearised the optical power response by pre-distorting the current driving the microLED
PAPR	Trade-off between Linearity and PAPR	High PAPR. Linearity less affected

Table 6-7 – Summary of difference between the microLED/CCFBK driver and microLED/COFBK driver

Chapter 7 : Conclusions and Future Works

7.1. Summary and Conclusions

The thesis has presented three different CMOS drive ICs for microLED arrays, namely the CMOS Generation V Digital driver, the CMOS Current Feedback (CCFBK) driver and the CMOS Optical Feedback (COFBK) driver, which use two different modulation schemes for VLC. The drive ICs have been characterised and the performance of the microLED on CMOS devices for VLC applications has been analysed. In this chapter, the contribution of the obtained results from the drivers to the future development of CMOS driven microLED arrays are presented and some conclusions are reached. A critical review of the microLED/CMOS driver based VLC as a method of communication in the future is also discussed.

By making use of standard CMOS foundry technologies, this work demonstrates the feasibility of integrating microLED emitters and CMOS photosensor in a single pixel to create a hybrid technology. The linearization of the microLED optical power signal using optical feedback is one of the capabilities of the hybrid technology and is demonstrated in the application to VLC. Other applications, such as ambient optical power and lifetime control and single pixel transceivers, are possibilities of the new hybrid microLED-CMOS sensor integration technology.

As discussed in Chapter 2, the thesis emphasised on OFDM as the chosen modulation scheme for VLC application due to its higher data transmission rate and reduced susceptibility to ISI when compared to the simple OOK modulation. Nevertheless, OOK was also considered in the thesis and was implemented as a modulation scheme with the Generation V microLED/CMOS digital driver. OOK was considered and implemented for two purposes

1. As part of the ESPRC sponsored HYPIX project (as a partial funder of the Ph.D. project), which sought to produce the maximum possible output power from an array of microLED/CMOS driver for its optically pumped polymer lasing experiment.
2. As a continuation of the previous works of microLED/CMOS drivers (Generation I to Generation IV), which were also being used for communication (VLC)

Furthermore, the design of the Generation V microLED/CMOS driver gave an indication of the limitation of both microLED and CMOS drivers for a given pixel size and technology process node. The Generation V microLED/CMOS driver also highlights the integration

technique in which a thick metal layer was used both as an intermediate electrode to allow good electrical connection between the driver and the microLED and as a mechanical protection layer for the underlying CMOS circuitry during the bonding process. This allowed the microLED to be bonded directly on top of the CMOS driver without the use of an off-set bond-stack as implemented in the previous Generation IV driver. The employment of the thick metal layer permits more effective use of the area in the pixel to increase the drive current to the microLED. To recap, the Generation V microLED/CMOS driver was able to produce pixel drive current up to 330mA that is about two times that of the Generation IV driver. The bandwidth was found to be 123MHz which is similar to the Generation IV driver. The optical power produced by a single pixel is up to around 12mW, which is more than three times greater that of the Generation IV driver. The peak intensity observed was 124W/cm^2 using a 6-pixel strip, which is the highest peak intensity ever recorded under the HYPIX project. It is important to note that the optically pumped polymer lasing experiment is still ongoing at the time of writing of the thesis. The Generation V MicroLED/CMOS driver, however, is expected to be able to trigger lasing in the polymer.

In order to increase the data transmission rate, OFDM was chosen as the preferred modulation scheme over OOK. Two analogue drivers, CCFBK driver and COFBK driver, were designed specifically for OFDM. Chapter 4 outlines the design and characterisation of the microLED/CCFBK driver. The CCFBK driver is the first analogue CMOS drive IC for microLED that uses OFDM as the modulation scheme. The driver supplies the microLED with current linearly proportional to the input voltage signal. The microLED/CCFBK driver was able to produce current up to about 66mA, producing about 3.6mW of optical power. Although the current supplied by the CCFBK driver has a linear response, the optical power output from the microLED/CCFBK driver does not. This is due to the inherent non-linearity of the microLED L-I characteristic. The chapter also looked at improving the linearity of the optical power output signal by carefully choosing the bias voltage to the input and limiting the range of the output signal (optical power range). The reduction in the optical power range also means that the PAPR of the OFDM signal reduces. This is significant as high PAPR is required in an OFDM transmission.

Optical feedback was proposed in order to linearize the optical power output where PAPR is not sacrificed in order to achieve greater linearity. Chapter 5 presented and discussed the design and characterisation of the microLED/COFBK driver. The COFBK driver is the first

CMOS drive IC that integrates a microLED and photodiode into a single pixel, in this case, for linearization purposes which is designed to implement OFDM modulation scheme for a VLC application. The optical power output from the microLED/COFBK driver is detected by a photodiode and is compared with the input signal. The non-linearity of the microLED optical power is then corrected by the COFBK driver by actively pre-distorting the microLED drive current. The microLED/COBFK driver produces a drive current of 60mA and optical power output of 2.5mW. The optical power output was measured to be lower than the expected microLED model and bare die measurement due to the modification made to the microLED design in order to produce higher feedback light for linearization purposes. A linearity comparison was made between the microLED/CCFBK driver and microLED/COFBK driver in which the microLED/COFBK driver showed a reduction about 5.3% in the degree of non-linearity of the DC response for a similar optical power range. The linearity of the AC response was also compared at a frequency of 500 kHz where again, the microLED/COFBK driver showed an improvement in SFDR up to 16 dB and a reduction in THD down to 0.66%. However, the linearity of the microLED/COFBK driver worsen as the frequency of the input signal is increased. This is mainly caused by instability of the COFBK driver response in which the bandwidth of the TIA drops below the design value that causes gain-peaking in the frequency response. The drop in the bandwidth of the TIA was traced to the additional load of the multiple photodiodes that were initially added to the driver to assist the detection of the light in the feedback path. Overall, despite the stability issue at higher frequencies, the microLED/COFBK driver has shown capabilities of improving the linearity of the microLED optical power over that of the microLED/CCFBK driver by integrating both emitter and sensor within a pixel.

Chapter 6 compares and highlights the advantage of a more linear driver for an OFDM signal. OFDM transmission of 64-QAM, 128-QAM, 256-QAM and 512-QAM were applied to both microLED/CCFBK driver and microLED/COFBK driver. The experiment was conducted with an OFDM bandwidth of 800 kHz due to the gain-peaking in the frequency response exhibited by the microLED/COFBK driver. In the experiments, the microLED/COFBK driver showed a lower BER, approximately half that of the microLED/CCFBK driver for all QAM thus, showing the advantage of using a microLED/CMOS drive IC with higher linearity. While the linearity of the microLED/CCFBK driver can be increased by reducing the optical power range, the reduction in signal amplitude causes the SNR to decrease thus increasing BER. A maximum data rate of 468Mbits/s was found using the microLED/CCFBK driver with 64-QAM in a separate experiment.

7.2. Future Work

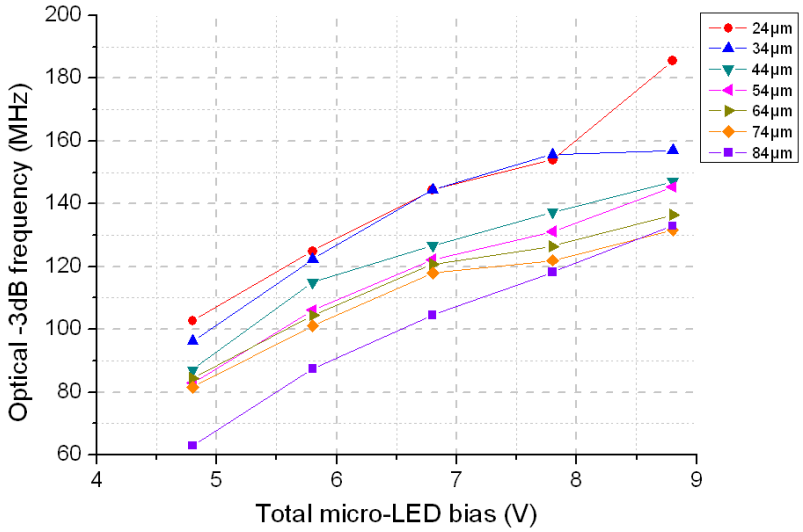

Figure 7-1 – Bandwidth versus bias for various pixel diameters from a 450nm wavelength microLED. Measurement was taken by Dr. Jonathan McKendry, Institute of Photonic University of Strathclyde

A high bandwidth transmitter is very much desirable in order to increase the data transmission rate. One of the ways to increase the data rate is by having a higher bandwidth microLED. This can be achieved by reducing the inherent parasitic capacitance of the microLED which can be done by reducing the diameter of the microLED. This is shown in Figure 7-1 where the bandwidth increases as the diameter of the microLED shrinks from 84µm down to 24µm. In the case of CMOS technologies, as the CMOS device dimensions shrink in newer process technologies, the minimum gate length of a transistor in that process is reduced. Therefore, smaller transistors can be utilised and thus allowing the pixel dimension to be reduced without the reduction in the drive strength. Furthermore, a gold bump diameter down to 10µm have been reported [124, 125, 126], which further indicates the prospect of pixel downscaling. However, a thermal study of the pixel downscaling is required as the current flow may reach some hundreds of mA in square pixel with a pitch of some tens of µm which could reduce the performance of both CMOS circuitry and microLED. Contrariwise, if the CMOS pixel pitch is not reduced, greater driving strength can be achieved. Furthermore, it would also provide more complex circuits (e.g. CCFBK driver and COFBK driver) a greater flexibility in the design.

As discussed in Chapter 5, the gain of the feedback network plays a significant role in the performance of the driver where a high feedback gain contributes to a higher bandwidth. Moreover, the microLED/COFBK driver also suffers from gain-peaking in its frequency response due to the multiple photodiodes that were added to increase feedback light detection. In addition, the forward light from the microLED has slightly dropped in order to increase the amount of the feedback light. Although the calculations of the feedback network in Chapter 5 (Equation 5-27 to Equation 5-29) have given a rough estimate, more precise modelling of the feedback network i.e. the feedback light from the microLED (β_L) and the photodiode's responsivity ($\Re_{PD}$) is necessary in order to reduce the process variations in the feedback network thus, improve the performance of the microLED/COFBK driver.

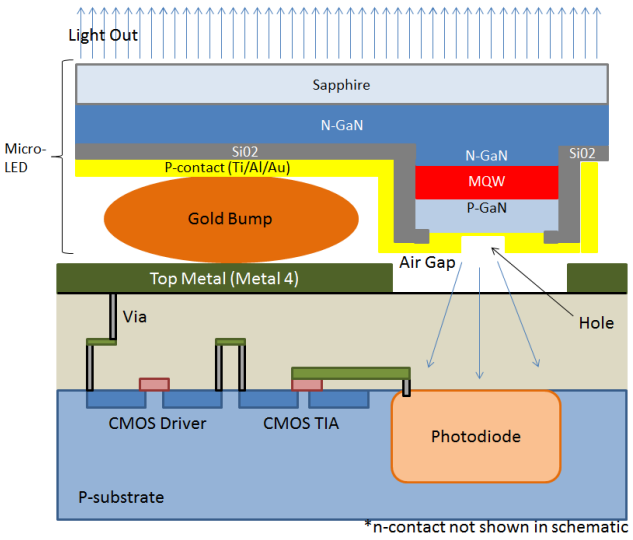

Figure 7-2 - Schematic cross section of the proposed microLED and CMOS integration to increase the feedback light for microLED/COFBK driver

One of the possible solutions proposed to minimize the loss of the forward light and to improve the feedback light detection is by shifting the microLED so that it is positioned directly on top of the photodiode. In this case, the metal layer is placed around the microLED and only a small hole is made underneath, so that the feedback light can reach the photodiode. A schematic cross-section diagram of the proposed microLED-CMOS integration is shown in Figure 7-2. The size of the hole, however, would determine how much loss in the forward light; i.e. the bigger the hole opening, the higher the forward light loss. Furthermore, depending on the microLED beam angle, the photodiode potentially could have a smaller area. This would be an advantage to the design as the TIA would gain higher bandwidth, hence reducing the gain-peaking artefact. Moreover, some process technologies offer a dedicated

process for image sensor. For instance, AMS foundry provides a dedicated image sensor process for its 0.35µm technology. In this process, an anti-reflective coating is included which improves the light absorption and supresses scattering from topographical features. Thus the study of the integration methods between the microLED and photodiode includes (but not exhaustively):

1. The modelling of the feedback light propagation behaviour in the CMOS oxide and nitride layer before it impinges the photodiode
2. The optimum position of the photodiode to maximise the detection of the feedback light
3. The type and design of the photodiode to maximise the responsivity to the feedback light.
4. The area of the photodiode to optimized the bandwidth of the feedback network

7.3. Critical Discussion and Future of MicroLED for VLC Application

Three CMOS drive ICs for microLED arrays have been developed for VLC purposes. The first is the Generation V microLED/CMOS digital driver, aimed to generate maximum possible optical power output from the array of 400 microLEDs (40x10) for optically pumped polymer lasing and VLC purposes. An OOK scheme was implemented with the Generation V driver. The microLED/CCFBK driver and microLED/COFBK driver, on the other hand, look to improve on the transmission data rate by implementing OFDM as its modulation scheme. The microLED/COFBK driver has shown superior BER performance than the microLED/CCFBK driver, producing lower BER with higher QAM. This highlights the advantage of having a highly linear optical power output for OFDM transmission. Despite demonstrating the importance of linearization, the demonstration was only conducted at modest frequencies due to the gain-peaking response problem by the microLED/COFBK driver. The cause of the problem was investigated and discussed in Chapter 5. Unfortunately, time constraints and limited funding have prevented the COFBK driver from having a re-spin to solve the problem. Nevertheless, both drivers have addressed the prospective of communication using visible light, edging closer to potential multi Gb/s data transmission from an LED source. The drivers provide a foundation for the future, to improve the performance of each element and in turn, lead to performance improvements of the whole system.

While the thesis has presented drivers that potentially could reach Gb/s data transmission, it still covers only a small portion of the VLC system. A high bandwidth light source is important in determining the overall transmission data rate. In this thesis, a high bandwidth light source was achieved using microLED which is only up to 100µm in diameter. While the small size allows the microLED to have low parasitics and therefore high bandwidth, the optical power produced by a single microLED pixel is significantly lower than a commercial LED for the same current drive. However, the optical power density (W/cm^2) of a microLED is greater than the commercial products. Therefore, an array of microLED of the same area as a single commercial LED device, potentially, have greater optical power and higher efficiency.

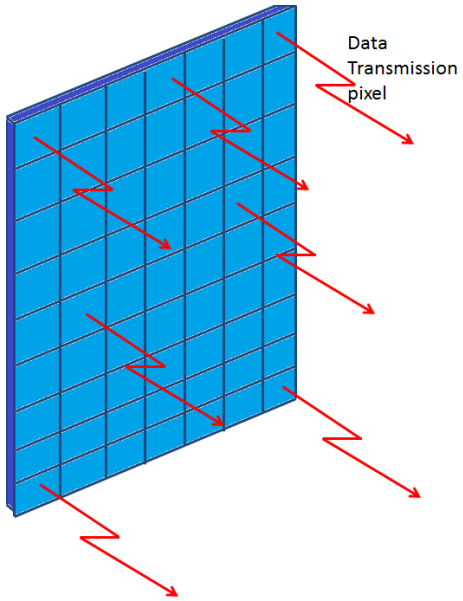

Figure 7-3 – Illustration of array of microLED with multiple pixel as data transmission while others for illumination

The option of using array of microLEDs as a single illumination unit could open up possibilities to further increase the transmission data rate. Some of the possibilities are

1. Using some of the pixels within the array for illumination while others to transmit data as illustrated in Figure 7-3. Therefore the data rate is increased by n times that of a single pixel; where n is the number of pixels that are used to transmit data. This is equivalent to the Multiple Input and Multiple Output (MIMO) technique used in RF.
2. Using Red, Green and Blue (RGB) array of microLEDs to create white light. Therefore, each colour within the RGB pixel is able to transmit data, making greater use of the available bandwidth within the visible spectrum. This technique is also known as wavelength-division multiplexing (WDM) which could also enable bidirectional communication over the channel link.

So far, the thesis only focuses on the transmission side of the VLC. As discussed in Chapter 6, the responsivity of the receiver and also the channel link plays a part in determining the performance of the data transmission. As a rule of thumb, the performance of the data transmission would improve as the SNR increases thus reducing the system BER. This can be done on the receiver side by using a higher responsivity photodiode or by reducing the distance between the transmitter and receiver. The distance presented in this thesis (Chapter 6) was set using a single microLED at a distance of 1cm from the receiver. While the distance of 1cm may be sufficient for inter-connection communication between two devices, it is not appropriate, in general, for VLC applications where it requires to illuminate an area (i.e. light on a ceiling to a device on a table). This is due to the divergent nature of the microLED emission which means that any increase in the distance between the transmitter and receiver is met with a square increment in the beam size, reducing the optical power focussed on the particular area. Nonetheless, with the help from an optical setup to focus the divergence emission into a narrower beam, the optical power can be increased at a greater distance. Coupled with array of microLEDs as mentioned earlier, the area of illumination can also can be increased. Nevertheless, an in-depth study of the receiver end is also required to see how the MIMO technique affecting the performance of the system.

Another important aspect to take into account is the power consumption of the VLC system. As presented in the thesis, drive current of 330mA from a single microLED pixel produces about 12mW of optical power. This is about 1W of power consumption from 3.3V voltage source. Depending on the applications and light intensity requirements for the data transmission, the power consumption could be too high especially for a battery powered devices such as mobile phones. This might not be the case for mains powered devices such as lighting appliances in household. Therefore, a further study of power consumption by a VLC device is required to understand its feasibility and practicality in comparison to an RF device.

7.4. Conclusions

The project has presented three CMOS drive ICs for microLED arrays for VLC applications implemented using 0.35µm CMOS technology. A summary of the significant achievement attained during the duration of the project is summarised in Table 7-1. The Generation V microLED/CMOS driver is an improvement from the previous works under the HYPIX project which implements OOK as the modulation scheme and studies the maximum possible optical power produced by a 100µm square pixel. The result has shown a maximum drive current

about 330mA, producing about 12mW of optical power. The bandwidth of the driver was measured to be about 123MHz and peak intensity of 124W/cm^2 was recorded. The microLED/CCFBK driver is the first CMOS drivers for microLED which was designed specifically to implement OFDM as the modulation scheme. The microLED/CCFBK driver produces about 65mA of drive current and 3.5mW optical power. The driver has shown the ability to transmit up to about 468 Mb/s. The microLED/COFBK driver on the other hand was designed to improve on the linearity of the optical power output using optical feedback. Furthermore, the driver is the first CMOS driver which integrates emitter (microLED) and sensor (photodiode) in a single pixel for communication purposes. While the microLED/COFBK driver was met with issues regarding the gain peaking in the frequency response, it has proven that it is able to improve the linearity of the optical power output signal. With the improved linearity, a higher number of QAM OFDM signal can be transmitted, producing a lower BER than the less linear microLED/CCFBK driver counterpart. The results could pave the way to a more robust design of the optical feedback driver in order to improve the performance and potentially further increase the transmission data rate.

Driver	Achievement
MicroLED/Generation V driver	Highest output current for microLED/CMOS array per pixel
	Highest optical power output and peak intensity per pixel
MicroLED/CCFBK Driver	First demonstration of microLED/CMOS drive IC for OFDM modulated scheme
	Data rate up to 468Mb/s per pixel was achieved
MicroLED/COFBK Driver	First demonstration of microLED/CMOS driver which integrates emitter and sensor in a single pixel for communication purpose
	First demonstration of linearity improvement using optical feedback

Table 7-1 – Summary of significant achievements during the duration of the project

Appendix A

A.1. Generation I: 16x4 current controlled MicroLED driver Array

The first generation microLED driver chip was fabricated using AMS 0.35µm High Voltage Process. An array of 16x4 was realized and each pixel is 100um x 200um in size. The driver, at this stage, was not designed for communication purposes but rather for optically pumped polymer lasing experiment and Time Correlated Single Photon Counting (TCSPC). For this reason, each pixel includes a Single Photon Avalanche Diode (SPAD) which takes about 100x100um of the total pixel pitch. Therefore, the effective size of the CMOS array driver on its own is about 100um x 100um. MicroLED was bump-bonded straight on top of the pixel, using top metal layer as both electrode and shield to the circuitry underneath. The design consists of both low and high voltage transistor, thus making it possible to switch up to 50V.

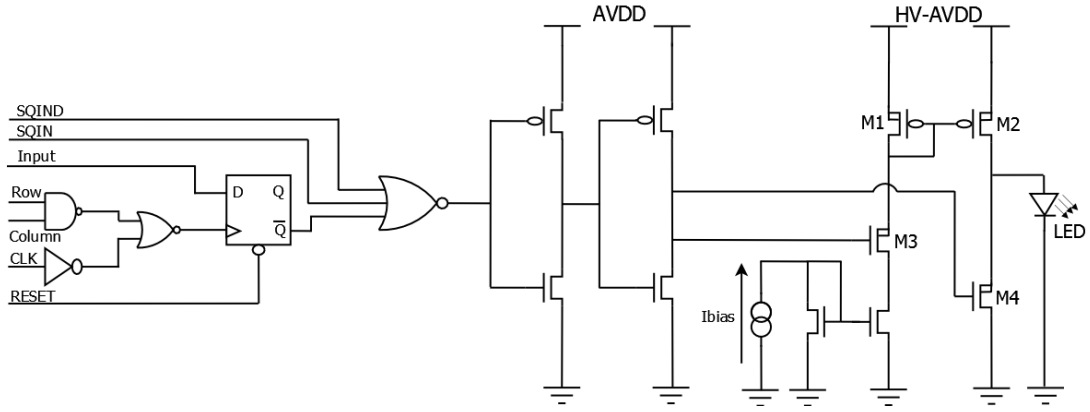

Figure A-1: Generation I microLED/CMOS driver [82]

The first generation microLED CMOS driver was designed based on current-controlled concept, where the current through the microLED is determined by the input bias current (Ibias). Therefore the current flows through the microLED is a trade-off between the device's I-V curve and Ibias. D-type flip flop was used for addressing while SQIND and SQIN signals are both used for timing.

The driver was able to produce only up to 5mA of current through the microLED and generated slightly less than 10uW of optical power. The use of high voltage (thick-oxide) transistors, labelled M1 to M4, further underline the limitation of the circuit as these transistors are physically very large and occupy the majority of the pixel.

A.2. Generation II: 16x16 Voltage controlled MicroLED driver Array

The second generation microLED driver chip was fabricated using AMS 0.35µm Standard Process. An array of 16x16 was implemented and each pixel is 100x100um. The addressing logic is kept the same as previous generation using standard 3.3V transistors. This is then being converted to a user-defined voltage (LED_VDD) by a level-shifter which could have a maximum value of 5V. Again, by using a higher voltage transistor, the physically larger transistors have taken the majority of the pixel area. The addition of current starved inverter allows pulse mode operation which is mainly used for polymer lasing experiments.

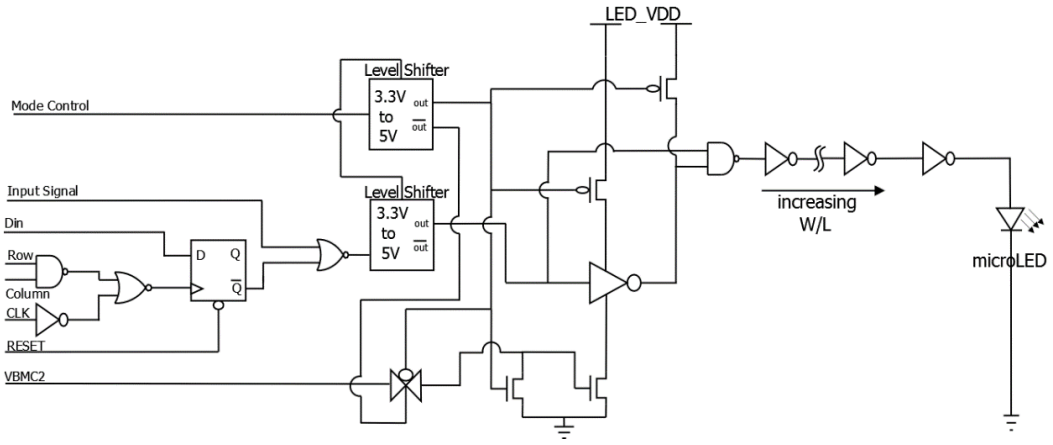

Figure A-2: Generation II microLED/CMOS driver [82]

The main difference from the first generation is the change from current controlled to voltage controlled driver. This is made to increase the optical power and to reduce minimum optical pulse width for polymer lasing purposes. The driver is based on chains of inverters driving the microLED. The chains of inverters were designed with ever-increasing width-to-length (W/L) ratios. This is to reduce the load capacitance on the input signal while maximizing the drive strength of the circuit.

Unfortunately, Generation II was hit by bonding problems. The same method of bonding was applied where microLEDs were bump-bonded straight to the top of the CMOS chip. As generation II had change its process, the thickness of the top metal layer in AMS 0.35µm Standard Process is almost three times less than its predecessor which uses the High Voltage Process [89]. As a result, the top metal layer could not withstand the pressure during flip-chip bump-bonding process and cracks. This caused short-circuit between the electrodes (top metal) and the circuitry underneath. Because of this, thick metal layer has been identified as essential should the same bonding technique is to be applied in the future.

A.3. Generation III: 8x8 Voltage controlled MicroLED Driver Array

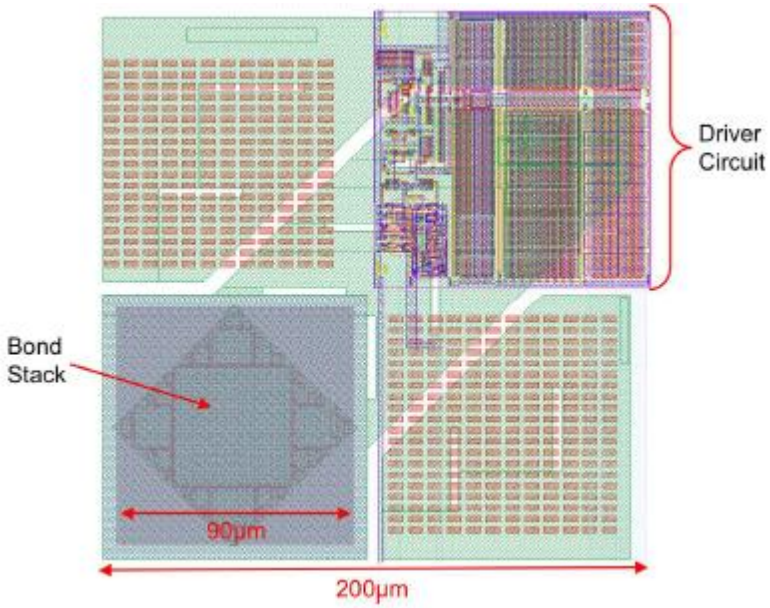

Figure A-3: Generation III microLED/CMOS driver layout [82]

The third generation microLED driver was designed in the wake of the bonding problem faced in generation II and was again fabricated using AMS 0.35µm Standard Process. Keeping the circuit architecture exactly the same, some changes were made to add mechanical strength to the metal electrode upon which the microLED were bump bonded by introducing a bond-stack to each pixel. Bond-stacks are constructed using all four metal layers in process with a very dense array of vias connecting each layer thus allowing no circuitry to be placed underneath them. To incorporate the addition of the bond-stack, the pixel size was increased to 200µm x 200µm and the array was reduced to 8x8. From a pixel fill-factor point of view, this is area inefficient as the microLED and CMOS driver only occupied 50% of the pixel pitch as shown in Figure A-3. Nevertheless, the inclusion of bond-stacks has made the design very robust to any mechanical damage during bonding process.

The driver was able to perform two modes of operation: continuous wave (CW) and pulse mode. This can be selected using “mode_control” pin and the pulse width can be determined by changing the input voltage on “VBMC2”. The driver is a voltage controlled type therefore the characteristic is fully determined by the microLED I-V characteristic. A significant increase was observed as the driver was able to driver up to 90mA current with optical power reaching about 550µW. Serious crosstalk problem was observed in this design. This is mainly

because the microLED ground being a global signal, common to every pixel in the array. Any changes in the "ground" potential would see unaddressed pixel turning on as shown in Figure A-4.

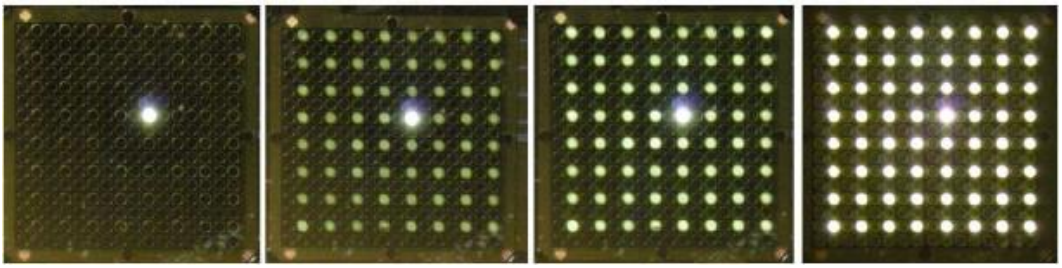

LED_GND = -1 **LED_GND = -2** **LED_GND = -3** **LED_GND = -4**

Figure A-4 Crosstalk problem on the generation III microLED/CMOS driver [82]

A.4. Generation IV: 16x16 Voltage controlled MicroLED Driver Array

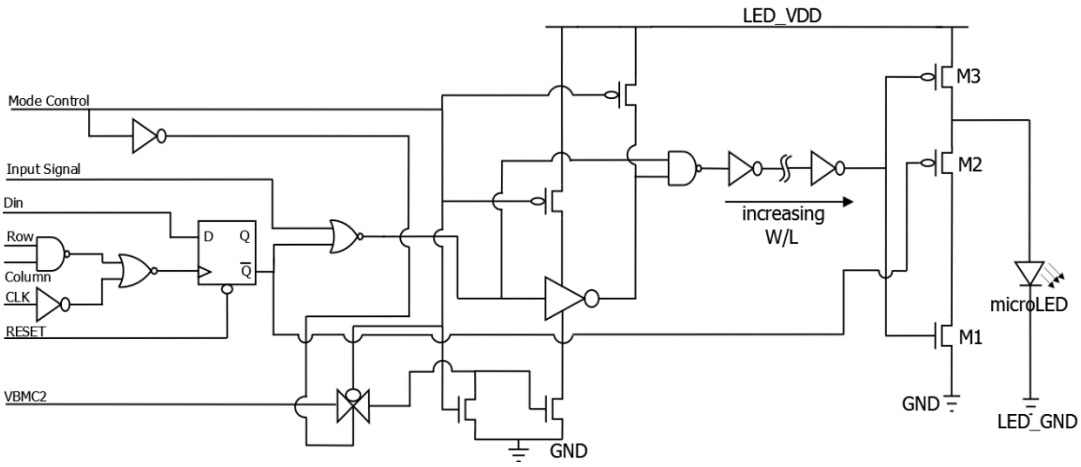

Figure A-5: Generation IV microLED/CMOS driver [82]

Fourth generation microLED driver again was fabricated using AMS 0.35µm Standard Process. An array of 16x16 was implemented this time and each pixel is 100µmx100µm. The main objective of the new design was to reduce the pixel area back to 100µmx100µm. This was made possible by using a smaller bond-stack and the replacement of the physically large, high voltage (5V) transistors with 3.3V transistors. Bond-stack area was made smaller reducing the area from 100µmx100µm (on the previous generation) to 60µmx60µm. Although this step was able to reduce the pixel size, the driver's fill factor is still very low at 64%.

To compensate the voltage reduction across the microLED, LED_GND was made tuneable in a reverse bias condition. Therefore the current flowing through the microLED is dictated by the reverse bias condition set to LED_GND which is fully determined by its I-V characteristics. Nonetheless, it is important to remember that cross-talk was an issue in generation III due to LED_GND being a global signal as mentioned in the previous section. To overcome this problem, transistor M2 is placed in between the two NMOS-PMOS (M1-M3) inverter transistor. Without transistor M2, when LED_GND is negatively bias, GND become more positive and therefore M1 starts to discharge current via microLED. By placing the M2, it blocks the path hence reducing the crosstalk effect.

Another extra feature that was included in the Fourth Generation MicroLED driver in the ability to switch ***input_signal*** between ***common_input*** *or* ***parallel_ input***. ***Common_input*** means that the array would have a signal common input while ***Parallel_input*** means that each column of the drivers can be modulated by a separate input signal. This would allow the array to be driver with up to 16 independent parallel data simultaneously.

The replacement of physically large 5V transistors (including level shifter) with standard 3.3V transistors means that more space is available within the pixel for a large 3.3V transistor. The driver was able to produce up to about 180mA of current through the microLED and generated about 3.5mW of optical power.

References

[1] A. Goldsmith, Wireless Communications, Cambridge University, 2005.

[2] J. S. Belrose, "Fessenden and Marconi: their differing technologies and transatlantic experiments during the first decade of this century," IEEE, Sept 1995. [Online]. Available: http://www.ieee.ca/millennium/radio/radio_differences.html. [Accessed 2013].

[3] "The United Kingdom Frequency Allocation Table," [Online]. Available: http://stakeholders.ofcom.org.uk/spectrum/information/uk-fat/. [Accessed 2013].

[4] J. Condliffe, "Will Li-Fi be the new Wi-Fi?," NewScientist, [Online]. Available: http://www.newscientist.com/article/mg21128225.400-will-lifi-be-the-new-wifi.html#.UzOUGc5a6I4. [Accessed 2012].

[5] C. Schilling, "Effects of exposure to very high frequency radio frequency radiation on six antenna engineers in two separate incidents," *Occupational Medicine,* vol. 50, no. 1, pp. 49-56, 2000.

[6] ANSES, "Health Effects of lighting systems using light-emitting diodes (LEDs)," Jan. 2013. [Online]. Available: www.anses.fr/en/content/led---light-emitting-diodes. [Accessed 2 2013].

[7] T. Komine, Y. Tanaka, S. Haruyama and M. Nakagawa, "Basic Study on Visible Light Communication using Light Emitting Diode Illumination," in *Proceedings of 8th International Symposium on Microwave and Optical Technology (ISMOT),* Montreal, Canada, 2001.

[8] E. T. Won, D. Shin, D. Jung, Y. Oh, T. Bae, H.-C. Kwon, C. Cho and J. Son, "Visible Light Communication : Tutorial," 2008. [Online]. Available: http://ieee82.org/802_tutorials/2008_03/15-08-0114-02-000-VLC_Tutorial_MCO_Samsung-VLC-Oxford_2008-03-17.pdf.. [Accessed 2011].

[9] "JEITA standards," Japan Electronics and Information Technology Industries Association (JEITA), 3 2007. [Online]. Available: www.jeita.or.jp/cgi-bin/standard_e/list.cgi?cateid=1&subcateid=50. [Accessed 2011].

[10] C. Pohlmann, "Visible Light Communication," in *Seminar of Communication Standard in Medical,* Lubeck, 2010.

[11] "Visible Light Communication Consortium (VLCC) Released Visible Light Communication Standard Based on IrDA core specification," Business Wire, March 2009. [Online]. Available:

www.businesswire.com/news/home/20090312006284/en/Visible-Light-Communications-Consortium-VLCC-Released-Visible#.UuHUSbQZ7IU. [Accessed 2011].

[12] V. V. Huynh, L. N. Tuan and Yeong Min Jan, "Priority MAC based on multi-parameter for IEEE 802.15.7," *International Conference on ICT Convergence (ICTC),* pp. 257-260, 2011.

[13] "IEEE 802.15 WPAN-Visible Light Communication Interest Group," IEEE, [Online]. Available: http://www.ieee802.org/15/pub/IGvlc.html. [Accessed 2011].

[14] C. H. Sterling, Military Communications: From Ancient Times to the 21st Century, ABC-CLIO, 2007.

[15] G. W. Dunnington, J. Gray and F.-E. Dohse, Carl Friedrich Gauss: Titan of Science, The Mathematical Association of America, 2004, pp. 122-127.

[16] L. P. Caron Jr, Morse Code: The Essential Language, Amatuer Radio Relay League, 1996.

[17] A. Ghatak, Optics, Tata McGraw-Hill, 2008.

[18] R. G. Gould, "The LASER: Light Amplification by Stimulated Emission of Radiation," in *The Ann Arbor Conference on Optical Pumping*, Michigan, USA, June 1959.

[19] R. N. Hall, G. Fenner, J. Kingsley, T. Soltys and R. Carlson, "Coherent Light Emission From GaAs Junctions," *Physical Review Letters,* vol. 9, pp. 366-369, Nov. 1962.

[20] O. Brader and H. Lui, "Laser Safety and the Eye: Hidden Hazards and Practical Pearls," Presented at the American Academy of Dermatology, Feb. 1996.

[21] J. Khan and J. Barry, "Wireless Infrared Communications," *Proceedings of IEEE,* vol. 85, no. 2, pp. 265-298, Feb. 1997.

[22] OSRAM-OptoSemiconductor, "Eye Safety of IREDs used in Lamp Applications - Application Notes," 2010. [Online]. Available: http://www.osram-os.com/Graphics/XPic2/00052113_0.pdf/Application_Note_Eye_Safety.pdf. [Accessed 2012].

[23] H. Round, "A note Carborundum," *Electrical World,* vol. 19, p. 309, 1907.

[24] J. A. Edmond, H.-S. Kong and C. H. C. Jr, "Blue LEDs, UV photodiodes and high-temperature rectifiers in 6H-SiC," *Physica B: Condensed Matter,* vol. 185, no. 1-4, pp. 453-460, April 1993.

[25] R. Braunstein, “Radiative Transition in Semiconductor,” *Physical Review,* vol. 99, no. 6, pp. 1892-1893, 1955.

[26] E. F. Schubert, Light Emittind Diodes, Cambridge University Press, 2003.

[27] “Takeda Award 2002 Achievement Fact Sheet,” April 2002. [Online]. Available: http://www.takeda-foundation.jp/en/award/takeda/2002/fact/pdf/fact01.pdf. [Accessed 2012].

[28] “High-Power InGaN/GaN Double-Heterostructure Violet Light Emitting Diodes,” *Appl. Phys. Lett.,* vol. 62, no. 19, 1993.

[29] J. Kovac, L. Peternai and O. Lengyel, “Advanced Light Emittind Diodes Structures for Optoelectronics Applications,” *Thin Solid Films,* vol. 433, no. 1-2, pp. 22-26, 2003.

[30] “The Market for High Brightness LEDs in Lighting Applications: Market Review and Forecast 2013,” April 2013. [Online]. Available: http://www.strategies-u.com/articles/reports/market-for-high-brightness-leds-in-lighting-applications-2013.html. [Accessed 2013].

[31] “Phasing Out Incandescent Bulbs in EU: Technical Briefing,” European Comission, Dec. 2008. [Online]. Available: http://ec.europa.eu/energy/efficiency/. [Accessed 2011].

[32] M. Akanegawa, Y. Tanaka and M. Nakagawa, “Basic Study on Traffic Information Systems Using LED Traffic Lights,” *IEEE Transactions on Intelligent Transportation Systems,* vol. 2, no. 4, pp. 197-203, 2001.

[33] G. Pang, T. Kwan, H. Liu and C. Chan, “LED Wireless: A novel use of LEDs to transmit audio and digital signals,” *IEEE Industry Applications Magazine,* vol. 8, Jan 2002.

[34] T. Komine and M. Nakagawa, “Integrated Ststems of White LED Visible Light Communications and Power Line Communications,” *IEEE Transactions on Consumer Electronics,* vol. 49, Feb. 2003.

[35] The OMEGA Project, [Online]. Available: http://www.ictomega.eu. [Accessed 2011].

[36] Smart Lighting Engineering Research Centre, [Online]. Available: http://smartlighting.rpi.edu. [Accessed 2011].

[37] Ultra Parallel Visible Light Communication (UPVLC), [Online]. Available: http://gow.epsrc.ac.uk/NGBOViewGrant.aspx?GrantReg=EP/K00042X/1.

[38] H. Hass, “TEDtalk: Wireless Data From Every Light Bulb,” TED, [Online]. Available: http://www.ted.com/talks/harald_haas_wireless_data_from_every_light_bulb.html.

[39] T. Komine and M. Nakagawa, “Fundamental Analysis For Visible Light Communication System Using LED Lights,” *IEEE Transactions on Consumer Electronics*, vol. 50, no. 1, pp. 100-107, Feb. 2004.

[40] Y. Tanaka, T. Komine, S. Haruyama and M. Nakagawa, “Indoor Visible Light Communication Utilizing Plural White LEDs as Lighting,” in *The 12th IEEE International Symposium on Personal, Indoor and Mobile Radio Communications (PIMRC 2001)*, San Diego, CA, Sept. 2001.

[41] H. L. Minh, D. O'Brien, G. Faulkner, L. Zeng, K. Lee, D. Jung, Y. Oh and E. Won, “100-Mb/s NRZ Visible Light Communications Using a Postequalized White LED,” *IEEE Photonics Technology Letters*, vol. 21, pp. 1063-1065, Aug 2009.

[42] J.Grubor, S. Lee, K. Langer, T. Koonen and J. Walewski, “Wireless High Speed Data Transmission With Phosphorent White Light LEDs,” in *European Conference of Optical Communications (ECOC 2007)*, Berlin, Germany, Jun 11, 2007.

[43] R. Chang, “Orthogonal Frequency Multiplexed Data Transmission System”. U.S. Patent 3,488,455, 1966.

[44] J. Salz and S. Weinstein, “Fourier Transform Communication System,” in *The 1st ACM Symposium On Problems in the Optimization of Data Communications Systems*, New York, USA.

[45] A. Peled and A. Ruiz, “Frequency Domain Data Transmission Using Reduced Computational Complexity Algorithm,” in *IEEE International Conference of ICASSP*, Apr. 1980.

[46] I. Teletar, “Capacity of Multi-Antenna Gaussian Channels,” *European Transactions on Telecommunications*, vol. 10, no. 6, pp. 585-595, Nov./Dec. 1999.

[47] L. Cimini Jr., “Analysis And Simulation of a Digital Mobile Channel Using Orthogonal Frequency Division Multiplexing,” *IEEE Transactions on Communications*, Vols. CM-33, pp. 665-675, 1985.

[48] R. Lasalle and M. Alard, “Principles of Modulation and Channel Coding for Digital Broadcasting For Mobile Receivers,” *EBU Technical Review*, pp. 168-190, 1987.

[49] I. Koffman and V. Roman, “Broadband Wireless Access Solutions Based on OFDM Access in IEEE 802.16,” *IEEE Communications Magazine*, vol. 40, pp. 96-103, 2002.

[50] U. Reimers, "Digital Video Broadcasting," *IEEE Communications Magazine,* vol. 36, pp. 104-110, 1998.

[51] J. Armstrong, "OFDM for Optical Communications," *Journal of Lightwave Technology,* vol. 27, no. 3, Feb. 2009.

[52] A. R. Bahai, B. R. Saltzber and M. Ergen, Multi-Carrier Digital Communications Theory and Applications of OFDM, Springer, 2004.

[53] O.Gonzalez, R. Perez-Jimenez, S. Rodriguez, J. Rabadan and A. Ayala, "Adaptive OFDM System For Communication Over the Indoor Wireless Optical Channel," *IEEE Proceedings on Optoelectronics,* vol. 153, pp. 139-144, 2006.

[54] Hranilovic, "On the Design of Bandwidth Efficient Signalling For Indoor Wireless Optical Channels," *International Journal on Communications,* vol. 18, pp. 205-228, 2005.

[55] J. Armstrong and A. Lowery, "Power Efficient Optical OFDM," *Electronics Letters,* vol. 42, pp. 370-372, 2006.

[56] R. Abu-Alhiga and H. Hass, "Subcarrier Index Modulation OFDM," in *IEEE 20th International Symposium on Personal, Indoor and Mobile Radio Communications,* Sept. 2009.

[57] D. Tsonev, S. Sinanovic and H. Hass, "Novel Unipolar Orthogonal Frequency Division Multiplexing (U-OFDM) for Optical Wireless," in *IEEE 75th Vehicular Technology Conference (VTC Spring),* May 2012.

[58] N. Fernando, Y. Hong and E. Viterbo, "Flip-OFDM for Optical Wireless Communications," in *Information Theory Workshop (ITW),* Oct. 2011.

[59] J. Armstrong and B. Schmidt, "Comparison of Asymmetrically Clipped Optical OFDM and DC-Biased Optical OFDM in AWGN," *Communications Letters, IEEE,* vol. 12, no. 5, pp. 343-345, May 2008.

[60] N. Cvijetic and W. Ting, "WiMAX Over Free-Space Optics - Evaluating OFDM Multi-Subcarrier Modulation In Optical Wireless Channels," in *Sarnoff Symposium,* Princeton, USA, 2006.

[61] R. Prasad, OFDM for Wireless Communication, Artech House Publisher, 2004.

[62] S. S. Das, F. Tariq, M. I. Rahman, F. B. Frederiksen, E. D. Carvalho and R. Prasad, "Impact of Nonlinear Power Amplifier on Link Adaptation Algorithm of OFDM Systems," in *Vehicular Technology Conference* , 2007.

[63] V. Ahirwar and S. Rajan, “Tradeoff Between PAPR Reduction and Decoding Complexity in Transformed OFDM Systems,” in *International Symposium on Information Theory (ISIT),* Sept. 2005.

[64] B. Inan, S. Lee, S. Randel, I. Neokosmidis, A. Koonen and J. Walewski, “Impact of LED Nonlinearity on Discrete Multitone Modulation,” *IEEE/OSA Journal of Optical Communications and Networking,* vol. 1, no. 5, pp. 439-451, Oct. 2009.

[65] H. Elgala, R. Mesleh and H. Hass, “A Study of LED nonlinearity Effects on Optical Wireless Transmission using OFDM,” in *Wireless and Optical Communications Networks,* Apr. 2009.

[66] D. Dardari, V. Tralli and A. Vaccari, “A Theoretical Characterization of Nonlinear Distortion Effects in OFDM Systems,” *IEEE Transactions on Communications,* vol. 48, no. 10, pp. 1755-1764, Oct. 2000.

[67] X. Li and L. Cimini Jr, “Effects of Clipping and Filtering on the Performance of OFDM,” *IEEE Communications Letters,* vol. 2, no. 5, pp. 131-133, May 1998.

[68] I. Stefan, H. Elgala, R. Mesleh, D. O'Brien and H. Haas, “Optical Wireless OFDM System on FPGA: Study of LED Nonlinearity Effects,” in *IEEE 73rd Vehicular Technology Conference (VTC Spring),* Yokohama, May 2011.

[69] “An Overview of Linear Amplifier Systems,” Application Notes on Ultra RF, [Online]. Available: http://www.cree.com/ftp/appnote1.pdf. [Accessed 2011].

[70] V. Petrovic and W. Gosling, “Reduction of intermodulation distortion by means of modulation feedback,” in *IEE Conference on Radio Spectrum Conversion Techniques*, 1983.

[71] F. Tabatabai, Linearization Techniques to Suppress Optical Nonlinearity, Ph.D. Thesis, 2008.

[72] T. Bennett and R. Clements, “Feedforward - An Alternative Approach To Amplifier Linearization,” *RF, Radio and Electronic Engineer,* vol. 44, no. 5, pp. 257-262, 1974.

[73] H.-G. Ryu, “Combination of PAPR Reduction And Linearization For The OFDM Communication System,” *Wireless Communications and Mobile Computing,* vol. 11, no. 1, pp. 46-52, Jan. 2011.

[74] W. Shieh, H. Bao and Y. Tang, “Coherent Optical OFDM: Theory and Design,” *Optics Express,* vol. 16, no. 2, pp. 841-859, 2008.

[75] K. Acolatse, Y. Bar-Ness and S. K. Wilson, “Novel Techniques of Single-Carrier Frequency-Domain Equalization for Optical Wireless Communications,” *EURASIP Journal of Advance Signal Process,* vol. 2011, no. 4, pp. 1-13, Jan. 2011.

[76] J. Grubor, V. Jungnickel and K.-D. Langer, "Adaptive Optical Wireless OFDM System with Controlled Asymmetric Clipping," in *Conference Record of the 41st Asilomar Conference on Signals, Systems and Computers (ACSSC)*, Nov. 2007.

[77] H. Zimmermann, Silicon Optoelectronic Integrated Circuits, Springer, 2004.

[78] J. McKendry, R. P. Green, A. Kelly, Z. Gong, B. Guilhabert, D. Massuobre, E. Gu and M. D. Dawson, "High Speed Visible Light Communication Using Individual Pixels in a Micro-Light Emittind Diode Array," *Photonics Technology Letters*, vol. 22, no. 18, pp. 1346-1348, Sept. 2010.

[79] J. McKendry, D. Massoubre, S. Zhang, B. Rae, R. Green, E. Gu, R. Henderson, A. Kelly and M. Dawson, "Visible-Light Communication Using a CMOS-Controlled Micro-Light-Emitting-Diode-Array," *Journal of Lightwave Technology*, vol. 30, no. 1, pp. 61-67, Jan. 2012.

[80] "HYPIX," [Online]. Available: http://hypix.photonics.ac.uk/.

[81] G. Tsiminis, Y. Wang, P. E. Shaw, A. Kanibolotsky, I. Perepichka, M. Dawson, P. Skabara, G. A. Turnbull and I. D. W. Samuel, "Low-threshold organic laser based on an oligofluorene truxene with low optical losses," *Applied Physics Letters*, vol. 94, 2009.

[82] B. Rae, Micro-Systems for Time-Resolved Fluorescence Analysis Using CMOS Sigle-Photon Avalanche Diodes and MicroLEDs, Ph.D. Thesis, 2009.

[83] J. McKendry, Micro-Pixellated AlInGaN Light-Emitting-Diode Arrays for Optical Communications and Time-Resolved Fluorescene Lifetime Measurements, Ph.D. Thesis, 2011.

[84] C. Jeon, H. Choi and M. Dawson, "Fabrication of Matrix-addressable, InGaN-based Microdisplay of High Array Density," *IEEE Photonics Technology Letters*, vol. 15, pp. 1516-1518, 2003.

[85] C.Jeon, H. Choi and M. Dawson, "High Density Matrix-addressable AlInGaN-based 368nm Microarray Light Emitting Diodes," *IEEE Photonics Technology Letter*, vol. 16, pp. 2421-2423, 2004.

[86] D. Massoubre, J. McKendry, B. Guilhabert, Z. Gong, I. Watson, E. Gu and M. Dawson, "Fabrication of Planar GaN-based Micro-pixel Light Emitting Diode Arrays," *IEEE LEOS Annual Meeting Conference Proceedings, 2009*, pp. 84-85, Oct. 2009.

[87] S. Zhang, S. Watson, J. McKendry, D. Massoubre, A. Cogman, E. Gu, R. Henderson, A. Kelly and M. Dawson, "1.5Gbit/s Multi-Channel Visible Light Communications

Using CMOS-Controlled GaN-Based LEDs," *Journal of Lightwave Technology,* vol. 31, no. 8, pp. 1211-1216, Apr. 2013.

[88] B. Inan, S. J. Lee, S. Randel, I. Neokosmidis, A. Koonen and J. Walewski, "Impact of LED Nonlinearity on Discrete Multitone Modulation," *Journal of Optical Communications and Networking,* vol. 1, no. 5, pp. 439-451, Oct. 2009.

[89] "0.35um HBT BiCMOS process parameter," May 2009. [Online]. Available: http://asic.ams.com. [Accessed 2011].

[90] S. Lee, R. Hon, S. X. Zhang and C. Wong, "3D stacked flip chip packaging with through silicon vias and copper plating or conductive adhesive filling," in *Electronic Components and Technology Conference*, June 2005.

[91] Y. Choi, J. Shin and K.-W. Paik, "A study on the 3D-TSV interconnection using wafer-level non-conductive adhesives (NCAs)," in *Electronic Components and Technology Conference (ECTC)*, May 2011.

[92] N. Khan, D. Wee, O. S. Chiew, C. Sharmani, L. S. Lim, H. Y. Li and S. Vasarala, "Three chips stacking with low volume solder using single re-flow process," in *Electronic Components and Technology Conference (ECTC)*, USA, June 2010.

[93] "Optocap Ltd.," [Online]. Available: www.Optocap.com.

[94] "Palomar Technologies," [Online]. Available: www.palormartechnologies.com.

[95] "Finetech GmbH & Co. KG," [Online]. Available: http://www.finetech.de/home.html.

[96] "Opal Kelly XEM3010's User Manual," 2009. [Online]. Available: http://www.opalkelly.com. [Accessed 2012].

[97] J. Herrnsdorf, "CMOS LEDs: Pulsing with BERT," in *HYPIX Project Report*, June 2013.

[98] J. Herrnsdorf, Y. Wang, J. J. McKendry, Z. Gong, D. Massoubre, B. Guilhabert, G. Tsiminis, G. A. Turnbull, I. D. Samuel, N. Laurand, E. Gu and M. D. Dawson, "Micro-LED pumped polymer laser: A discussion of future pump sources for organic lasers," *Laser and Photonics Review,* vol. 7, pp. 1065-1078, Sept. 2013.

[99] Y. Wang, G. Tsiminis, A. L. Kanibolotsky, P. J. Skabara, I. D. Samuel and G. A. Turnbull, "Nanoimprinted polymer lasers with threshold below 100 W/cm2 using mixed-order distributed feedback resonators," *Optics Express,* vol. 21, no. 12, pp. 14362-14367, Aug. 2013.

[100] B. Razavi, Design of Analog CMOS Integrated Circuit, McGraw-Hill , 2001.

[101] P. E. Allen and D. R. Holberg, CMOS Analog Circuit Design, Oxford University Press, 2002.

[102] “Digital Handheld Laser Power and Energy Meter Console,” Thorlabs, [Online]. Available: http://www.thorlabs.com/newgrouppage9.cfm?objectgroup_id=3341.

[103] “PDA10A - Si Fixed Gain Detector,” Thorlabs, [Online]. Available: http://www.thorlabs.com/thorproduct.cfm?partnumber=PDA10A.

[104] “ESG Vector Signal Generator (EC4438C),” Agilent Technologies Inc., [Online]. Available: www.home.agilent.com/en/pd-1000004297%3Aepsg%3Apro-pn-E4438C/.

[105] “Digital Signal Analyser (DSA90804A),” Agilent Technologies, [Online]. Available: www.home.agilent.com/en/pd-1308273-pn-DSA90804A/.

[106] J. McKendry, *RE: MicroLED leakage light measurement,* Personal Email, 2011.

[107] M. Ingels and M. Steyaert, Integrated CMOS Circuits for Optical Communications, Springer, 2003.

[108] H. Tian, B. Fowler and A. Gamal, “Analysis of temporal noise in CMOS photodiode active pixel sensor,” *Solid-State Circuits, IEEE Journal of* , Vols. 92-101, no. 1, p. 36, Jan 2001.

[109] Hamamatsu, “OPTO-SEMICONDUCTOR HANDBOOK,” [Online]. Available: http://www.hamamatsu.com/resources/pdf/ssd/e02_handbook_si_photodiode.pdf.

[110] S. M. Sze and K. K. Ng, Physics of Semiconductor Devices, Wiley-Interscience, 2006.

[111] S. Radovanovi´c, High Speed Photodiodes in CMOS Technology, Ph.D. Thesis, 2004.

[112] M. Li, 5 GHz Optical Front End in 0.35um CMOS, Ph.D. Thesis, 2007.

[113] Y. J. Chen, An Integrated CMOS Optical receiver with clock and data recovery circuit, 2005: MSc. Thesis.

[114] G. Koklu, R. Etienne-Cummings, Y. Leblebici, G. De Micheli and S. Carrara, “Characterization of standard CMOS compatible photodiodes and pixels for Lab-on-Chip devices,” *Circuits and Systems (ISCAS), 2013 IEEE International Symposium on,* pp. 1075-1078, May 2013.

[115] P. R. Gray, Analysis and Design of Analog Integrated Circuits, John Wiley & Sons, 1984.

[116] C. Niclass, M. Sergio and E. Charbon, “A Single Photon Avalanche Diode Array Fabricated in Deep-Submicron CMOS Technology,” *Design, Automation and Test in Europe, 2006. DATE '06. Proceedings ,,* vol. 1, pp. 1-6, March 2006.

[117] “OSLON SSL (LBCPDP-GYHY-35) - Technical Data Sheet,” OSRAM Opto Semiconductor, 2011.

[118] F. Rusek, D. Persson, B. K. Lau, E. G. Larsson, T. L. Marzetta, O. Edfors and F. Tufvesson, “Scaling up MIMO: opportunities and challenges with very large arrays,” *IEEE Signal Processing Magazine* , vol. 30, no. 1, pp. 40-60, 2013 .

[119] D. Jokanovic and M. Josipovic, “RF spectrum congestion: Resolving an interference case,” *Microwaves, Communications, Antennas and Electronics Systems (COMCAS), 2011 IEEE International Conference on,* pp. 1-4, Nov. 2011.

[120] I. Cisco Systems, “RF Spectrum Policy: Future-Proof Wireless Investment Through Better Compliance,” 2009. [Online]. Available: http://www.cisco.com/c/en/us/products/collateral/wireless/spectrum-expert/prod_white_paper0900aecd8073bef9.pdf. [Accessed 2013].

[121] T. Communcations, “Congestion in the Radio Frequency Spectrum,” 2012 Sept. [Online]. Available: http://blog.taitradio.com/2012/09/06/congestion-in-the-radio-frequency-spectrum/. [Accessed 2013].

[122] B. Mulgrew, P. Grant and J. Thompson, Digital Signal Processing: Concepts and Applications, Palgrave Macmillan, 2002.

[123] N. Cvijetic and Ting Wang, “WiMAX over Free-Space Optics - Evaluating OFDM Multi-Subcarrier Modulation in Optical Wireless Channels,” *Sarnoff Symposium, 2006 IEEE,* pp. 1-4, March 2006.

[124] T. Yokoshima, K. Nomura, Y. Yamaji, K. Kikuchi, H. Nakagawa, K. Koshiji, M. Aoyagi, R. Iwai, T. Tokuhisa and M. Kato, “Formation of Au Microbump Arrays for Flip-Chip Bonding Using Electroless Au Deposition from a Non-Cyanide Plating Bath,” *Transaction of Japan Institute of Electronics Packaging,* vol. 2, no. 1, pp. 109-115, 2009.

[125] H. Yuyang, Z. Yuxiang, Y. Zhizhen, C. Guoxin, L. H. C, B. Lifeng, Y. Hui and Z. Yaohui, “Indium bump array fabrication on small CMOS circuit for flip-chip bonding,” *Journal of Semiconductors,* vol. 32, no. 11, November 2011.

[126] “Gold Bonding Wire for Chip & Wafer-level Bumping Applications,” Heraeus Materials Technology, [Online]. Available: http://heraeus-contactmaterials.com/media/webmedia_local/media/downloads/documentsbw/factsheets_bw_2012/Factsheet_AW6_2012.pdf. [Accessed 2013].